Low Temperature AC Susceptibility of the Frustrated Spin-1/2 Antiferromagnetic Kagomé System Herbertsmithite

Master's thesis
Written by *Thomas Sahl Christensen*
September 5, 2023

Supervised by
Kim Lefmann

University of Copenhagen

UNIVERSITY OF
COPENHAGEN

NAME OF INSTITUTE:	Faculty of Science
NAME OF DEPARTMENT:	Niels Bohr Institute
AUTHOR(S):	Thomas Sahl Christensen
EMAIL:	bqc703@alumni.ku.dk
TITLE AND SUBTITLE:	Low Temperature AC Susceptibility of the Frustrated Spin-1/2 Antiferromagnetic Kagomé System Herbertsmithite -
SUPERVISOR(S):	Kim Lefmann
HANDED IN:	05.09.2023
DEFENDED:	19.09.2023

NAME ______________________

SIGNATURE __________________

DATE ______________________

Abstract

This thesis studies the temperature-dependent AC susceptibility of titanium, cerium magnesium nitrate ($Ce_2Mg_3(NO_3)_{12} \cdot 24H_2O$), and herbertsmithite ($ZnCu_3(OH)_6Cl_2$) in the temperature range of ~ 0.015-6 K. Through measurements of titanium, we find an estimated critical onset temperature of $T_{\mathrm{c,onset}} \approx 74.3\,\mathrm{mK}$ and $T_{\mathrm{c,onset}} \approx 77\,\mathrm{mK}$ in terms of a heating and a cooling series, respectively using an excitation frequency of $\nu = 333\,\mathrm{Hz}$. The large deviation from the literature value ($\sim 450\,\mathrm{mK}$) [1], and the reported value (468 mK) by Ref. [2], is believed to be governed by the presence of impurities. Further, we find a frequency-dependence in $T_{\mathrm{c,onset}}$ which is believed to originate from induced eddy currents heating the sample. This interpretation is strengthened by the frequency-dependence being suppressed as a result of reducing the drive field. Anyhow, from these measurements the phase (Θ) required to separate the in-phase (χ') and out-of-phase (χ'') susceptibility for a variety of frequencies is extracted.

From measurements of $Ce_2Mg_3(NO_3)_{12} \cdot 24H_2O$, we utilize its approximate Curie behaviour to obtain an estimate of the sample temperature. We find that a cold finger temperature of $\sim 13\,\mathrm{mK}$ results in a sample temperature of $T_{\mathrm{sample}} \approx 27\,\mathrm{mK}$ and $T_{\mathrm{sample}} \approx 30\,\mathrm{mK}$ for $\nu = 333\,\mathrm{Hz}$ and $\nu = 1433\,\mathrm{Hz}$, respectively. In addition, we obtain a correction to the cold finger temperature outside the reliable range of the thermometer.

Finally, we present both high-temperature DC susceptibility measurements and low-temperature AC susceptibility measurements for $ZnCu_3(OH)_6Cl_2$. From the DC susceptibility measurements we find a Curie Weiss temperature of $\theta_{\mathrm{CW}} = -248(57)\,\mathrm{K}$ yielding an effective moment of $\mu_{\mathrm{eff}} = \sqrt{8C}\mu_{\mathrm{B}} = 1.91(10)\mu_{\mathrm{B}}$ and a g-factor of $g = 2.20(12)$. The large uncertainties are governed by overestimated uncertainties from the data.

From the low-temperature AC susceptibility measurements of $ZnCu_3(OH)_6Cl_2$, we find the intriguing occurrence of a peak in the in-phase component (χ') at $\sim 50\,\mathrm{mK}$, as well as an onset in the out-of-phase component (χ'') at $\sim 200\,\mathrm{mK}$. A Curie Weiss fit conducted in the range $\sim 0.02\,\mathrm{K}$-$6\,\mathrm{K}$ yields a Curie Weiss temperature of $\theta_{\mathrm{CW}} = -0.0561(10)\,\mathrm{K}$ – a factor of ~ 5000 smaller in magnitude than $\theta_{\mathrm{CW}} = -248(57)\,\mathrm{K}$ (high-temperature). Based on measurements for various excitation frequencies we cannot reject a minuscule frequency-dependence in the features observed. However, the lack of a signal in the 3rd harmonic susceptibility (χ_3), suggests the absence of spin glass behavior. Upon applying a DC field, subtraction of a background term is unable to position the susceptibility curves on a comparative scale for unknown reasons. However, subtracting an arbitrary offset, reveals signs of saturation effects in χ', and a suppression of the onset in χ'' for increasing DC fields. The former effect is in agreement with the observed behavior by Refs. [3, 4], whereas the latter effect is yet to be investigated.

Acknowledgements

First of all, I would sincerely like to thank, Kim Lefmann my supervisor, Emma Y. Leander, Henrik Rønnow, Ivica Zivkovic, and Finn Berg Rasmussen: Kim for his supervision, ideas and encouragement as well as his acceptance when mistakes occurred regarding the dilution refrigerator. Emma for the great cooperative work in the laboratory as well as having someone to share both the good and the frustrating times with during the project. Henrik Rønnow for teaching both Emma and I about the workings of the dilution refrigerator, both in general and for the specific instrument. Ivica for visiting our laboratory and sharing his experimental expertise both in AC susceptometry and dilution refrigeration, and helping us modify the system. Finn for sharing his ideas operating the dilution system to reach the lowest temperatures, as well as his interesting stories about his time in the field of dilution refrigeration.

I would like to thank Marianne L. Jensen for ordering necessary materials such as GE-vanish and stycast as well as dealing with the frustrating difficulty of importing the latter to Copenhagen.

Further, I would like to thank the NBI Mechanical and Electronic Workshop for providing us with the necessary utilities, such as coil forms, titanium, stycast, etc. I would, especially, like to thank Bent N. Jensen for repairing broken cables and wires crucial for the workings of the dilution refrigerator and the AC susceptometer.

In addition, I would like to thank Lars Lemming who, in cooperation with the workshop, repaired the broken IVC can, after taking damage from falling to the floor.

Thanks to Claus B. Sørensen for sharing his overall knowledge regarding the instrumentation in the laboratory.

Thanks to Mickey S. Pedersen for synthesizing the powder sample of herbertsmithite.

Last but not least, a huge thanks to my friend Emil J. P. Frost for proofreading the entire thesis and suggesting improvements. In addition to that, I am truly thankful for our long standing friendship of 5 years which comes with plenty unforgettable great memories that dates back to the beginning of the first year on the bachelor.

Contents

1 Introduction

Magnetic frustration is associated with high ground state degeneracy and (in the quantum case) quantum entanglement in the magnetic system. The phenomenon originates from quantum mechanical exchange interactions that cannot be simultaneously minimized [5–7]. Frustration suppresses the magnetic ordering temperature way below the temperature scale determined by the exchange interaction $\mathcal{J}$ [8]. Further, it introduces the possibility of a variety of exotic states, where spins may freeze in a random orientation and remain stuck in one of its many degenerate ground state configurations [7]. Early studies show that magnetic frustration were studied even back in 1950s [9]. The popularity of the research field has grown substantially since P. W. Anderson proposed the resonating-valence bond (RVB) state in 1973 [10, 11], and further, proposed a connection to high-temperature superconductivity in 1987 [12]. The RVB state is believed to represent the ground state of a quantum spin liquid (QSL), in broad sense, characterized by long-range quantum entanglement, fractional excitations, and no magnetic order down to absolute zero [5, 6, 13–15]. Given quantum effects are most evident at low temperature near absolute zero, it requires accessibility to such extreme environments in order to experimentally investigate the field of frustration. Nowadays, temperatures near absolute zero are easily obtained with the 3 dominating refrigeration techniques being helium-4 evaporation, ^{3}He-^{4}He dilution, and nuclear magnetic refrigeration covering the kelvin, millikelvin, and microkelvin range, respectively [16]. At these temperatures, AC susceptometry proves a valuable and versatile tool, probing the dynamic magnetic properties by measuring the material's response to a small oscillating magnetic field [17–20]. In this thesis, the AC susceptometry technique is utilized to measure the temperature-dependent AC susceptibility using a variety of excitation frequencies and DC background fields at dilution temperatures for titanium, cerium magnesium nitrate, and herbertsmithite.

Section 2 introduces the basic theory of magnetism such as paramagnetism, ferromagneitsm, and antiferromagnetism and its origins. From there on, it presents magnetic frustration and the relevant states of matter this may bring. Towards the end of the section, the concept of AC susceptibility is presented along with the AC susceptibility characteristics of the states of matter relevant to this thesis.

Section 3 introduces the theoretical model of the cooling process in a dilution refrigerator. Then it moves on to the practical functionality behind the dilution refrigerator, and shows illustrative graphs of some of the cooldowns conducted throughout the year. In the last half of the section, the concept of AC susceptometry is reviewed as well as various considerations and key concepts when working in the field.

Section 4 presents measurements for titanium with the purpose of determining the phase required to separate the AC susceptibility in terms of the in-phase (χ') and the out-of-phase component (χ'').

Section 5 utilizes cerium magnesium nitrate as a thermometer to convert between the recorded cold finger temperature and the sample temperature. Further, it proposes a correction to the recorded cold finger temperature outside the reliable range of the thermometer.

Section 6 shows intriguing measurements of the highly frustrated compound herbertsmithite, which, with its perfect kagomé layers consisting of Cu^{2+} ions, remains a leading QSL candidate [6, 13–15].

2 Magnetism

2.1 Magnetic susceptibility

In vacuum, the magnetic flux density **B** relates linearly to the magnetic field strength **H**:

$$\mathbf{B} = \mu_0 \mathbf{H} \tag{1}$$

where the constant of proportionality, $\mu_0 = 4\pi \times 10^{-7}\,\mathrm{Hm}^{-1}$ is the permeability of free space. The magnetic flux density and the magnetic field strength are measured in the SI-units tesla (T) and ampere per meter (Am^{-1}) respectively. However, both of these quantities are usually in literature referred to as the magnetic field, and the letters 'B' and 'H' are further used to specify the magnetic field of interest. This thesis will proceed adopting this syntax.

If a magnetic solid is present in the region of the applied field, the relationship between **B** and **H** takes the general form:

$$\mathbf{B} = \mu_0 \left(\mathbf{H} + \mathbf{M}\right) \tag{2}$$

where **M** represents the magnetization of the solid, which is defined as the magnetic moment per unit volume [7, 21]. The magnetization for magnetic materials remain field-dependent and can be a complicated function. In theory, the magnetic susceptibility represents the relationship between the magnetization and the applied field, and is in its most general form defined as:

$$\boldsymbol{\chi} = \frac{\partial \mathbf{M}}{\partial \mathbf{H}} \tag{3}$$

where the susceptibility is a tensor such that $\chi_{\alpha\beta} = \frac{\partial M_\alpha}{\partial H_\beta}$, with $\alpha, \beta \in \{x, y, z\}$ [17, 22–24]. In isotropic cases, it reduces to a scalar independent of the direction of the spatial coordinates. In most cases for small fields, the magnetization remains linear and therefore becomes:

$$\mathbf{M} = \chi \mathbf{H} \tag{4}$$

meaning the magnetic field **B** becomes:

$$\mathbf{B} = \mu_0 \left(1 + \chi\right) \mathbf{H} = \mu_0 \mu_\mathrm{r} \mathbf{H} \tag{5}$$

where $\mu_\mathrm{r} = 1 + \chi$ is the relative permeability for the material of interest. However, one has to be careful when it comes to the definition of fields in magnetic materials, since the internal field inside a material $\mathbf{B_i}$ and $\mathbf{H_i}$, which are produced by the magnetic moments, can differ significantly from the applied fields $\mathbf{B_a}$ and $\mathbf{H_a}$ due to the fact that the internal fields can be highly positioned dependent [7]. In principal, the internal magnetic field can be broken into two components for an arbitrary shape:

$$\mathbf{H_i}\left(\mathbf{r}\right) = \mathbf{H_a}\left(\mathbf{r}\right) + \mathbf{H_d}\left(\mathbf{r}\right) \qquad \mathbf{B_i}\left(\mathbf{r}\right) = \mathbf{B_a}\left(\mathbf{r}\right) + \mathbf{B_d}\left(\mathbf{r}\right) \tag{6}$$

However, for an ellipsoidal shape, the demagnetization field is uniform, meaning it can be written as:

$$\left(H_\mathrm{d}\right)_i = -\sum_j N_{ij} M_j, \tag{7}$$

where **N** represents the demagnetization tensor. If the magnetization points along one of the principal axes of the ellipsoidal shape, it can be diagonalized such that **N** becomes a scalar. Further, when measuring susceptibility, one has to keep in mind that the measured susceptibility corresponds to the experimental susceptibility (χ_{exp}) which relates to the applied field, which further relates to the intrinsic susceptibility (χ_{int}) as follows:

$$\chi_{\text{exp}} = \frac{\chi_{\text{int}}}{1 + N\chi_{\text{int}}}. \tag{8}$$

However, for weak magnetism ($N\chi_{\text{int}} \ll 1$) one has $\chi_{\text{exp}} \approx \chi_{\text{int}}$, meaning the effect of demagnetization can be ignored. Although, in case of ferromagnetism or superconductivity this effect remains significant [7].

2.2 A single atom in a magnetic field

The energy of an electron in a magnetic field due to it's intrinsic angular momentum (spin) is given by $E = -\boldsymbol{\mu}_{\mathbf{e}} \cdot \mathbf{B}$ where $\boldsymbol{\mu}_{\mathbf{e}} = -g\mu_{\text{B}}\mathbf{s}$ represents the electron's intrinsic magnetic moment. Thus, the energy becomes:

$$E = g\mu_{\text{B}} m_s B \approx \pm\mu_{\text{B}} B, \tag{9}$$

using $m_s = \pm\frac{1}{2}$ and $g \approx 2$ [7, 21, 23, 24] . In addition, the electrons possess orbital angular momentum, and for a system of multiple electrons, the total angular momentum is given by $\hbar\mathbf{L} = \sum_i \mathbf{r}_i \times \mathbf{p}_i$, where the sum is taken over all electrons in the system. Neglecting the external magnetic field, the unperturbed Hamiltonian for the Z number of electrons of an atom is given by:

$$\hat{\mathcal{H}}_0 = \sum_{i=1}^{Z} \left[\frac{\mathbf{p}_i^2}{2m_{\text{e}}} + V_i \right], \tag{10}$$

where V_i represents the potential for the i'th electron. By adding a magnetic field the Hamiltonian should include the energy shift caused by the coupling between the magnetic field and the intrinsic angular momentum of each electron, and the kinetic momentum has to be replaced by the canonical momentum, $\mathbf{p}_i \to (\mathbf{p}_i + e\mathbf{A})^2$. Therefore, the perturbed Hamiltonian takes the form:

$$\hat{\mathcal{H}} = \hat{\mathcal{H}}_0 + \hat{\mathcal{H}}' = \sum_{i}^{Z} \left[\frac{(\mathbf{p}_i + e\mathbf{A})^2}{2m_{\text{e}}} + V_i \right] + g\mu_{\text{B}}\mathbf{B} \cdot \mathbf{S} \tag{11}$$

where $\mathbf{S} = \sum_i \mathbf{s}_i$ represents the total spin in the system [7, 21, 23, 24]. The magnetic field is given by $\mathbf{B} = \boldsymbol{\nabla} \times \mathbf{A}$ and the gauge $\mathbf{A}(\mathbf{r}) = \frac{\mathbf{B}\times\mathbf{r}}{2}$ is chosen. By expanding the squared term, one obtains:

$$\begin{aligned} \hat{\mathcal{H}} &= \hat{\mathcal{H}}_0 + \sum_{i}^{Z} \frac{1}{2m_{\text{e}}} \left[(e\mathbf{A}(\mathbf{r}_i))^2 + e\left(\mathbf{p}_i \cdot \mathbf{A}(\mathbf{r}_i) + \mathbf{A}(\mathbf{r}_i) \cdot \mathbf{p}_i\right) \right] + g\mu_{\text{B}}\mathbf{B} \cdot \mathbf{S} \qquad (12) \\ &= \hat{\mathcal{H}}_0 + \sum_{i}^{Z} \left[\frac{e}{4m_{\text{e}}} \left(\mathbf{p}_i \cdot (\mathbf{B} \times \mathbf{r}_i) + (\mathbf{B} \times \mathbf{r}_i) \cdot \mathbf{p}_i\right) + \frac{e^2}{8m_{\text{e}}} (\mathbf{B} \times \mathbf{r}_i)^2 \right] + g\mu_{\text{B}}\mathbf{B} \cdot \mathbf{S} \qquad (13) \end{aligned}$$

Further, using that $[\mathbf{p}, \mathbf{B} \times \mathbf{r}] = 0$, $\mathbf{p} \cdot (\mathbf{B} \times \mathbf{r}) = \mathbf{B} \cdot (\mathbf{r} \times \mathbf{p})$ the Hamiltonian can be simplified to:

$$\hat{\mathcal{H}} = \hat{\mathcal{H}}_0 + \mu_{\text{B}} (\mathbf{L} + g\mathbf{S}) \cdot \mathbf{B} + \sum_{i}^{Z} \frac{e^2}{8m_{\text{e}}} (\mathbf{B} \times \mathbf{r}_i)^2 \tag{14}$$

The second term $\mu_{\text{B}} (\mathbf{L} + g\mathbf{S}) \cdot \mathbf{B}$ in Eq. (14) is considered the paramagnetic term which describes the energy gain of aligning the magnetic moment of the atom with the applied field. This term typically remains the dominant term and it corresponds to a positive magnetic susceptibility $\chi > 0$. The third term $\sum_i^Z \frac{e^2}{8m_{\text{e}}} (\mathbf{B} \times \mathbf{r}_i)^2$ in Eq. (14) is the diamagnetic term, caused by the magnetic moments pointing anti-parallel with respect to the applied field, which corresponds to a negative magnetic susceptibility $\chi < 0$. The main case where the diamagnetic term remains of significance is for materials where the total angular momentum $\mathbf{J} = \mathbf{L} + \mathbf{S}$ takes a value of $\mathbf{J} = 0$. This typically happens for atoms with filled shell configurations [7, 21, 24].

2.3 Diamagnetism

2.3.1 Larmor Diamagnetism

The diamagnetic term in Eq. (14) gives rise to the diamagnetic susceptibility for which an expression can be fairly easily derived using first order perturbation theory. If one considers an atom with no unfilled electron shells, so the paramagnetic term in Eq. (14) can be neglected to first order and a magnetic field is applied along the z axis, one has that the ground state energy correction due to the last term in Eq. (14) is given by:

$$\Delta E_0^{(1)} = \frac{e^2B^2}{8m_e}\sum_{i=1}^{Z}\langle(x_i^2+y_i^2)\rangle = \frac{e^2B^2}{12m_e}\sum_{i=1}^{Z}\langle r_i^2\rangle \tag{15}$$

where a spherically symmetrically atom has been assumed, implying that $\langle x_i^2\rangle = \langle y_i^2\rangle = \frac{1}{3}\langle r_i^2\rangle$ [7, 21]. Thus, for a system with N atoms contained in a volume V at $T = 0\,\mathrm{K}$ one obtains a magnetization:

$$M = -\frac{dE}{dB} = -\frac{N}{V}\frac{e^2B}{6m_\mathrm{e}}\sum_{i=1}^{Z}\langle r_i^2\rangle, \tag{16}$$

and using $\mathbf{B} \approx \mu_0\mathbf{H}$ for small magnetic susceptibilities:

$$\chi_\mathrm{Larmor} = \mu_0\frac{dM}{dB} = -\frac{N}{V}\frac{e^2\mu_0}{6m_\mathrm{e}}\sum_{i=1}^{Z}\langle r_i^2\rangle \tag{17}$$

which is known as the *Larmor diamagnetic susceptibility.* For noble gasses and ionic salts the electrons in the outer shell have roughly the same radial distance, meaning the sum in Eq. (17) can be approximated as $Z_\mathrm{eff}r^2$ where Z_eff represents the number of electrons in the outer shell [7, 21].

2.4 Paramagnetism

2.4.1 Van Vleck Paramagnetism

As mentioned in Section 2.3.1, if $\mathbf{J} = 0$, the first order correction to the ground state energy from the paramagnetic term from Eq. (14) vanishes [7, 21]. However, using second order perturbation theory, a paramagnetic effect remains, since excited states with $\mathbf{J} \neq 0$ are accounted for

$$\Delta E_0^{(2)} = \sum_n \frac{|\langle 0|\mu_\mathrm{B}\left(\mathbf{L}+g\mathbf{S}\right)\cdot\mathbf{B}|n\rangle|^2}{E_0-E_n} = \mu_\mathrm{B}^2B^2\sum_n\frac{|\langle 0|\left(L_z+gS_z\right)|n\rangle|^2}{E_0-E_n} \tag{18}$$

where $\mathbf{B} = B\hat{z}$. And by assuming the same circumstances as in Section 2.3.1 the magnetization is given by

$$M = \frac{N}{V}2\mu_\mathrm{B}^2B\sum_n\frac{|\langle 0|\left(L_z+gS_z\right)|n\rangle|^2}{E_n-E_0} \tag{19}$$

for N atoms contained in a volume V at $T = 0\,\mathrm{K}$. Thus, the susceptibility $\chi \approx \mu_0\frac{\partial\mathbf{M}}{\partial\mathbf{B}}$ becomes:

$$\chi_\mathrm{vV} = \frac{N}{V}2\mu_\mathrm{B}^2\mu_0\sum_n\frac{|\langle 0|\left(L_z+gS_z\right)|n\rangle|^2}{E_n-E_0} \tag{20}$$

which is a positive quantity and known as the *Van Vleck paramagnetic susceptibility.* For an atom with no unfilled electron shells, the susceptibility of the system becomes a sum of the Larmor and the van Vleck suceptibility from Eq. (17) and Eq. (20), respectively:

$$\chi = \chi_\mathrm{vV} + \chi_\mathrm{Larmor} = \frac{N}{V}\mu_0\left[2\mu_\mathrm{B}^2\sum_n\frac{|\langle 0|\left(L_z+gS_z\right)|n\rangle|^2}{E_n-E_0} - \frac{e^2}{6m_\mathrm{e}}\sum_{i=1}^{Z}\langle r_i^2\rangle\right] \tag{21}$$

2.4.2 Curie Law ($\mathbf{J} \neq 0$)

The Curie law predicts that the magnetic susceptibility relates to the temperature through an inverse proportionality. It arises from the paramagnetic term in Eq. (14) given this term is non-zero, which occurs when $\mathbf{J} \neq 0$. Further, it is based on the assumption that no interactions between the magnetic moments are present. It remains valid, however, under weak interactions or in the regime where the interactions are significantly smaller than the thermal fluctuations [16].
The paramagnetic term from Eq. (14) can be rewritten in terms of the total angular momentum $\mathbf{J}$ as such:

$$\hat{\mathcal{H}} = \mu_{\mathrm{B}}\mathbf{B} \cdot (\mathbf{L} + g\mathbf{S}) = g_J \mu_{\mathrm{B}} \mathbf{B} \cdot \mathbf{J}, \tag{22}$$

where g_J represents the *Landé g-factor* and is given by [7]:

$$g_J = \frac{1}{2}(g+1) + \frac{1}{2}(g-1)\left[\frac{S(S+1) - L(L+1)}{J(J+1)}\right]. \tag{23}$$

Assuming an applied magnetic field along the z axis, the energy becomes:

$$E = \mu_{\mathrm{B}} g_J B m_J \tag{24}$$

where the quantum number m_J can take the following values $m_J = -J, -J+1, -J+2 ... J-2, J-1, J$. Given the energy from Eq. (24), the partition function becomes:

$$Z = \sum_{m_J=-J}^{m_J=J} e^{-\mu_{\mathrm{B}} g_J \frac{B m_J}{k_{\mathrm{B}} T}} = \frac{\sinh\left[\frac{1}{2}\mu_{\mathrm{B}} g_J \frac{B(2J+1)}{k_{\mathrm{B}} T}\right]}{\sinh\left[\frac{1}{2}\mu_{\mathrm{B}} g_J \frac{B}{k_{\mathrm{B}} T}\right]} \tag{25}$$

which results in the following magnetization:

$$M = \frac{1}{2} n \mu_{\mathrm{B}} g_J \left[(2J+1)\coth\left(\frac{1}{2}\mu_{\mathrm{B}} g_J \frac{B(2J+1)}{k_{\mathrm{B}} T}\right) - \coth\left(\frac{1}{2}\mu_{\mathrm{B}} g_J \frac{B}{k_{\mathrm{B}} T}\right)\right] \tag{26}$$

In order to obtain the susceptibility, we consider small magnetic fields, thus by applying the following approximation $\coth(x) \approx \frac{1}{x} + \frac{x}{3}$ for $x \ll 1$ the susceptibility becomes:

$$\chi = \lim_{B \to 0} \mu_0 \frac{\partial M}{\partial B} = \frac{n \mu_0 \mu_{\mathrm{B}}^2 g_J^2 J(J+1)}{3 k_{\mathrm{B}} T} = \frac{C_{\mathrm{Curie}}}{T} \tag{27}$$

which is known as the *Curie law susceptibility.* Note, this term is temperature-dependent and it diverges at $T = 0$, in comparison to the previous mentioned paramagnetic or diamagnetic contributions to the total susceptibility. If the Curie susceptibility contribution remains non-zero it will become the dominant term for the total magnetic susceptibility. A full derivation of the Curie law is given in Appendix M.

2.5 Ferromagnetism & Antiferromagnetism

Up until this point, only free electrons and their interactions with an applied field have been considered. However, interactions in terms of dipole-dipole or exchange interactions in between the magnetic moments give rise to the most interesting phenomena such as the emergence of order (ferromagnetism & antiferromagnetism) as well as magnetic frustration. Proceeding, we will look into how some of these interactions modify the magnetic susceptibility.

2.5.1 Interactions

The first interaction to be considered is the dipole-dipole interaction which has an energy equivalent to

$$E = \frac{\mu_0}{4\pi r^3}[\boldsymbol{\mu}_1 \cdot \boldsymbol{\mu}_2 - \frac{3}{r^2}(\boldsymbol{\mu}_1 \cdot \mathbf{r})(\boldsymbol{\mu}_2 \cdot \mathbf{r})] \tag{28}$$

for two magnetic dipoles $\boldsymbol{\mu}_1$ and $\boldsymbol{\mu}_2$ separated by $\mathbf{r}$ [7]. Thus, the dipole-dipole energy depends on the degree of mutual alignment and their separation. This interaction is on an energy scale equivalent to a temperature of 1 K, meaning it is extremely weak and may only be accountable for magnetic order at milliKelvin temperatures, such as paramagnetic salts [7, 16]. Therefore, regarding long-range order, the exchange interaction remains the underlying cause. It originates from Coulomb repulsion in combination with Pauli's exclusion principle and the fermionic anti-symmetric wavefunction [7]. Considering a simple model containing two electrons, the total wavefunction is a product of the spatial wavefunction $\psi_{\text{space}}(\mathbf{r}_1, \mathbf{r}_2)$ and the spin function χ_{spin}, where the latter is a linear combination of the possible spin states of the system. Therefore, to uphold the requirement of a total anti-symmetric wavefunction under particle exchange, the spatial part has to be symmetric if the spin part is anti-symmetric and vice-versa. Thus, one either has a single state ($S = 0$) denoted Ψ_{S} or the triplet state ($S = 1$) denoted Ψ_{T} which are given as:

$$\Psi_{\text{S}} = \frac{1}{\sqrt{2}}[\psi_\alpha(\mathbf{r}_1)\psi_\beta(\mathbf{r}_2) + \psi_\alpha(\mathbf{r}_2)\psi_\beta(\mathbf{r}_1)]\chi_{\text{S}} \tag{29}$$

$$\Psi_{\text{T}} = \frac{1}{\sqrt{2}}[\psi_\alpha(\mathbf{r}_1)\psi_\beta(\mathbf{r}_2) - \psi_\alpha(\mathbf{r}_2)\psi_\beta(\mathbf{r}_1)]\chi_{\text{T}} \tag{30}$$

along with their corresponding energies E_{S} and E_{T}. The Hamiltonian can be expressed in terms of these energies and parameterized using the two spins $\mathbf{S}_1 \cdot \mathbf{S}_2$:

$$\hat{\mathcal{H}} = \frac{1}{4}(E_{\text{S}} + 3E_{\text{T}}) - (E_{\text{S}} - E_{\text{T}})\mathbf{S}_1 \cdot \mathbf{S}_2 \tag{31}$$

where the spin-depdendent term may be rewritten as:

$$\hat{\mathcal{H}}^{\text{spin}} = -2\mathcal{J}\mathbf{S}_1 \cdot \mathbf{S}_2 \tag{32}$$

with the exchange constant defined as $\mathcal{J} = \frac{E_{\text{S}} - E_{\text{T}}}{2}$. This can be generalised to a many-body system assuming the interaction applies between all neighbouring atoms, which results in the Hamiltonian of the Heisenberg model:

$$\hat{\mathcal{H}} = -\sum_{ij} \mathcal{J}_{ij}\mathbf{S}_i \cdot \mathbf{S}_j \tag{33}$$

A positive exchange parameter ($\mathcal{J}_{ij} > 0$) causes the triplet state to be favoured and therefore gives rise to the spins aligning (ferromagnetism), whereas a negative exchange parameter ($\mathcal{J}_{ij} < 0$) puts the singlet state as the lowest energy, and therefore motivates an anti-alignment between the spins (antiferromagnetism) [7].

2.5.2 Ferromagnetism

The appropriate Hamiltonian for a Heisenberg magnet in the presence of an applied field can be written in terms of the Heisenberg model including the Zeeman effect, meaning the Hamiltonian takes the following form:

$$\hat{\mathcal{H}} = -\sum_{ij} \mathcal{J}_{ij}\boldsymbol{S}_i \cdot \boldsymbol{S}_j + g\mu_B \sum_j \boldsymbol{S}_j \cdot \boldsymbol{B} \tag{34}$$

assuming $\boldsymbol{L} = 0$ and, hence, $\boldsymbol{J} = \mathbf{S}$. In the case of ferromagnetism we have a positive exchange parameter $\mathcal{J}_{ij} > 0$. The Weiss-model builds on the approximation of a mean-field, which can be parameterized as $\boldsymbol{B}_{\mathrm{mf}} = \lambda \boldsymbol{M}$ where $\lambda = \frac{2V}{Ng^2\mu_{\mathrm{B}}^2} \sum_j \mathcal{J}_{ij}$ ($\sum_j \mathcal{J}_{ij} \to z\mathcal{J}$ if only z nearest neighbors accounted for) is the parameter which represents the strength of the molecular field [7, 24]. Thus, the model assumes that all magnetic ions in the system experiences the same molecular field. Given such a mean-field, the Hamiltonian from Eq. (34) can be written as:

$$\hat{\mathcal{H}} = g\mu_{\mathrm{B}} \sum_i \mathbf{S}_i \cdot (\mathbf{B} + \mathbf{B}_{\mathrm{mf}}) \tag{35}$$

which is written on a similar form compared to Eq. (22). Thus, for arbitrary value of $\mathbf{J}$ (assuming $\mathbf{L} = 0$ and $\mathbf{J} = \mathbf{S}$), the magnetization of the system follows the magnetization from Eq. (26), where $B \to B + \lambda M$.

$$M = \frac{1}{2} n\mu_{\mathrm{B}} g_J \left[(2J+1) \coth\left(\frac{1}{2}\mu_{\mathrm{B}} g_J \frac{(B+\lambda M)(2J+1)}{k_{\mathrm{B}}T} \right) - \coth\left(\frac{1}{2}\mu_{\mathrm{B}} g_J \frac{B+\lambda M}{k_{\mathrm{B}}T} \right) \right] = M_s \mathcal{B}_J(y) \tag{36}$$

where $\mathcal{B}_J(y)$ represents the Brillouin function, $M_{\mathrm{s}} = n g_J \mu_{\mathrm{B}} J$ represents the saturation magnetization, and the variable y is given by:

$$y = \frac{g_J \mu_B J (B + \lambda M)}{k_B T} \tag{37}$$

With no magnetic field present, one has to find simultaneous solutions for the following two equations:

$$M = M_{\mathrm{s}} \mathcal{B}_J(y), \qquad M = \frac{k_{\mathrm{B}} T y}{g_J \mu_{\mathrm{B}} J \lambda} \tag{38}$$

in order to obtain the temperature-dependence of the magnetization. For temperatures above a certain temperature denoted *Curie temperature*, T_{C} there are no simultaneous solution except for $y = 0$, causing the magnetization to be zero. However, for temperatures $T < T_{\mathrm{C}}$ there are three solutions, one at $M = 0$ and two at $M = \pm$ some non-zero value (see Fig. 1 (left)). The first solution ($M = 0$) is unstable and any fluctuations will push the system into the either of the two non-zero solutions. By numerically solving the system of equations in Eq. (38), one obtains the temperature-dependence of the magnetization shown in Fig. 2 (left), which reveals a second-order phase transition, as the derivative of the magnetization contains a discontinuity at $T = T_{\mathrm{C}}$.

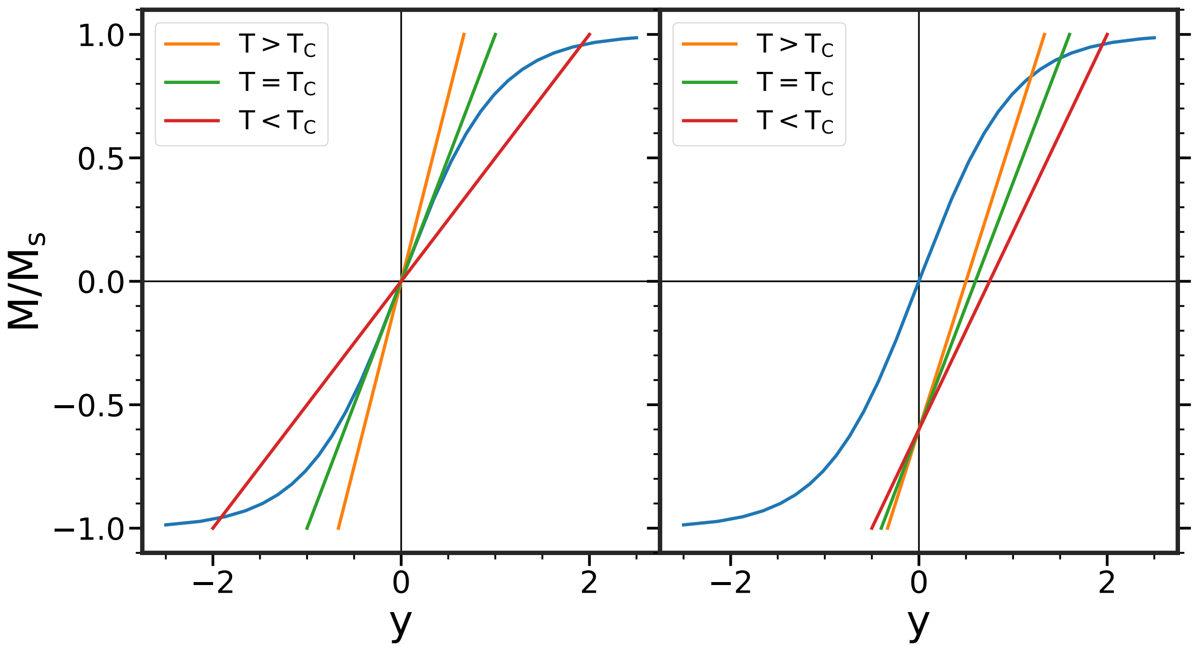

Figure 1: Left: Graphical solution of Eq. (38) for $\mathbf{J} = \frac{1}{2}$. **Right**: Graphical solution of Eq. (39) for $\mathbf{J} = \frac{1}{2}$ and $B = 3\,\mathrm{T}$.

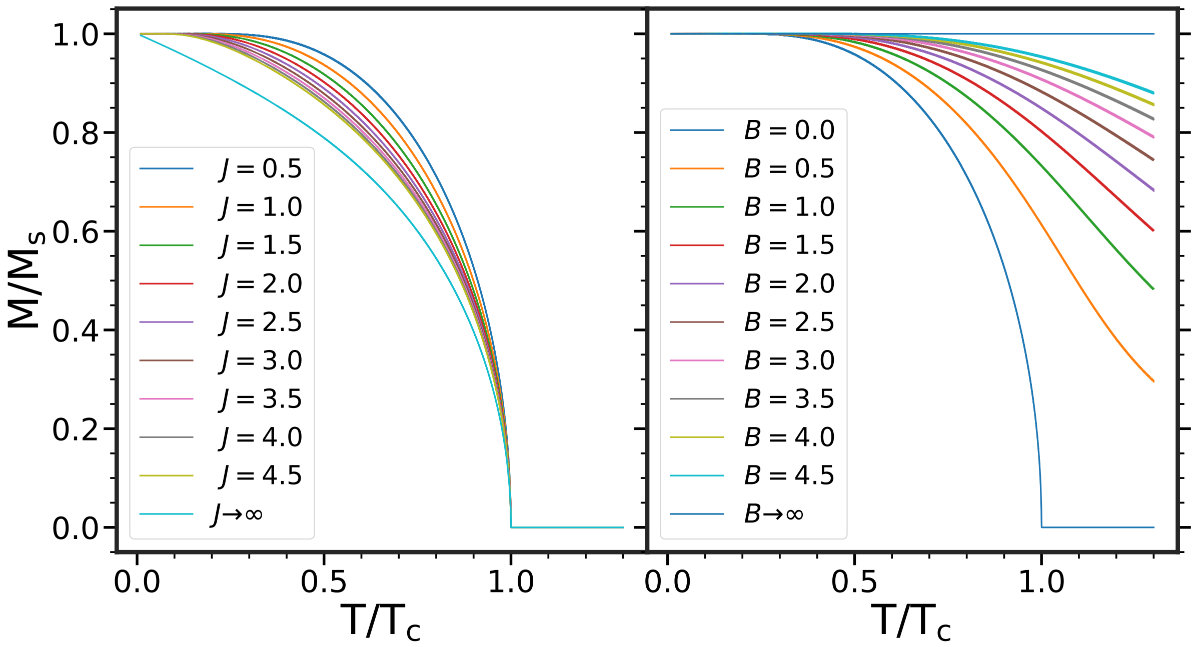

Figure 2: Numerical solutions of Eq. (38) and (39). **Left**: Magnetization as a function of temperature for various values of $\mathbf{J}$ and $\mathbf{B} = 0$. **Right**: Magnetization as a function of temperature for various magnitudes of applied field and $\mathbf{J} = \frac{1}{2}$.

If a magnetic field is present, simultaneous solutions for the following two equations:

$$M = M_s \mathcal{B}_J(y), \qquad M = \frac{k_\mathrm{B} T y}{g_J \mu_\mathrm{B} J \lambda} - \frac{B}{\lambda}, \tag{39}$$

which differ slightly from Eq. (38), have to be found (see Fig. 1 (right) for graphical illustration). This yields the magnetization shown in Fig. 2 (right). Note that if a magnetic field is present, the spontaneous second-order phase transition from zero magnetization to a finite magnetization below a critical temperature is eliminated as the magnetization remains continuous and is non-zero regardless of the temperature due to it being energetically favoured for the moments to align along the applied field. By considering a small magnetic field, thus, a small magnetization, similarly to the case in Section 2.4.2, the susceptibility becomes:

$$\chi = \frac{C_\mathrm{Curie}}{T - \lambda C_\mathrm{Curie}} = \frac{C_\mathrm{Curie}}{T - T_\mathrm{C}} \tag{40}$$

which is known as the *Curie Weiss Law.* The Curie temperature $T_\mathrm{C} = \lambda C_\mathrm{Curie}$ represents the point where the moments align resulting in long range order and the magnetization approaches a saturated magnetization [7, 24].

2.5.3 Antiferromagnetism

In the case of antiferromagnetism the exchange energy from Eq. (34) is negative i.e. $\mathcal{J}_{ij} < 0$ causing it to be energetically favoured for the nearest neighbour magnetic moments to align anti-parallel to one another. The lattice can be considered as two sub-lattices, where one contains the moments with spin-up and the other one contains the moments with spin-down as illustrated in Fig. 3.

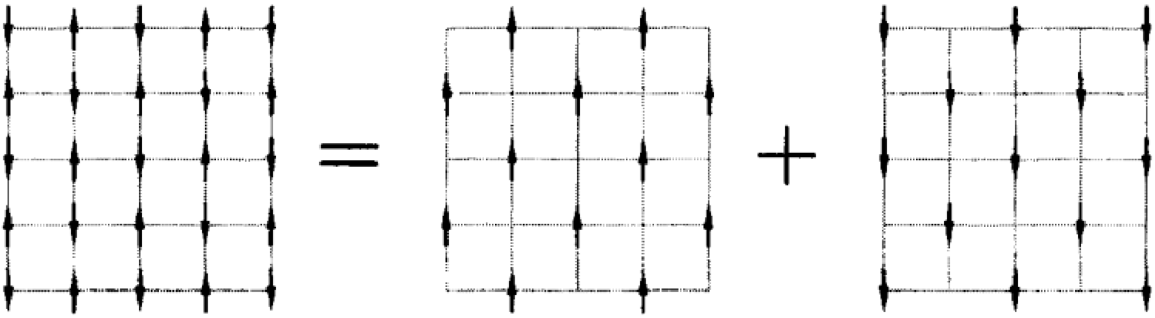

Figure 3: An antiferromagnet on a square lattice may be decomposed into two sub-lattices, with one containing spin-up moments and the other containing spin-down moments. From [7].

If one assumes the absence of an applied magnetic field and that the molecular field on one sub-lattice is proportional to the magnetization of the other sub-lattice, the mean field for each sub lattice caused by the molecular field alone can be written as:

$$\mathbf{B}_+ = -|\lambda|\mathbf{M}_-, \qquad \mathbf{B}_- = -|\lambda|\mathbf{M}_+ \tag{41}$$

where the sub-lattice containing the moments with spin-up has been labeled with '+' and the sub-lattice containing the moments with spin-down has been labeled with '-'. Similarly, from Section 2.5.2 the magnetization becomes:

$$M_\pm = M_\mathrm{s} \mathcal{B}_J(y), \qquad y = -\frac{g_J \mu_\mathrm{B} J |\lambda| M_\mp}{k_\mathrm{B} T} \tag{42}$$

The magnitude of the magnetization for the two sub-lattices should be equivalent i.e. $|M_+| = |M_-| = M$. Thus, the magnetization for each sub-lattice follow the magnetization for ferromagnetism shown in Fig. 2 (left) up until the transition temperature denoted *Néel temperature*, T_N at which point the magnetization for each sub-lattice remain zero. For temperatures $T < T_\mathrm{N}$ the net magnetization for this model will be zero since the magnetization from each sub-lattice points in opposite directions. However, commonly the *staggered magnetization* is defined as the order parameter for antiferromagnets, which represents the difference in the magnetization i.e $M_+ - M_-$ and remains non-zero for temperatures $T < T_\mathrm{N}$, where $T_\mathrm{N} = \frac{\mu_\mathrm{B} g_\mathrm{J}(J+1)|\lambda| M_\mathrm{s}}{3k_\mathrm{B}} = |\lambda| C_\mathrm{Curie}$ [7, 24]. Anyhow, for small applied magnetic fields, the magnetic susceptibility becomes:

$$\chi = \frac{C_\mathrm{Curie}}{T + T_\mathrm{N}} \tag{43}$$

which as well as Eq. (40) is known as the Curie Weiss Law, where $-T_\mathrm{C} \to T_\mathrm{N}$. This is not always the case, in general, it is expressed as $\chi = \frac{C}{T-\theta_\mathrm{CW}}$, where θ_CW is referred to as the *Curie Weiss temperature*. Here, one has $\theta_\mathrm{CW} > 0$ and $\theta_\mathrm{CW} < 0$ for a ferromagnet and an antiferromagnet, respectively. Experimentally, a fit to a Curie Weiss-dependence is typically carried out for the inverse susceptibility vs temperature ($\chi^{-1} = \frac{T-\theta_\mathrm{CW}}{C}$), where the intersection with the temperature axis corresponds to θ_CW [7, 25]. Based on the above derivation one expects that $T_\mathrm{N} = |\theta_\mathrm{CW}|$, however, the Néel temperature is often found to deviate from the Curie Weiss temperature, which is due to the simplified model considered in this section, and the deviation is typically enhanced significantly by magnetic frustration [7, 24].

2.6 Frustration

The antiferromagnetic exchange interaction between spins presented in Section 2.5.3 opens the door to the phenomenon of magnetic frustration, which contains various exotic ground states where some are known as *spin glass*, *spin ice*, and quantum spin liquids with all being not fully understood and the latter has yet to be observed [7]. As shown in Fig. 3 and Fig. 4 (left) having an antiferromagnetic exchange interaction between spins on a square lattice, it remains nice and easy to obtain a configuration of alternating up and down spins, where the energy is minimized. However, by introducing a triangular geometry as shown in Fig. 4 (middle), it becomes impossible to orient all three spins such that a nearest-neighbour antiferromagnetic interaction is satisfied fully between every spin. Instead, the system offers a multiplicity of equally unsatisfied states, meaning the ground state is highly degenerate [5, 7]. Frustration suppresses long range order in terms of temperature, such that a paramagnetic phase, described by a Curie Weiss-dependence, takes place for temperatures way below the Curie Weiss temperature. Therefore, a frustration parameter is defined as the ratio between the Curie Weiss temperature and the Néel temperature ($f = \frac{|\theta_\mathrm{CW}|}{T_\mathrm{N}}$) where a large value for the ratio remains a signature of frustration [5, 13–15].

2.6.1 Spin Glass

In a broad sense, a spin glass is defined as a magnetic system with random mixed interactions between the spins giving rise to a highly degenerate ground state. Below a well defined so-called *freezing temperature* (T_f), the moments freeze in one of the degenerate ground states, which is highly irreversible and metastable, yet lacking long-range magnetic order [7, 17, 20]. At high temperatures, the behaviour of the magnetic moments is governed by the thermal fluctuations, giving rise to a paramagnetic behaviour. This is reflected in a Curie Weiss-like magnetic susceptibility. Upon

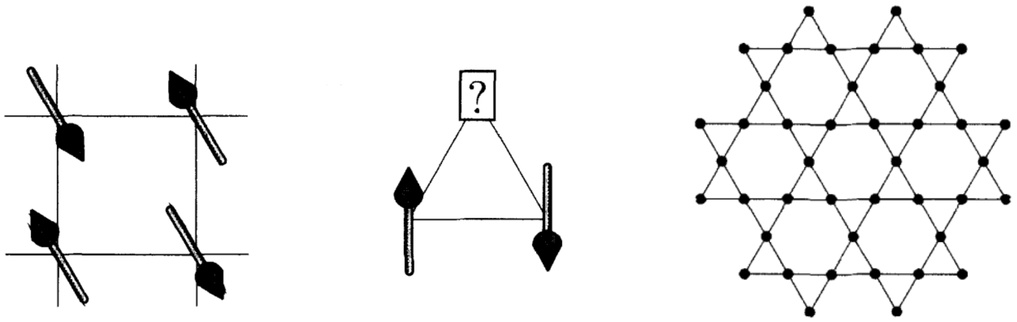

Figure 4: Left: Antiferromagnetic nearest-neighbour interactions on a square lattice **Middle**: Antiferromagnetic nearest-neighbour interactions on a triangular lattice. **Right**: The kagomé lattice. From [7]

reaching the freezing temperature, the magnetic susceptibility shows a cusp, and begins to decrease [7, 26]. Given the spin glass system lacks magnetic order below the freezing temperature, a field-cooled (FC) and zero-field-cooled (ZFC) splitting (see Fig. 109 (top) Appendix L) still occurs in the DC magnetic susceptibility which is one of the signatures [7]. However, the main probe technique to study such systems is through AC susceptibility as various interesting and distinguishable features are captured, which will be discussed further in Section 2.9 and 2.10 [20].

2.6.2 Quantum Spin Liquid (QSL)

A quantum spin liquid (QSL) is a state of matter which is characterized by long-range quantum entanglement, fractional excitations in terms of spinons and no magnetic order down to $T = 0\,\mathrm{K}$, yielding a frustration parameter that would approach infinity. Therefore, the moments remain liquid-like and no spontaneous broken symmetry occurs [5, 6, 15]. The wave function for such a state of matter may be seen as a resonating-valance bond (RVB) state, and it is predicted to be the ground state of various frustrated materials. For instance the compound herbertsmithite ($\mathrm{ZnCu_3(OH)_6Cl_2}$) which possesses a kagomé structure shown in Fig. 4 (right) remains the most promising compound to hold such a ground state, but this is yet to be observed [5, 6, 15].

Valence Bonds (VB): The state of dimer valence bonds is a non-magnetic state and is found to be the ground state of various materials [27, 28]. A dimer valence bond represents a scenario where two spins are highly quantum entangled with one another, owing up to an antiferromagnetic interaction, with these two spins forming a spin-0 singlet state. Imagine such a static and localized dimer valence bond being the case for all the spins in the lattice arrangement as shown in Fig. 5 (top left); the overall ground state would have spin-0, causing the material in a sense to be non-magnetic and contain excitations in terms of magnons ($\Delta S = 1$) [5]. However, often the arrangement of valence bonds is not unique which typically breaks translational and rotational lattice symmetry. Further, the phenomenon lacks long-range entanglement, which means that such a state does not describe a true quantum spin liquid [5, 13].

Resonating Valance Bond (RVB): However, if one allows these valence bonds to undergo quantum fluctuations, one obtains the resonating valence bond state which was proposed in 1973 by the American physicist P. W. Anderson [10, 11]. In 1987 P. W. Anderson further proposed for it to underlie the physics of high-temperature superconductivity [5, 12, 15]. Recently, it has been shown that the RVB wavefunction remains the ground state for various models, for instance the nearest-neighbour Heisenberg model on the kagomé lattice as seen in Fig. 4 (right) [5, 13]. For such a state there is no preferred ordering pattern and the overall wavefunction is a superposition of all the different pairing configurations of two spins, where the bond may be short range as seen in Fig. 5 (left middle) or long range as seen in Fig. 5 (left bottom). The long range bonds remain weaker compared to the short range bonds, which is illustrated by the variation in the blue color [5]. The exotic RVB state excitations take the form of electrically neutral spin-$\frac{1}{2}$ spinons, which arise from breaking a valence bond between a formed pair. These unpaired electrons may adjust the already fluctuating valance bonds, resulting in two new unpaired electrons, which visually will appear as a free spin propagating through the lattice as shown in Fig. 5 (right) [5].

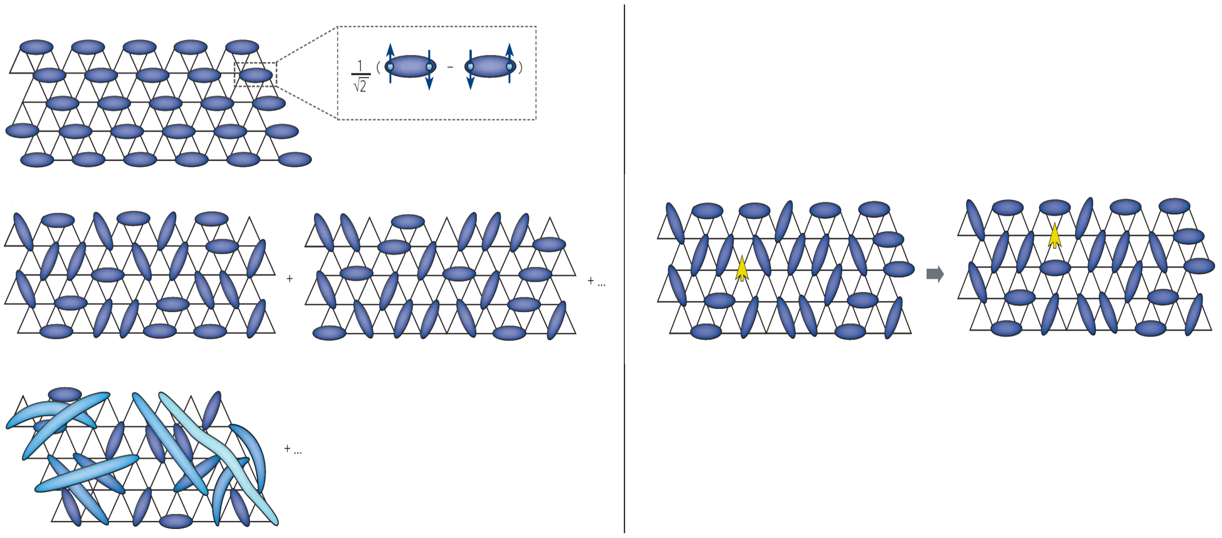

Figure 5: **Left**: Illustration of valance-bond state and resonating valance-bond state. **Top**: Static singlet valance-bond dimers, with the insert illustrating a singlet state. **Middle**: Superposition of short-range valence bonds. **Bottom**: Superposition of long-range valance bonds, where a longer bound has a lighter blue color representing a weaker bound, and, hence, easier to break and form non-zero spin states. **Right**: A Spinon is a fractional excitation propagating through the lattice by modifying the already resonating valence bonds. From [5].

In the broad picture, there are two types of quantum spin liquids characterized by either gapped or gapless spinon excitations. In terms of a gapped spinon excitation spectrum, it requires a certain amount of energy to break the dimer singlets. The temperature-dependent susceptibility for an isolated dimer singlet with a spin gap takes the form:

$$\chi(T) \propto \frac{1}{T\left(3+\exp\left[\frac{\Delta}{k_{\mathrm{B}}T}\right]\right)} \tag{44}$$

which is known as Bleaney-Bowers equation, where Δ represents the energy gap. for high temperatures it behaves Curie-like and as T → 0 K, the susceptibility goes exponentially to zero [7, 27, 29]. If the excitation spectrum is gapless, the valence bonds are easily broken. Here, the uniform antiferromagnetic spin-$\frac{1}{2}$ chain serves as a simplified picture, where the magnetic susceptibility approaches a finite value as T → 0 K. Ref [29, 30] show numerical calculations for both the dimer scenario and the uniform antiferromagnetic spin-$\frac{1}{2}$ chain which are shown in Fig. 6 and fitted using a polynomial expansion [30]. However, it has to be emphasized that these are indeed simplified models and are only utilized to obtain suggestions of the true temperature-dependent susceptibility of a gapped and a gapless quantum spin liquid. As mentioned, a true quantum spin liquid has yet to be observed, and experimentally identifying such a state remains subtle and difficult to prove. It remains significantly easier to state what the material of interest is not, rather than what it is. This means that there is not a single experimental feature which, alone, identifies a quantum spin liquid [5, 15]. In terms of magnetic susceptibility, a large frustration parameter ($f = \frac{|\theta_{\mathrm{CW}}|}{T_{\mathrm{N}}}$) remains a good indication, meaning a susceptibility vs temperature curve which reveals no sign of magnetic order or spin freezing.

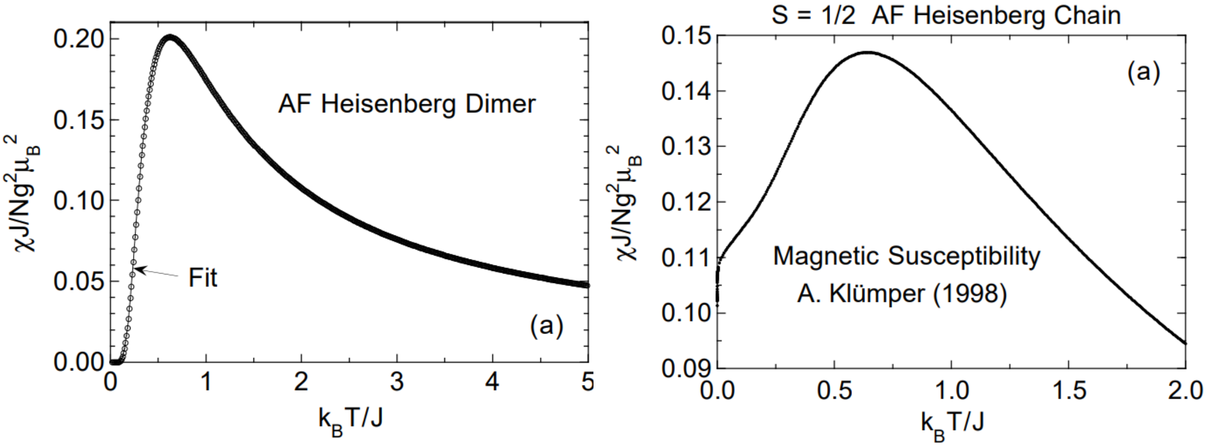

Figure 6: Numerical calculations along with fits using polynominal expansions. **Left**: The antiferromagnetic Heisenberg dimer singlet showing an exponential decay to zero as $T \to 0\,\mathrm{K}$. **Right**: The uniform antiferromagnetic spin-$\frac{1}{2}$ chain showing an approach towards a finite value as $T \to 0\,\mathrm{K}$. From [29, 30]

2.7 Superconductivity

Superconductivity is characterized by two fundamental properties: zero DC resistivity and perfect diamagnetism. It was first discovered by H. K Onnes in 1911 after witnessing the former property (zero DC resistivity) for the material Mercury at the temperature of liquid helium. H. K Onnes investigated the validity of the Drude theory by measuring resistivity for various materials such as gold and platinum which yielded results consistent with Drude theory. However, in the case of Mercury an unexpected drop in resistivity was observed at the critical temperature $T_{\mathrm{c}} = 4.2\,\mathrm{K}$ which differed from any theory regarding electrical transport, and therefore revealed a new phenomenon at the given time [31, 32].

In 1957, Barden, Cooper, and Schrieffer presented the very first microscopic theory of superconductivity known as *BCS theory*, covering the conventional superconductors (mainly Type-I and a few Type-II, both introduced in Section 2.7.2). The theory describes the formation of singlet Cooper pairs, which essentially is an energetically favoured bound state between two electrons with opposite momentum and spin ($\mathbf{k}\uparrow, -\mathbf{k}\downarrow$). The effective electron-electron interaction is mediated by phonons and remains attractive within the Debye frequence (ω_D) of the Fermi surface. Unlike metals, where the electron states are filled up to the Fermi energy (ϵ_{F}) with a finite density of states at the Fermi level ($g(\epsilon_{\mathrm{F}})$), BCS theory predicts the existence of a temperature-dependent energy gap ($\Delta(T)$) which separates the occupied states from the excited states by $2\Delta(T)$. The energy gap represents the binding energy of the Cooper pairs, and it relates to the critical temperature as follows: $2\Delta(T=0) = 3.52 k_{\mathrm{B}} T_{\mathrm{c}}$ [1, 22, 23, 31, 32].

2.7.1 Meissner-Ochsenfeld Effect - Perfect Diamagnetism

The property of perfect diamagnetism was unravelled in 1933 by the two german physicists F. W. Meissner and R. Ochsenfeld, when they observed the expulsion of an applied magnetic field by a material in it's superconducting state, suggesting an interior magnetic field of $\mathbf{B} = 0$ [31]. Utilizing the general form for the magnetic field from Eq. (2) in Section 2.1 and imposing that $\mathbf{B} = 0$ inside the material at temperatures of $T < T_\mathrm{c}$, one obtains:

$$\mathbf{B} = \mu_0(\mathbf{H} + \mathbf{M}) = 0 \quad \Rightarrow \quad \mathbf{M} = -\mathbf{H} \tag{45}$$

meaning that the material produces a magnetization which is equal in size and opposite in direction to the applied magnetic field. For such a magnetization, one easily arrives at the magnetic susceptibility:

$$\chi = \frac{d\boldsymbol{M}}{d\boldsymbol{H}}\bigg|_{\boldsymbol{H}=0} = -1 \tag{46}$$

which yields the value for perfect diamagnetism. The magnetization opposite to the applied field is produced by tiny shielding currents driven on the surface of the material. The phenomenon is illustrated in Fig. 7 and an additional feature to note, is that the density of the field lines near the surface increases as the magnetic field is expelled resulting in a larger field magnitude in this region [31].

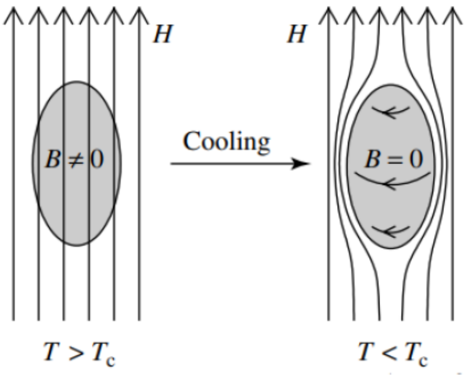

Figure 7: Left: Magnetic field lines piercing the material at $T > T_\mathrm{c}$. **Right**: Magnetic field lines being repelled from within the body of the material at $T < T_\mathrm{c}$. Additionally, the density of the magnetic field lines increases near the material's surface. From [31].

In reality, the magnetic field does penetrate the surface of the superconductor slightly over a length scale referred to as the *London Penetration Depth* (λ_L) which takes part in the London equation:

$$\nabla^2\mathbf{B} = \frac{1}{\lambda_\mathrm{L}^2}\mathbf{B} \tag{47}$$

first derived by Fritz London and Heinz London [22, 32]. One-dimensional solutions to Eq. (47) takes the form $B = B_0 \exp\left(-\frac{x}{\lambda_\mathrm{L}}\right)$, which shows that the magnetic field decays exponentially over a distance λ_L (commonly $\sim$ 50-500 nm), which is given by:

$$\lambda_\mathrm{L} = \sqrt{\frac{m_\mathrm{e}}{\mu_0 n_\mathrm{s} e^2}} \tag{48}$$

where m_e and e represent the mass and the charge of the electron and n_s represents the superfluid density [22, 23, 31, 32].

2.7.2 Type I and Type II Superconductors

The perfect diamagnetic susceptibility ($\chi = -1$) is only true in the limit of a weak applied magnetic field. In general, there are two types of superconductors: **type-I** and **type-II** and as the external field is increased, the material responds in two possible ways defined by the type. A type-I superconductor is able to expel an applied field entirely up to a certain strength of the applied field referred to as the critical field, $\mathrm{H_c}$. At this point, it remains energetically favourable for the material to leave the supercondcuting state, meaning it transfers to a normal metal spontaneously [31, 32] as shown in Fig. 8 (left). A type-II superconductor acquires the perfect diamagnetism up to an initial critical field (H_{c1}), at which point the material enters a 'mixed state' where field lines pierce the material at certain regions. These flux lines take the form of vortices carrying quantized magnetic flux ($\phi_0 = \frac{h}{2e}$). These vortices contain a core which essentially has transitioned to a normal metal, however a circulating super-current at the edge of the region ensures a screening of the magnetic field in the bulk of the material [31, 32]. A further increase in the magnetic field causes the magnetization in the material to gradually approach zero, and at a field equivalent to H_{c2}, the superconductivity is eliminated as shown in Fig. 8 (right).

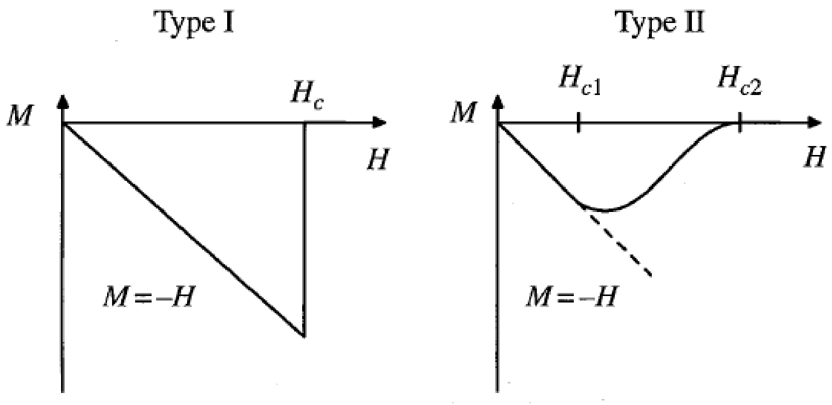

Figure 8: Left: The magnetization sketched as a function of the applied field for a Type-I superconductor, where it follows $\mathbf{M} = -\mathbf{H}$ up to a cutoff point $H = H_{\mathrm{c}}$, at which point the superconductivity breaks down spontaneously. **Right**: The magnetization sketched as a function of the applied field for a Type II superconductor, where it behaves as a Type I superconductor for an applied field $H < H_{\mathrm{c1}}$ at which point the material enters the vortex phase, causing the magnetization to gradually approach a value of zero as the external field approaches a second critical field, i.e. $H \to H_{\mathrm{c2}}$. From [32].

Further, the critical field for both types of superconductors remain temperature-dependent and the temperature-dependence is illustrated in Fig. 9. In case of Type-I superconductors, experimental data are well approximated by the following empirical expression:

$$H_{\mathrm{c}}(T) = H_{\mathrm{c}}(0)\left[1 - \left(\frac{T}{T_c}\right)^2\right] \tag{49}$$

for temperatures $T \ll T_{\mathrm{c}}$ and as the temperature approaches the critical temperature, the relation between the critical field and the temperature approaches a linear dependence:

$$H_{\mathrm{c}}(T) \propto [T_{\mathrm{c}} - T] \tag{50}$$

as described by Ginzburg-Landau theory [1, 22, 32].

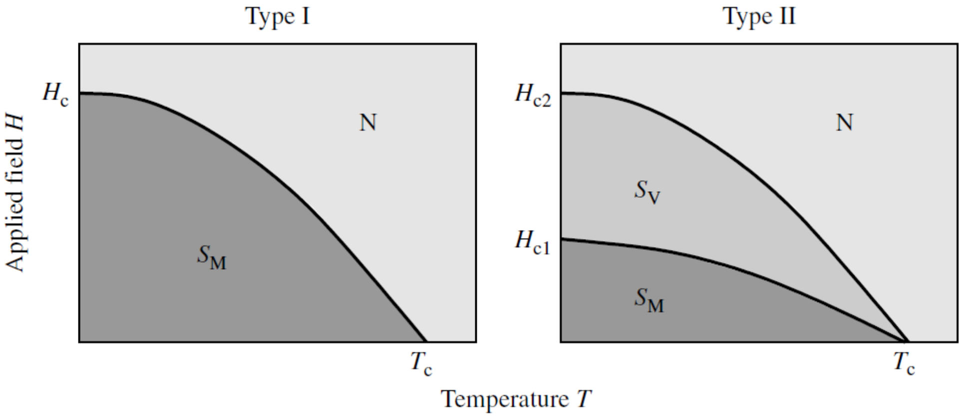

Figure 9: **Left**: The temperature-dependence of the critical field (H_c) for a Type-I superconductor. **Right**: The temperature-dependence of the critical fields (H_{c1} & H_{c2}) for a Type-II superconductor. S_M, and S_V and N represent the Meissner, mixed, and normal phase, respectively. From [31].

2.8 AC susceptibility

The AC susceptibility, unlike DC susceptibility, represents the dynamic response of a material subject to a small sinusoidal field ($\mathbf{H}_{AC} = \mathbf{H}_{AC,0}\cos(\omega t)$) with a typical field strength of $H_{AC,0} < 1\,\text{Oe}$ in the frequency range 0.1-10^4 Hz, allowing one to directly probe the ground state of the spin system [17]. The definition of susceptibility from Section 2.1 applies to AC susceptibility as well, it is just important to note it differs by having an oscillating field giving rise to an oscillating magnetization:

$$\chi_{AC} = \frac{\partial \mathbf{M}_{AC}}{\partial \mathbf{H}_{AC}} \tag{51}$$

Thus, instead of measuring the magnetization of the sample using a static finite field (DC case), AC susceptibility represents the slope of the magnetization curve. An oscillating field may be used in a combination with a static field causing the total field to take the form $\mathbf{H} = \mathbf{H}_{DC} + \mathbf{H}_{AC,0}\cos(\omega t)$. This enables various magnetic field regions of the magnetization to be probed as illustrated in Fig. 10. Therefore, with a DC field present, the susceptibility becomes the slope of the curve evaluated at the strength of the DC field [17]:

$$\chi_{AC} = \frac{\partial \mathbf{M}}{\partial \mathbf{H}}\bigg|_{\mathbf{H}_{DC}} \tag{52}$$

Since the AC susceptibility represents the dynamic response of a given material subjected to an oscillating field, one can imagine that given the magnetic moments in the material either share a single relaxation time or there are a spread of relaxation times, the response will be frequency-dependent. This frequency-dependence is generally divided into three characteristic regimes: the isothermal regime, the adiabatic regime, and the intermediate regime [17].

- The isothermal regime ($\omega \ll \frac{1}{\tau}$) covers the scenario where the magnetic moments in the system have a fast relaxation time with respect to the frequency of the excitation field such that the moments have time to equilibrate for every oscillation of the excitation field and, therefore, respond instantaneously exchanging energy with the lattice. In this regime one has $\chi_{AC} \approx \chi_{DC}$ and the measured susceptibility is typically referred to as the *isothermal susceptibility*, χ_T
- The adiabatic regime ($\omega \gg \frac{1}{\tau}$) regards the case where the perturbation of the system occurs at a significantly higher frequency than the timescale of the natural relaxation time of the system. Therefore, the system does not manage to respond properly and exchange energy with the

lattice. The measured susceptibility for this regime is known as the *adiabatic susceptibility*, χ_{S}.

- The intermediate regime ($\omega \approx \frac{1}{\tau}$) remains the regime where the response in more complex. If the excitation frequency is slightly slower or faster than the natural relaxation of the system, a phase lag in the response occurs, meaning that the response is decomposed into an in-phase component which reflects an inductive response and an out-of-phase component which represents energy dissipation.

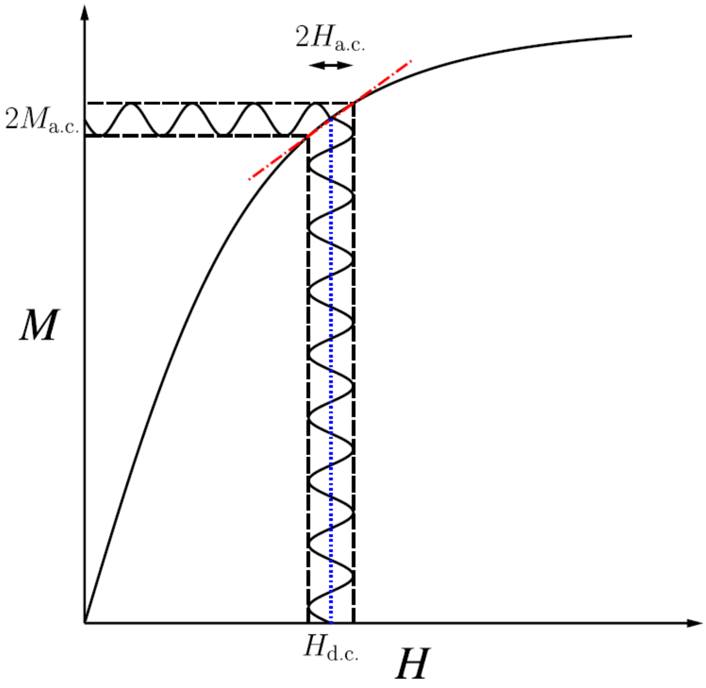

Figure 10: Figure illustrating how an AC field in combination with a DC field allows one to probe various regions on the magnetization curve. The red line represents the gradient of the magnetization curve evaluated at the H_{DC}. From [17].

Thus, the AC susceptibility can be written as a complex quantity:

$$\chi_{\mathrm{AC}}(\omega) = \chi'(T,\omega) + i\chi''(T,\omega) \tag{53}$$

where both the real and the imaginary component may be temperature and frequency-dependent [17]. The sinusoidal field causes the magnetization to be periodic, thus, assuming a driving force of $H_{\mathrm{AC}}(t) = H_{\mathrm{AC},0}\cos(\omega t)$ the magnetization can expanded in a Fourier series as follows:

$$M(t) = H_{\mathrm{AC},0}\sum_{n=1}^{\infty}\left[\chi'_n\cos(n\omega t) + \chi''_n\sin(n\omega t)\right] \tag{54}$$

with the complex susceptibility on the form $\chi_n = \chi'_n + i\chi''_n$, which includes the linear terms ($n = 1$) and the non-linear terms ($n > 1$) of the susceptibility [17–19, 33, 34]. Based of Eq. (54) the Fourier coefficients (χ'_n & χ''_n) are defined as:

$$\chi'_n = \frac{1}{\pi H_{\mathrm{AC},0}}\int_{\omega t=0}^{\omega t=2\pi} M(t)\cos(n\omega t)d(\omega t), \quad \chi''_n = \frac{1}{\pi H_{\mathrm{AC},0}}\int_{\omega t=0}^{\omega t=2\pi} M(t)\sin(n\omega t)d(\omega t) \tag{55}$$

Further, accounting for demagnetization using Eq. (8) and assuming an experimental complex susceptibility on the form $\chi_{\text{exp}} = \chi'_{\text{exp}} + i\chi''_{\text{exp}}$, one obtains:

$$\chi_{\text{int}} = \frac{\chi'_{\text{exp}} - N\left(\left(\chi'_{\text{exp}}\right)^2 + \left(\chi''_{\text{exp}}\right)^2\right)}{\left(1 - N\chi'_{\text{exp}}\right)^2 + \left(N\chi''_{\text{exp}}\right)^2} + i\frac{\chi''_{\text{exp}}}{\left(1 - N\chi'_{\text{exp}}\right)^2 + \left(N\chi''_{\text{exp}}\right)^2} \tag{56}$$

which is on the form $\chi_{\text{int}} = \chi'_{\text{int}} + i\chi''_{\text{int}}$, meaning the first and the second term of Eq. (56) correspond to the in-phase and the out-of-phase component of the intrinsic susceptibility [17, 33].

2.9 Fundamental Harmonic Susceptibilities

Focusing on the fundamental harmonics ($n = 1$), the in-phase part (χ') measures the inductive response (energy storage) of the material subject to a field and, therefore, the meaning of this quantity is equivalent to the magnetic susceptibility in case of a static field presented in the earlier sections. The out-of-phase part (χ'') relates to dissipation in the material in terms of AC losses. The latter (χ'') relates to the average energy loss per unit volume over a period $T = \frac{2\pi}{\omega}$ of the AC field by [18, 19]:

$$E = \frac{\mu_0}{T}\int_{t=0}^{t=T} H_{\text{AC}}(t)\frac{dM}{dt}dt = \frac{1}{2}\mu_0\omega H_{\text{AC},0}^2\chi'' \tag{57}$$

which in addition reveals that the out-of-phase component has to be positive ($\chi'' > 0$). In case of an electrically conducting sample, there will be a contribution to both the in-phase and the out-of-phase component of the magnetic susceptibility due to induced eddy currents. Theses eddy currents will, obeying Lenz's law, give rise to a screening effect producing an interior magnetic field that opposes the applied magnetic field, contributing to the in-phase component. Further, due to resistance in the material, there will be a loss of energy in terms of generated heat, which will contribute to the dissipative component (χ'') [18].

2.9.1 Frequency Dependent Models

A model which is commonly used directly or as a starting point to describe the frequency-dependence of the AC susceptibility is the Debye relaxation model, which initially was formulated to describe relaxation in dielectrics involving an AC electric field [17, 18]. It assumes that the system of interest possesses a single relaxation time τ where the magnetization relaxes as $M(t) = M(0)\exp\left(-\frac{t}{\tau}\right)$ if the applied field is removed. From this model, the complex susceptibility becomes:

$$\chi(\omega) = \frac{1}{1 + i\omega\tau} \tag{58}$$

The sign in the denominator of Eq. (58) varies based on the convention used regarding the sign ($\chi = \chi' \pm i\chi''$) [17]. Anyhow, from Eq. (58), one obtains that the in-phase and the out-of-phase component are given as follows:

$$\chi'(\omega) = \chi_{\text{S}} + \frac{\chi_{\text{T}} - \chi_{\text{S}}}{1 + (\omega\tau)^2}, \qquad \chi''(\omega) = \frac{\chi_{\text{T}} - \chi_{\text{S}}}{1 + (\omega\tau)^2}\omega\tau \tag{59}$$

where χ_{T} and χ_{S} correspond to the isothermal and adiabatic susceptibility, respectively [17, 35]. The in-phase and the out-of-phase components as a function of $\omega\tau$ are shown in Fig. 11, where the left plot corresponds to Eq. (59) and the right plot shows a Cole-Cole plot, which is commonly shown when investigating relaxation processes [17]. As mentioned, in the DC limit, the spins are able to follow the applied field since the excitation frequency is significantly lower than the relaxation time, at which point from Eq. (59) one has $\chi' \to \chi_\mathrm{T}$ and $\chi'' \to 0$, which in addition is illustrated in Fig. 11 (left). In the limit of high excitation frequency, the moments are not able to respond quickly enough for the given relaxation time, causing the susceptibility to fall off such that $\chi' \to \chi_\mathrm{S}$ and $\chi'' \to 0$. The most interesting feature occurs when the excitation frequency approximately matches the relaxation time of the moments, which results in a peak in the out-of-phase component at $\omega\tau = 1$ as seen in Fig. 11 (left). This allows one to extract the relaxation time for the given system [17, 18].

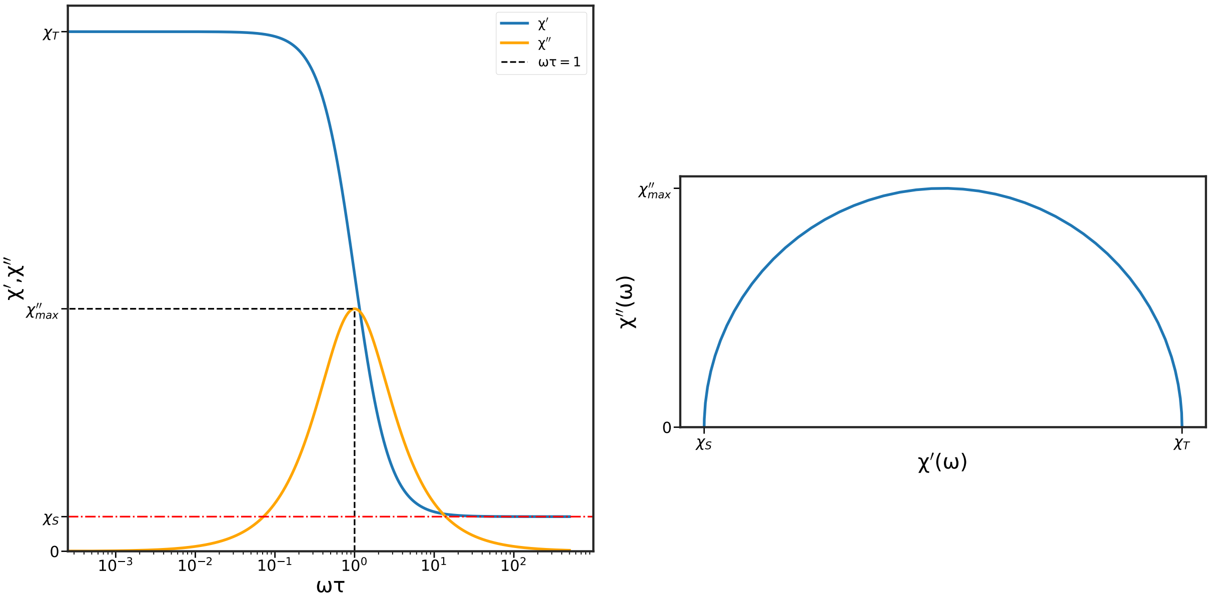

Figure 11: Plot showing features from the Debye model in Eq. (58). **Left**: The in-phase and the out-of-phase component from Eq. (59) as a function of $\omega\tau$ on a log-scale. **Right**: A Cole-Cole plot for the Debye model 58, which yields a perfect semi-circle.

The Debye model from Eq. (58) considers a single relaxation time of the system. Thus, it neglects interactions between the moments which is a decent approximation of *superparamagnets* (cluster of free spins) and single molecule magnets, and, therefore, it has been very helpful in the study of these [17, 18]. However, in most systems, the presence of completely non-interacting moments is unlikely, and these interactions lead to clustering effects which results in a distribution of relaxation times [17]. These complexities are accounted for in the generalised Debye model:

$$\chi(\omega) = \chi_\mathrm{S} + \frac{(\chi_\mathrm{T} - \chi_\mathrm{S})}{1 + (i\omega\tau)^{1-\alpha}} \tag{60}$$

where α ($0 \leq \alpha \leq 1$) has been introduced to account for a spread of relaxation times. This modifies the Cole-Cole plot in Fig. 11 (right) such that it becomes an arc instead of a semi-circle and spin glasses may reach a value of $\alpha = 0.9$ [17, 35]. Two alternative approaches to account for a distribution of relaxation times are the Cole-Davidson:

$$\chi(\omega) = \chi_\mathrm{S} + \frac{(\chi_\mathrm{T} - \chi_\mathrm{S})}{(1 + (i\omega\tau))^{\beta}} \tag{61}$$

where the parameter β has been introduced, or a combination of Eq. (60) and 61 yielding the Havriliak-Negami model:

$$\chi(\omega) = \chi_\mathrm{S} + \frac{(\chi_\mathrm{T} - \chi_\mathrm{S})}{[1 + (i\omega\tau)^{1-\alpha}]^{\beta}} \tag{62}$$

which utilizes both α and β [17]. It is important to note that these models are ad hoc adjustments to improve the agreement between experimental measurements and theory [17]. Regardless of the model, it is certain that a frequency-dependence of $\chi'(\omega)$ and $\chi''(\omega)$ are always caused by the presence of one or more relaxation processes [35].

2.9.2 AC Susceptibility Characteristics

Paramagnets: The AC susceptibility of a paramagnet resembles the DC susceptibility very closely, as the in-phase component follows a Curie Weiss law nearly identical to the DC susceptibility, depending on the field strength. The out-of-phase component should remain temperature-independent in the paramagnetic regime given the material of interest is an insulator, otherwise there would be a contribution due to induced eddy currents [18]. Further, in the frequency range accessible (0.1-10^4 Hz) to AC susceptometry, the moments are free to relax in accordance to the excitation field as the spin-spin relaxation time lies in the order of $\sim 10^{-9}$-10^{-10} s. Therefore, the out-of-phase component should remain zero [17, 18, 35]. Experimentally, a non-zero component will also originate from background and instrumentation effects. Anyhow, if a DC field is applied in addition with an oscillating field, it will create a net magnetization and spin-lattice relaxation may occur due to direct phonon processes, causing the out-of-phase component to be non-zero, which can be studied by AC susceptibility and approximated using the variations of the Debye model presented in Section 2.9.1.

Spin Glasses: The AC susceptibility is very commonly used to characterize spin glasses as the transition to the metastable state is not captured by specific heat measurements [17, 20]. Above the spin glass transition, a paramagnetic behaviour is reflected in both the in-phase compoent – showing a Curie Weiss-like behaviour – and the out-of-phase component being zero. At the transition, a cusp in the in-phase component appears associated with the freezing temperature (T_f), along with an onset of dissipation in the out-of-phase component [17, 18, 20, 35–37]. The signature of a spin glass is that these two features remain frequency-dependent, such that for increasing frequency the cusp in the in-phase component along with the dissipation in the out-of-phase component are shifted towards higher temperatures see Fig. 109 (bottom) Appendix L) [25]. The frequency-dependence of the AC susceptibility may be studied using the generalised Debye model presented in Section 2.9.1 and the relaxation time may be fitted as a function of the freezing temperature using Vogel-Fulchers law:

$$\tau(T) = \tau_0 \exp\left\{ \frac{E_\mathrm{a}}{k_\mathrm{B}(T - T_0)} \right\} \tag{63}$$

where E_a and τ_0 represent the activation energy and the characteristic relaxation time, respectively and T_0 is a parameter that accounts for the interactions between the moments [17, 18, 20, 26, 35, 37].

Superconductors: The AC susceptibility for a type-I superconductor resembles the DC susceptibility in the in-phase component (χ'), such that in the high temperature regime $T > T_\mathrm{c}$ it remains close to temperature-independent. However, in the case of electrical conductive materials, there may be a slight measured temperature-dependence, due to screening effects caused by induced eddy currents [18]. Upon reaching the critical temperature, the material will enter the superconducting phase showing an in-phase component of $\chi' = -1$ in terms of SI units. The out-of-phase component (χ''), however, will reveal a small positive value for temperatures $T > T_\mathrm{c}$, due to the AC losses of the induced eddy currents which will increase with frequency [2, 18]. At the phase transition, the out-of-phase component will display a peak at the point where magnetic irreversibility occurs. The height of the peak increases with frequency, and for decreasing temperature, the out-of-phase component will approach zero, reflecting the zero-loss state. The AC susceptibility has been measured for titanium by Ref. [2] and shown in Appendix E.

The AC susceptibility of a type-II superconductor shows a similar behaviour in the broad picture. However, there are various small features reflected in the behaviour, which are associated with more complex processes that differ from type-I superconductivity [17]. The features displayed in the in-phase and the out-of-phase component associated with the supercondcuting transition remain frequency-dependent, in the sense that these are shifted towards higher temperatures for increasing frequency (see Fig. 81 (top) Appendix F) [17, 38]. In addition, these type-II superconductors are commonly polycrystalline (powder or a pellet), which typically causes a broader transition and reveals two critical temperatures T_{c1} and T_{c2}: the former representing the bulk of the material becoming superconducting, and the latter associated with the coupling between the grain boundaries which is more sensitive to the applied field [17, 39, 40].

2.10 Higher Harmonic Susceptibilities

The higher harmonic susceptibilities represent the non-linear contributions to the total magnetic susceptibility, and in terms of AC susceptometry, these terms give rise to a signal at a frequency n times the excitation frequency. For instance the 3rd ($n = 3$) harmonic susceptibility is a contribution detected at a frequency of 3ω where ω remains the driving frequency of the excitation field [35]. In general, these terms are only significant near a phase transition. For instance, the 3rd harmonic susceptibility reveals a peak at a phase transition (paramagnetic to ferromagnetic, paramagnetic to spin glass or superconducting transition) and may be utilized as a confirmation of such transition, whereas the second harmonic susceptibility is associated with occurrence of spontaneous magnetization [17, 35]. Further, it remains a tool to distinguish states of matter from one another which show similar behaviour in the fundamental ($n = 1$) harmonic susceptibility [17].

Superconductors: The higher harmonic susceptibilities are greatly studied – in particular the third harmonic susceptibility $\chi_3 = \chi_3' + i\chi_3''$ for type-II high-temperature superconductors. Their presence relate to the flux dynamics in the material and are described by various critical models such as the Bean critical model [38, 40–42]. However, these critical models fail to describe the frequency- and amplitude-dependence of the applied field which have been observed experimentally, meaning these higher harmonics are not fully understood [38, 40–42]. The higher harmonic susceptibilities for type-I superconductors do not seem to be of much interest among researchers, however. Regardless of the type of superconductors, the transition is non-linear and contains non-linear processes which therefore are characterized by the these non-linear terms [41]. In this thesis the 3rd harmonic contribution has been measured for titanium which is presented in Section 4.7.

Spin Glass: The third ($n = 3$) harmonic susceptibility reveals a sharp negative peak near the freezing temperature, which in addition to the frequency-dependent fundamental ($n = 1$) harmonic susceptibility contributes to the signature of a spin glass. However, the third harmonic susceptibility plays a central role in distinguishing a spin glass from a superparamagnet as these share similar experimental features regarding the fundamental harmonic susceptibility, yet have a completely different microscopic configurations [17, 26]. A spin glass shows a very sharp negative peak in the third harmonic susceptibility, whereas a superparamagnet shows a very broad negative peak which does not go to zero instantly [17, 43].

3 Design and Instrumentation

This chapter is divided into a section covering the cryogenic aspect along with the instrumentation utilized to reach temperatures of mK, and a section covering AC susceptometry and the design of the susceptometer used to measure the AC susceptibility of titanium, cerium magnesium nitrate (CMN) and herbertsmithite.

Section 3.1 introduces dilution refrigeration and presents the method of cooling from a theoretical and a practical aspect. Section 3.2 presents the actual cryogenic instruments along with various graphs regarding the cooling and the operation. The software recording the various temperatures in the system was made by Jonas Hyatt in relation to his Master's thesis [44]. Section 3.3 introduces the concept of AC susceptometry in a more practical manner along with relevant complications and considerations. Further, it presents the experimental method translating measured voltage to susceptibility.

The final section 3.4 presents the design utilized to obtain the measurements presented in this thesis.

3.1 Dilution Refrigeration

Up until the 1950s, one could only achieve temperatures way below 1 K using demagnetization of a paramagnetic salt (magnetic refrigeration), however this method was replaced with ^{3}He refrigerators which reached their limit at temperatures of $T \approx 0.3\,\mathrm{K}$. Later, it was suggested to make use of the properties of a liquid mixture between the two helium isotopes ^{3}He and ^{4}He to reach even lower temperatures. This was carried out in reality at Leiden University in 1965 where a temperature of $T \approx 0.22\,\mathrm{K}$ was reached [16]. With time, this method has been improved greatly, where a minimum temperature of $T \approx 2\,\mathrm{mK}$ has been reached [16]. Nowadays, the dilution refrigerator is widely used to reach temperatures $T \leq 0.3\,\mathrm{K}$ as the main method which has the substantial advantage of being a continuous refrigeration method which can run stable for months [16, 45].

3.1.1 Phase Separation of Helium

Dilution refrigeration utilizes the properties of ^{3}He-^{4}He mixtures. The fraction of these isotopes in the mixture may be defined as:

$$x_3 = \frac{n_3}{n_3 + n_4}, \qquad x_4 = 1 - x_3 \tag{64}$$

where n_3 represents the number of ^{3}He atoms, and n_4 represents the number of ^{4}He atoms. There are various remarkable features of these isotope mixtures and the x-T phase diagram shown in Fig. 12 presents the relevant ones regarding dilution refrigeration. One feature to note is the lambda-line which marks the temperature-concentration boundary for super-fluidity of the mixture. For instance, pure ^{4}He ($x_3 = 0$) which is a Bose liquid becomes superfluid at a temperature of $T \approx 2.177\,\mathrm{K}$, and pure ^{3}He ($x_3 = 1$) which is a Fermi liquid becomes superfluid below $\sim 3\,\mathrm{mK}$ [46, 47]. And as the concentration of ^{3}He increases, the temperature to obtain superfluidity of the mixture is suppressed. At a concentration of $x_3 \approx 67.5\%$ the Lambda line reaches the phase-separation line. The second feature to note is the phase-separation line; above temperatures of $T \approx 0.87\,\mathrm{K}$, the isotopes ^{3}He and ^{4}He are fully miscible. However, below temperatures of $T \approx 0.87\,\mathrm{K}$ there is a forbidden region referred to as the "two-phase region" on Fig. 12, which marks a temperature-dependent restriction on the concentration of ^{3}He in the mixture. Thus, if a mixture with a ^{3}He-concentration of $x_3 > 6.6\%$ is cooled to temperatures $T < 0.87\,\mathrm{K}$, the mixture will begin to separate into a light ^{3}He-rich phase, where the concentration of ^{4}He approaches zero as the temperature decreases, and a heavy ^{4}He-rich phase, where $x_3 \rightarrow 6.6\%$. The light phase will float on top of the heavy phase, and if ^{3}He is removed from the diluted (bottom) phase, new ^{3}He atoms from the concentrated phase will dilute themselves into the diluted phase such that the concentration of ^{3}He remains at $x_3 = 6.6\%$. The dilution of the ^{3}He into the heavy phase is an endothermic process, meaning the ^{3}He atoms absorb heat from the surroundings as they transfer from the pure phase to the diluted phase [16, 45].

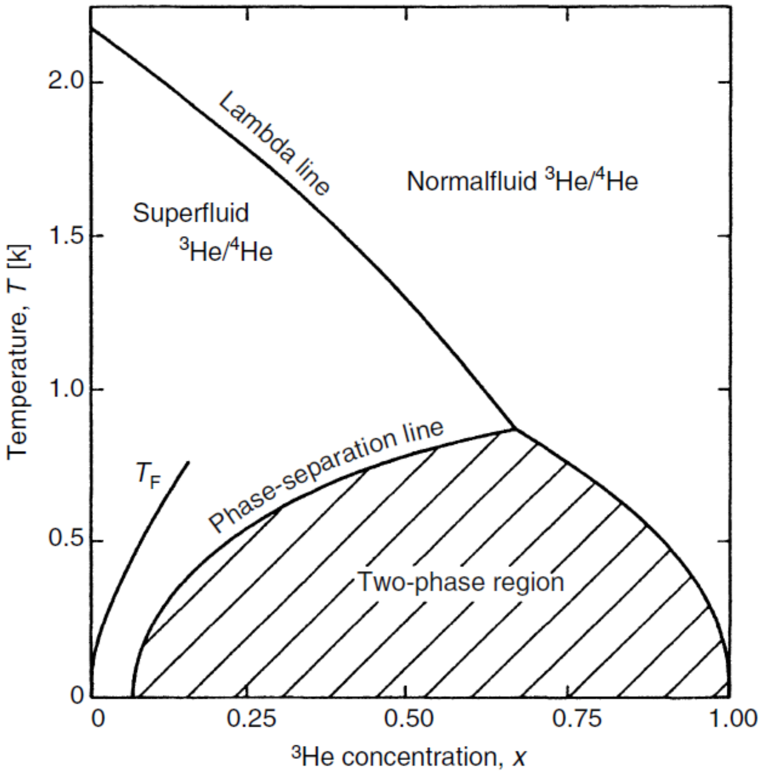

Figure 12: Phase diagram of liquid ^{3}He-^{4}He mixtures for temperatures $T \leq 2.3\,\mathrm{K}$ approximately. The Lambda line represents the temperature-concentration boundary for superfluidity of the mixture. The phase-separation line represents the temperature dependent restriction on the concentration of ^{3}He of the mixture [16]

3.1.2 Cooling Power of the Dilution Process

The cooling power briefly introduced in the previous section arises simply from the difference in enthalpy between the two phases, and from a theoretical aspect, the cooling power can be expressed as:

$$\dot{Q} = \dot{n}_3 \left[H_{3,\mathrm{d}}(T) - H_{3,\mathrm{c}}(T) \right] \tag{65}$$

where $\dot{n}_3$ represents the molar flow rate of ^{3}He from the concentrated phase to the dilute phase, $H_\mathrm{d}(T)$ and $\mathrm{H_c(T)}$ represent the enthalpy of ^{3}He in the dilute and the concentrated phase, respectively [16, 45]. Thus, given the enthalpy of the concentrated phase remains lower than the enthalpy of the dilute phase, i.e. $H_\mathrm{d}(T) > H_\mathrm{c}(T)$ and ^{3}He is continuously transferred from the concentrated phase to the dilute phase, one will have a cooling power $\dot{Q} > 0$. The enthalpy is given by the following:

$$H(T) - H(T=0) = \int_0^T C(T')dT' \tag{66}$$

meaning the heat capacities of ^{3}He in the two phases must be obtained in order to determine the cooling power of the dilution process. In both the diluted phase and the concentrated phase, the heat capacity varies linearly with temperature for low enough temperatures due to the fact both phases are Fermi liquids. However, pure ^{3}He differs by being a strongly interacting Fermi liquid, and the heat capacity cannot be computed using current theories. Experimental data of Greywall [16, 48] yield the following:

$$C_{3,\mathrm{c}}(T) = 2.7N_\mathrm{A}k_\mathrm{B}T \tag{67}$$

at a temperature of $T < 40\,\mathrm{mK}$ and saturated vapour pressure. Using the expression from Eq. (67) the enthalpy of pure ^{3}He becomes:

$$H_{3,\mathrm{c}}(T) = H_{3,\mathrm{c}}(T=0) + \int_0^T 2.7N_\mathrm{A}k_\mathrm{B}T'dT' = H_{3,\mathrm{c}}(T=0) + 1.35N_\mathrm{A}k_\mathrm{B}T^2 \tag{68}$$

On the other hand, the diluted phase is weakly interacting and may, therefore, be reasonably approximated as a Fermi gas with an effective mass of $m^* \approx 2.5m_3$, where m_3 is the mass of ^{3}He. For such a gas, the heat capacity is given by:

$$C_{3,\mathrm{d}}(T) = N_\mathrm{A}k_\mathrm{B}\frac{\pi^2}{2}\frac{T}{T_\mathrm{F}} \approx 13N_\mathrm{A}k_\mathrm{B}T \tag{69}$$

with Fermi temperature $T_\mathrm{F} = \frac{\hbar^2}{2m^*k_\mathrm{B}}(3\pi^2 n_3)^{2/3}$ where $n_3 = \frac{N_\mathrm{A}x_3}{V_\mathrm{m}}$ and $V_\mathrm{m} = V_{4,\mathrm{m}}\,(1 + 0.284x_3)$ with molar volume of pure ^{4}He of $V_{4,\mathrm{m}} = 27.589\,\mathrm{cm^3mol^{-1}}$. Thus, with a ^{3}He concentration of $x_3 = 6.6\%$ in the dilute phase, the Fermi temperature becomes $T_\mathrm{F}(6.6\%) = 0.38\,\mathrm{K}$ [16, 45]. Assuming thermodynamic equilibrium between the two phases i.e. $\mu_{3,\mathrm{c}} = \mu_{3,\mathrm{d}} \implies H_{3,\mathrm{c}} - T_\mathrm{c}S_{3,\mathrm{c}} = H_{3,\mathrm{d}} - T_\mathrm{d}S_{3,\mathrm{d}}$, and using that $S = \int_0^T \frac{C(T')}{T'}dT'$ one has:

$$H_{3,\mathrm{d}}(T) = H_{3,\mathrm{c}}(T=0) + 11.4N_\mathrm{A}k_\mathrm{B}T^2 \tag{70}$$

By using Eq. (68), (70) and (65) one obtains the following expression for the cooling power of the dilution process:

$$\dot{Q} = \dot{n}_3(95T_\mathrm{d}^2 - 11T_\mathrm{c}^2) \tag{71}$$

The maximum cooling power occurs when there is thermal equilibrium between the concentrated and the diluted phase ($T_\mathrm{c} = T_\mathrm{d}$) at which point the cooling power becomes:

$$\dot{Q} = 84\dot{n}_3T^2 \tag{72}$$

This may be the case if new ^{3}He is not supplied to the concentrated phase, at which point the minimum temperature can be reached, but the cooling will deplete eventually. However, in a real dilution refrigerator, the ^{3}He is circulating such that it is continuously added to the concentrated phase upholding the cooling effect. The added ^{3}He in reality is warmer than the temperature of the concentrated and the diluted phase, which will impact the temperature and the cooling power, but as long as the temperature of the concentrated phase satisfies the following condition:

$$T_\mathrm{c} < 2.9T_\mathrm{d} \tag{73}$$

there will be a cooling effect. This condition implies that the temperature of the concentrate still has to be close to the running temperature of the refrigerator, meaning it is crucial that the incoming ^{3}He is pre-cooled before it reaches the concentrated phase [16, 45].

3.1.3 Dilution Refrigeration in Practice

Figure. 13 shows a diagram of a working dilution refrigerator revealing the relevant components along with the flow path of the liquid helium. This part is typically an insert, which during operation is positioned in a cryostat kept at temperatures of $T \leq 4\,\mathrm{K}$ using a pulse-tube cooler or a helium bath. By following the diagram from Fig. 13, ^{3}He enters through a thin tube referred to as the *condenser line* where it has been pre-cooled to $T \approx 1.5\,\mathrm{K}$ and therefore liquefied (either by using a 1K pot or a compressor). It reaches the main flow impedance which ensures the helium proceeds without evaporating. It continues through a heat exchanger which is in thermal contact with the *still*, which ideally is kept at a temperature of $T \sim 0.6 - 0.9\,\mathrm{K}$. It proceeds to the second flow impedance which plays the same role as the main flow impedance. It continues through additional heat exchangers which ensure the ^{3}He is brought close to the base temperature before entering the concentrated phase of the mixture located in the top of a volume referred to as the *mixing chamber* where $x_3 \sim 100\%$. A larger tube is connected to the dilute phase of the mixture from the lower part of the mixing chamber where $x_3 \sim 6.6\%$. The tube follows through the same heat exchanger, which ensures the incoming helium to be pre-cooled before entering the mixing chamber, and proceeds to the still. Thus, the dilute phase extends from the mixing chamber to the still where the concentration of ^{3}He is significantly lower ($x_3 < 1\%$). However, the vapour above the dilute phase in the still consists mainly of ^{3}He ($x_3 > 90\%$) since the vapour pressure of ^{3}He is significantly higher compared to ^{4}He. Finally, the ^{3}He is pumped away and resupplied to the condenser line creating a closed ^{3}He circulation circuit. As the ^{3}He is pumped from the still, the ^{3}He in the dilute phase in the mixing chamber will be driven to the still due to the osmotic pressure difference, which consequently results in ^{3}He from the concentrated phase to enter the dilute phase and producing a cooling effect. In order to reach the base temperature, one typically supplies heat in the still in order to raise the temperature causing ^{3}He to evaporate faster, which consequently increases the flow rate $\dot{n}_3$ and further improves the cooling power (See Eq. 71). In addition, too much heat supply in the still may reduce the cooling power, as ^{4}He will evaporate in the process, causing the circulating helium to be a ^{3}He-^{4}He mixture deteriorating the flow rate. Further, it puts a heat load on the heat exchangers as the specific heat of ^{3}He in a ^{3}He-^{4}He mixture is significantly higher compared to pure ^{3}He. So the temperature in the mixing chamber is highly dependent on the temperature in the still, and one has to find a balance.

Finally, the heat exchangers, especially the final heat exchanger prior to reaching the mixing chamber, remain the most critical part of a dilution refrigerator and the minimum temperature is determined from these. At low temperature ($T \leq 20\,\mathrm{mK}$), the thermal boundary resistances between helium and the other materials in the helium circuit is given by:

$$R_{\mathrm{K}} = \frac{\alpha}{A} T^{-3} \tag{74}$$

where α remains a constant for the material specifically and A represents the surface area of the interface between the two materials. Thus, for decreasing temperature, one requires a large surface area to overcome this effect. Accounting for the thermal boundary resistance, Eq. (72) modifies to:

$$\dot{Q} = 84\left(\dot{n}_3 T_{\mathrm{mc}}^2 - \frac{5.2\dot{n}_3^2 R_{\mathrm{K}}}{A}\right) \quad \Rightarrow \quad T_{\mathrm{mc}}^2 = \frac{\dot{Q}}{84\dot{n}_3} + \frac{5.2\dot{n}_3 R_{\mathrm{K}}}{A} \tag{75}$$

where the expression for T_{mc}^2 represents the minimum mixing chamber temperature when there is no heat load [16, 49]. This remains one of the main restrictions on the minimum temperatures for the dilution refrigerator. The boundary resistance increases rapidly for decreasing temperature, reducing the cooling effect substantially. Furthermore, in order to minimize the final term in Eq. (75), one would require a huge surface area between the heat exchangers and the circulating helium. Therefore, obtaining temperatures closer and closer to absolute zero comes with requirements which become unrealistic quickly.

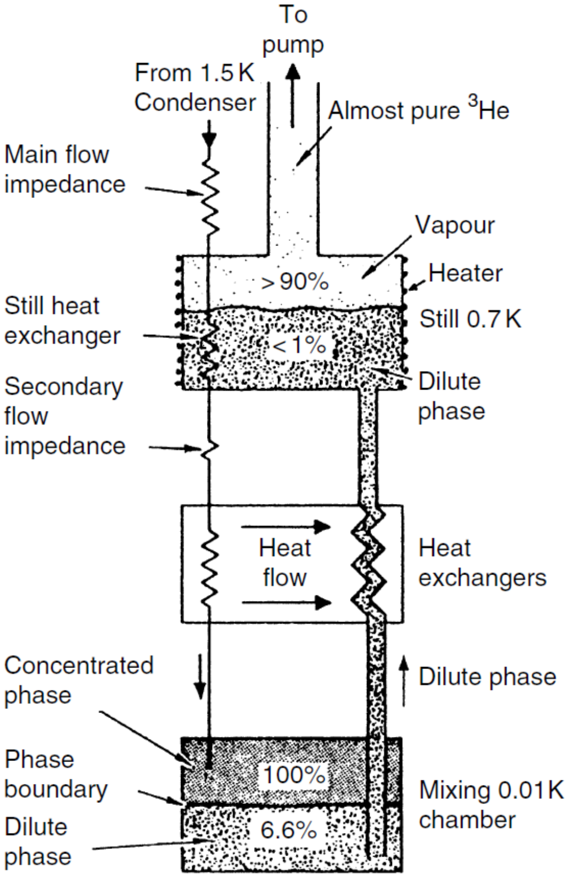

Figure 13: Schematic of a ^{3}He-^{4}He dilution refrigerator. ^{3}He enters the condenser line where it liquifies. It proceeds through various heat exchangers and flow impedances ensuring an adequate low temperature. It enters the mixing chamber which contains a concentrated phase of ^{3}He and a dilute phase of ^{3}He and ^{4}He. The dilute phase extends through a thicker tube all the way to the still, where mainly ^{3}He evaporates and is resupplied to the condenser line using a pump. The percentages in the mixing chamber and in the still represent the concentration of ^{3}He. From [16].

3.2 The Cryogenic Instrumentation

In this project, the cryogenic instruments consist of a two staged cryocooler (Cryomech PT415 Pulse Tube Compressor) and the MCK 50-100 Dilution Refrigerator (DR) which is specified to have a cooling power of $\dot{Q} = 100\,\mu$W at a temperature of $T = 100\,$mK [50]. The former is used to bring a volume referred to as the *outer vacuum chamber* (OVC) to a temperature of T $\leq 4.2\,$K. The OVC contains a 16 Tesla Cryogen-Free superconducting electromagnet along with various temperature sensors for the different internal components such as the 1st stage, 2nd stage, upper and lower heat exchangers etc. The base temperature of the cryocooler is $T \approx 2.8\,$K and it takes approximately 40 hours to reach a temperature of $T \approx 4.2\,$K [51, 52]. A typical cooldown of the OVC is presented in Fig. 14, where one may notice that the temperature of the 1st stage, 2nd stage, and the switch decreases rapidly in the beginning compared to the rest of the components. The inner and outer part of the superconducting electromagnet are thermally linked to the 1st and 2nd stage, but, it remains the largest mass in the OVC, which consequently results in a slower cooling. When the temperature of the magnet reaches 100 K, the cooling begins to approach the base temperature more rapidly as the phonon heat capacity goes down. Hereafter, the 1st stage and the upper heat exchanger stabilize at approximately 40 K and 15 K, respectively, whereas the remaining components stabilize at $T \leq 4.2\,\mathrm{K}$.

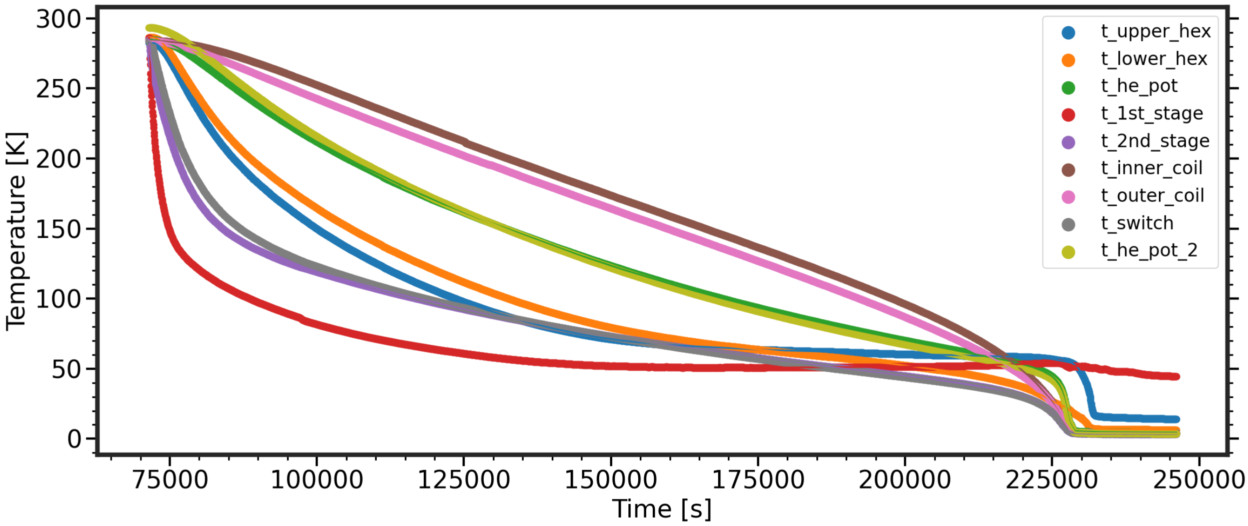

Figure 14: A typical cooldown of the OVC using the two staged cryocooler. Measurement taken 20/10/22.

The system is fitted with an exchange tube which is referred to as the *sleeve* and designed to accommodate the insertable DR. This tube contains multiple heat exchangers such as the 1st stage, 2nd stage and upper and lower heat exchanger which along with added exchange gas, ensures an optimised temperature gradient adequate to cool the mixture of helium utilized in the dilution process. Initially, this exchange gas in the sleeve only brings the relevant components (still & mixing chamber) of the DR to base temperature very slowly. Then, exchange gas is further added into the *inner vacuum chamber* (IVC) to enhance the speed of the entire process. The IVC contains the probe which is mounted onto a cold-finger extending inside the mixing chamber of the DR. The temperature of the dilution system is recorded by 3 ruthenium oxide (RuO_2) resistors – one located in the still, one located inside the mixing chamber, and the final one located on the cold finger.

A typical example of adding exchange gas into the IVC is depicted in Fig. 15. The bottom plot represents the pressure over time, where initially a large peak in the pressure occurs which reflects the increasing pressure due to the exchange gas being added. Subsequently, the pressure decreases over time due to the cooling of the exchange gas, and stabilizes at the base temperature. The insert shows when the exchange gas is evacuated through the still using a molecular turbo pump, causing the pressure in the still to increase for a short time, at which point it drops back to $P_{\mathrm{still}} < 5 \times 10^{-4}$ mbar, whereas the pressure in the IVC approaches the base pressure more slowly. The top plot in Fig. 15 shows the temperature of the components in the OVC, and the initial peaks for various components represent the system's response to the added heat load in terms of exchange gas. Further, when the gas is evacuated, smaller peaks are seen in the upper and lower heat exchanger. Finally, the middle plot shows the temperature of the still and mixing chamber, which start decreasing as the exchange gas is added – as one would expect. One may notice that the temperature of the thermometer labeled 't_mixing_chamber_2' begins to decrease earlier compared to the thermometer labled 't_mixing_chamber_1' due to the fact that the former is located on the cold-finger in the IVC, whereas the latter is located inside the mixing chamber. At this point, the dilution process can be initiated.

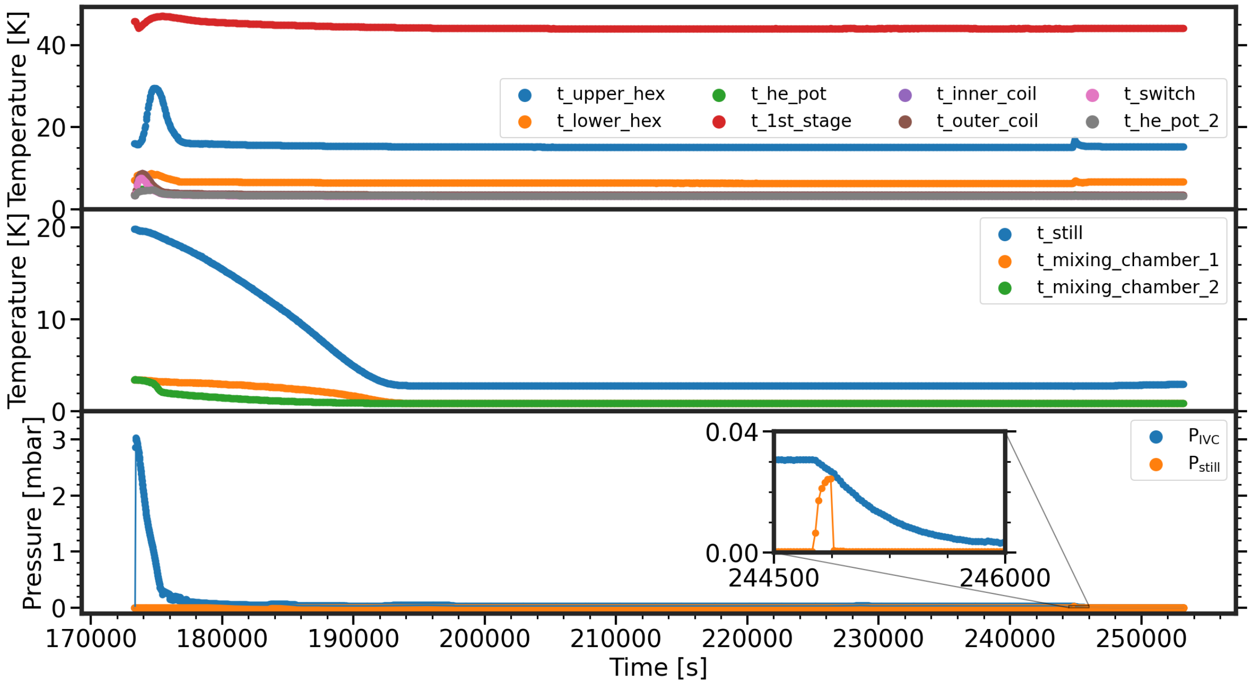

Figure 15: A graph showing exchange gas being added to the IVC to ensure the still and the mixing chamber reach a temperature $T \leq 4.2\,\mathrm{K}$. Measurement taken 21/10/22. **Top**: The temperature of the internal components of the OVC; notice the increase in the temperature – especially for the upper heat exchanger at $t \approx 175000\,\mathrm{s}$ and $t \approx 245000\,\mathrm{s}$ which represent the system's response to heat load in terms of exchange gas being added and removed, respectively. **Middle**: The temperature of the still and the mixing chamber decrease upon the exchange gas being added. The thermometer denoted 't_mixing_chamber_2' is attached to the cold-finger whereas the thermometer denoted 't_mixing_chamber_1' is located inside the mixing chamber. **Bottom**: The pressure in the IVC and the still. The initial peak in the pressure of the IVC represent the increase in pressure due to exchange gas. The insert shows the time ($t \approx 245000\,\mathrm{s}$) where the exchange gas is pumped out of the system through the still using a molecular turbo pump.

The gas handling system contains two storage tanks with the capacity of 70 L and 20 L where the corresponding pressure of the ^{3}He-^{4}He mixtures is $P_{\mathrm{70L,dump}} \approx 735\,\mathrm{mbar}$ and $P_{\mathrm{20L,dump}} \approx 720\,\mathrm{mbar}$. The mixture is added to the system and a compressor is utilized to increase the pressure in order to ease the condensation. The final temperature remains highly dependent on the amount of helium in the system and the ratio of ^{3}He and ^{4}He, and since the two storage tanks contain a mixture of the ^{3}He and ^{4}He it may be difficult to control. However, reaching a point where one is close to emptying the dumps such that the system contains the majority of the helium, letting the system stabilize, and, subsequently, removing the helium in portions from the system until the lowest temperature is reached, proved to be a sufficient and consistent method. When a certain configuration of helium has been chosen, the temperature in the mixing chamber can be lowered even further by increasing the temperature in the still as mentioned in Section 3.1.3. However, depending on the configuration of helium, there is a limit of heating in the still due to the circulation pressure denoted P_5 as this should ideally remain $P_5 \leq 1000\,\mathrm{mbar}$. The system's response to a ramp in heat in the still is illustrated in Fig. 16 which shows the temperature of the still and the mixing chamber along with the circulation pressure. The left plot corresponds to a helium configuration of $P_{\mathrm{70L,dump}} \approx 5\,\mathrm{mbar}$ and $P_{\mathrm{20L,dump}} \approx 96\,\mathrm{mbar}$ and the right plot corresponds to a helium configuration of $P_{70L,dump} \approx 5\,\mathrm{mbar}$ and $P_{\mathrm{20L,dump}} \approx 260\,\mathrm{mbar}$. The helium configuration is defined as the amount of helium that remains in the storage tanks when circulation has been established. Therefore, there is a larger amount of helium in the system for the configuration with $P_{70\mathrm{L,dump}} \approx 5\,\mathrm{mbar}$ and $P_{20\mathrm{L,dump}} \approx 96\,\mathrm{mbar}$.

Regarding the left plot in Fig. 16, notice the temperature of the still is fluctuating initially as shown by the arrow in the top plot. This is typically an indication that the system contains too much helium, such that the level of liquid helium exceeds the top of the still, causing it to evaporate in a non-smooth manner. The circulating helium, in this case, most likely has a too much ^{4}He, which can cause a larger heat load on the heat exchangers, and, therefore, results in a higher mixing chamber temperature as mentioned in Section 3.1.3. Upon ramping the heat to a higher level, one may notice that the temperature in the still becomes more stable since the level of liquid helium is lowered as more helium is circulating. The ramping in heat is, in addition, reflected in the simultaneous decrease in the mixing chamber temperature and a simultaneous increase in the circulation pressure (highlighted by the arrow) shown in the middle plot and the bottom plot, respectively. At the final ramp, the circulation pressure reaches $P_5 \approx 1000\,\mathrm{mbar}$, which marks the maximum amount of heat, one can apply for this configuration of helium, and the mixing chamber temperature stabilizes at $T_{\mathrm{mc}} \approx 42\,\mathrm{mK}$.

As for Fig. 16 (right), helium has been removed from the system and, thus, the still temperature remains more stable and the initial mixing chamber temperature is significantly lower. In addition, the initial circulation pressure prior to applying heat in the still takes a lower value. Moving on in time, the expected behavior is seen: the mixing chamber temperature decreases upon applying heat in the still, and, consequently, the circulation pressure increases. Finally, the circulation pressure reaches $P_5 \approx 1000\,\mathrm{mbar}$ and the temperature of the still and mixing chamber stabilize at $T_{\mathrm{still}} \approx 900\,\mathrm{mK}$ and $T_{\mathrm{mc}} \approx 18\,\mathrm{mK}$, respectively.

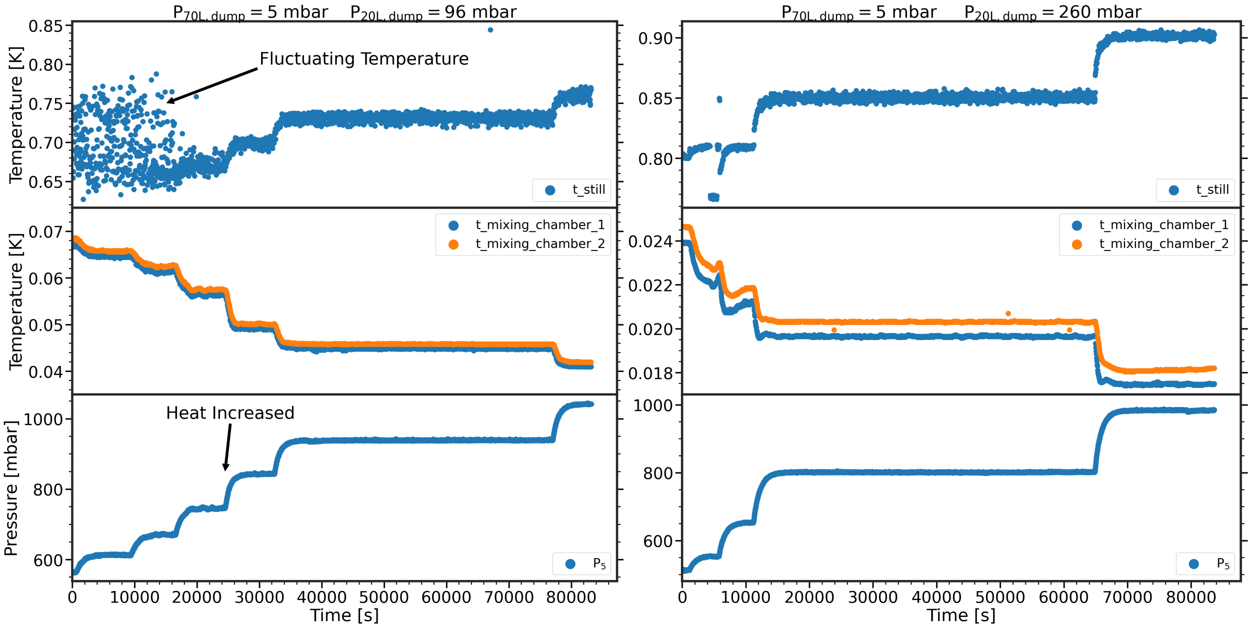

Figure 16: Graph of the circulation pressure and the temperature of the mixing chamber and still during operation while ramping up the heat in the still for two different configurations of helium. An increase in the circulation pressure and temperature of the still along with a decrease in the temperature of the mixing chamber reflect an increase in the heating. Measurement taken 28/10/22. **Top**: Temperature of the still as a function of time. **Middle**: Temperature of the mixing chamber as a function of time. **Bottom**: Circulation pressure as a function of time. **Left**: A helium configuration of $P_{70\mathrm{L,dump}} \approx 5\,\mathrm{mbar}$ and $P_{20\mathrm{L,dump}} \approx 96\,\mathrm{mbar}$ **Right**: A helium configuration of $P_{70\mathrm{L,dump}} \approx 5\,\mathrm{mbar}$ and $P_{20\mathrm{L,dump}} \approx 260\,\mathrm{mbar}$.

3.3 AC Susceptometry

The previous chapter introduced magnetic susceptibility from a theoretical perspective. This section will proceed in a more practical manner and clarify how one measures magnetic susceptibility, more specifically AC susceptibility.

In general, measuring magnetic susceptibility regardless of DC or AC susceptibility relies on Faraday's law which is given by:

$$\mathcal{E} = -\frac{d\Phi}{dt} \tag{76}$$

This implies that a change in magnetic flux (Φ) with respect to time through a closed path gives rise to an induced electromotive force ($\mathcal{E}$) and, therefore, an induced current in the closed path [53]. In the DC case, the change in magnetic flux is accomplished by physical movement of the sample (vibrating sample magnetometer). However, in the AC case, the change in magnetic flux is obtained simply by applying an oscillating excitation field while the sample remains static in position. A conventional AC susceptometer consists of an excitation coil and two detector coils, which allows one to study the susceptibility as a function of frequency, drive amplitude, and temperature [17, 18, 26, 33, 39, 54].

The excitation coil (commonly referred to as the primary or drive coil) produces an AC magnetic field when driven by an AC source. Inside the excitation coil, a set of detector coils are positioned such that they experience near-identical field from the excitation coil. The detector coils are oppositely wound and electrically connected in series, meaning the change in magnetic flux produced by the excitation coil, induces a net voltage difference across the detector coils, which theoretically will be zero, given the two detector coils are identical and positioned symmetrically in accordance to the excitation field. If one positions a sample in one of the detector coils and leaves the other empty as illustrated on Fig. 17, the induced voltage will be caused by the magnetization of the sample alone. Thus, one will have

$$\mathcal{E} = -\left(\frac{d\phi_1}{dt} + \frac{d\phi_2}{dt}\right) = -\mu_0 N_\mathrm{s}\left[\int\left(\frac{d\boldsymbol{H}(t)}{dt} + \frac{d\boldsymbol{M}(t)}{dt}\right)\cdot d\boldsymbol{a} - \int \frac{d\boldsymbol{H}(t)}{dt}\cdot d\boldsymbol{a}\right], \tag{77}$$

where N_s is the number of turns for the detection coil. This reduces to the following expression

$$\mathcal{E} = -\mu_0 N_s A\frac{d\boldsymbol{M}(t)}{dt} \quad \longrightarrow \quad -\mu_0 N_s \alpha G\frac{d\boldsymbol{M}(t)}{dt}. \tag{78}$$

This is, however, only true if the sample in focus is uniformly magnetized and have identical cross sectional area as the detector coil. In reality, this is not the case. Thus, experimentally, a calibration constant is introduced for the particular AC susceptometer which is separated into a part which is dependent on the geometry of the coils (α), and a part which is dependent on the quantity of the sample (G), hence the arrow in Eq. (78) [34].

3.3.1 Considerations & Complications

There are various effects which are typically disregarded with pen and paper that may play a role when working with an AC susceptometer [18, 39]. Such things, may be:

1. Nonidentical detector coils.
2. Inhomogeneous driving field.
3. Probe environment.

4. Sensitivity & capacitive coupling.
5. Noise & ground loops.

Firstly, it remains impossible to construct identical detection coils, meaning a mismatch signal is inevitable, and may easily become significant. Secondly, the detection coils will undoubtedly experience an inhomogeneous driving field, which will further enhance the mismatch signal, meaning the system in general is sensitive to alignment of the detector coils. There are multiple balancing methods to compensate for the offset, such as using a "trim coil", inductively coupled to the detection coils, that has to be driven with correct phase and adequate amplitude in order to null the signal. Further, one can utilize a sample rod such that the sample may be positioned into each coil and, subsequently, subtracting the two signals. However, achieving a successful compensation remains difficult as the balancing point varies with temperature and frequency. Finally, one can adjust the detecting coils along the axis of the primary coil minimizing the offset [18, 39, 54].

The probe environment should ideally be free of any magnetic materials within the vicinity of the drive field, as this may produce unwanted effects which typically varies with frequency and temperature. In addition, the drive field gives rise to induced eddy currents which can feed the detection coils with an unwanted signal at a different phase with respect to the signal of interest. If there are any of such effects they should be accounted for using a measurement with empty coils. Depending on the temperature of interest, the eddy currents might give rise to further complications in terms of heating; heat is produced in the metallic parts of the susceptometer which consequently raises the temperature of the sample, especially if the sample is conducting [18]. The heat of such eddy currents scales quadratically with both the excitation frequency and the strength of the field ($\dot{Q} \propto \nu^2 \mathrm{H}_{\mathrm{AC}}^2$) [16]. This complication is mainly relevant for temperatures at the order of mK.
The sensitivity is mainly enhanced through the number of turns for the detection coils, and as a rule-of-thumb one wants to select the smallest wire in terms of diameter, which will in addition make it more difficult to wind two identical coils – just a slight imperfection will affect the inductance and, therefore, the balance point [39]. A large number of turns brings unwanted effects such as increasing the capacitive coupling between turns as well as the drive coil and the detection coils, which will yield a background signal in the imaginary part of the voltage when the two components have been separated [55]. Further, it will increase significantly for increasing frequency. Therefore, one has to find a balance which yields a satisfying signal of the sample [18, 55].

Some of the points mentioned above should be considered when diving into AC susceptometry, however, at the end of the day, the importance of these depends on the physics one strives to measure. In case of superconductivity, the signal becomes of significant magnitude, at which point the background signal and possible noise become of minor effect. In case of paramagnetism, the signal becomes noticeable in the mK range, as the susceptibility roughly follows a Curie law ($\chi \propto \frac{1}{T}$). If one wishes to pursue frustrated magnetism which possesses a minor magnetization for small external fields, it may become a challenge to distinguish the signal due to the sample from the background and the potential noise. Key decisions which lead to satisfying measurements typically come down to trial and error.

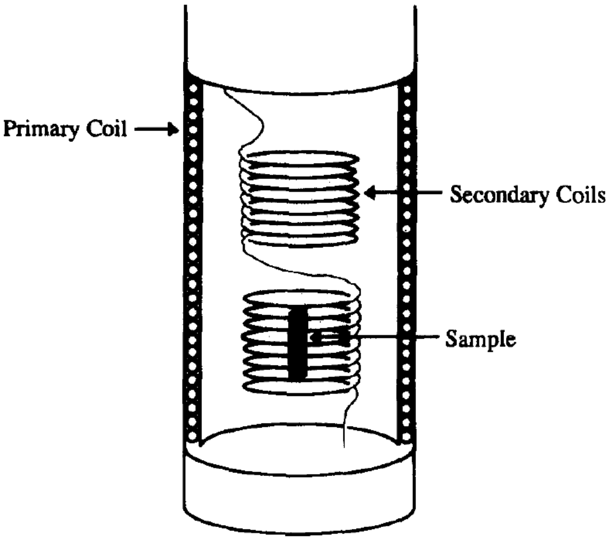

Figure 17: Sketch showing a traditional susceptometer which consists of a primary coil that contains two smaller oppositely wound coils in series. In the ideal case with two secondary coils being identical, the voltage across is cancelled with no sample present. However, a sample present in one of the coils, disturbs the balance and, consequently, yields a voltage difference across the coils. From [39].

3.3.2 Experimental Approach - Induced Voltage to Susceptibility

Experimentally, the voltage induced across the secondary coils is typically measured by a lock-in amplifier which uses phase-sensitive detection to measure small AC signals at a given reference frequency and phase with respect to the reference signal [56]. The raw, measured voltage difference has to be separated with the proper phase in order to extract the in-phase and the out-of-phase component of the susceptibility. And this section presents a method of obtaining the proper phase for an arbitrary harmonic.

The driving field can in general be written as $H = H_0 \cos(\omega t + \phi_S)$, where ϕ_S represents the phase to which the lock-in is synchronized. The induced voltage is given by Eq. (78), and, in general, the magnetization of the sample is a nonlinear function of the external field and has a phase lag with respect to the driving field. Such a magnetization can be written as a Fourier expansion:

$$M(\omega t) = H_0 \sum_{n=1}^{\infty} \left[\chi_n' \cos[n(\omega t + \phi_S)] + \chi_n'' \sin[n(\omega t + \phi_S)]\right] \tag{79}$$

Then, the induced voltage becomes:

$$\mathcal{E} = C_S \omega H_0 \sum_{n=1}^{\infty} n \left[\chi_n' \sin[n(\omega t + \phi_S)] - \chi_n'' \cos[n(\omega t + \phi_S)]\right] \tag{80}$$

where C_S cover the prefactors from Eq. (78) such that $C_S = \mu_0 N_s \alpha G$. The lock-in amplifier multiplies the input signal with the phase shifted n'th harmonic of the reference signal, which, subsequently, is passed through a low-pass filter. This process can be expressed as:

$$\mathcal{E}_n^{x,y} = C_{\text{int}} \int_{\omega t=0}^{\omega t=2\pi} \mathcal{E}_{\text{in}}(\omega t) \mathcal{E}_{\text{ref}}^{x,y}(\omega t) d(\omega t) \tag{81}$$

where C_{int} is the constant of integration. Reference [34] states that the form of the reference signal is nontrivial. The following forms are presented:

$$\mathcal{E}^x_{\text{ref}} = \sin\left[n(\omega t + \phi_D)\right], \quad \mathcal{E}^x_{\text{ref}} = \sin(n\omega t + \phi_D) \tag{82}$$

where the left proposition leads to the no phase adjustment regardless of the harmonic order, whereas the right proposition does. Reference [34] finds that $\mathcal{E}^x_{\text{ref}} = \sin(n\omega t + \phi_D)$ is the proper expression, with $\mathcal{E}^y_{\text{ref}} = \mathcal{E}^x_{\text{ref}}\left(\phi_D + \frac{\pi}{2}\right)$. By inserting this in Eq. (81), one obtains:

$$\mathcal{E}^x_n = C_S \frac{n\omega H_0}{\sqrt{2}}\left[\chi'_n \cos(n\phi_S - \phi_D) + \chi''_n \sin(n\phi_S - \phi_D)\right], \tag{83}$$

$$\mathcal{E}^y_n = C_S \frac{n\omega H_0}{\sqrt{2}}\left[\chi'_n \sin(n\phi_S - \phi_D) - \chi''_n \cos(n\phi_S - \phi_D)\right] \tag{84}$$

where the $C_{\text{int}} = \frac{1}{\pi\sqrt{2}}$ from Eq. (81). If the lock-in phase is set such that $\phi_D = n\phi_S$ the expressions for $\mathcal{E}^x_n$ and $\mathcal{E}^y_n$ in Eq. (83) reduce to the following [19, 34]

$$\mathcal{E}^x_n = C_S \frac{n\omega H_0}{\sqrt{2}}\chi'_n, \qquad \mathcal{E}^y_n = -C_S \frac{n\omega H_0}{\sqrt{2}}\chi''_n \tag{85}$$

where the signal has been separated into an in-phase and an out-of-phase n'th Fourier component. Thus, one has to initially determine the phase which separates the first harmonic components, and if one wishes to separate n'th harmonic components, the new phase will be $\phi'_D = n\phi_D$. Instead of changing the phase on the actual instrument, equivalently one may rotate the raw data using:

$$\begin{bmatrix} \mathcal{E}^x_n \\ \mathcal{E}^y_n \end{bmatrix} = \begin{bmatrix} \cos\Theta & -\sin\Theta \\ \sin\Theta & \cos\Theta \end{bmatrix} \cdot \begin{bmatrix} X_n \\ Y_n \end{bmatrix} \tag{86}$$

where X_n and Y_n represent the raw data. There exist multiple methods to determine the phase. However, a convenient method is utilizing the property of a superconductor having zero loss for small applied drive fields ($H < H_{\text{c}}$), meaning $\chi''_1 = 0$. Further, one can utilize a paramagnetic material such as cerium magnesium nitrate (CMN) which should equivalently have $\chi''_1 = 0$ and be temperature independent. However, due to the two secondary coils not being identical, there will be a capacitive contribution in the imaginary part which scales with frequency. Thus, one would witness an out-of-phase component different from zero, which will remain temperature independent, however. In addition, the calibration constant C_S can be determined experimentally by accounting for demagnetization and subsequently imposing $\chi'_1 = -1$ in SI units utilizing a superconductor, or by knowing the coil geometry and the sample volume very precisely. However, plenty of effects may have an impact, making it far from trivial obtaining the proper units. Unfortunately, even if one performed the conversion properly, this is sample-specific. Therefore, research articles typically report the converted susceptibility in arbitrary units and focuses on identifying phase transitions and the behaviour as a function of the possible variables (frequency, temperature, field strength) [18, 26].

3.4 Design - AC Susceptometer

The design of the AC suceptometer has been constructed by the NBI Mechanical and Electronic Workshop and used in a previous Master's Thesis [57]. Thus, the material of the coil housing and the coil forms along with the coaxial type remain the same. Minor modifications regarding the detection coils and a few metallic screws have been made in order to improve the overall performance. The coil form for both the primary coil and the secondary coils were made of the material referred to as *PEEK* (*polyether ether ketone*) which is non-magnetic and has a low thermal conductivity.

3.4.1 The Primary Coil

The primary coil was constructed with the following parameters: an inner radius of $R = 7.25\,\text{mm}$, a length of $l = 25\,\text{mm}$, and $N = 940$ turns with a wire of 0.2 mm in diameter. A theoretical normalized field profile is determined for the given length and inner radius of the primary coil using:

$$B(z) = \frac{\mu_0 n I}{2}\left(\frac{z+\frac{l}{2}}{\sqrt{R^2+\left(z+\frac{l}{2}\right)^2}} - \frac{z-\frac{l}{2}}{\sqrt{R^2+\left(z-\frac{l}{2}\right)^2}}\right) \tag{87}$$

where R represents the inner radius and l represents the length. The profile is depicted in Fig. 18 along with the ideal position of the detection coils assuming identical detection coils, and symmetric driving field. The length of each detection coil along with the separation corresponds to the parameters mentioned in the following section (Section 3.4.2).

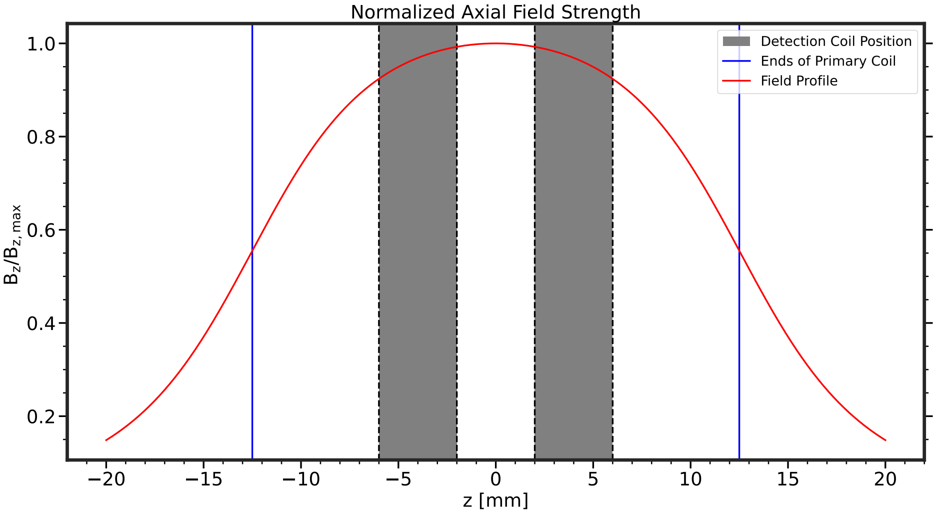

Figure 18: The theoretical axial field profile of the primary coil. The grey area corresponds to the position of the detection coils. The blue lines represent the ends of the primary coil.

3.4.2 The Secondary Coils

Initially, the secondary coils made for the previous Master's thesis [57] consisted of 220(1) turns for each coil, using a coil form with a separation of 1 mm. Ideally, the secondary coils should be separated with a larger distance in order to avoid flux coupling, and the other detection coil might pickup the signal from the sample in focus, yielding a reduction in the signal. A common separation length is the length of one detection coil (4 mm in our case), however, one may separate them further [39]. In addition, a reasonable amount of turns are typically 800-1200 turns, however, it depends on the setup, sample size, and physics one wishes to pursue [55].

Starting the project, we decided to wind a new set of secondary coils, using an identical coil form with a coil separation of 4 mm (see Fig. 65 Appendix A). The coils ended up with the following parameters: an inner radius of $R = 5.2\,\text{mm}$, a length of $l = 4\,\text{mm}$ and $N = 460(1)$ turns using a copper wire of 0.1 mm in diameter. The coil form contains cylindrical space for the sample with a diameter of 3 mm.

3.4.3 The Positioning of the Coils

A housing for the coils was constructed for the Master's thesis of Mathias Mikkelsen [57]. The housing could be attached onto a stainless steel stand, which further could be screwed onto the cold finger.

The primary coil was positioned in the housing (see Fig. 64 in Appendix A) and the secondary coils were positioned inside the primary coil and fixed with designed non magnetic thread. The secondary coils were adjusted along the axis at room temperature, such that the signal would be minimized to a certain extend. Obviously, this position might differ slightly from the symmetrical positioned presented in Fig. 18 as the detection coils remain non-identical and the primary coil in reality will not produce a completely symmetric field, thus changing the balancing point as mentioned in Section 3.3.1. The positioning of the coil system on the cold finger can be seen in Fig. 19, where the left image and the right image show the configurations which result in a perpendicular and parallel DC field, respectively, if such field is present.

3.4.4 The Electrical Circuit

The electrical circuit for the inductive susceptometer consists of a primary circuit and a secondary circuit. The primary circuit contains a resistor ($R = 100\,\Omega$) in series with the primary coil, which produces the excitation field at a set excitation frequency using a voltage signal generator. The resistor allows one to determine the current in the circuit, from Ohm's law by measuring the voltage drop across this resistor and from there then compute the strength of the magnetic field. The secondary circuit consists of two detection coils wound oppositely such that the net voltage is minimized as mentioned in Section 3.3.

The voltage is typically measured using a lock-in amplifier, which measures the amplitude and the phase with respect to the phase of some reference voltage, which results in an in-phase signal and an out-of-phase signal. The reference voltage is typically the voltage produced by the signal generator. Two variations of such a circuit were used. In the first configuration which is depicted in Fig. 20 (left), an external signal generator (Keysight N9310A Signal Generator) was utilized in the primary circuit to produce the driving field and the voltage drop across the resistor was measured using an oscilloscope (Tektronix TBS1072B oscilloscope). A lock-in amplifier (Standford Research Systems SR830 Lock-in amplifier) was used in the secondary circuit to measure the voltage drop across the secondary coils and the reference voltage was set to the voltage produced by the external signal generator. This configuration was used to measure the AC susceptibility of titanium and CMN. Due to noise, the oscilloscope had a difficult time measuring the voltage drop accurately at low supply voltages, and regarding the reference voltage for the lock-in amplifier, there was a minimum voltage it could lock on to if a Transistor-Transistor Logic (TTL) wave was not used – and the external signal generator did not seem to fulfill this requirement. Therefore, it puts a lower limit on the voltage supply and, therefore, the current in the circuit along with the induced magnetic field. And, as mentioned in Section 3.3.1, too high current produces heat due to resistance in the wires, and additional heat is produced by induced eddy currents in metallic parts nearby which scales with the strength and the frequency of the driving field, meaning one ideally want to use a small field to prevent heating the sample.

Thus, for the second configuration, (see Fig. 20 (right)) the built-in signal generator of the lock-in amplifier was used for the primary circuit, and a TTL output was supplied as a reference to an additional lock-in amplifier of the same model, which further was utilized to measure the voltage drop across the resistor. The lock-in amplifier in the secondary circuit takes its own produced signal as a reference. This circuit configuration was used to measure the AC susceptibility of herbertsmithite. This circuit is best of the two in our case as it allows us to decrease the field further and eliminate the heat produced due to the resistive parts in the circuit and induced eddy currents.

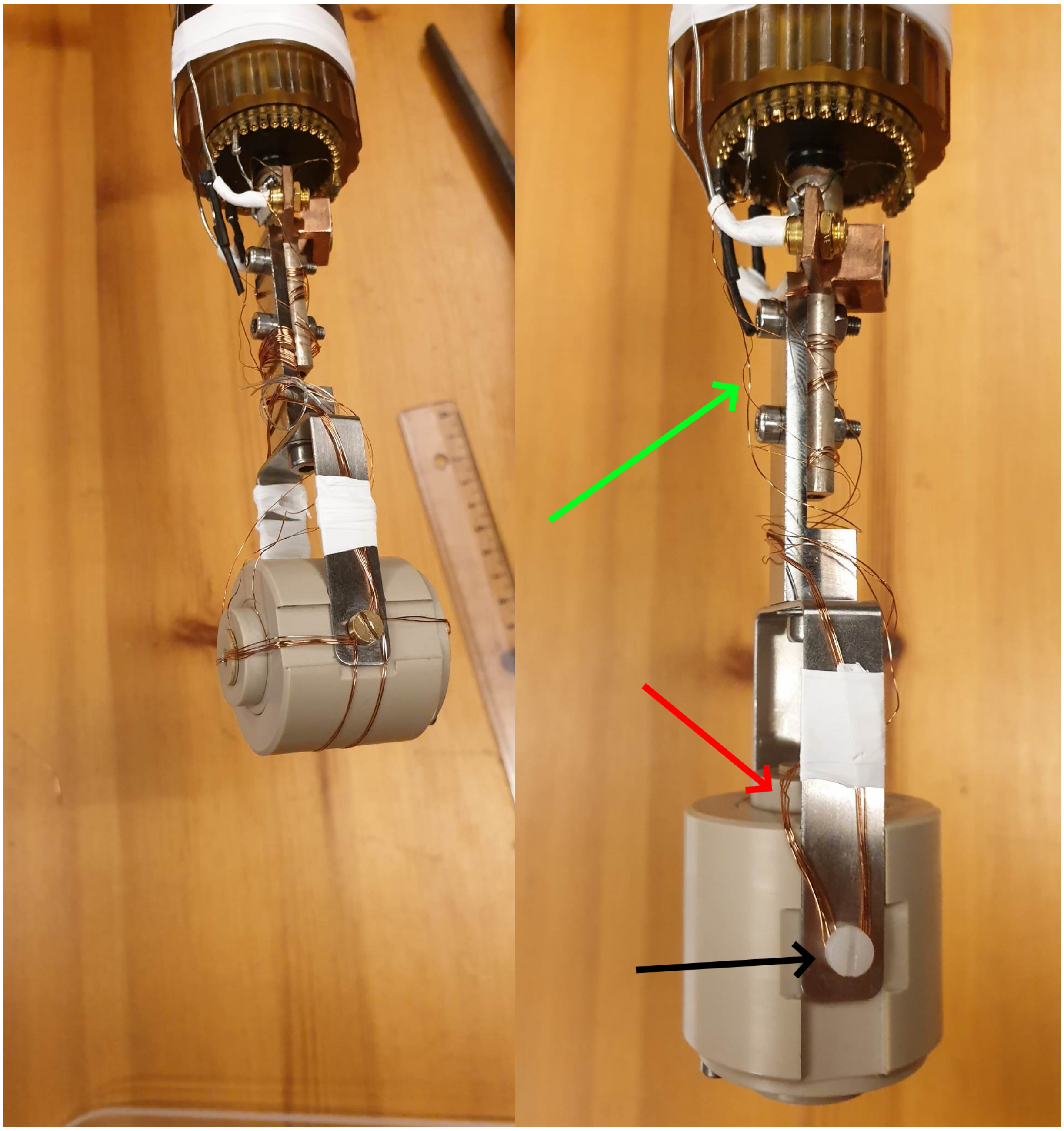

Figure 19: Left: This configuration (configuration 1) results in a DC field perpendicular to the excitation field, if DC field is present. This configuration was used initially for all the samples (titanium, CMN and herbertsmithite). **Right**: This configuration (configuration 2) results in a DC field parallel to the excitation field, if DC field is present. It was used for the last measurement series of herbertsmithite and the background measurement of Stycast. This, however, changes the background signal compared to the perpendicular configuration because of the IVC can. The **black** arrow points at the nylon screws which replaced the metal screws seen in configuration 1. The red points at the copper wires used for thermalization to the sample. The green arrow points at the copper wires from the coils.

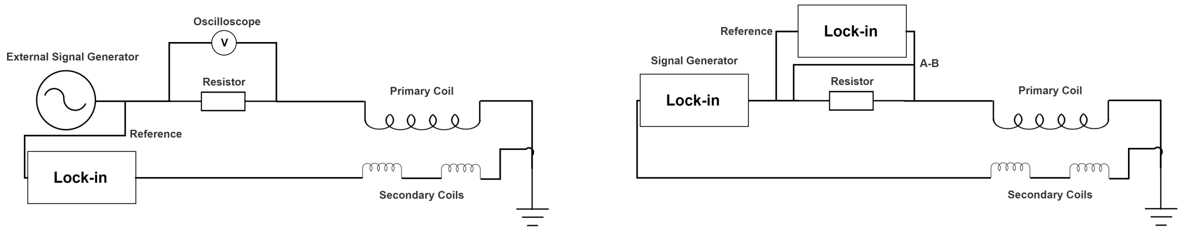

Figure 20: Schematic overview of the wired circuits that were used. The two circuits consist of a primary circuit and a secondary circuit. The primary contains a resistor ($R = 100\,\Omega$) in series with the primary coil where the current is determined from Ohm's law by measuring the voltage drop across the resistor. The secondary contains a set of detection coils in series and oppositely wound where the voltage across the coils is measured using a lock-in amplifier (Standford Research Systems SR830 Lock-in amplifier). **Left**: This circuit was used for the measurements regarding Ti & CMN (Oscilloscope was replaced with lockin for CMN). It consists of an external signal generator (Keysight N9310A Signal Generator) and an oscilloscope (Tektronix TBS1072B oscilloscope) to measure the voltage across the resistor. **Right**: This circuit was used for the measurements regarding herbersmithite. It utilizes the built-in oscillator of the lock-in amplifier and an additional lock-in amplifier to measure the voltage across the resistor.

4 The AC Susceptibility of Titanium

The very first test of the susceptometer and the two new detection coils was performed utilizing a superconductor, as it generates a large signal. As mentioned in Section 3.3.2 superconductors allow for an easy phase determination, which is required to separate the real and the imaginary component of the measured voltage across the detection coils. However, the transition temperature (T_c) has to be in the appropriate temperature range matching the temperature range of a dilution refrigerator (0.002 - 1 K). Therefore, inspired by Amann *et al.* [2] and in an attempt to recreate some of the results, titanium was chosen which, being a Type-I superconductor and having a critical temperature $T_c \approx 450\,\mathrm{mK}$, marks it as a suitable candidate. The results of Amann *et al*, are attached in Appendix E.

4.1 The Sample and Positioning

A cylindrically shaped piece of titanium (3 mm in length and 2.6 mm in diameter) was cut from a titanium rod by the NBI Mechanical and Electronic Workshop (see Fig. 66 (left) Appendix B), which matched the dimensions of the detection coils, ensuring the entire sample would fill close to the entire space of a single detection coil. The titanium sample was positioned into one of the detection coils such that the excitation field was applied along the cylindrical axis. Due to lack of GE-vanish or Stycast, the thermal contact was established with 5 insulating copper wires of 200 micron diameter held in place between the sample and the inner walls of the sample space using friction. The other end of the copper wires were wrapped around the cold finger and held in place by a stainless steel holder designed for the susceptometer which further was screwed onto the cold finger (see Fig. 19 (left)).

4.2 Sampling of Data

The sampling of the data was done using a script, which initially was meant to obtain a rough temperature behaviour of the susceptibility. It samples the data by measuring a single voltage data point for each temperature data point, meaning the measurements presented in the whole of Section 4 remain without statistical uncertainties.

4.3 Overview And Temperature Control

Initially, it should be mentioned that the temperature for the following measurements in Section 4 is recorded by the thermometer located on the cold finger and referred to as T_{mc2}. In Section 3.2, it is, however, referred to as 't_mixing_chamber_2'. Anyhow, for the measurements shown in Section 4.5, an excitation field of $H_{\mathrm{AC}} \approx 36\,\mathrm{Am}^{-1} \approx 0.45\,\mathrm{Oe}$ was utilized in zero DC field. Measurements were performed for various excitation frequencies while cooling from a finite temperature to the base temperature and while heating from the base temperature up to a finite temperature. The process of heating the sample is done by running a current through a resistor located in the mixing chamber. The progress of the temperature as a function of time for these measurements are shown in Fig. 21. Regarding the heating series, the current in the resistor was varied 3 times across the entire measuring period, and at certain temperature intervals to capture the important features such as the superconducting transition. Therefore, as shown in Fig. 21 (left) at time $\approx 0\,\mathrm{s}$, the heat is applied and kept constant, meaning that as the temperature increases, the rate of change of the temperature will decrease and the temperature will approach a finite value. At a temperature of $T_{\mathrm{mc2}} \approx 70\,\mathrm{mK}$ (time $\approx 3000\,\mathrm{s}$) the current is increased further in order to reach higher temperatures, which is illustrated by the sudden change of the curve. Finally, at a temperature of $T_{\mathrm{mc2}} \approx 90\,\mathrm{mK}$ (time $\approx 5000\,\mathrm{s}$) the current is increased yet again to wrap up the measurement. As for the cooling series, the heat in the mixing chamber is turned off at time $= 0\,\mathrm{s}$, causing the mixing chamber and the sample to approach the base temperature close to linearly as shown in Fig. 21 (right). For temperatures $T < T_{\mathrm{c}}$, the heat is applied in the still to produce a larger cooling effect in order to save time, as measurements, in general, are time consuming.

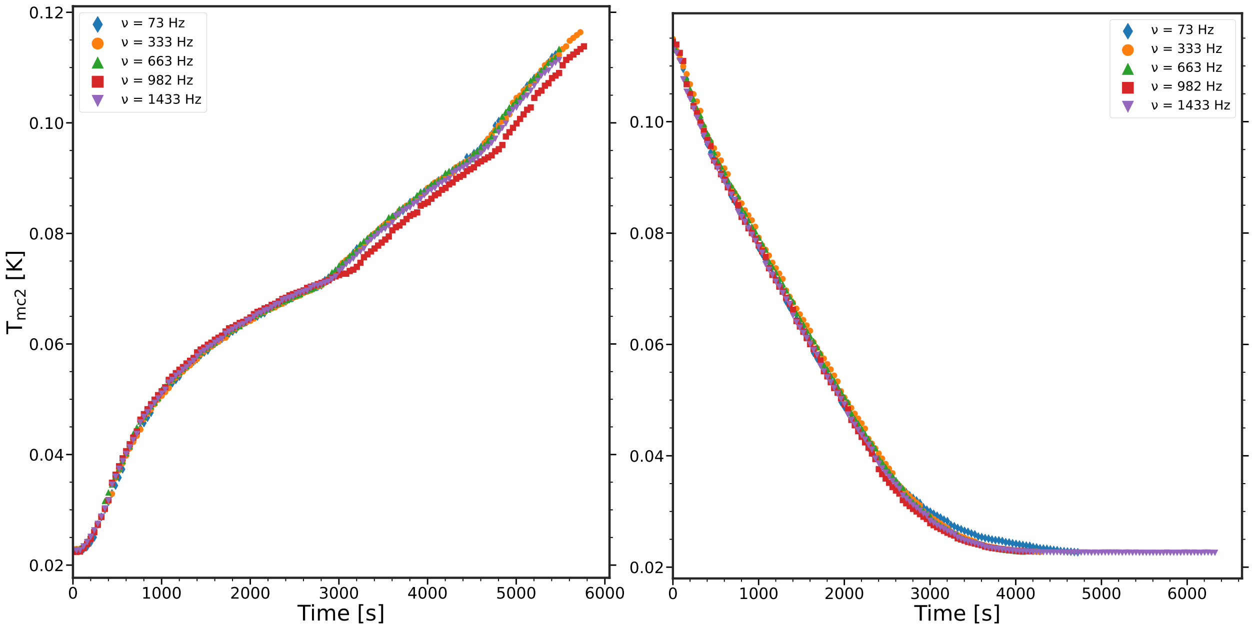

Figure 21: Cold finger temperature T_{mc2} as a function of time during the AC susceptibility measurements for a field strength of $H_{\mathrm{AC}} \approx 36\,\mathrm{Am}^{-1}$ and excitation frequencies of $\nu = 73\,\mathrm{Hz}$ (◆), 333 Hz (●), 663 Hz (▲), 982 Hz (■), and 1433 Hz (▼). **Left**: Measurements taken while heating. The heat is varied at time $\approx 0\,\mathrm{s}$, 3000 s, and 5000 s. **Right**: Measurement taken while cooling. The heat is turned off at time $= 0\,\mathrm{s}$.

For the measurements shown in Section 4.6, the excitation field was lowered to $H_{\mathrm{AC}} \approx 21\,\mathrm{Am}^{-1} \approx 0.27\,\mathrm{Oe}$ and similar measurements were done in order to compare the effect. However, measurements using an excitation frequency of $\nu = 73\,\mathrm{Hz}$ for the given field strength ($H_{\mathrm{AC}} \approx 21\,\mathrm{Am}^{-1}$) were not performed due to lack of time in the period of measuring. The process of heating and cooling was done in a similar manner (see Fig. 22) in order to be consistent and eliminate other potential factors when comparing the effect due to the change in field strength.

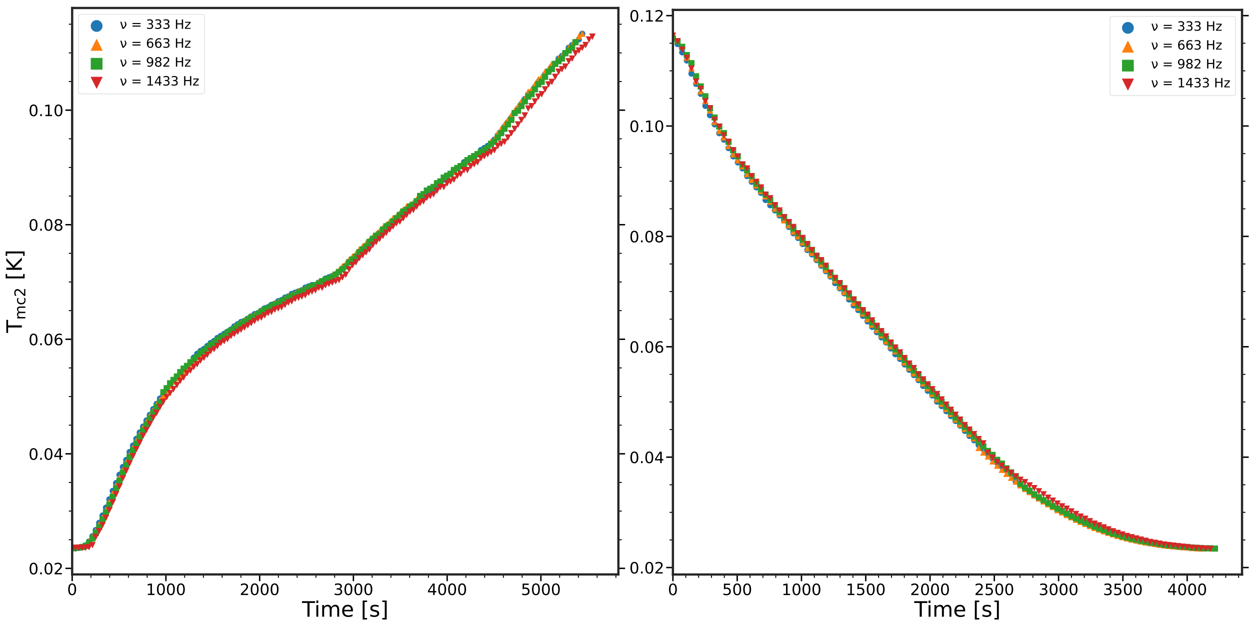

Figure 22: Cold finger temperature T_{mc2} as a function of time during the AC susceptibility measurements for a field strength of $H_{\mathrm{AC}} \approx 21\,\mathrm{A m^{-1}}$ and excitation frequencies of $\nu = 333\,\mathrm{Hz}$ (●), 663 Hz (▲), 982 Hz (■), and 1433 Hz (▼). **Left**: Measurements taken while heating. The heat is varied at time ≈ 0 s, 3000 s and 5000 s. **Right**: Measurement taken while cooling. The heat is turned off at time = 0 s

Further, to test the DC magnet, measurements for various strengths of DC fields perpendicular to the AC field were performed. These measurements were taken while heating the sample, and after every measurement the DC field was turned off while cooling back to the base temperature. Finally, non-linear components of the magnetic susceptibility such as 3rd harmonic susceptibilities were measured. The temperature control pictured in Fig. 21 and 22 was implemented for these measurements as well for the sake of consistency.

4.4 Conversion from Raw Data to Susceptibility

As mentioned in Section 3.3.2 and 3.4.4, the voltage across the detection coils is measured with a lock-in amplifier, which measures the voltage in terms of an amplitude and the phase with respect to some reference signal. Without any phase adjustment, the measured signal is referred to as the raw data denoted X_n and Y_n, where the former (X_{n}) and the latter (Y_{n}) correspond to Eq. (83) and (84) (LHS), respectively, with Y_n being $\frac{\pi}{2}$ (90°) out of phase with respect to X_n. In order to separate the raw data into components proportional to the in-phase harmonic susceptibility (χ_n') and the out-of-phase harmonic susceptibility (χ_n''), one has to rotate the raw data in the complex plane with the proper phase. Focusing on the fundamental harmonic order ($n = 1$), the phase can be determined by imposing $\chi_1'' = 0$ in the case of a superconductor due to zero loss. Further, the calibration constant (C_S) presented in Section 3.3.2 can be determined for the specific sample by imposing $\chi' = -1$ after accounting for demagnetization. The measured susceptibility corresponds to the experimental susceptibility (χ_{exp}) and $\chi' = -1$ remains only true for the internal susceptibility in SI units. Recall the conversion between experimental susceptibility and internal susceptibility in SI units:

$$\chi_1' = \frac{\chi_{1,\mathrm{exp}}' - N\left(\left(\chi_{1,\mathrm{exp}}'\right)^2 + \left(\chi_{1,\mathrm{exp}}''\right)^2\right)}{\left(1 - N\chi_{1,\mathrm{exp}}'\right)^2 + \left(N\chi_{1,\mathrm{exp}}''\right)^2}, \qquad \chi_1'' = \frac{\chi_{1,\mathrm{exp}}''}{\left(1 - N\chi_{1,\mathrm{exp}}'\right)^2 + \left(N\chi_{1,\mathrm{exp}}''\right)^2} \tag{88}$$

where N represents the demagnetization factor [17, 18]. In accordance with the above description of conversion, the raw data has been rotated with the required phase (Θ) in the complex plane using Eq. (86) such that $\mathcal{E}_1^y = 0$. Subsequently, the separated voltage has been scaled using Eq. (85) and (88) where αG in $C_S = \mu_0 N_\mathrm{s} \alpha G$ has been adjusted such that $\chi_1' = -1$. All the quantities such as H_AC, Θ, ν and C_S used in the conversion from voltage to susceptibility are reported in Table 1 and 2 for two different strengths of excitation field. The phase Θ has been estimated by averaging the angle needed to obtain $\chi_1'' = 0$ for the lowest 5 data points in the case of $H_\mathrm{AC} \approx 36\,\mathrm{Am}^{-1}$ and the lowest 10 data points in the case of $H_\mathrm{AC} \approx 21\,\mathrm{Am}^{-1}$ in terms of temperature. The calibration constant (C_S) has been average over the 5 lowest data points, which results in $\chi' = -1$.

The demagnetization factor has been estimated as $N = 0.2661$ using an approximation for a cylindrical geometry from M. Sato and Y. Ishii [58] for the given sample dimensions. The raw data X_1 and Y_1 for the majority of the measurements are shown in Appendix C and D.

4.5 1st Harmonic Measurements at 36 A/m

4.5.1 Comparison of Heating & Cooling Measurements at Fixed Excitation Frequency

The AC susceptibility as a function of T_mc2 for an excitation field of strength $H_\mathrm{AC} = 36.2(1)\,\mathrm{Am}^{-1} \approx 0.45\,\mathrm{Oe}$ and frequency of $\nu = 982\,\mathrm{Hz}$ is shown in Fig. 23. The in-phase component (χ_1') follows a seemingly constant behaviour near $\chi_1' = 0$ for high temperatures, at which point it drastically changes at the estimated critical onset temperatures $T_\mathrm{c,onset} = 0.0669\,\mathrm{K}$ and $T_\mathrm{c,onset} = 0.0673\,\mathrm{K}$ approaching a value of $\chi_1' = -1$ (perfect diamagnetism) for the heating and the cooling series, respectively. The critical onset temperature $T_\mathrm{c,onset}$ for χ_1' has been estimated utilizing the intersection between linear fits below and above the transition, and the peak temperature for χ_1'' has been estimated by taking the maximum value of χ_1''. This method has been utilized for the remaining measurements in Section 4.

The out-of-phase component (χ_1'') takes a small positive value above the estimated critical temperatures, which reflects the AC losses due to induced eddy currents in the sample. During the superconducting transition, the out-of-phase component (χ_1'') reveals a peak at $T_\mathrm{peak} = 0.0599\,\mathrm{K}$ and $T_\mathrm{peak} = 0.0623\,\mathrm{K}$ for the heating and the cooling series, respectively, at which point it rapidly approaches a value of $\chi_1'' = 0$, marking the superconducting zero-loss state. The peak in the out-of-phase component (χ_1'') marks the point of magnetic irreversibility (see Section 2.9.2).

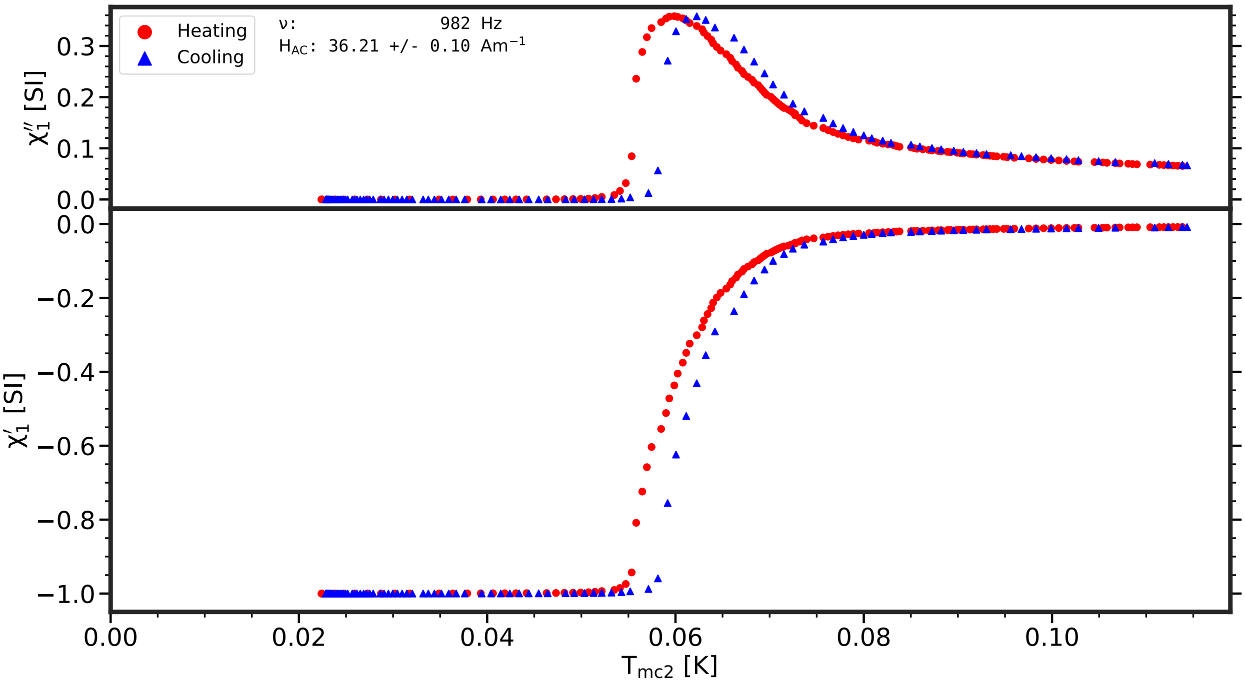

Figure 23: The AC susceptibility as a function of T_{mc2} for $H_{\mathrm{AC}} = 36.21(10)\,\mathrm{Am}^{-1}$ and $\nu = 982\,\mathrm{Hz}$ while heating (●) and cooling (▲). **Top**: The out-of-phase component (χ_1''). **Bottom**: The in-phase component (χ_1'').

As stated earlier, pure titanium is known to have a critical temperature of $T_c \approx 450\,\mathrm{mK}$ and Amann *et al* [2] reports a critical temperature of $T_c = 468\,\mathrm{mK}$ in the absence of a DC field (see Fig. 78 Appendix E), which is in good agreement with additional literature of the same matter [59]. This differs largely from the estimated critical temperatures for the heating and cooling series in Fig 23. This may be caused by poor thermalization, creation of heat at the sample stage, perhaps an inaccurate thermometer, or an impure sample. The first and the second of the suggested causes will be investigated in the current section (Section 4), whereas the third is brought up in Section 5. The final suggested cause is, however, very likely as the sample stems from the NBI workshop.

By comparing the two series from Fig. 23, one may notice that the curves are separated in terms of temperature, and the estimated quantities (T_c & T_{peak}) differ between the heating and the cooling series. Such a difference is typically an indication of imperfect thermalization between the cold finger and the sample. However, it appears to be seemingly good as the estimated quantities differ only by a few millikelvin. Therefore, a lack of thermalization is doubtfully enough explanation for the large deviation between the estimated critical temperatures and the literature value for critical temperature ($T_c \approx 450\,\mathrm{mK}$).

4.5.2 Heating & Cooling Measurements For Various Frequencies

In various studies, especially regarding type-II superconductors, a frequency dependence in the in-phase component (χ_1') and the out-of-phase component (χ_1'') is witnessed [17, 38, 42]. However, Amann *et al* [2] reports a frequency dependence in the out-of-phase component (χ_1'') alone for titanium (type-I superconductor) (see Fig 79 Appendix E), where the initial value of χ_1'' for $T > T_c$ increases for increasing frequency along with the height of the peak ($\chi_1''(T_{\mathrm{peak}})$). In an attempt to replicate this frequency dependence, AC susceptibility measurements were performed as a function of T_{mc2} for various frequencies while heating and cooling the sample. These measurements are shown in Fig. 24.

Focusing on the temperature dependent behavior, the in-phase component (χ_1') for each frequency measurement shows a close to constant behavior above some temperature $T_{\text{c,onset}}$ at which point χ_1' approaches a value of $\chi_1' = -1$. The out-of-phase component (χ_1'') takes a small positive value for high temperatures which increases with frequency. At some temperature T_{peak}, the out-of-phase component (χ_1'') reveals a peak and approaches a value of $\chi_1'' = 0$ for $T < T_{\text{peak}}$. The estimated quantities ($T_{\text{c,onset}}$ & T_{peak}) for each frequency are reported in Table 1 for both the heating series and the cooling series. Comparing the two series (heating & cooling), there is a similar separation in terms of temperature, cf. $T_{\text{c,onset}}$ and T_{peak} in Table 1. There is a $\sim$ 2-3 mK difference in $T_{\text{c,onset}}$ and T_{peak} between heating and cooling except for $\nu = 1433\,\text{Hz}$. As mentioned in Section 4.5.1, this is indicative of imperfect thermalization between the cold finger and the sample.

Further, an increase in χ_1'' for increasing frequency is captured – both at T_{peak} and at temperatures above $T_{\text{c,onset}}$ which is in agreement with Amann *et al* [2] and explained by increased dissipation in terms of heat in the sample.

Moving on, the unexpected, but interesting, feature to notice is a clear frequency dependence of the onset critical temperature in χ_1' for both series which consequently yields a highly frequency dependent peak temperature in χ_1'', as these two quantities go hand in hand. This feature is clear both visually from the measurements shown in Fig. 24 and by the estimated quantities reported in Table 1. For instance, by comparing $T_{\text{c,onset}} = 0.0721\,\text{K}$ ($\nu = 333\,\text{Hz}$) and $T_{\text{c,onset}} = 0.0579\,\text{K}$ ($\nu = 1433\,\text{Hz}$) for the heating series, one obtains a reduction of $\Delta T_{\text{c,onset}} = 14.2\,\text{mK}$, which is without doubt noticeable. This occurrence is suspected to be caused by produced heat from either induced eddy currents in the metallic surroundings or the resistive part of the primary coil, raising the sample temperature. Thus, we expect that the mixing chamber temperature probe underestimates the true sample temperature. As mentioned in Section 3.3.1, the heat due to induced eddy currents scales quadratically with ν and H_{AC}, meaning if the excitation field is lowered, this change should be reflected in the new estimated $T_{\text{c,onset}}$ and T_{peak}, given the above suspicion regarding an induction of heat around the sample remains correct.

Heading

ν [Hz]	73	333	666	982	1433
H_{AC} [Am^{-1}]	36.37(12)	36.7(2)	36.53(11)	36.21(10)	36.8(2)
Θ [radians]	1.61012(7)	1.697950(11)	1.805140(4)	1.901763(7)	2.02803(6)
$C_S \times 10^9$ [$\frac{\text{sV}}{\text{Am}^{-1}}$]	1.67904(19)	1.688222(17)	1.75424(3)	1.86435(4)	1.95932(16)
$T_{\text{c,onset}}$ [K]	0.0729	0.0721	0.0689	0.0637	0.0579
T_{peak} [K]	0.0681	0.0677	0.0650	0.0599	0.0426

Cooling

ν [Hz]	73	333	666	982	1433
H_{AC} [Am^{-1}]	36.32(11)	36.48(12)	36.69(11)	36.3(2)	36.05(10)
Θ [radians]	1.61011(10)	1.69799(3)	1.80515(2)	1.901762(6)	2.028155(6)
$C_S \times 10^9$ [$\frac{\text{sV}}{\text{Am}^{-1}}$]	1.68172(17)	1.70039(7)	1.74615(3)	1.858946(4)	2.00047(2)
$T_{\text{c,onset}}$ [K]	0.0746	0.0741	0.0715	0.0669	0.0595
T_{peak} [K]	0.0708	0.0697	0.0677	0.0623	0.0493

Table 1: The quantities used to convert from raw data to susceptibility along with the estimated critical temperature $T_{\text{c,onset}}$ for χ_1' and the estimated peak temperature T_{peak} for χ_1'' regarding the measurements shown in Fig. 24. **Top**: Corresponds to the measurement in Fig. 24 (left). **Bottom**: Corresponds to the measurement in Fig. 24 (right).

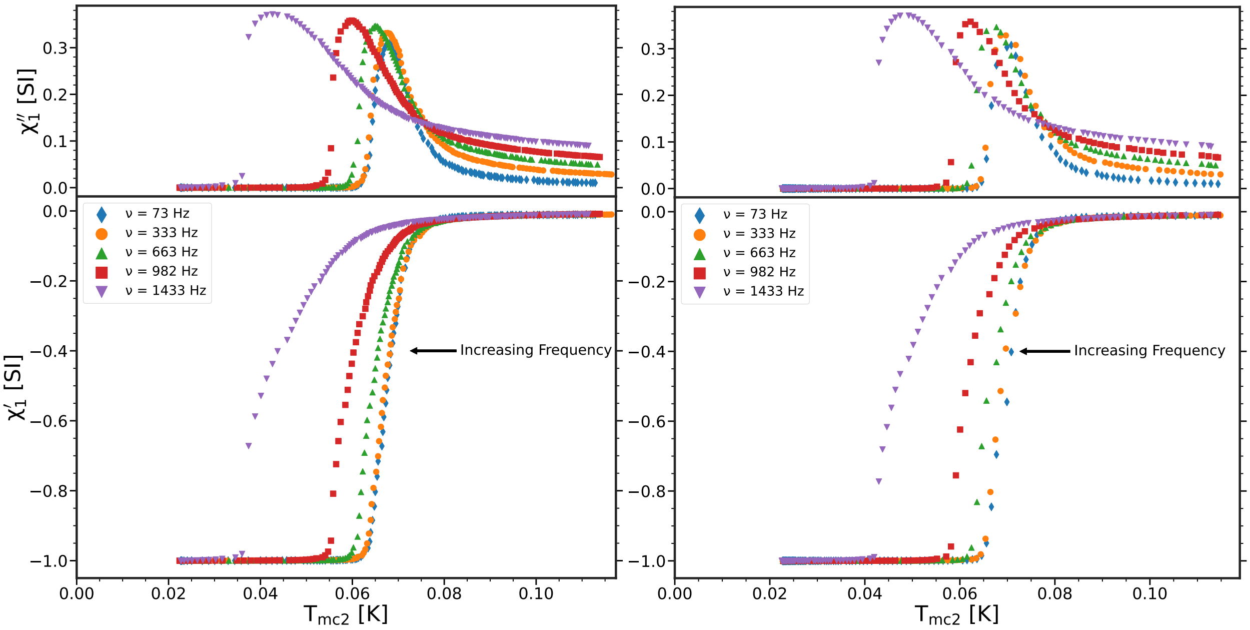

Figure 24: AC susceptibility as a function of T_{mc2} for $H_{\text{AC}} \approx 36\,\text{Am}^{-1}$ and for excitation frequencies of $\nu =$ 73 Hz (◆), 333 Hz (●), 663 Hz (▲), 982 Hz (■), and 1433 Hz (▼). **Top**: The out-of-phase component (χ_1''). **Bottom**: The in-phase component (χ_1'). **Left**: Measurements taken while heating. **Right**: Measurements taken while cooling.

4.6 1st Harmonic Measurements at 21 A/m

In Section 4.5, AC susceptibility measurements utilizing a field of $H_{\mathrm{AC}} \approx 36\,\mathrm{Am}^{-1}$ for various frequencies captured a significant reduction in $T_{\mathrm{c,onset}}$ and T_{peak} for the in-phase component (χ_1') and the out-of-phase component (χ_1''), respectively for increasing excitation frequency. Therefore, similar measurements to the ones in Section 4.5, are presented in the upcoming section where the excitation field has been lowered to a field strength of $H_{\mathrm{AC}} \approx 21\,\mathrm{Am}^{-1} \approx 0.26\,\mathrm{Oe}$ with the purpose of investigating the effect of field reduction.

4.6.1 Comparison of Heating & Cooling Measurements at Fixed Excitation Frequency

The AC susceptibility as a function of T_{mc2} for an excitation field of the strength $H_{\mathrm{AC}} = 21.9(2)\,\mathrm{Am}^{-1}$ and a fixed excitation frequency of $\nu = 982\,\mathrm{Hz}$ is shown in Fig. 25. The in-phase component (χ_1') remains approximately zero constant for temperatures above $T_{\mathrm{c,onset}} = 0.0730\,\mathrm{K}$ and $T_{\mathrm{c,onset}} = 0.0756\,\mathrm{K}$ in case of the heating and cooling series, respectively, at which point the superconducting transition occurs, attaining the perfect diamagnetism $\chi_1' = -1$. The out-of-phase component (χ_1'') takes a small positive value for high temperatures, and begins to grow in value as the temperature approaches the estimated critical onset temperatures, at which point it peaks at $T_{\mathrm{peak}} = 0.0695\,\mathrm{K}$ and $T_{\mathrm{peak}} = 0.0715\,\mathrm{K}$ in the case of the heating and the cooling series, respectively. As the temperature decreases further, the zero-loss state is obtained, reflected by $\chi_1'' = 0$.

Figure 25 shows that the two series remain separated in terms of temperature. This is further reflected by the difference ($\sim 3\,\mathrm{mK}$) in the estimated critical onset temperatures ($T_{\mathrm{c,onset}} = 0.0730\,\mathrm{K}$ & $T_{\mathrm{c,onset}} = 0.0756\,\mathrm{K}$ for the heating and the cooling, series respectively). This separation is a minor improvement, if any at all, compared to the separation shown in Fig. 23 and reflected by the difference in the estimated critical onset temperatures reported in Table 1, i.e. $T_{\mathrm{c,onset}} = 0.0637\,\mathrm{K}$ and $T_{\mathrm{c,onset}} = 0.0669\,\mathrm{K}$ for the heat and the cooling series, respectively – especially considering a roughly 40 % reduction of the excitation field strength. Similarly, one may compare the estimated peak temperatures which leads to the same conclusion. However, as mentioned in Section 4.5.1, an imperfect thermalization between the cold finger and the sample proved adequate in explaining this occurrence, and surely this thermalization should remain independent of any changes in the field strength. It should, however, depend on the rate of change in the temperature, which was performed in a similar manner for every measurement to a certain extent as mentioned in Section 4.3.
The new estimated critical onset and peak temperatures for both series reveal a significant increase as a result of lowering the field. By comparing the estimated quantities from Table 1 and 2, one obtains a large increase in $T_{\mathrm{c,onset}}$ and T_{peak} with the weaker field; the discrepancies are collected in Table 2. This will be elaborated on in Section 4.6.2, as this effect is captured across the entire measured frequency range.

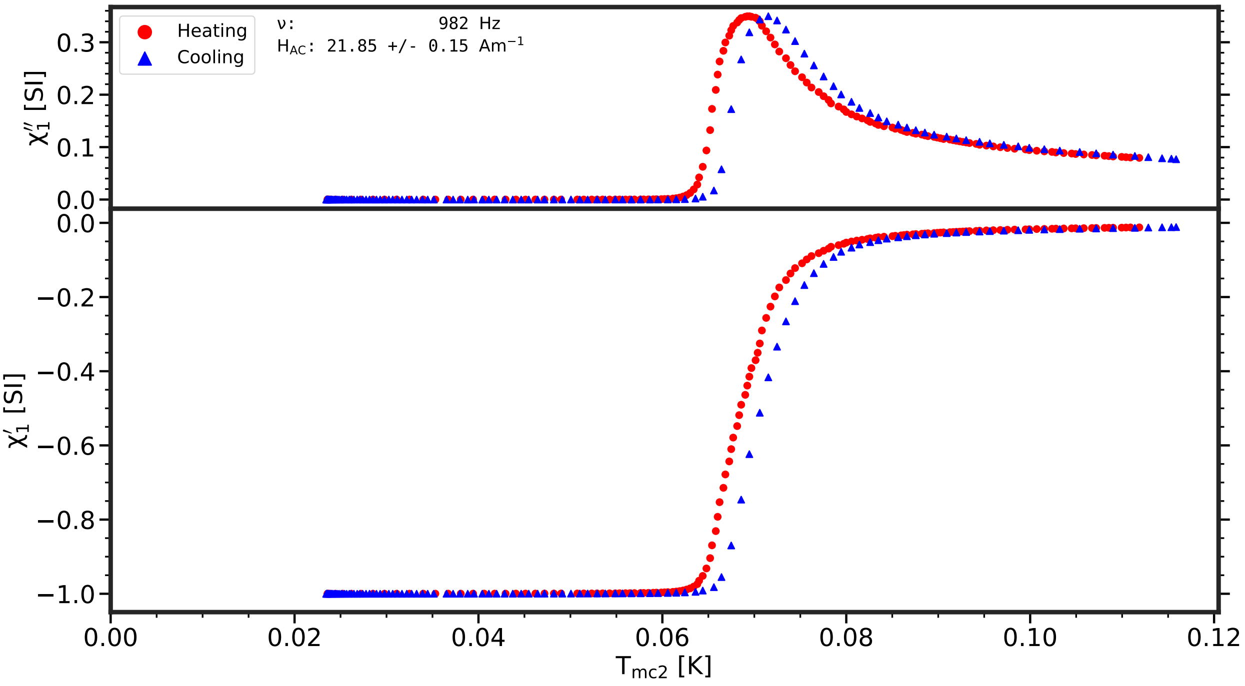

Figure 25: AC susceptibility as a function of T_{mc2} for $H_{\mathrm{AC}} = 21.9(2)\,\mathrm{Am}^{-1}$ and $\nu = 982\,\mathrm{Hz}$ while heating (●) and cooling (▲). **Top**: The out-of-phase component (χ_1''). **Bottom**: The in-phase component (χ_1'').

4.6.2 Heating & Cooling Measurements For Various Frequencies

The AC susceptibility measurements as a function of $\mathrm{T}_{\mathrm{mc2}}$ for the excitation field of $H_{\mathrm{AC}} \approx 21\,\mathrm{Am}^{-1}$ and a variety of frequencies are shown in Fig. 26. The in-phase component (χ_1') remains close to temperature independent above some estimated temperature $T_{\mathrm{c,onset}}$, at which point it undergoes a rapid change and converges towards $\chi_1' = -1$, attaining the superconductivity. Meanwhile, the out-of-phase component (χ_1'') takes a positive value for high temperatures and peaks at some temperature T_{peak}, at which point it converges towards $\chi_1'' = 0$, reflecting the superconducting zero loss state. The height of the peak $\chi_1''(T_{\mathrm{peak}})$ continues to increase with frequency, so does the value χ_1'' at high temperatures. The estimated quantities $T_{\mathrm{c,onset}}$ and T_{peak} corresponding to χ_1' and χ_1'' respectively are reported in Table 2 along with the increase in each of these quantities ($\Delta T_{\mathrm{c,onset,36\,Am^{-1}\rightarrow 21\,Am^{-1}}}$ & $\Delta T_{\mathrm{peak,36\,Am^{-1}\rightarrow 21\,Am^{-1}}}$) as a result of lowering the field from $H_{\mathrm{AC}} \approx 36\,\mathrm{Am}^{-1}$ to $H_{\mathrm{AC}} \approx 21\,\mathrm{Am}^{-1}$.

As discussed in Section 4.6.1, the separation between the heating and the cooling curve for excitation frequency $\nu = 982\,\mathrm{Hz}$ does not reveal a significant difference as a result of lowering the field, nor does it reveal a noticeable difference for the measurements taken at the remaining excitation frequencies. This is consistent with imperfect thermalization.

As briefly mentioned in Section 4.6.1, the estimated critical onset and peak temperatures for the excitation frequency $\nu = 982\,\mathrm{Hz}$ does increase as a result of lowering the field. Additionally, one may notice visually from Fig. 26 that the same phenomenon occurs at the remaining frequencies. By examining the estimated values for $T_{\mathrm{c,onset}}$ and T_{peak} in Table 2 and, further, $\Delta T_{\mathrm{c,onset,36\,Am^{-1}\rightarrow 21\,Am^{-1}}}$ and $\Delta T_{\mathrm{peak,36\,Am^{-1}\rightarrow 21\,Am^{-1}}}$, the effect of lowering the field becomes quite clear. This observation is a strong indication of heat being produced by the excitation field, causing the temperature of the sample to be frequency- and field-dependent. Furthermore, the fact that the largest improvement occurs for the measurements at the highest excitation frequency ($\nu = 1433\,\mathrm{Hz}$), as one may see in Table 2 (row 7 & 8), agrees with the explanation that the heat might stem from induced eddy currents rather than the resistive part of the primary coil.

In addition, the curves for each frequency in Fig. 26 appears to be significantly more gathered compared to the curves in Fig. 24, meaning that the excitation frequency appears to have less of an impact in terms of temperature variations of the sample at the given field strength of $H_{\mathrm{AC}} \approx 21\,\mathrm{Am}^{-1}$. This might indicate that the heating is close to be minimized, meaning that if the field was lowered further, it may not have revealed a huge difference, and, therefore, the estimated ($T_{\mathrm{c,onset}}$) potentially remains close to the true critical onset temperature recorded by the thermometer on the cold finger for the given sample. It was the plan to lower the excitation field further. Unfortunately, an incident occurred regarding helium entering the IVC, meaning that I was forced to retrieve the circulating helium, and investigating the titanium sample further remained low on our list of priorities.

Anyhow, the estimated $T_{\mathrm{c,onset}}$ from Table 2 has been plotted in Fig. 27 as a function of the excitation frequency.

The estimated critical onset temperature ($T_{\mathrm{c,onset}}$) appears to converge towards some finite value as the excitation frequency approaches zero, such that $T_{\mathrm{c,onset}}(\nu = 0) \approx T_{\mathrm{c,onset}}(\nu = 333\,\mathrm{Hz})$. However, it should be emphasized that the estimated temperature quantities will unavoidably differ from the true temperature quantities of the sample, due to the imperfect thermalization. In general, this imperfection causes the measured temperature on the cold finger to deviate from the sample temperature across the entire temperature regime. How much it differs is investigated in Section 5, where cerium magnesium nitrate is utilized to estimate whether the thermometer can even be trusted, estimate the sample temperature, and, finally, obtain a corrected mixing chamber temperature outside its reliable range.

Finally, it remains ideal to comment on the remaining quantities H_{AC}, Θ, and C_S reported in Table 1 and 2 for the heating series and cooling series.

Increasing the frequency reduces the current in the circuit for a constant voltage supply due to the frequency-dependence of the impedance of the primary coil. Thus, in order to obtain a similar excitation field for all the measurements, one has to increase the voltage supply when increasing the excitation frequency, which was done. Obviously, this will naturally cause the field strength to differ slightly from each frequency measurement, and, further, there will be statistical fluctuations contributing.

The phase for each frequency appears to differ slightly moving from a field of $H_{\mathrm{AC}} \approx 36\,\mathrm{Am}^{-1}$ to $H_{\mathrm{AC}} \approx 21\,\mathrm{Am}^{-1}$, and, given the uncertainties (σ_Θ) the differences are statistically significant, which suggests that the phase could be field-dependent. Possibly due to experimental reasons, such as coil imperfections.

The calibration constant (C_S) appears to be frequency-dependent and some of this might originate from instrumental effects. Further, there will always be a background signal present, which unavoidably is frequency-dependent due to the coil imperfections. In addition, C_S does appear to differ - given the small uncertainties - moving from $H_{\mathrm{AC}} \approx 36\,\mathrm{Am}^{-1}$ to $H_{\mathrm{AC}} \approx 21\,\mathrm{Am}^{-1}$ if one compares the reported values in Table 1 and 2. If one compares the heating series with the cooling series for both the excitation fields, one may notice a trend that the calibration constant remains slightly larger if the field value is slightly smaller. For instance, Table 2 (row 4) reports $H_{\mathrm{AC}} = 21.9(1)\,\mathrm{Am}^{-1}$ and $C_S = 1.84283(5) \times 10^{-9}\,\frac{\mathrm{sV}}{\mathrm{Am}^{-1}}$ for the heating series, whereas $H_{\mathrm{AC}} = 21.6(2)\,\mathrm{Am}^{-1}$ and $C_S = 1.86556(4) \times 10^{-9}\,\frac{\mathrm{sV}}{\mathrm{Am}^{-1}}$ for the cooling series at a constant excitation frequency of $\nu = 982\,\mathrm{Hz}$. The uncertainties on the two reported excitation fields suggest that these fields are statistically identical, since one obtains a Z-value of $\sim 1.34\sigma$ where

$$Z = \frac{\overline{X}_2 - \overline{X}_1}{\sqrt{(\sigma_{\overline{X}_2})^2 + (\sigma_{\overline{X}_1})^2}}. \tag{89}$$

This is the case for the majority of the excitation frequencies. This suggests that, the statistical difference in the calibration constants (C_S) between the heating and the cooling series, either originates from some other factor, unless the uncertainties on the excitation fields are overestimated.
However, as we will see in Section 5, using the electrical circuit (see Fig. 20 (left)) with a lock-in amplifier measuring the excitation field, yields a significantly smaller statistical uncertainty, meaning that if the same occurrence would persist, one could argue for a field dependent C_S for small variations of the field. Although, this is pure speculation, but it would be interesting and perhaps useful to map the calibration constants over small variations of the driving field in terms of amplitude for each frequency.
Finally, recall that the calibration constant (C_S) consists of a part dependent on the geometry of the coils (α) and a part dependent on the sample (G). The geometry of the coils might change ever so slightly over time for various reasons. One example would be: when changing sample, the coil system along with the coil wires have to be reattached, which unavoidably result in movement of the wires. Thus, it remains impossible to obtain the exact same positioning of the wires. This often results in a small background change ($\sim 1 \times 10^{-7}$ V) compared to a previous measuring session. This could change the required scaling factor (α) representing the geometry of the coils, meaning that C_S could potentially vary for the same sample, if it was measured again. It might even change the frequency-dependence due to the fact that the wire position has changed, thus, the turn-to-turn capacitive coupling has been modified.

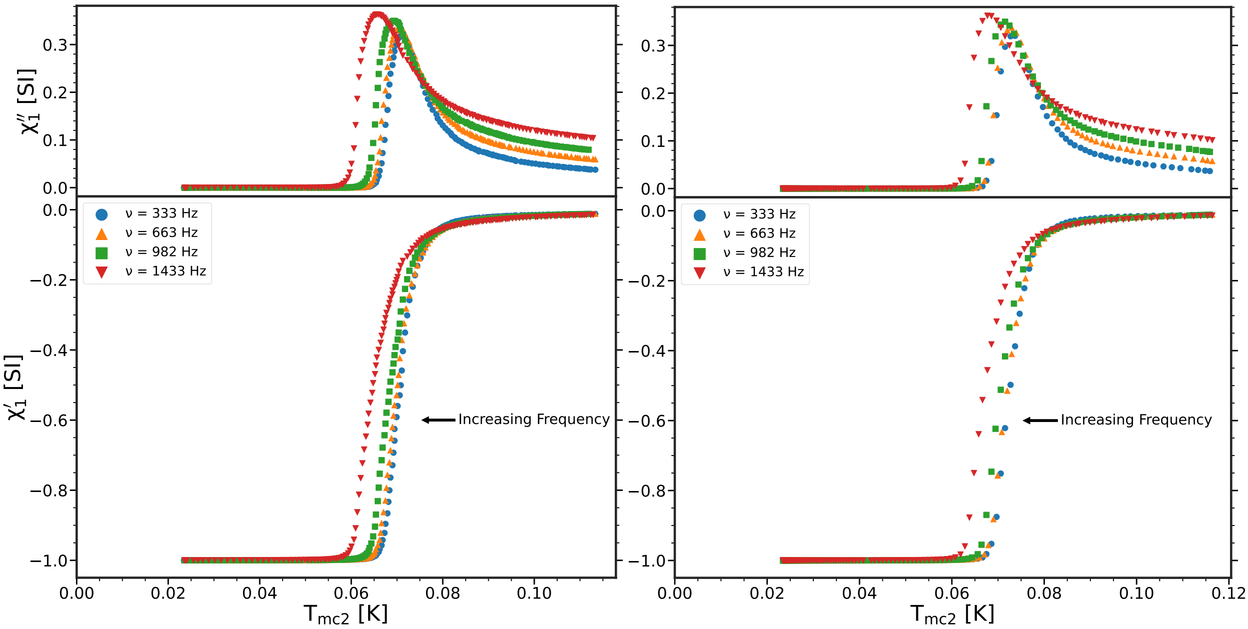

Figure 26: AC susceptibility as a function of T_{mc2} for $H_{\mathrm{AC}} \approx 21\,\mathrm{Am}^{-1}$ and for excitation frequencies of $\nu =$ 333 Hz (●), 663 Hz (▲), 982 Hz (■), and 1433 Hz (▼). **Top**: The out-of-phase component (χ_1''). **Bottom**: The in-phase component (χ_1'). **Left**: Measurements taken while heating. **Right** Measurements taken while cooling.

Heating

ν [Hz]	333	666	982	1433
H_{AC} [Am^{-1}]	21.6(2)	21.5(2)	21.9(1)	21.8(2)
Θ [radians]	1.70541(5)	1.81142(2)	1.90707(1)	2.033416(7)
$C_S \times 10^9$ [$\frac{\mathrm{sV}}{\mathrm{Am}^{-1}}$]	1.68361(11)	1.74685(4)	1.84283(5)	1.993681(16)
$T_{\mathrm{c,onset}}$ [K]	0.0743	0.0738	0.0730	0.0692
T_{peak} [K]	0.0711	0.0706	0.0695	0.0660
$\Delta T_{\mathrm{c,onset,36\,Am^{-1}\rightarrow 21\,Am^{-1}}}$ [K]	0.0022	0.0049	0.0093	0.0113
$\Delta T_{\mathrm{peak,36\,Am^{-1}\rightarrow 21\,Am^{-1}}}$ [K]	0.0034	0.0056	0.0096	0.0230

Cooling

ν [Hz]	333	666	982	1433
H_{AC} [Am^{-1}]	21.2(2)	21.3(2)	21.6(2)	21.8(2)
Θ [radians]	1.70540(2)	1.81145(2)	1.907045(8)	2.033307(3)
$C_S \times 10^9$ [$\frac{\mathrm{sV}}{\mathrm{Am}^{-1}}$]	1.713192(13)	1.76437(2)	1.86556(4)	1.993605(9)
$T_{\mathrm{c,onset}}$ [K]	0.0770	0.0763	0.0756	0.0717
T_{peak} [K]	0.0737	0.0730	0.0715	0.0677
$\Delta T_{\mathrm{c,onset,36\,Am^{-1}\rightarrow 21\,Am^{-1}}}$ [K]	0.0029	0.0052	0.0087	0.0122
$\Delta T_{\mathrm{peak,36\,Am^{-1}\rightarrow 21\,Am^{-1}}}$ [K]	0.0040	0.0053	0.0093	0.0184

Table 2: The quantities used to convert from raw data to susceptibility along with the estimated critical temperature $T_{\mathrm{c,onset}}$ for χ_1' and the estimated peak temperature T_{peak} for χ_1'' regarding the measurements shown in Fig. 26. Further, it contains the increase in the estimated critical onset and peak temperature $\Delta T_{\mathrm{c,onset,36\,Am^{-1}\rightarrow 21\,Am^{-1}}}$ and $\Delta T_{\mathrm{peak,36\,Am^{-1}\rightarrow 21\,Am^{-1}}}$, respectively, lowering the excitation field from $H_{\mathrm{AC}} = 36\,\mathrm{Am}^{-1}$ to $H_{\mathrm{AC}} = 21\,\mathrm{Am}^{-1}$. **Top**: Corresponds to the measurement in Fig. 26 (left). **Bottom**: Corresponds to the measurement in Fig. 26 (right).

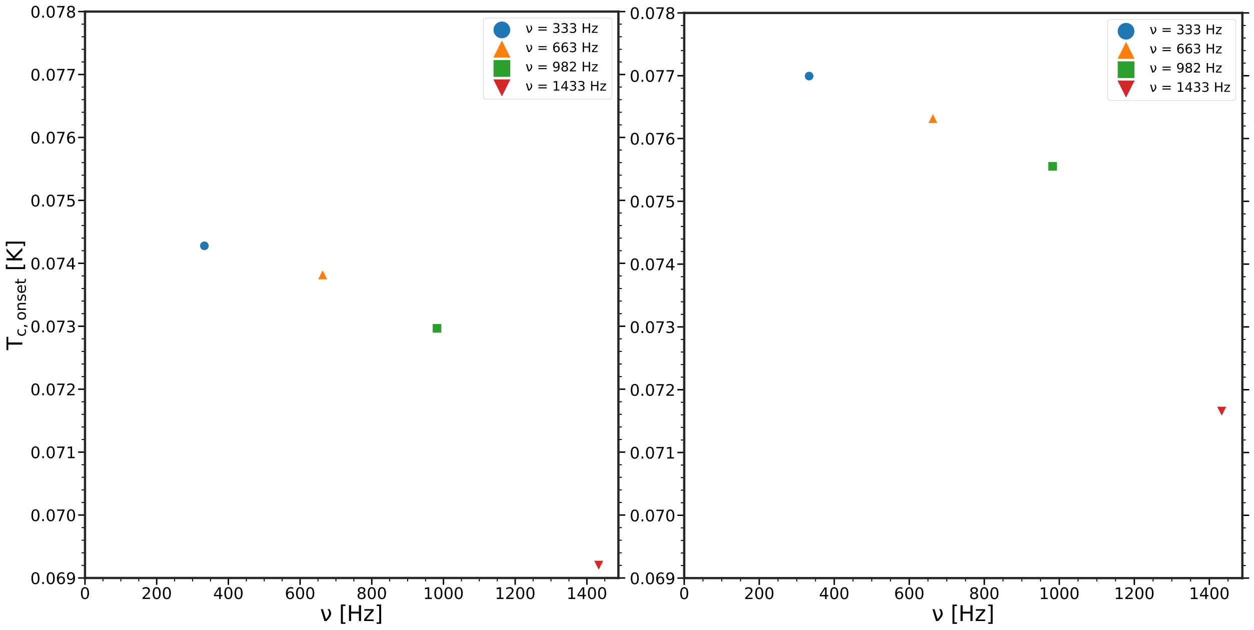

Figure 27: **Left**: Critical temperatures extracted from the measurement taken while heating. **Right**: Critical temperatures extracted from the measurement taken while cooling.

4.6.3 Measurements For Various Strengths of DC Background Field.

Moving forward with an excitation field of $H_{\mathrm{AC}} \approx 21\,\mathrm{Am}^{-1}$, AC susceptibility measurements were performed for various strengths of DC magnetic fields as a function of T_{mc2}. These measurements are shown in Fig. 28. The in-phase component (χ_1') shows a clear suppression of the critical onset temperature along with a broader transition for increasing DC fields. Similarly, the out-of-phase component (χ_1'') shows a peak which occurs at lower temperatures and becomes more broad for increasing DC fields. The estimated critical onset temperatures $T_{\mathrm{c,onset}}$ for χ_1' and the peak temperatures for χ_1'' are reported in Table 3 for the corresponding strength of DC field. The observed response to an applied DC field in Fig. 28 is in agreement with Amann *et al* [2] (see Fig. 80 Appendix E), and this behavior is in agreement with what one would expect for a type-I superconductor as mentioned in Section 2.7.2.

For further comparison with Amann *et al* and the theory in Section 2.7.2, the applied DC field has been plotted in Fig. 29 as a function of the estimated $T_{\mathrm{c,onset}}$ from Table 3. The data points shown in Fig. 29 (left) appear to have a linear trend in the given field-temperature regime, which is similar to Amann *et al* (see Fig. 80 Appendix E). A linear fit (black dashed line) has been applied to the points in Fig. 29, which yields a slope of $\left(\frac{dH}{dT}\right)_{T=T_{\mathrm{c}}} = -260.25(6)\,\frac{\mathrm{Am}^{-1}}{\mathrm{mK}} = -3270.4(8)\,\frac{\mathrm{Oe}}{\mathrm{K}}$ and an intersect of $H_{\mathrm{c}}(T_{\mathrm{c}} = 0) = 18662(4)\,\mathrm{Am}^{-1}$. This slope fit parameter differs significantly from a slope of $-443\,\frac{\mathrm{Oe}}{\mathrm{K}}$ reported by Amann *et al* (see Fig. 80 Appendix E).
In addition, a fit (black solid line), based on the emperical relation from Eq. (49) in Section 2.7.2 has been applied yielding the following fit parameters: $H_{\mathrm{c}}(0) = 10707(2)\,\mathrm{Am}^{-1}$ and $T_{\mathrm{c}} = 71.606(3)\,\mathrm{mK}$. As mentioned in Section 2.7.2, experimental data yield that the critical field as a function of the critical temperature may be described by Eq. (49) in the high field regime and tends to become more linear in accordance to Eq. (50) in the low field regime. Fig. 29 (right) shows a combination of the two relations with Eq. (49) used in the high field regime and Eq. (50) used in the low field regime.
Ideally, Eq. (49) would have to be applied onto the high field regime. However, additional data points for high fields were not conducted due to complications with the dilution refrigerator. Further, it would be interesting to investigate whether measurements would follow the relation in the high field regime, since the fit from Eq. (49) does yield a fit parameter $H_{\mathrm{c}}(0) = 10707(2)\,\mathrm{Am}^{-1} = 134.54(2)\,\mathrm{Oe}$, equivalent to $B_{\mathrm{c}} = 0.013454(2)\,\mathrm{T}$, which remains larger than the literature value $B_{\mathrm{c}} \approx 0.01\,\mathrm{T}$ for titanium [1]. This is unexpected. The superconducting energy gap, thus the binding energy of a cooper pair is approximately $\Delta(0) = 1.764 k_B T_{\mathrm{c}} \approx 0.011\,\mathrm{meV}$ in our case. This is substantially lower compared to a titanium piece with $T_{\mathrm{c}} \approx 450\,\mathrm{mK}$. Surely a lower binding energy would, as a consequence, yield a lower critical field $H_{\mathrm{c}}(0)$ compared to the literature value of the critical field. An explanation could be that the titanium sample experiences a weaker DC field than the ones reported in Table 3 due to the fact that the DR inset adjustment might be off. This would mean that the sample is not positioned within the maxima of the field profile – it is very unlikely that this is the case. A titanium of high purity was ordered and we attempted a cooldown using this. Unfortunately, complications regarding the dilution refrigerator occurred which prevented us to do so.

H_{DC} [Am^{-1}]	0	1977.80	3211.02	6142.82
$T_{\mathrm{c,onset}}$ [K]	0.0730	0.0627	0.0581	0.0496
T_{peak} [K]	0.0695	0.0544	0.0491	0.0367

Table 3: A table containing the estimated critical onset temperatures and peak temperatures of the measurements shown in Fig. 28 for the various DC fields. Further, these points are plotted as H_{DC} vs $T_{\mathrm{c,onset}}$ in Fig. 29.

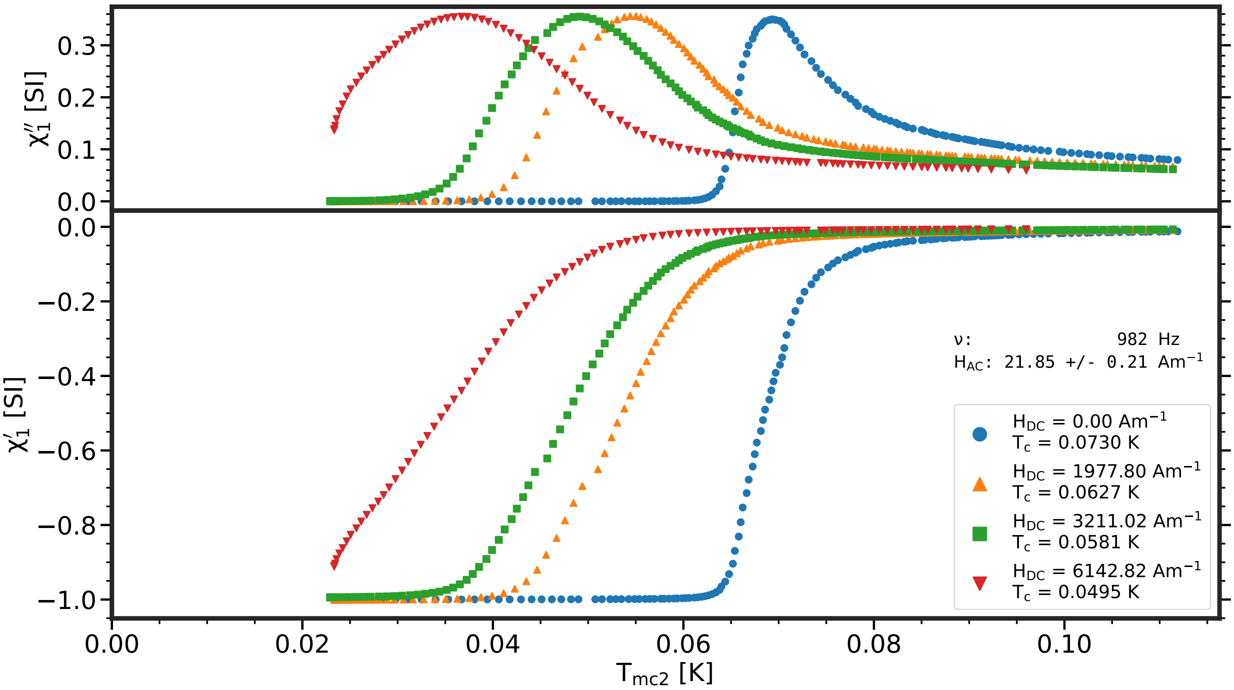

Figure 28: AC susceptibility as a function of T_{mc2} for $H_{\mathrm{AC}} = 21.9(2)\,\mathrm{Am}^{-1}$ and for DC background fields of $H_{\mathrm{DC}} = 0\,\mathrm{Am}^{-1}$ (●), $1977.80\,\mathrm{Am}^{-1}$ (▲), $3211.02\,\mathrm{Am}^{-1}$ (■), and $6142.82\,\mathrm{Am}^{-1}$ (▼). **Top**: The out-of-phase component (χ_1''). **Bottom**: The in-phase component (χ_1').

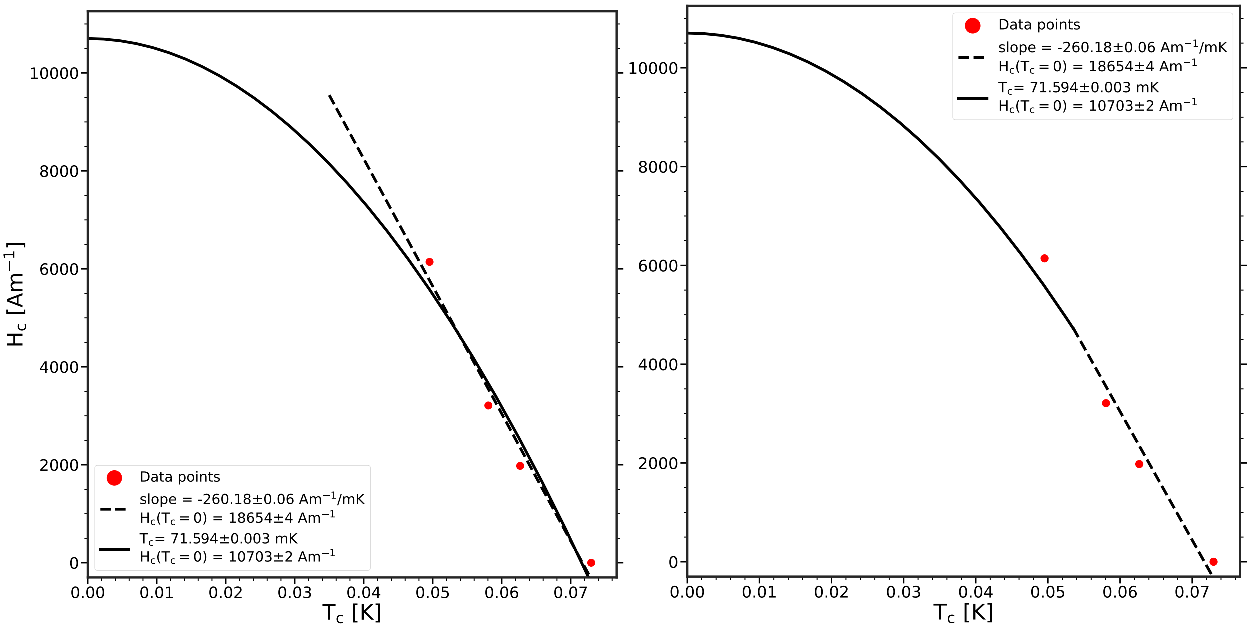

Figure 29: The critical field as a function of the estimated critical temperature from Table 3. **Left**: Both a fit using the empirical relation from Eq. (49) (black solid line) and a linear fit (black dashed line) have been applied. **Right**: The two fits have been combined, using the black solid line in the high field regime, and the black dashed line in the low field regime.

4.7 3rd Harmonic Susceptibility Measurements at 21 A/m Field

The non-linear higher harmonic susceptibilities, especially the 3rd harmonic magnetic susceptibility are investigated in various articles for type-II superconductors. However, there seem to be an ambiguity regarding the separation of these components since articles seem to present the higher harmonic susceptibilities differently. As mentioned in Section 3.3.2, the phase adjustment required to separate the in-phase component (χ'_n) and the out-of-phase component (χ''_n) properly regardless of the harmonic order n follows $\Theta_n = n \cdot \Theta_{n=1}$, where $\Theta_{n=1}$ represents the phase adjustment required to separate the fundamental harmonic component. This section presents 3rd harmonic AC susceptibility measurements using various excitation frequencies for the scenarios, where the phase Θ_3 has been adjusted such that $\Theta_3 = 0$, $\Theta_{n=1}$ and $3 \cdot \Theta_{n=1}$. Further, it compares the measurements for the different scenarios with experimental observations for type-II superconductors from various studies. Finally, it should be mentioned that an additional phase adjustment of $\Theta_3 = \frac{\pi}{2} + 3 \cdot \left(\Theta_{n=1} - \frac{\pi}{2}\right)$ is shown in Appendix I and may be compared to Ref. [40] for the curious reader.

4.7.1 Phase Adjustment of $\Theta_3 = 0$

The 3rd harmonic AC susceptibility for a phase adjustment of $\Theta_3 = 0$ is presented in Fig. 30. The out-of-phase component (χ''_3) remains positive in the high temperature regime and as temperature decreases, a positive peak occurs just below $T \approx 0.08\,\mathrm{K}$ near the superconducting transition. The peak seems to be suppressed for increasing excitation frequency. As temperature decreases further, a rapid change occurs followed by a negative peak, which seems to be moderately larger in magnitude compared to the positive peak and increase slightly with frequency. As temperature goes even lower the out-of-phase component (χ''_3) converges to a value of $\chi''_3 = 0$ for all the utilized excitation frequencies.

The in-phase component (χ'_3) takes a positive value for the measurements at $\nu = 333\,\mathrm{Hz}$, but remains negative for the measurements at $\nu = 1433\,\mathrm{Hz}$ in the high temperature regime. At a temperature slightly below $T \approx 0.08\,\mathrm{K}$, χ_3' reveals a negative peak, which – similarly to the out-of-phase component – seems to be suppressed in magnitude and become more broad as frequency is increased. As temperature decreases further, χ_3' shows a sharp positive peak, which appears to increase in magnitude and width as frequency increases. As the temperature decreases further, χ_3' approaches zero.

The separation in terms of temperature between the various curves at different frequency may be caused by the generated heat at the sample stage, deduced from the comparison between Fig. 24 and 26, or at least this may contribute to the separation. Whether there is supposed to be a frequency-dependent separation due to other effects remains unknown. One may notice that similar to Fig. 23 and 25, the separation in terms of temperature between the heating series and the cooling series proceed, to exist, which, as mentioned, was assumed to be caused by the imperfect thermalization between the sample and the cold finger.

However, if one mainly focuses on the temperature-dependent features, comparing to similar measurements on the superconducting compound $\mathrm{FeSe_{0.5}Te_{0.5}}$ by Pal *et al* [38] (see Fig. 81 Appendix F), one might notice that they observe similar temperature-dependent features. The in-phase component (χ_3') in Fig. 81 takes a value of $\chi_3' = 0$ for all the frequency curves at high temperatures. Approaching the superconducting transition they all reveal a negative peak which appears to decrease in magnitude as frequency increases. As temperature decreases further, a positive peak occurs which seems to increase in magnitude as frequency increases, at which point a finite value is approached. The out-of-phase component (χ_3'') in Fig. 81 remains zero ($\chi_3'' = 0$) at high temperatures, at which point a positive peak is observed approaching the superconducting transition. The positive peak is suppressed as the frequency increases. As temperature continues to decrease, a negative peak occurs which seem to show almost no frequency-dependence in terms of magnitude. The similarities to note between the measurements in Fig. 30 and the measurements in Fig. 81 by Pal *et al* [38] are as follows: both components reveal peaks with the same sign and in the same order. The majority of the peaks seem to respond similarly to frequency changes. The differences to note are: the measurements in Fig. 30 reveal a non-zero value ($\chi_3' \neq 0$, $\chi_3'' \neq 0$) for high temperatures and a value of zero ($\chi_3' = 0$, $\chi_3'' = 0$) at low temperatures while the measurements in Fig. 81 by Pal *et al* [38] show the opposite behavior at temperatures above and below the superconducting transition, respectively. This difference in behavior might be related to the fact that the measurements in Fig. 26 show $\chi_1'' \neq 0$ for high temperatures due to presumed dissipation caused by generated eddy currents and $\chi_1'' = 0$ in the superconducting phase. However, 1st harmonic susceptibilities shown in Fig. 81 Pal et al reveal the opposite behavior [38], which is quite common regarding $\chi_1'' \neq 0$ for type II superconductors near the phase transition. Further, given the in-phase component (χ_1') proceeds to decrease at the lowest recorded temperature of $T \approx 2\,\mathrm{K}$ indicates that the sample remains in the transition regime, which might further contribute to the differences. Although it is not reported, given the similarities it might suggest that the presented 3rd harmonic AC susceptibility measurements by Pal *et al* [38], correspond to a phase adjustment of $\Theta' = 0$. With that in mind, one has to recall that Pal *et al* investigates a type-II superconductor, in which dynamical processes such as flux creep, flux flow and thermally assisted flux flow along with flux pinning may occur [17, 38, 42]. Finally, for the curious reader, one may compare the Cole-Cole plots from Fig. 74 and 75 in Appendix D with the Cole-Cole plots by Pal *et al* (see Fig. 82 Appendix F) and notice some of the similarities.

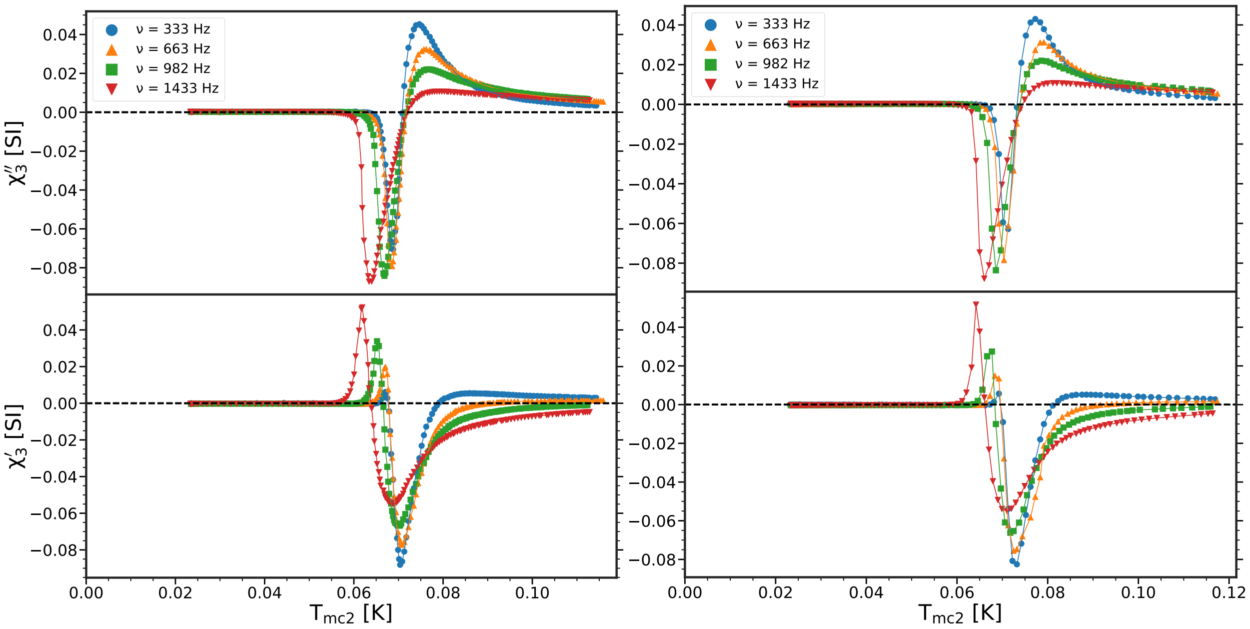

Figure 30: 3rd harmonic ($\Theta_3 = 0$) AC susceptibility as a function of T_{mc2} for $H_{\mathrm{AC}} \approx 21\,\mathrm{Am}^{-1}$ and for excitation frequencies of $\nu = 333\,\mathrm{Hz}$ (●), 663 Hz (▲), 982 Hz (■), and 1433 Hz (▼). The linear spline connecting the data points is simply to guide the eye. **Top**: The out-of-phase component χ_3''. **Bottom**: The in-phase component χ_3'. **Left**: Measurements taken while heating. **Right**: Measurements taken while cooling.

4.7.2 Phase Adjustment of $\Theta_3 = \Theta_{n=1}$

The 3rd harmonic AC susceptibility for a phase adjustment corresponding to $\Theta_3 = \Theta_{n=1}$ (see Table 2 for $\Theta_{n=1}$) is shown in Fig. 31. The out-of-phase component (χ_3'') is negative for $\nu = 333\,\mathrm{Hz}$ and positive for $\nu = 1433\,\mathrm{Hz}$ at high temperatures. It decreases slightly for $\nu = 333\,\mathrm{Hz}$ and increases slightly for $\nu = 1433\,\mathrm{Hz}$ as temperature decreases. The measurements for all the excitation frequencies show a large positive peak which decreases in magnitude and increases in width for increasing frequency, followed by a small and sharp negative peak below $T_{\mathrm{mc2}} \approx 65\,\mathrm{mK}$, at which point $\chi_3'' \to 0\,\mathrm{K}$. The small negative peak appears to grow in magnitude for increasing frequency. The in-phase component (χ_3') begins at a positive value in the high temperature regime. It proceeds to increase as the temperature is lowered, at which point it peaks. The positive peak show a suppression in magnitude in magnitude and increase in the width for increasing frequency. At $T_{\mathrm{mc2}} \approx 67\,\mathrm{mK}$, the in-phase component (χ_3') reveals a negative large peak, which seems to be enhanced slightly in magnitude and perhaps width as frequency is increased. For the remaining of the temperature regime it yields a value of zero ($\chi_3' = 0$). Polichetti *et al* [42] report measurements of 3rd harmonic components separated using $\Theta_3 = \Theta_{n=1}$ on the compound $\mathrm{Y_1Ba_2Cu_3O_{7-x}}$. Although, the plots provided in the article [42] remain difficult to compare with, due to the chosen excitation fields ($H_{\mathrm{AC}} \approx$ 4-8 Oe) being notably larger compared to the field utilized in Fig. 31 ($H_{\mathrm{AC}} \approx 0.26\,\mathrm{Oe}$). This usually has a large impact on the 3rd harmonic susceptibility behaviour [40]. Nevertheless, the in-phase component (χ_3') from the measurements by Polichetti *et al* [42] shown in Fig. 83 begins at zero ($\chi_3' = 0$) for high temperature, at which point a positive peak occurs, which grows in magnitude and width for decreasing frequency. For lower temperatures, the measurement for $\nu = 1607\,\mathrm{Hz}$ reveals a negative peak, however, this feature appears to be suppressed for the remaining excitation frequencies ($\nu = 10.7\,\mathrm{Hz}$ & $\nu = 107\,\mathrm{Hz}$). The out-of-phase component (χ_3'') (see Fig. 83 Appendix G) for $H_{\mathrm{DC}} = 0\,\mathrm{Oe}$ takes a value of zero ($\chi_3'' = 0$) in the high temperature regime. At $T \approx 91\,\mathrm{K}$, a large distinct positive peak occurs followed by a gradual decrease towards a value of zero ($\chi_3'' = 0$) as the temperature is lowered. The similarities there are to spot between the measurements in Fig. 31 and the measurements in Fig. 83 by Polichetti *et al* [42] are as follows: for the in-phase component (χ_3'), the peaks come with the same sign in the same order in terms of temperature, and both, positive peaks appear to increase in magnitude as frequency is decreased. The out-of-phase component (χ_3'') show a large sharp peak which appear quite similar between the measurement for $\nu = 333\,\mathrm{Hz}$ in Fig. 31 and the measurement by Polichetti *et al* [42] for $H_{DC} = 0\,\mathrm{Oe}$ at $\nu = 107\,\mathrm{Hz}$ (Fig. 83). The differences to note are as follows: the in-phase component takes a value of zero ($\chi_3' = 0$) at high temperatures in the measurements by Polichetti *et al* [42], whereas it remains positive from the measurements shown in Fig. 31. Further, the negative peak in the measurements by Polichetti *et al* [42] seems to almost disappear for decreasing frequency, therefore, be significantly more frequency-dependent compared to the measurements shown in Fig. 31. The out-of-phase component is zero ($\chi_3'' = 0$) at high temperatures in the measurements by Polichetti *et al* [42] for $\nu = 107\,\mathrm{Hz}$ and $H_{DC} = 0\,\mathrm{Oe}$, whereas it takes a negative value and decreases slightly as temperature decreases in the measurements shown in Fig. 31 for $\nu = 333\,\mathrm{Hz}$. For the frequencies of $\nu = 633\,\mathrm{Hz}$, 982 Hz, and 1443 Hz a negative peak occurs shown in Fig. 31, however, frequencies of this order are not presented by Polichetti *et al* [42]. Further, it might also be highly dependent on the material, meaning a comparison is difficult.

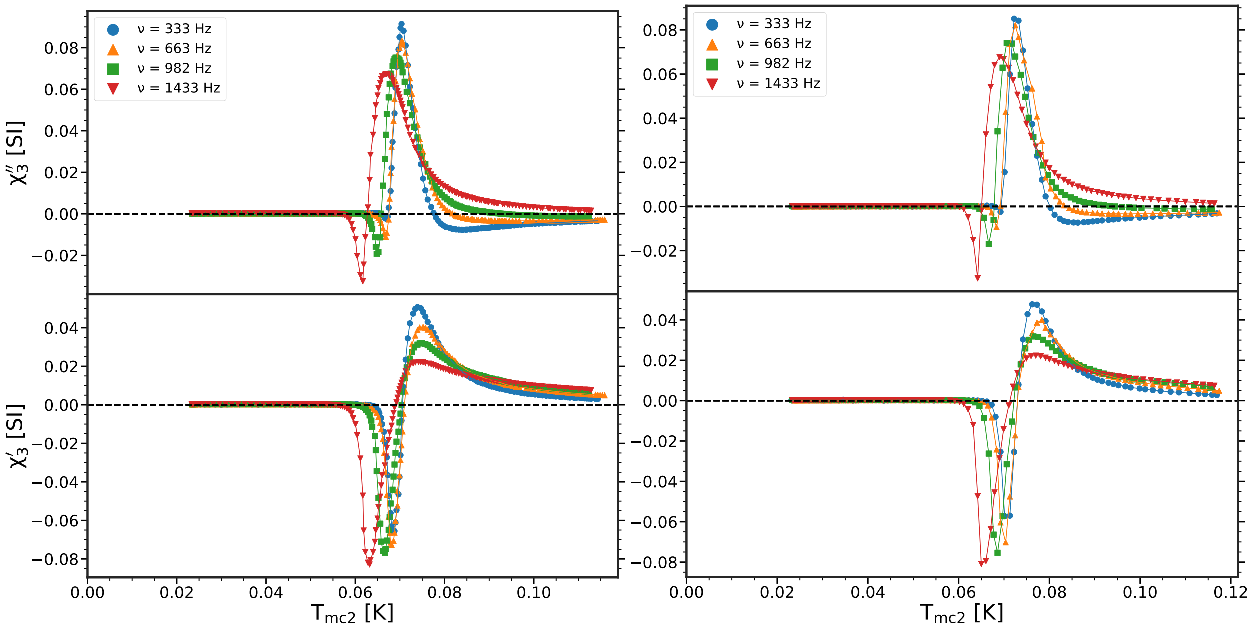

Figure 31: 3rd harmonic ($\Theta_3 = \Theta_{\mathrm{n}=1}$) AC susceptibility as a function of T_{mc2} for $H_{\mathrm{AC}} \approx 21\,\mathrm{Am}^{-1}$ and for excitation frequencies of $\nu = 333\,\mathrm{Hz}$ (●), 663 Hz (▲), 982 Hz (■), and 1433 Hz (▼). The linear spline connecting the data points is simply to guide the eye. **Top**: The out-of-phase component (χ_3''). **Bottom**: The in-phase component (χ_3'). **Left**: Measurements taken while heating. **Right**: Measurements taken while cooling.

4.7.3 Phase Adjustment of $\Theta_3 = 3 \cdot \Theta_{\mathbf{n}=1}$

The 3rd harmonic AC susceptibility for a phase adjustment of $\Theta_3 = 3 \cdot \Theta_{\mathrm{n}=1}$ (in accordance with [34]) is shown in Fig. 32. The out-of-phase component (χ_3'') remains positive in the high temperature regime for all excitation frequencies. As the temperature approaches the transition temperature from above, the value of the out-of-phase component (χ_3'') increases slightly, revealing a small broad positive peak. The peak is suppressed as frequency increases, and at a frequency of $\nu = 1433\,\mathrm{Hz}$, the peak ceases to exist and the temperature-dependence across the high temperature regime appears close to constant. As temperature decreases, the curves rapidly change and show a distinct negative peak which seem to show a tiny trend of decreasing magnitude for increasing frequency. As temperature is lowered further, the out-of-phase component goes to zero ($\chi_3'' = 0$). The in-phase component (χ_3') begins at negative values in the high end of the measured temperature interval. As temperature decreases, it shows a negative peak, which appear to become broader and shrink in magnitude for increasing frequency. Subsequently, it shows a sharp positive peak, which carries a tiny trend of increasing magnitude for increasing frequency. For the remaining lower part of the temperature interval, it stays at zero ($\chi_3' = 0$). Gioacchino *et al* [41] have conducted similar measurements on the compound $\mathrm{NdO_{1-0.14}F_{0.14}FeAs}$, and they observe temperature-dependent features (see Fig. 84 Appendix H), which to some extend show similar behaviour to the measurements presented in Fig. 32. From the measurements by Gioacchino *et al*, the in-phase component (χ_3') from Fig. 84 (left) takes a value of zero ($\chi_3' = 0$) in the high end of the temperature interval. As temperature is lowered a sharp negative peak occurs, which seem to show a tiny frequency dependence if any at all. As temperature decreases further, a positive peak appears which does seem to decrease in magnitude and sharpness as frequency increases. For the remaining temperature interval, it gradually approaches a value of zero ($\chi_3' = 0$). The out-of-phase component (χ_3'') from Fig. 84 (right) shows a value of zero ($\chi_3'' = 0$) at high temperatures followed by a large sharp negative peak and approaches a value of zero ($\chi_3' = 0$) gradually for decreasing temperatures. The peak appears to decrease slightly in magnitude for increasing frequency, however, the width remains close to unchanged. Focusing only on the temperature dependent behavior, the similarities to note between the measurements in Fig. 32 and the measurements in Fig. 84 by Gioacchino *et al* [41] are as follows: the in-phase component (χ_3'), going from high to low temperatures, reveals firstly a negative peak followed by a positive peak across all frequencies. The out-of-phase component (χ_3'') shows a large sharp distinct negative peak, which seems to show a tiny trend of decreasing magnitude with increasing frequency. The differences to note are as follows: The negative peak for the in-phase component (χ_3') shows a decrease in magnitude and sharpness in Fig. 32 as frequency decreases, which differs from the in-phase component (χ_3') in Fig. 84, where there seems to be no clear frequency-dependence. Regarding the positive peak for the in-phase component (χ_3'), there seems to be a frequency-dependence from the measurements by Gioacchino *et al* [41] shown in Fig. 84 (left), and close to no frequency-dependence in the measurements from Fig. 32 (apart from the shift in temperature – presumably due to induced eddy currents). The out-of-phase component (χ_3'') in Fig. 32 differs from out-of-phase component (χ_3'') by Gioacchino *et al* [41] shown in Fig. 84 by taking a positive value at high temperatures. Further, it shows a small negative broad peak at $T_{\mathrm{mc2}} \approx 0.07\,\mathrm{K}$, which decreases slightly with frequency. The abrupt decay for the negative peak in the lower part of the temperature in Fig. 32 differs from the gradual decay shown in Fig. 84. Gioacchino *et al* [41] do not report any phase adjustment, however, given the similarities mentioned it might be possible that the measurements by Gioacchino *et al* [41] (see Fig. 84 Appendix H) correspond to a phase adjustment of $\Theta_3 = 3 \cdot \Theta_{\mathrm{n=1}}$.

According to Ref. [34] the phase adjustment $\Theta_3 = 3 \cdot \Theta_{\mathrm{n=1}}$ would separate the in-phase component (χ_3') and the out-of-phase component (χ_3'') properly. Although, one would have to further investigate this, in order to draw any conclusions regarding the correct phase adjustment. With that being said, one has to be cautious, as the choice of the phase adjustment can have an impact on the interpretation of such measurements for various frequencies, since the measurements using a $\Theta_3 = 3 \cdot \Theta_{n=1}$ differ largely from the two previous representations shown in Section 4.7.1 and 4.7.2 in appearance. In addition, there appears to be less of a response to a change in excitation frequency regarding the representation using $\Theta_3 = 3 \cdot \Theta_{n=1}$. This is strengthened, by a comparison between the Cole-Cole plots from Fig. 77, 75, and 76. The first-mentioned Cole-Cole plot, seems somewhat static whereas the two remaining ones appear to create a spiral motion of the circular closed loops. Regardless of the phase adjustment, the measurements do reveal that during the superconducting transition the full magnetic AC susceptibility is governed by the presence of non-linear terms as well. However, the linear terms still remain dominant.

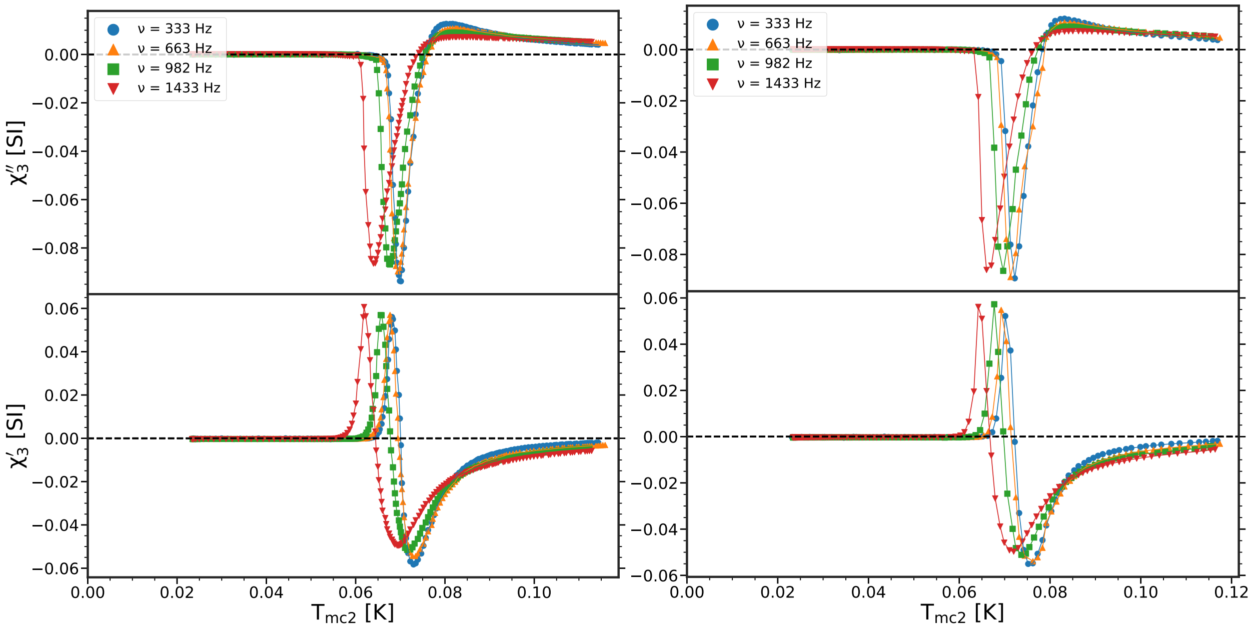

Figure 32: 3rd harmonic ($\Theta_3 = 3 \cdot \Theta_{\mathrm{n}=1}$) AC susceptibility as a function of T_{mc2} for $H_{\mathrm{AC}} \approx 21\,\mathrm{Am}^{-1}$ and for excitation frequencies of $\nu = 333\,\mathrm{Hz}$ (●), 663 Hz (▲), 982 Hz (■), and 1433 Hz (▼). The linear spline connecting the data points is simply to guide the eye. **Top**: The out-of-phase component (χ_3''). **Bottom**: The in-phase component (χ_3'). **Left**: Measurements taken while heating. **Right**: Measurements taken while cooling.

5 The AC Susceptibility of Cerium Magnesium Nitrate

In Section 4 it was witnessed that the excitation frequency had a noticeable effect on the temperature of the sample. Further, it is expected that even for the lowest excitation frequency, the sample temperature differs from the temperature (T_{mc2}) recorded by the thermometer positioned on the cold finger due to imperfect thermalization. Finally, it is known that the thermometer T_{mc2} begins to deviate from the true temperature at higher temperatures. Fig. 69 shows a measurement initiated prior to the dilution refrigeration. It records $T_{\mathrm{mc2}} \approx 0.9\,\mathrm{K}$, at which point the system remains at $T \approx 4\,\mathrm{K}$. Therefore, this section investigates the difference between the recorded cold finger temperature and the actual sample temperature and proposes a model which converts between the former and the latter. In addition, it utilizes the same model to obtain the point of deviation for the cold finger thermometer and corrects for this. The correction utilizes the paramagnetic salt cerium magnesium nitrate (CMN) which, due to its paramagnetic behavior way into the mK range, is widely used within thermometry, especially at dilution temperatures [7, 16, 60–62].

5.1 Cerium Magnesium Nitrate

Cerium magnesium nitrate ($\mathrm{Ce_2Mg_3(NO_3)_{12} \cdot 24H_2O}$) remains one of – the among many – paramagnetic hydrated salts suitable for magnetic cooling and thermometry as it sustains a paramagnetic behaviour down to temperatures of $\theta_{\mathrm{CW}} \lesssim 0.002\,\mathrm{K}$, which makes it the paramagnetic salt with the lowest ordering temperature [16, 61, 62]. A disadvantage is that dehydration may occur if exposed to dry environments and partial vacuum, which is observed by Butterworth et al [60] who reports an increase of the Curie constant due to dehydration. This would presumably result in an increase of the ordering temperature as well. Although, the latter was not witnessed, possibly due to the experiment being conducted at high temperatures i.e. $T \approx 2\,\mathrm{K}$. Regarding ordering in CMN, there is still confusion about whether the compound orders antiferromagnetically or ferromagnetically, however, various articles present measurements which suggest an antiferromagnetic ordering [63, 64]. An additional disadvantage, as various other insulating materials: CMN has a poor thermal conductivity ($10^{-4}\,\frac{\mathrm{W}}{\mathrm{cm \cdot K}}$), meaning that it may be difficult to achieve thermal equilibrium inside the sample at low temperatures [16]. The compound is arranged in a structure which can be described by a rhombohedral primitive unit cell of the space group $\mathrm{R\overline{3}}$ with lattice unit vectors of $a = b = c = 13.165(6)\,\mathrm{Å}$ and lattice angles of $\alpha = \beta = \gamma = 49.37°$ containing 1 formula unit of $\mathrm{Ce_2Mg_3(NO_3)_{12} \cdot 24H_2O}$. Commonly to ease the mathematical description, a non-primitive hexagonal unit cell is used to express such a primitive unit cell which in this case contains 3 formula units of $\mathrm{Ce_2Mg_3(NO_3)_{12} \cdot 24H_2O}$ and yields the following lattice unit vectors: $a = b = 11.004(6)\,\mathrm{Å}$ & $c = 34.592(12)\,\mathrm{Å}$ and the following lattice angles: $\alpha = \beta = 90°$ & $\gamma = 120°$ [65]. The paramagnetic behaviour of CMN arises from the $\mathrm{Ce^{3+}}$ ions in which the interactions between these are particularly weak due to the large amount of water, which assures a large distance ($\sim 1\,\mathrm{nm}$), hence, lowering the ordering temperature significantly and causing it to obey the Curie law quite accurately close to absolute zero [16, 60–62]. The electron configuration of an $\mathrm{Ce^{3+}}$ ion is $\mathrm{[Xe]4f^1}$ meaning that it contains a single electron in the outer shell. Thus, given a total spin of $S = \frac{1}{2}$ and a total angular moment of $L = 3$, the energy level is split into two energy levels with terms $^2\mathrm{F}_{\frac{5}{2}}$ ($J = \frac{5}{2}$) and $^2\mathrm{F}_{\frac{7}{2}}$ ($J = \frac{7}{2}$) with a splitting of $\Delta E \sim 0.3\,\mathrm{eV}$ due to spin-orbit coupling, which corresponds to a temperature of $\sim 3000\,\mathrm{K}$ [7]. Given the large splitting, the latter ($^2\mathrm{F}_{\frac{7}{2}}$) remains unpopulated. Due to the presence of a weak crystal field, the ground state ($^2\mathrm{F}_{\frac{5}{2}}$) is split into 3 *Kramers* doublets characterized by the magnetic quantum number $m_{\mathrm{J}} = \pm\frac{1}{2}, \pm\frac{3}{2}, \pm\frac{5}{2}$ with an effective spin-$\frac{1}{2}$. The ground state doublet corresponds to $m_\text{J} = \pm\frac{5}{2}$, which is separated to the 1st excited doublet $m_\text{J} = \pm\frac{1}{2}$ by an energy of $\Delta E \sim 5\,\text{meV}$ ($\sim 50\,\text{K}$), meaning at the temperature of interest ($T \leq 4\,\text{K}$), the two highest doublets are essentially unoccupied [7, 60, 62].

5.2 The Sample and The Positioning

An elongated piece of CMN (see Fig. 66 (middle) Appendix B) with the approximate length-height-width dimensions of $5.3\,\text{mm} \times 1.7\,\text{mm} \times 2.4\,\text{mm}$ from the collection of CMN which presumably was used in the previous Master Thesis project of Mathias Mikkelsen [57] was the largest piece that would fit in the sample space. This piece of CMN was chosen in order to achieve the largest signal. Given the length of 5.3 mm, the sample extends further than a length of the detection coil ($\sim 4\,\text{mm}$). Therefore, it was positioned such that it would fill the entire detection coil and the remaining of the sample would extend towards the opposite end of the empty detection coil to avoid coupling between the sample and both of the detection coils. The thermal contact was established with 5 insulating copper wires of 200 micron diameter, which were thermally connected to the cold finger (see Fig. 19 (left)). The connection between the copper wires and the sample were established using GE-vanish specified to have a thermal conductivity of $0.034\,\frac{\text{W}}{\text{m}\cdot\text{K}}$ at temperatures of $T \leq 1\,\text{K}$ [66].

5.3 Sampling of Data

The lock-in amplifier was set with a time constant of $\tau = 100\,\text{ms}$ and the script was modified such that for each temperature measurement it would return the average of 5 measurements of the voltage each separated by 1 second, along with the statistical uncertainty on the mean $\frac{\sigma}{\sqrt{N}}$ assuming Gaussian fluctuations. The method of measuring assumes that the temperature of the sample remains close to constant within the time of measuring, which is reasonable as the heating of the sample was performed with caution and each measurement was conducted over several hours, which will be presented in Section 5.4.

5.4 Overview and Temperature Control

For the measurements in the entirety of Section 5, the excitation field was lowered to a field strength of $H_\text{AC} \approx 17\,\text{Am}^{-1}$ to minimize the produced heat. Measurements were conducted for various excitation frequencies while heating and cooling the sample. However, only the measurements for the heating series will be presented here (Section 5.6) as the temperature is varied with caution, whereas for the cooling series, the heat is turned off, causing a large change in temperature with respect to time which can be problematic given the low thermal conductivity of CMN. The measurements for the cooling series are shown in Appendix J.1 for the curious reader. The progress of the temperature during the measurements for the heating series is shown in Fig. 33, where the cold finger temperature begins at $T_\text{mc2} \approx 13\,\text{mK}$ and ends at $T_\text{mc2} \approx 240\,\text{mK}$ across a time window of $\sim 6\,\text{hr}$. Initially, at time $= 0\,\text{s}$, the heat on the still is turned off, meaning the temperature in the mixing chamber and for the sample increases slowly up to a finite temperature. At time $\approx 4000\,\text{s}$, heat is applied in the mixing chamber, however, this is varied slowly, in hope of achieving a stable temperature connection between the cold finger and the sample. Ideally, the curves in Fig. 33 should lie on top of one another, however, given the heat supply is done manually, it remains difficult to conduct every experiment under identical heat conditions, and it quickly becomes very time consuming.

Finally, a single measurement while adding helium to the system is shown in Section 5.7 and used to estimate the temperature outside the thermometers reliable range.

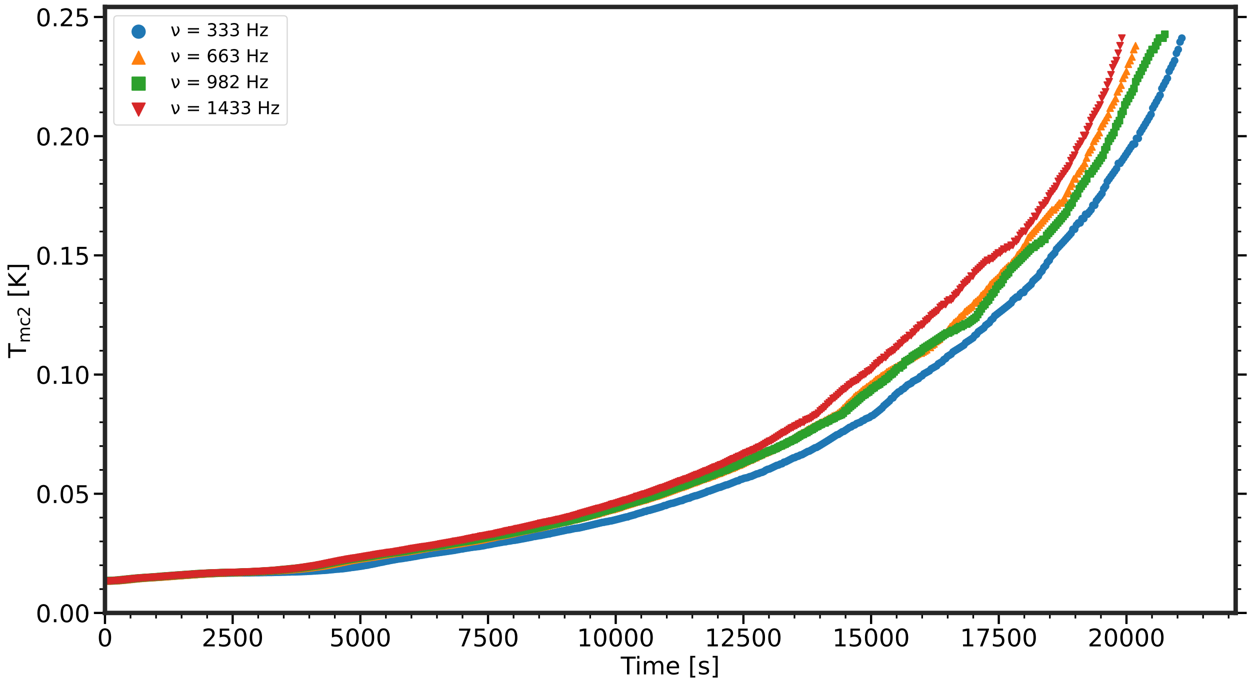

Figure 33: Cold finger temperature T_{mc2} as a function of time during the AC susceptibility measurements for a field strength of $H_{\mathrm{AC}} \approx 17\,\mathrm{Am}^{-1}$ and excitation frequencies of $\nu = 333\,\mathrm{Hz}$ (●), 663 Hz (▲), 982 Hz (■), and 1433 Hz (▼). The heating begins at time ≈ 4000 s.

5.5 Conversion from Raw Data to Susceptibility

The voltage across the detection coils was measured without any phase adjustments. Thus, the voltage was measured in terms of X_1 and Y_1 (see Fig. 87 Appenndix J) by the lock-in amplifier. The raw data has initially been rotated in the complex plane using Eq. (86) with the phase (Θ) for each frequency presented in Table 2 (heating) in order to separate the voltage in terms of an in-phase component ($\mathcal{E}_{\mathrm{n}}^{\mathrm{x}}$) and an out-of-phase component ($\mathcal{E}_{\mathrm{n}}^{\mathrm{y}}$). Subsequently, the separated voltages have been scaled in accordance with Eq. (85), using the utilized excitation frequencies and the calibration constants (C_{s}) from Table 2. The excitation fields (H_{AC}) used in the conversion to susceptibility are reported in Table 4. It should be noted that these fields are measured using an additional lock-in amplifier as the oscilloscope used for the titanium measurements in Section 4 captured a lot of noise for a field of $H_{\mathrm{AC}} \approx 17\,\mathrm{Am}^{-1}$. Thus, the circuit configuration remains the one shown in Fig. 20 (left), where the oscilloscope has been replaced with a lock-in amplifier. The susceptibility is reported in arbitrary units, due to the fact that the calibration constants from Table 2 remain geometry dependent. Hence, it does not convert to SI units accurately for a sample with a geometry that differs from the geometry used to determine the constant initially. In addition, the CMN sample is larger causing it to extend outside the detection coil which further causes a deviation.

The demagnetization has not been accounted for due to the arbitrary shape of the sample, and given a paramagnetic behaviour it can, in practice, be neglected.

5.6 Measurements at Cold Finger Temperature Regime of $T_{\mathrm{mc2}} \approx 13\text{-}250\,\mathrm{mK}$

The in-phase component (χ') as a function of T_{mc2} for various excitation frequencies is shown in Fig. 34 along with the reciprocal of the in-phase component (${\chi'}^{-1}$) (insert). The susceptibility appears to increase in a Curie-like manner as temperature decreases. At low temperatures ($T_{\mathrm{mc2}} \approx 17\,\mathrm{mK}$), the data reveals a strange bump (see Fig. 88 Appendix J), which is most likely connected to an instability of the sample temperature as a consequence of its low thermal conductivity. As mentioned in Section 5.1, CMN obeys the Curie law accurately in this temperature regime, meaning that one would expect a straight line when plotting the reciprocal susceptibility (χ'^{-1}) as a function of temperature. Although, as seen in Fig. 34 (insert), χ'^{-1} shows a curved line across all the excitation frequencies. The curvature does seem to decrease as frequency increases.

The insert for the excitation frequency of $\nu = 333\,\mathrm{Hz}$ shows a discontinuity, which is caused by the fact that the in-phase component (χ') crosses the zero. Such curvature in the reciprocal in-phase component (χ'^{-1}) is, commonly, caused by the presence of a temperature independent contribution (χ_0), which can easily go undetected in a χ' vs temperature plot. This temperature independent contribution can have various origins such as: core diamagnetism (from the sample or the environment) and van Vleck paramagnetism (Section 2.4), a background contribution from the fact that the signal of the coils alone is not completely eliminated, or a background contribution solely from the instrument [16, 25]. Either way, it remains unavoidable experimentally and this has to be accounted for when performing a fit using the Curie (Weiss) law. One additional feature that has to be accounted for is the temperature difference between the measured temperature by the thermometer and the sample. If the temperature difference is large, this will further contribute to a deviation in the Curie law, and, therefore, a deviation from a straight line in a χ'^{-1} vs T_{mc2} plot.

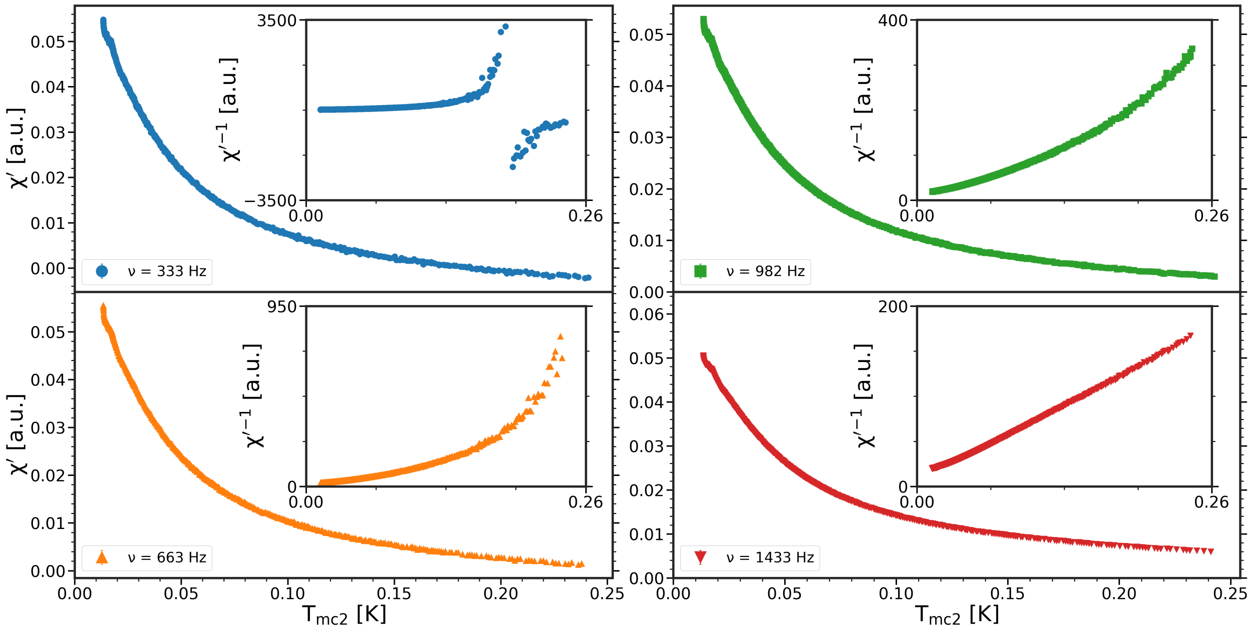

Figure 34: The in-phase component (χ') of the AC susceptibility as a function of T_{mc2} for $H_{\mathrm{AC}} \approx 17\,\mathrm{Am}^{-1}$ and for excitation frequencies of $\nu = 333\,\mathrm{Hz}$ (●), 663 Hz (▲), 982 Hz (🟩), and 1433 Hz (▼). Insert shows χ'^{-1}.

In order to account for the temperature difference between the cold finger and the sample, an approximate model from Pobell [16] utilized in a previous Master's thesis [57] is applied. If the experiment is carried out in a slow manner with small temperature variations, we can assume that during each measurement the sample remains close to a steady state. In the steady state, the heat leak from the warmer components to the sample remains equivalent to the heat transfer from the sample to the mixing chamber through the type of thermalization which in this case is the copper wires [16, 57]. The heat carried by these wires is:

$$\dot{Q} = \frac{A}{L} \int_{T_{\mathrm{mc2}}}^{T_{\mathrm{sample}}} \kappa(T) dT, \tag{90}$$

where A is their cross-sectional area, L is the length, and κ is the conductivity coefficient [16, 25, 57]. For copper, the conduction electrons yield the largest contribution to the thermal conductivity, and the thermal conductivity for the electrons relates – to a good approximation – linearly to the temperature at low temperatures ($T < 10\,\mathrm{K}$). Therefore, one has:

$$\kappa_{\mathrm{e}}(T) = \kappa_0 T, \tag{91}$$

which results in a heat transfer of:

$$\dot{Q} = \frac{A\kappa_0}{2L}\left(T_{\mathrm{sample}}^2 - T_{\mathrm{mc2}}^2\right) \quad \Rightarrow \quad 2\Delta = T_{\mathrm{sample}}^2 - T_{\mathrm{mc2}}^2, \tag{92}$$

where $\Delta = \frac{L\dot{Q}}{A\kappa_0}$ is a fit parameter to be determined and $\frac{L}{A\kappa_0}$ represents the thermal resistance [16]. Thus, the final fit function becomes:

$$\chi(T_{\mathrm{mc2}}) = \frac{C}{T_{\mathrm{sample}}} + \chi_0 = \frac{C}{\sqrt{T_{mc2}^2 + 2\Delta}} + \chi_0, \tag{93}$$

which does not diverge for $T_{\mathrm{mc2}} \to 0\,\mathrm{K}$ as one would expect. Physically, as $T_{\mathrm{mc2}} \to 0\,\mathrm{K}$, one would expect the temperature of the sample to plateau at a finite temperature value, meaning the susceptibility vs T_{mc2} would saturate.

The fit function from Eq. (93) was applied to χ' vs T_{mc2} data across the entire temperature range as shown in Fig. 35 by minimizing $\chi^2 = \sum_i (y_i - y_{\mathrm{fit},i})^2/\sigma_i^2$ [67], and the fit parameters for each excitation frequency are collected in Table 4.

According to Ref. [25], a Curie (Weiss) fit should ideally be applied to the reciprocal susceptibility vs temperature data. However, due to the discontinuity shown in the insert in Fig. 34 for an excitation frequency $\nu = 333\,\mathrm{Hz}$, it becomes difficult. Therefore, to be consistent, the fit function from Eq. (93) was applied on non-reciprocal data. Fitting to the reciprocal data yielded fit parameters that were not statistically different from the non-reciprocal fit (Table 4).

Visually, the fit appears reasonable for all the excitation frequencies as seen in Fig. 35. This is further strengthened by the low residuals as a function of temperature (see Fig. 89 Appendix. J) and the distribution of residuals, which resemble a Gaussian-like distribution centered around zero (see Fig. 90). The residuals as a function of temperature (see Fig. 89) do show that the fit begins to slightly deviate at low temperatures where the strange bump occurred (see Fig. 88), however this deviation is minor. Subtracting the fit parameter χ_0 and plotting the reciprocal susceptibility $(\chi' - \chi_0)^{-1}$ vs T_{mc2} yields a curve which nearly resembles a straight line as seen in Fig. 35 (insert). Although, there is a slight curvature at low temperature which reflects a saturation in the susceptibility, presumably as a consequence of a plateau in the temperature of sample. At the minimum sample temperature the cooling power mediated by the copper wires is equivalent to the heat transfer to the sample from the surroundings. This can be accounted for using the approximate relation between the cold finger temperature (T_{mc2}) and the sample temperature given by Eq. (92) which uses the estimated fit parameter Δ.

ν [Hz]	333	663	982	1433
H_{AC} [Am^{-1}]	17.36196(4)	17.01191(6)	17.05851(3)	17.11135(5)
C [a.u.]	$1.6769(15) \times 10^{-3}$	$1.6204(10) \times 10^{-3}$	$1.5649(6) \times 10^{-3}$	$1.4908(3) \times 10^{-3}$
Δ [K^2]	$2.733(6) \times 10^{-4}$	$2.841(4) \times 10^{-4}$	$3.110(3) \times 10^{-4}$	$3.5688(17) \times 10^{-4}$
χ_0 [a.u.]	$-8.874(17) \times 10^{-3}$	$-5.341(11) \times 10^{-3}$	$-3.329(7) \times 10^{-3}$	$-1.04(4) \times 10^{-4}$
$T_{\mathrm{sample,min}}$ [mK]	26.95(2)	27.366(15)	28.371(9)	29.883(6)
$T_{\mathrm{sample}}(T_{\mathrm{mc2}} = 0)$ [mK]	23.38(2)	23.838(17)	24.941(11)	26.716(6)

Table 4: A table containing the excitation fields of each excitation frequency measurement, fit parameters from applying the modified Curie fit in Eq. (93) on χ' vs T_{mc2} data from Fig. 35, the estimated minimum sample temperature ($T_{\mathrm{sample,min}}$), and the estimated sample temperature when the cold finger reaches absolute zero ($T_{\mathrm{sample}}(T_{\mathrm{mc2}} = 0)$).

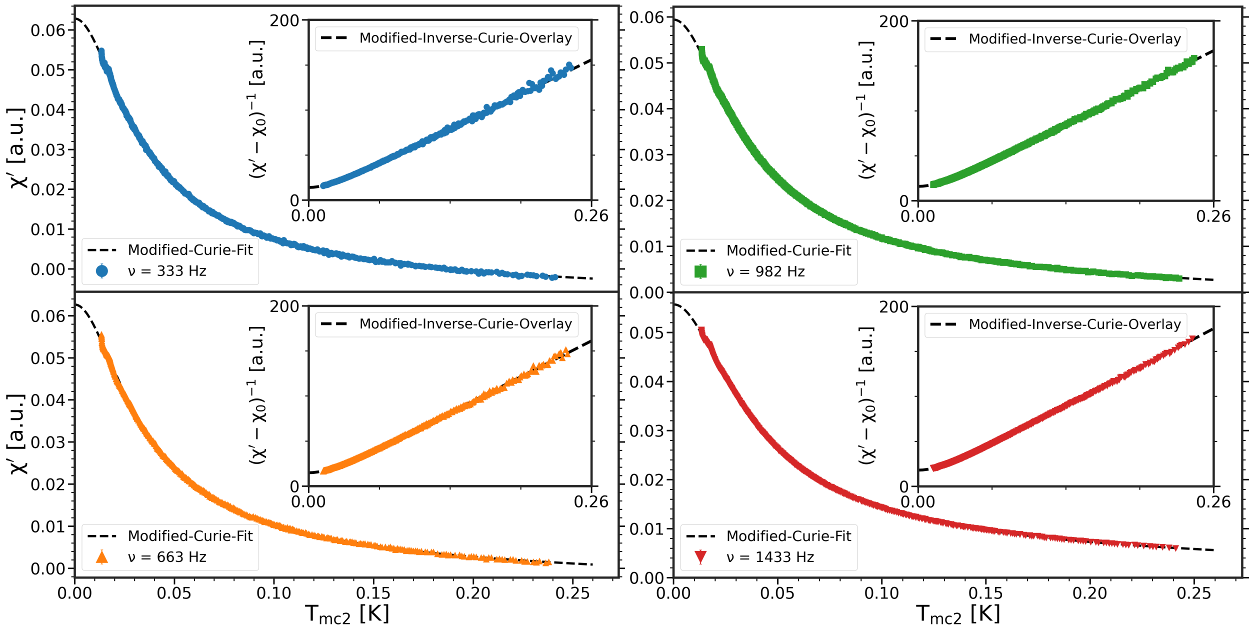

Figure 35: The in-phase component (χ') of the AC susceptibility as a function of T_{mc2} for $H_{\mathrm{AC}} \approx 17\,\mathrm{Am}^{-1}$ and for excitation frequencies of $\nu = 333$ Hz (●), 663 Hz (▲), 982 Hz (■) and 1433 Hz (▼), where the modified Curie fit function from Eq. (93) has been applied. The insert shows the $(\chi' - \chi_0)^{-1}$ as a function of T_{mc2}, with an overlay of the reciprocal of the modified Curie fit function from Eq. (93).

The in-phase component (χ') of the AC susceptibility as a function of the T_{sample} estimated using Eq. (92), is shown in Fig. 36 with an overlay of Eq. (93) (LHS) which contains T_{sample}.

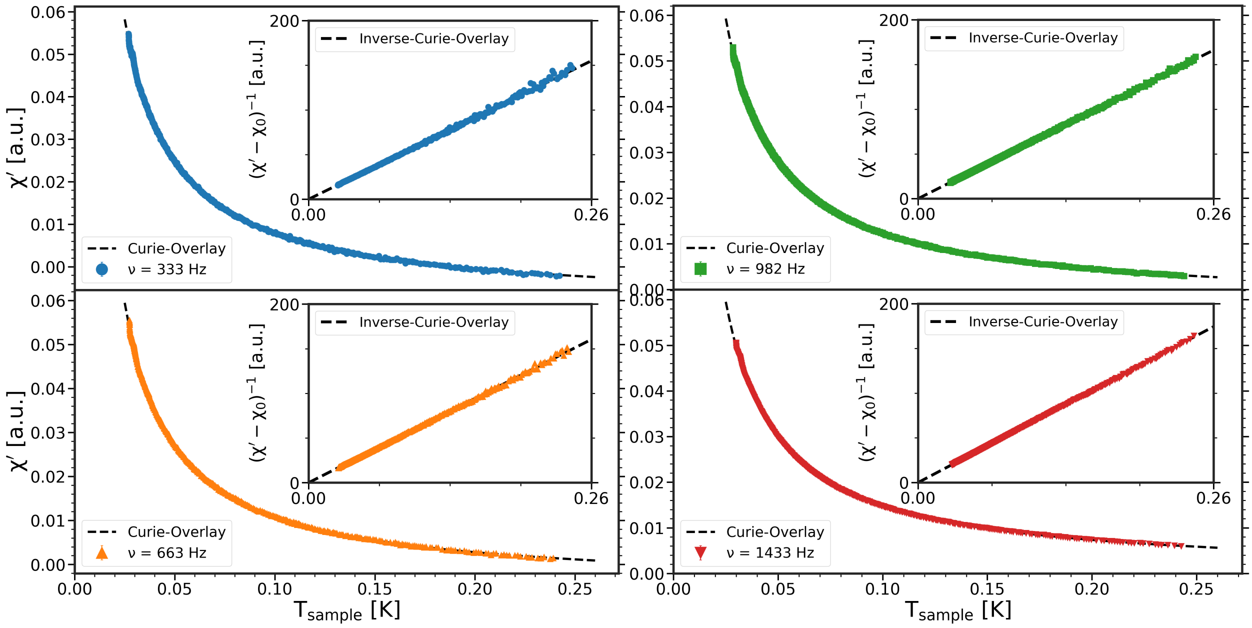

Figure 36: The in-phase component (χ') of the AC susceptibility as a function of T_{sample} for $H_{\text{AC}} \approx 17\,\text{Am}^{-1}$ and for excitation frequencies of $\nu = 333\,\text{Hz}$ (●), 663 Hz (▲), 982 Hz (■), and 1433 Hz (▼), where the Curie function from Eq. (93) (LHS) is included as an overlay. The insert shows the $(\chi' - \chi_0)^{-1}$ as a function of T_{sample}, with an overlay of the reciprocal of the Curie function from Eq. (93) (LHS).

Further, the sample temperature (T_{sample}) has been plotted in Fig. 37 (left) as a function of the cold finger temperature (T_{mc2}) for each excitation frequency using Eq. (92), where $T_{\text{sample}} \approx T_{\text{mc2}}$ for $T_{\text{mc2}}^2 \gg 2\Delta$. The insert highlights the behavior at low temperatures, where the relation between the cold finger temperature (T_{mc2}) and the sample temperature (T_{sample}) differs from the linear behavior. Further, it reveals that the final sample temperature (T_{sample}) and $T_{\text{sample}}(T_{\text{mc2}} = 0)$, also reported in table 4 (row 6), depends on the excitation frequency, which presumably is due to generated heat by induced eddy currents in metallic parts. The temperature ($T_{\text{sample}}(T_{\text{mc2}} = 0)$) has been plotted as a function of the excitation frequency in Fig. 37 (right). By using the heat transfer from Eq. (92) (LHS) and assuming that in case of eddy currents $\dot{Q}_{\text{eddy}} \propto \nu^2 H_{\text{AC}}^2$ [16] one can construct a fit function, which relates $T_{\text{sample}}(T_{\text{mc2}} = 0)$ to the excitation frequency as follows:

$$\dot{Q} = \frac{A\kappa_0}{2L}\left(T_{\text{sample}}^2 - T_{\text{mc2}}^2\right) = \beta + \alpha(2\pi\nu)^2 \quad \Rightarrow \quad T_{\text{sample}}\left(\nu, T_{\text{mc2}} = 0\right) = \sqrt{\tilde{\beta} + \tilde{\alpha}\left(2\pi\nu\right)^2} \tag{94}$$

where $\tilde{\beta} = \frac{2L}{A\kappa_0}\beta$ and $\tilde{\alpha} = \frac{2L}{A\kappa_0}\alpha$ are fit parameters. As seen in Fig. 37 (right), the fit function from Eq. (94) is applied and yields the following fit parameters: $\tilde{\alpha} = 2.206(10) \times 10^{-12}\,\text{K}^2\text{s}^2$ and $\tilde{\beta} = 535.3(6) \times 10^{-6}\,\text{K}^2$, such that for $\nu \to 0\,\text{Hz}$, one has that $T_{\text{sample}}\left(T_{\text{mc2}} = 0\right) \to 23.1(8)\,\text{mK}$ according to the fit. Visually, the fit seems reasonable, meaning heating caused by induced eddy currents could very well be the case. However, the statistical uncertainties remain small. These originate from the uncertainty on Δ alone, since we do not have the uncertainty on T_{mc2}. It is, therefore, difficult to obtain a statistical parameter which would indicate a good fit.

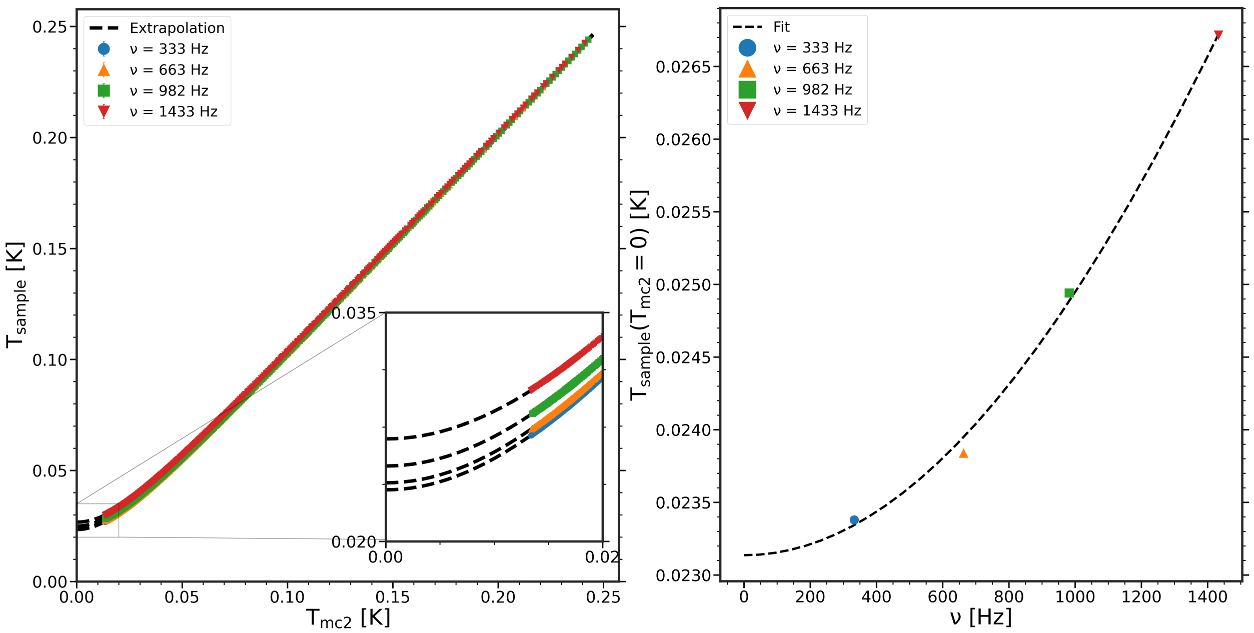

Figure 37: **Left**: The sample temperature (T_{sample}) as a function of cold finger temperature T_{mc2} for excitation frequencies of $\nu = 333\,\text{Hz}$ (●), $663\,\text{Hz}$ (▲), $982\,\text{Hz}$ (■), and $1433\,\text{Hz}$ (▼). The black dashed lines represent extrapolations to $T_{\text{mc2}} = 0\,\text{K}$. **Right**: $T_{\text{sample}}(T_{\text{mc2}} = 0)$ vs ν along with an applied fit from Eq. (94) (RHS). $T_{\text{sample}}(T_{\text{mc2}} = 0)$ has been extracted from the extrapolations from Fig. 37 (left).

Further, using the model earlier used to derive Eq. (94), one can in addition obtain the following fit function for the fit parameter Δ:

$$\Delta(\nu) = \frac{L}{A\kappa_0}\left(b + a(2\pi\nu)^2\right) \tag{95}$$

where $a = \frac{1}{2}\tilde{\alpha}$ and $b = \frac{1}{2}\tilde{\beta}$, where $\tilde{\alpha}$ and $\tilde{\beta}$ correspond to the fit parameters in Eq. (94). Applying the fit from Eq. (95), which is shown in Fig. 38 (right), yields the following fit parameters: $a = 1.103(5) \times 10^{-12}\,\text{K}^2\text{s}^2$ and $b = 267.6(3) \times 10^{-6}\,\text{K}^2$. The fit in Fig. 38 (right) appears to be reasonable and the fit parameter behaves as expected, by increasing for increasing frequency. This is nothing new compared to the fit in Fig. 37, but rather to show that one may extrapolate the parameter Δ to higher frequencies.

The fit parameter χ_0 shows a negative background and has a trend of decreasing magnitude for increasing frequency (see Table 4). This decreasing trend is visualized in the inserts of Fig. 34, where the degree of curvature is suppressed as the frequency increased. This fit parameter presumably relates to the background from imperfect coils, instrumentation, and the scaling factor (C_S) at which point it would indeed contain a frequency dependence.

The fit parameter C (see table 4) shows a decrease as frequency increases. This parameter corresponds to the Curie constant and, in theory, this should not contain a frequency-dependence, at least not for a paramagnetic sample. This parameter is sensitive to the scaling factor (C_S), such that a small change in (C_S) leads to a small change in C. The fact that the parameter remains frequency-dependent, could suggest that the frequency dependence of the scaling factor (C_S) has changed upon swapping the sample from titanium to CMN. The possibility of this was discussed briefly in the end of Section 4.6.2. The changes in the two fit parameters cause the in-phase component (χ') curves to be separated. However, by subtracting χ_0 they become closely stacked as shown in Fig. 38 (left).

Although, the important and promising feature is that the parameter Δ remains insensitive to changes in (C_S). This is crucial for the model in Eq. (92) to uphold.

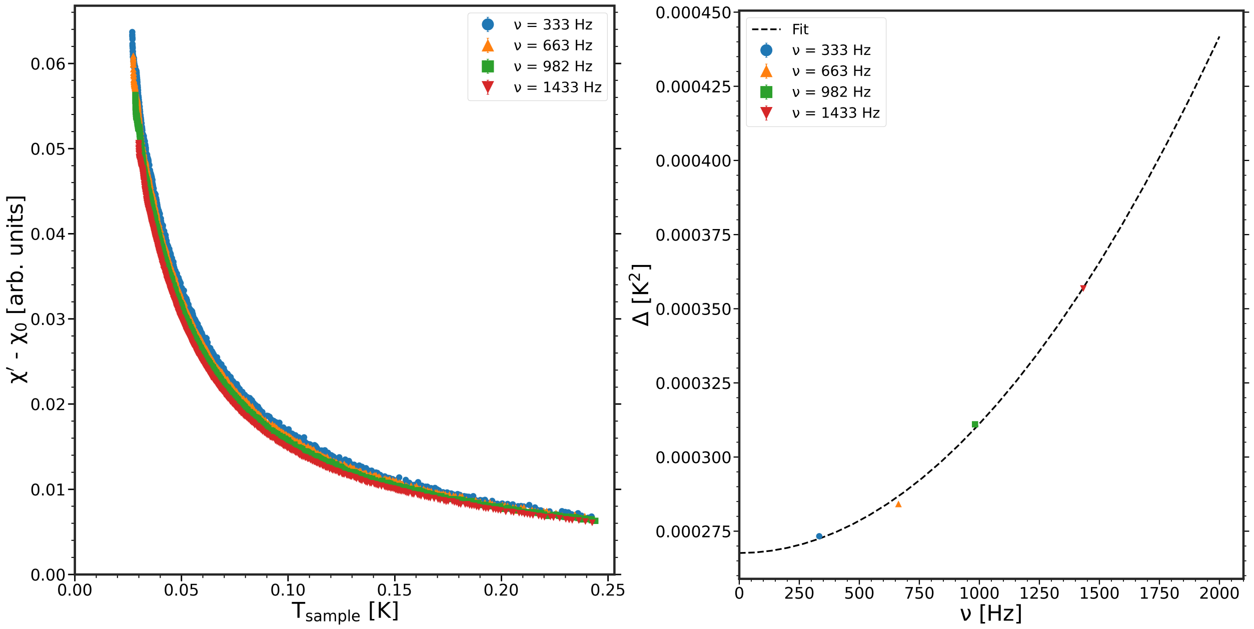

Figure 38: **Left**: The in-phase component $(\chi' - \chi_0)$ as a function of sample temperature T_{sample} $H_{\text{AC}} \approx 17\,\text{Am}^{-1}$ and for excitation frequencies of $\nu = 333\,\text{Hz}$ (●), $663\,\text{Hz}$ (▲), $982\,\text{Hz}$ (■), and $1433\,\text{Hz}$ (▼). The background term (χ_0) from table 4 has been subtracted, causing the curves to be closely stacked. **Right**: The fit parameter Δ from table 4 as a function of ν. The fit corresponds to Eq. (95).

5.6.1 The out-of-phase component (χ'')

The out-of-phase component (χ'') remains temperature independent as shown in Fig. 39, which is expected. As mentioned in Section 2.9.2, the spin-spin relaxation for paramagnetic materials is on the order of $\sim 10^{-9}$-$10^{-10}\,\text{s}$, meaning that the system responds effectively instantaneously – at least in the frequency regime accessible to AC susceptibility ($\sim 10\,\text{kHz}$) [17, 18, 35]. Thus, in the absence of a DC field, the imaginary component should remain zero. Due to background of the apparatus and the imperfect coils, the measured value will unavoidably differ from zero, however, it should not reveal a temperature dependence. The fact that no temperature dependence is witnessed in Fig. 39 strengthens the indication that the proper phase has been used to separate the data. The out-of-phase component (χ'') takes on negative values, which indicates a negative background. It will be seen in Section 6 that this background depends on the configuration used (see Fig. 19).

However, for illustrative purposes, the lock-in amplifier which measures the voltage drop across the resistor ($R = 100\,\Omega$), measures the voltage drop in terms of an amplitude and a phase with respect to the reference. Theoretically, the voltage drop across the resistor should be in phase with the current, which is proportional to the excitation field. Furthermore, the voltage induced in the secondary coils will be $\frac{\pi}{2}$ out of phase with the excitation field due to Faraday's law. Thus, theoretically, one will have to rotate the raw data with a phase corresponding to $\Theta = \frac{\pi}{2} + \theta_{\text{res}}$, where θ_{res} corresponds to the phase between voltage drop across the resistor and the reference voltage. Therefore, a common way to determine the phase needed to rotate the raw data, is to utilize a lock-in amplifier measuring across a resistor [39, 57]. In practise, the phase will change slightly across the circuit and it may further be altered by instrumentation background signals, temperature changes, frequency changes, etc. [18]. Therefore, as mentioned in Section 3.3.2 it is advised to utilize a superconductor to determine the phase which was done in Section 4 and, indeed works. Anyhow, the phase determined using the lock-in amplifier to measure across the resistor ($\Theta_{\mathrm{res,CMN}}$) is shown in Table 5. This phase clearly differs from the phase Θ also shown in Table 5. Anyhow, utilizing the phase $\Theta_{\mathrm{res,CMN}}$ for each frequency yields a temperature-dependent out-of-phase component (χ'') as shown in Fig. 40, which indicates that the in-phase component (χ') and the out-of-phase component χ'' have not been separated properly.

ν [Hz]	333	663	982	1433
Θ [radians]	1.70541(5)	1.81142(2)	1.90707(1)	2.033416(7)
$\Theta_{\mathrm{res,CMN}}$ [radians]	1.68940(9)	1.78264(9)	1.86681(5)	1.97909(4)
$\Delta\Theta$ [radians]	0.01600(10)	0.02878(9)	0.04026(5)	0.05433(8)

Table 5: Table comparing the phase Θ from table 2 (heating) and the phase ($\Theta_{\mathrm{res,CMN}} = \frac{\pi}{2} + \theta_{\mathrm{res,CMN}}$). The difference in phase is computed as $\Delta\Theta = \Theta - \Theta_{\mathrm{res,CMN}}$.

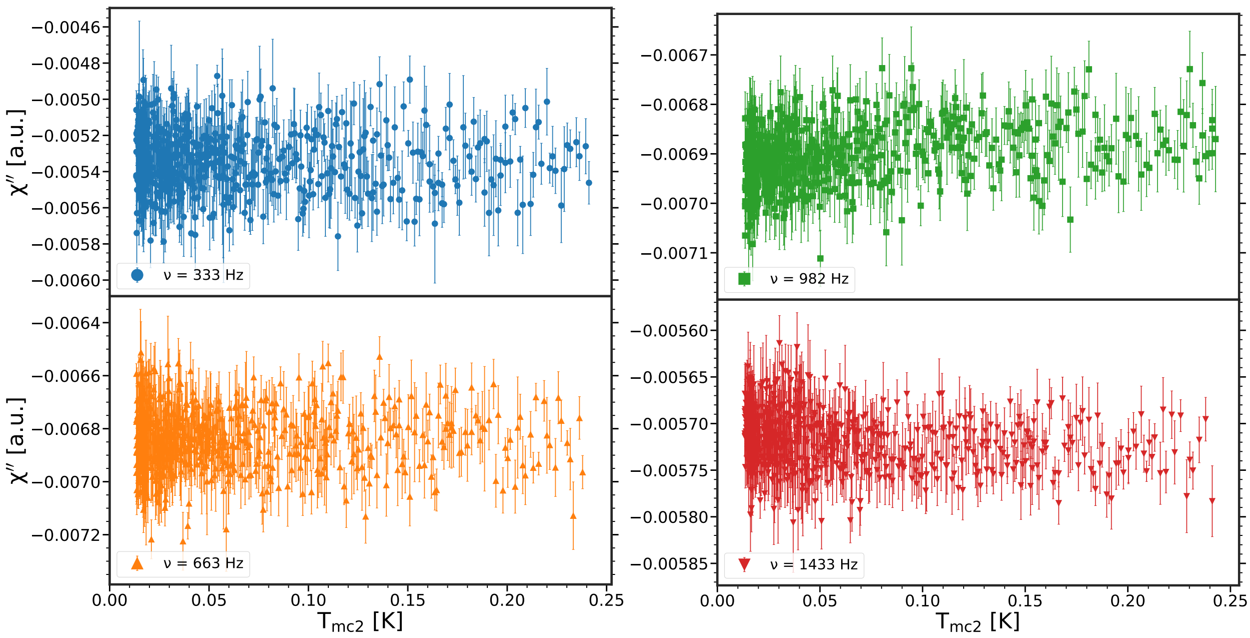

Figure 39: The out-of-phase component (χ'') of the AC susceptibility as a function of T_{mc2} for $H_{\mathrm{AC}} \approx 17\,\mathrm{Am}^{-1}$ and for excitation frequencies of $\nu = 333\,\mathrm{Hz}$ (●), 663 Hz (▲), 982 Hz (■), and 1433 Hz (▼), using the phase Θ from table 5

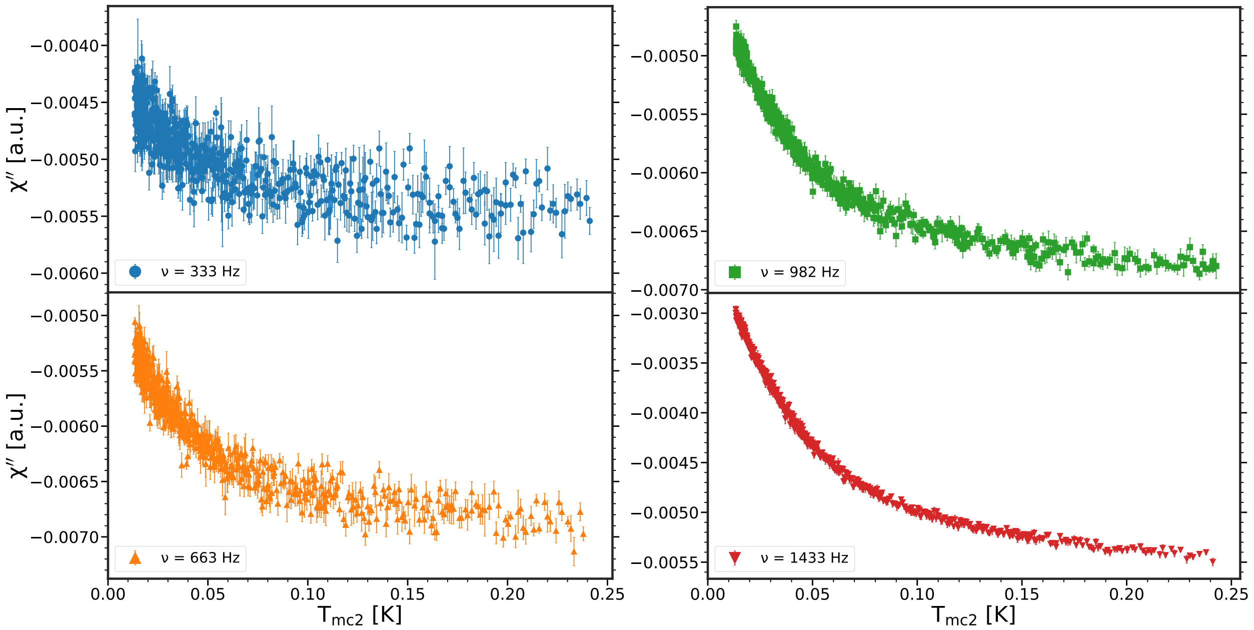

Figure 40: The out-of-phase component (χ'') of the AC susceptibility as a function of T_{mc2} for $H_{\mathrm{AC}} \approx 17\,\mathrm{Am}^{-1}$ and for excitation frequencies of $\nu = 333\,\mathrm{Hz}$ (●), $663\,\mathrm{Hz}$ (▲), $982\,\mathrm{Hz}$ (■), and $1433\,\mathrm{Hz}$ (▼) where the phase $\Theta_{\mathrm{res,CMN}}$ from table 5 has been used. Notice the temperature-dependence, which is typically an indicator that the in-phase component (χ') and the out-of-phase component (χ'') have not been separated properly.

5.7 Temperature Correction in the High Temperature Regime

The thermometer located on the cold finger denoted T_{mc2} deviates at high temperatures, such that it records $T \sim 0.9\,\mathrm{K}$ prior to beginning of the dilution process. However, the temperature of the entire system, at this point, should ideally be stable at approximately $T \sim 4\,\mathrm{K}$, and the temperature of the cold finger should lie thereabout. Therefore, the goal of this Section is to determine the point of deviation for the thermometer (T_{mc2}) and obtain an approximate correction.

Similar to the measurement of titanium shown in Fig. 69, a measurement of the AC susceptibility as a function of T_{mc2} for CMN has been conducted while adding helium to the system, such that the measurement has been taken while cooling down. This measurement is shown in Fig. 41. The in-phase component (χ') shows a Curie-like increase as the temperature decreases. The insert in Fig. 41 (left), shows an unexpected behavior in the low temperature regime, where the susceptibility appears to show a peak. This feature is believed to be an effect of a variation in the sample temperature, while the temperature of the cold finger continues to decrease. This was not reproducible. The out-of-phase component (χ'') remains approximately constant across the entire temperature range, which is expected.

The thermometer T_{mc2} shows that the measurement begins at a temperature of $T \approx 1\,\mathrm{K}$, however, the measurement was initiated when the helium at room temperature was added, at which point the temperature presumably is $T \sim 6\,\mathrm{K}$. If one assumes that the fit function in Eq. (93) accounts for an imperfect thermalization and remains reliable across a larger temperature regime, which it should, a deviation in the recorded temperature and the true temperature would be reflected in a deviation between the data points and the fit.

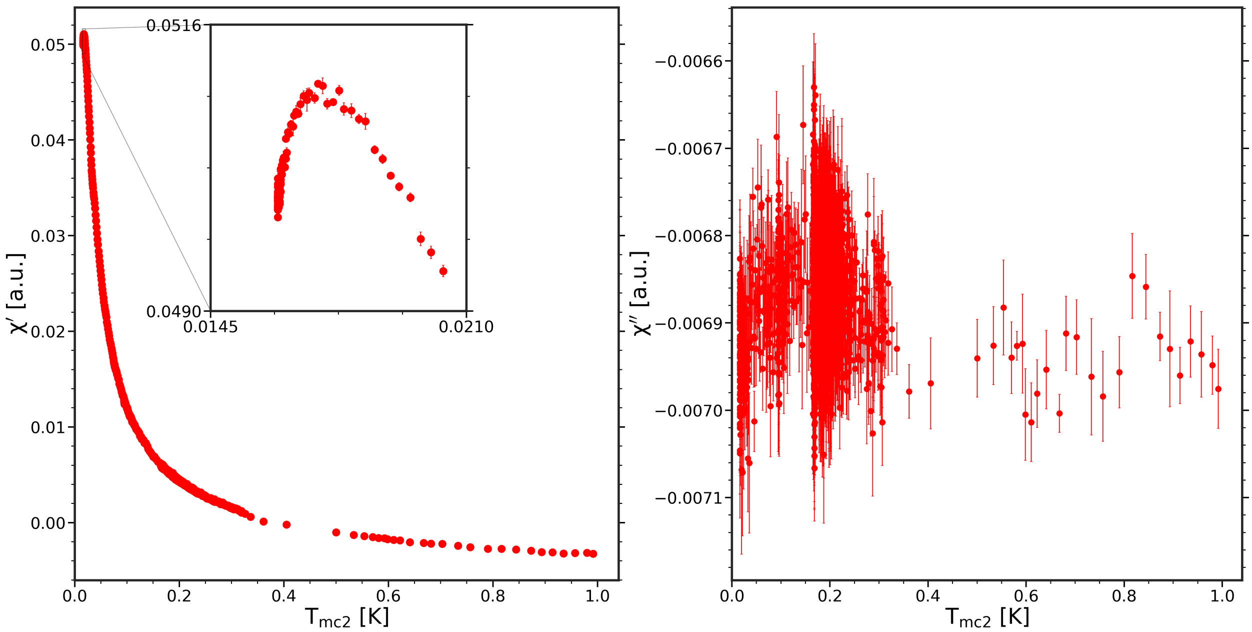

Figure 41: The AC susceptibility as a function of T_{mc2} for $H_{\mathrm{AC}} \approx 17\,\mathrm{Am^{-1}}$ at $\nu = 982\,\mathrm{Hz}$ while adding helium to the system. **Left**: The in-phase component (χ'). The insert shows an anomaly, which was not reproducible. **Right**: The out-of-phase component (χ'').

The fit function from Eq. (93) has been applied across a temperature range where, based on Section 5.6, T_{mc2} is reliable. The fit is shown in Fig. 42 (left) and represented by the dashed black line. It yields the following fit parameters: $C = 1.5952(7) \times 10^{-3}\,\mathrm{a.u.}$, $\chi_0 = -3.557(4) \times 10^{-3}\,\mathrm{a.u.}$, and $\Delta = 233.9(5) \times 10^{-6}\,\mathrm{K^2}$. The blue lines delimit the fitting interval, for which insert 1 highlights the low-temperature part, showing that the strange peak is neglected in the fit. Insert 2 highlights the other end of the fit where the data begins to deviate from the actual fit, which presumably is a result of the thermometer deviating from the true temperature. As temperature increases, the deviation becomes larger, as one would expect. The corresponding reciprocal susceptibility $(\chi' - \chi_0)^{-1}$ has been plotted in Fig. 42 (right) in which the deviation becomes significantly more clear. The point of deviation is chosen to be at the end of the fitting interval ($T_{\mathrm{mc2}} \approx 0.285\,\mathrm{K}$). From this point, the data points remain above the fit overlay and deviate further as temperature increases (see insert Fig. 42 (right)). Therefore, assuming the data should follow the modified Curie fit function from Eq. (93) as a function of the true cold finger temperature, one can determine the corrected cold finger temperature ($T_{\mathrm{mc2,corrected}}$) in a point-to-point correction using:

$$T_{\mathrm{mc2,corrected}} = \sqrt{\left(\frac{C}{\chi' - \chi_0}\right)^2 - 2\Delta}. \tag{96}$$

The result of the temperature correction is shown in Fig. 43 where the corrected data points (blue points) lie on the line of the fit. Equivalently, $(\chi' - \chi_0)^{-1}$ vs $T_{\mathrm{mc2,corrected}}$ is shown in Fig. 43 (right). The errors on $T_{\mathrm{mc2,corrected}}$ have been determined using the law of propagation of errors [67] with Eq. (96), which yields a large uncertainty due to the fact it goes as:

$$\sigma_{(\chi'-\chi_0)^{-1}} = \frac{\sqrt{\sigma_\chi^2 + \sigma_{\chi_0}^2}}{(\chi - \chi_0)^2}. \tag{97}$$

Given the whole measurement was conducted while cooling the sample, it has to be emphasized that it remains an approximate correction. Although, the corrected temperature does lie within the expected range ($\sim 5\,\mathrm{K}$) when the dilution process is initiated, which surely is promising.

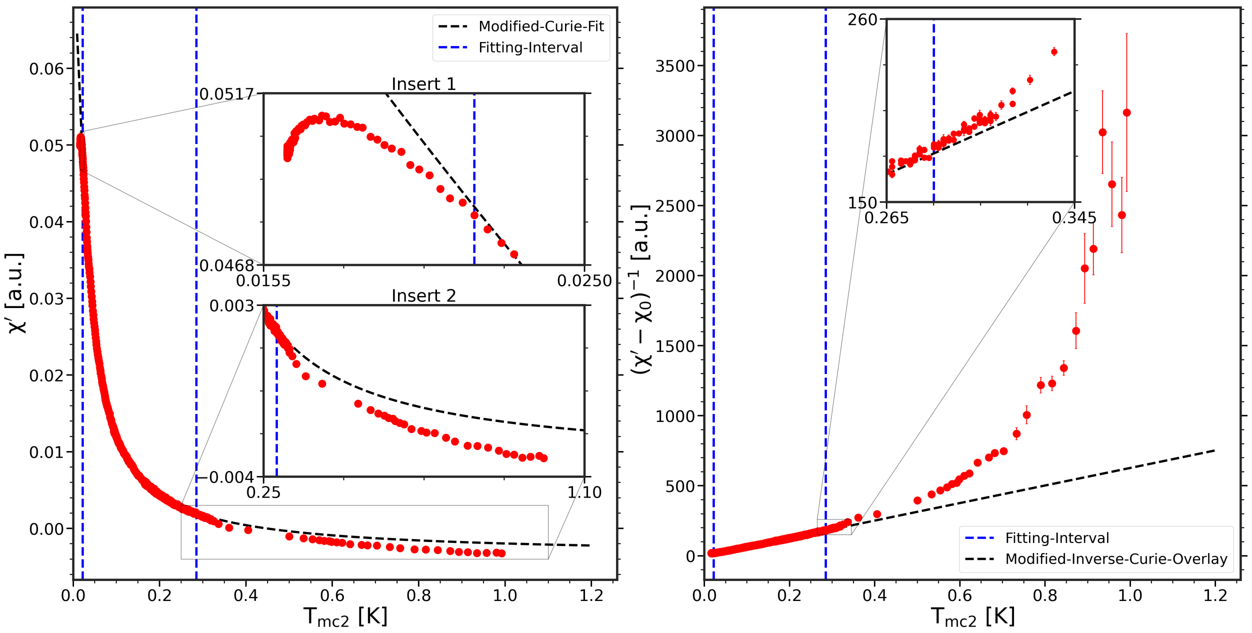

Figure 42: **Left**: The in-phase component (χ') vs T_{mc2} with a modified Curie fit (black dashed line) applied in accordance to Eq. (93). Insert 1 shows one end of the fitting interval (blue lines). Insert 2 shows the other end of the fitting interval ($\sim 0.285\,\mathrm{K}$) the data points begin to deviate increasingly as temperature increases. **Right**: The reciprocal in-phase component with χ_0 subtracted $(\chi' - \chi_0)^{-1}$ vs T_{mc2} to highlight the deviation from the fit-overlay. The insert shows the beginning of the deviation.

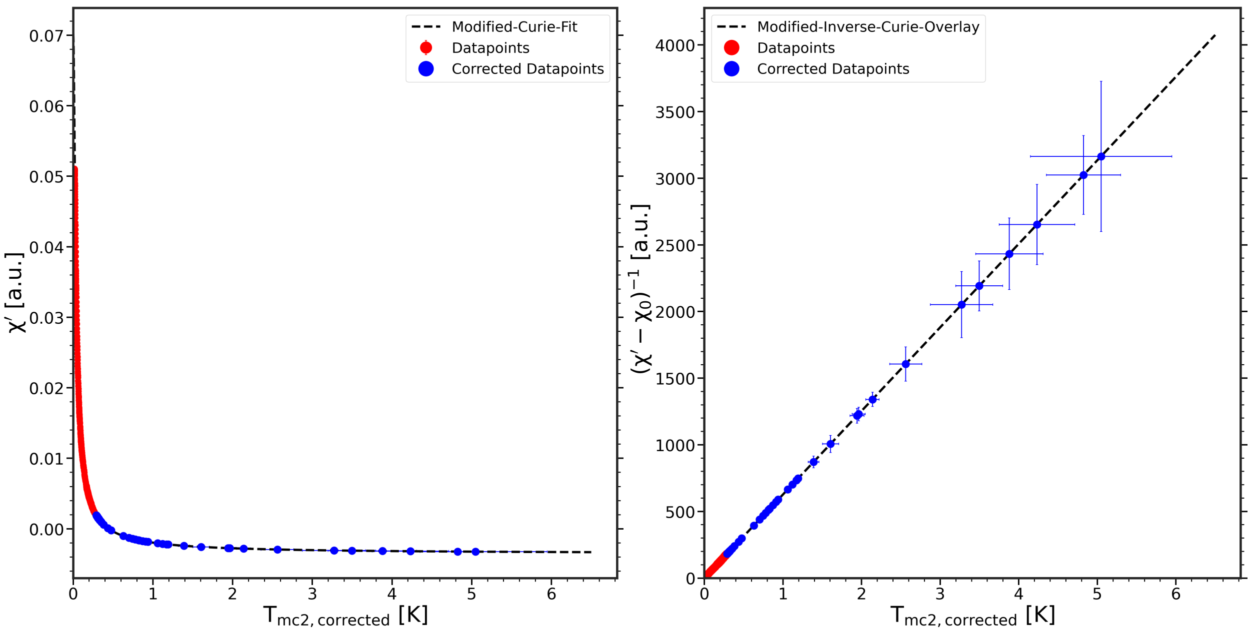

Figure 43: The AC susceptibility as a function of $T_{\mathrm{mc2,corrected}}$ with the original data points and the corrected data points using Eq. (96). **Left**: The in-phase component (χ'). **Right**: The reciprocal in-phase component $(\chi' - \chi_0)^{-1}$.

Moving forward, Fig. 44 shows $T_{\mathrm{mc2,corrected}}$ vs T_{mc2} where the blue points remain the corrected data points. The following fit function:

$$T_{\mathrm{mc2,corrected}}(T_{\mathrm{mc2}}) = aT_{\mathrm{mc2}}^5 + bT_{\mathrm{mc2}}^4 + cT_{\mathrm{mc2}}^3 + dT_{\mathrm{mc2}}^2 + eT_{\mathrm{mc2}} \tag{98}$$

was found to be the best candidate to describe the relation between $T_{\mathrm{mc2,corrected}}$ and T_{mc2} in the relevant temperature regime and it yields the following fit parameters: $a = 7.75(19)\,\mathrm{K}^{-4}$, $b = 0.172(6)\,\mathrm{K}^{-3}$, $c = -9.06(14)\,\mathrm{K}^{-2}$, $d = 6.37(8)\,\mathrm{K}^{-1}$ and $e = -0.81(3)$. Do note that the fit function does not describe the temperature regime where the thermometer T_{mc2} is reliable due to the fact that the transition from the regime of deviation (blue points) to the accurate regime (red points) does not have a continuous slope as shown in the insert of Fig. 44.

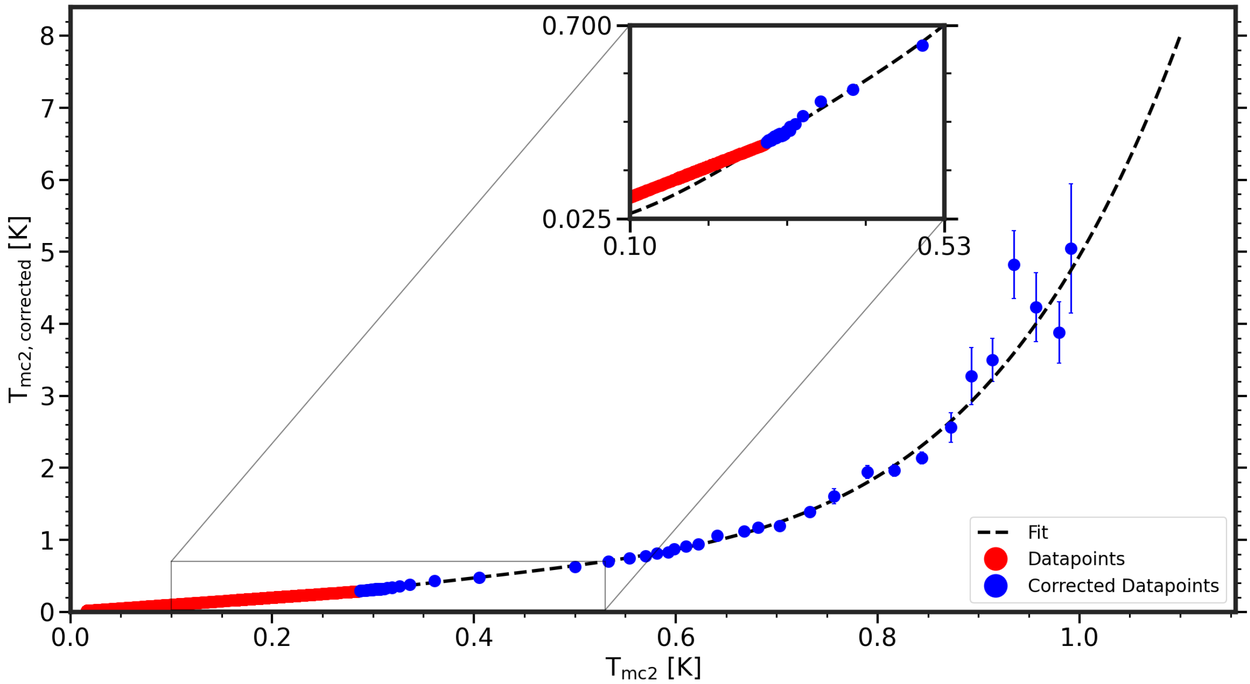

Figure 44: The corrected mixing chamber temperature ($T_{\mathrm{mc2,corrected}}$) vs T_{mc2} along with the fit function from Eq. (98)). The insert shows that the fit function does not describe the temperature regime where the T_{mc2} is reliable. The fit yields a p-value of $\sim 6e-7$.

6 The AC & DC Susceptibility of Herbertsmithite

Herbertsmithite ($ZnCu_3(OH)_6Cl_2$) is one of most promising candidates of hosting the ground state of a true quantum spin liquid due to its perfect kagomé layers of frustrated spin-$\frac{1}{2}$ Cu^{2+} ions separated by diamagnetic Zn^{2+} ions. Up to this date, it remains a widely studied material and displays experimental signatures of a quantum spin liquid at low temperatures since no magnetic order or spin freezing has been witnessed down to approximately 50 mK [13, 14, 68]. In order to investigate this material ourselves, low temperature ($\sim$ 0.03-6 K) AC susceptibility measurements for various excitation frequencies and DC fields have been conducted on a powder sample of herbertsmithite. In addition, high temperature (2-350 K) DC susceptibility measurements have been conducted by E. Y. Leander (PhD student in physics at NBI) at EPFL in Lausanne. The sample has been synthesized by M. S. Pedersen (PhD student in chemistry at SDU).

6.1 Herbertsmithite

Herbertsmithite belongs to the paratacamite family ($Zn_xCu_{4-x}(OH)_6Cl_2$) with the base material (x = 0) being of the formula $Cu_4(OH)_6Cl_2$ which exists in four polymorphs referred to as botallackite, atacamite, clinoatacamite, and claringbullite. These show antiferromagnetic long-range order at approximately 7.2 K, 9 K, 6.5 K, and 17 K, respectively. However, clinoatacamte remains the most stable polymorph and is the parent compound which leads to herbertsmithite [13, 15]. Besides having a Néel ordering temperature of 6.5 K, a transition is observed at 18 K which presumably is a valence bond solid state. This is shown in the proposed phase diagram in Fig. 47 (right) [13, 15]. It contains three different crystallographic copper sites, referred to Cu1, Cu2 and Cu3 in Fig. 45 (right), where Cu1 and Cu2, produce distorted kagomé layers and are both associated with octahedra consisting of $Cu(OH)_4Cl_2$. The remaining copper site (Cu3) takes part in octahedra of $Cu(OH)_6$ and is located in a distorted triangular layer, which connects the distorted kagomé layers and gives rise to an ABC stacking of these [15]. The crystal structure of clinoatacamite is shown in Fig. 45 (left) along the c-axis, where the the blue, cyan and teal colored atoms represent Cu1, Cu2, and Cu3, respectively. As seen in Fig. 45 (left), Cu1 and Cu2 span the corner sharing triangles giving rise to distorted kagomé layers, and Cu3 remains the bridge between these, which, in addition, is the placeholder for the Zn ion in the case of herbertsmithite [15].

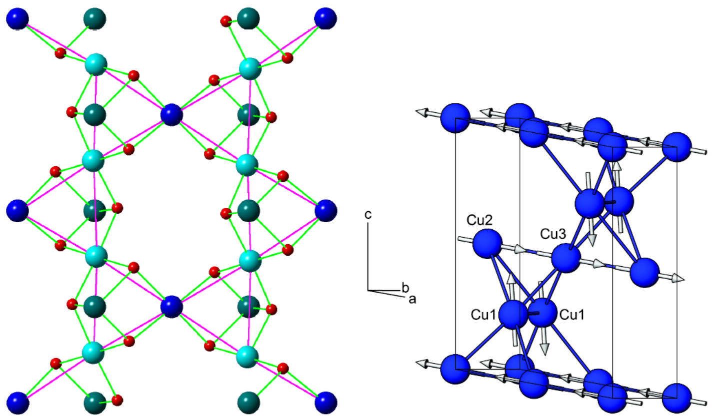

Figure 45: Left: Crystal structure of clinoatacamite along the c-axis. The large atoms correspond to the copper atoms, where the blue, cyan and teal atoms represent Cu1, Cu2, and Cu3 from the proposed magnetic structure in Fig. 45 (right). The Cu3 atom remains the placeholder for the Zn-ion site in herbertsmithite. **Right**: Proposed magnetic structure showing a monoclinic crystal structure. From [15].

As the doping percentage of the Zn ions increases, the structure begins to alter. When the doping exceeds approximately x = 0.33, the monoclinic (P21/n) structure as seen in Fig. 45 (right) transitions to a rhombohedral ($\mathrm{R\bar{3}m}$) structure containing undistorted kagomé layers in the a-b plane [13, 15]. At this point, a partial ordering still occurs at approximately the same temperature ($\sim 5\,\mathrm{K}$). As the doping percentage of Zn^{2+} increases further, the magnetic bridge between the kagomé layers is suppressed since more of the Cu^{2+} ions corresponding to the Cu3, shown in Fig. 45, is replaced by the Zn ions [13, 15]. At $\mathrm{x} \approx 0.6$ the partial ordering begins to disappear. The proposed phase diagram in Fig. 47 (right) suggests a spin glass state for $x > 0.6$ and the RVB state as $x \to 1$. Reference [69] have seen signs of the spin glass state at $x = 0.66$, but above this percentage nothing has been observed experimentally [13, 15].

The final structure of pure herbertsmithite ($x = 1$) is shown in Fig. 47 (left), where the top lattice structure shows the undistorted kagomé configuration viewed along the c-axis, which gives rise to the large frustration. Cu^{2+} occupies the sites in the kagomé layers and is the main contribution to the magnetic properties. Such ions possess an electron configuration of $[\mathrm{Ar}]3\mathrm{d}^9$, yielding 1 unpaired electron ($S = \frac{1}{2}$ & $L = 2$) in the outer shell resulting in a ground state term of $^2\mathrm{D}_{\frac{5}{2}}$ ($\boldsymbol{J} = \frac{5}{2}$) [7]. However, due to orbital quenching the angular moment becomes zero ($L = 0$) which leads to $J = S = \frac{1}{2}$. The lattice structure in Fig. 47 (bottom left) shows the ABC stacking of the layers viewed along the [110] direction, which are well separated by the Zn^{2+} ions. Zn^{2+} has an electron configuration of $[\mathrm{Ar}]3\mathrm{d}^{10}$ showing a filled outer shell ($S = 0$ & $L = 0$) and, therefore, has a ground state term of $^1\mathrm{D}_0$ ($\boldsymbol{J} = 0$). Given Zn^{2+} has a filled outer shell it behaves diamagnetically, in accordance to the Larmor diamagnetism presented in Section 2.3.1, causing this contribution to be both small and temperature-independent.

Given the symmetry in the structure, there is believed to be a single nearest-neighbour superexchange interaction between the frustrated Cu^{2+} ions which are separated by $\sim 3.414\,\text{Å}$ in the kagomé plane as shown in Fig. 46. The exchange parameter ($\mathcal{J}$) is illustrated with a black line between the triangular arrangement of 3 Cu^{2+} ions. The superexchange is mediated via the oxygen atoms with the $d_{x^2-y^2}$ orbitals from the Cu^{2+} ions symmetrically arranged along the threefold axis as shown in the insert of Fig. 46 [4, 70].

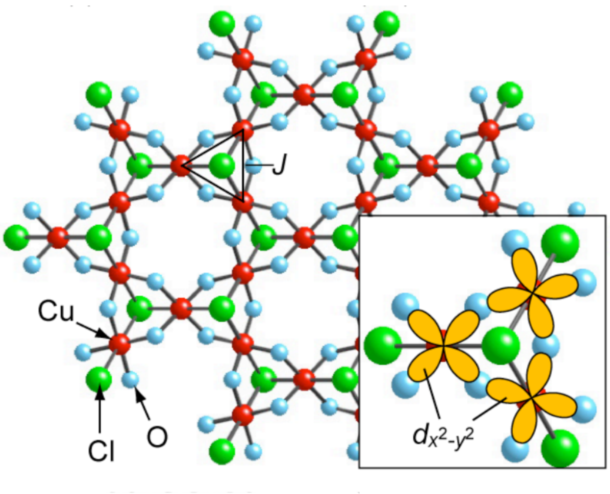

Figure 46: The crystal structure of herbertsmithite with the superexchange interaction shown with Cu being the red atoms, Cl being the green atoms and oxygen being the cyan colored atoms. The Zn atoms are not shown. **Insert**: A zoom-in of the triangular arrangement of the Cu ions, showing the $d_{x^2-y^2}$ orbitals overlapping with the oxygen atoms giving rise to the superexchange. From [70]

Magnetic susceptibility measurements show a deviation from a true Curie Weiss to a Curie Weiss-like behaviour at $\sim 200\,\mathrm{K}$. And by fitting a Curie Weiss relation above a temperature of $\sim 200\,\mathrm{K}$, the Curie Weiss temperature for herbertsmithite is estimated to take a variety of values. References [4, 71] (same author for both) report $\theta \sim -300\,\mathrm{K}$ which – according to the Refs. [4, 71] – corresponds to an antiferromagnetic superexchange of $\mathcal{J} \sim 17\,\mathrm{meV}$ using a series expansion correction for the kagomé lattice. Reference [70] reports a Curie Weiss temperature of $\theta \sim -241\,\mathrm{K}$, although they estimate a superexchange of $\mathcal{J} \sim 17\,\mathrm{meV}$ using a high expansion fit. To me, this indicates that Refs. [4, 71] and [70] determine the superexchange interaction energy differently. Obtaining a similar superexchange interaction while estimating a difference in $\sim 60\,\mathrm{K}$ in terms of the Curie Weiss temperature seems odd. Tabular values from Ref. [6] and [5] report $\theta \sim -314\,\mathrm{K}$ and $\theta \sim -241\,\mathrm{K}$, respectively. Anyhow, these susceptibility measurements share the feature of revealing no long-range magnetic order or spin freezing down to $\sim 50\,\mathrm{mK}$, showing a large Curie tail at low temperatures and for some studies observe a sudden upturn in the susceptibility at low temperatures [3]. It has been recognized that Dzyaloshinsky-Moriya (DM) interactions (anisotropic exchange interactions) may yield a sudden deviation [3]. However, invoking this interaction as an explanation alone would require a too large DM-interaction in magnitude which would presumably induce some ordering [13]. The large Curie tail and even the sudden upturn in the Curie tail at low temperatures are believed to be governed by the presence of magnetic impurities [3, 71]. And with that in mind, herbertmithite is prone to magnetic defects including: a kagomé site may be occupied by a Zn ion or a Cu ion may occupy an interlayer Zn-site. The former defect is believed to induce a dimer freezing in the two adjacent triangles, and, further, induce a staggered magnetization on nearby sites [3, 13, 15]. The latter defect is said to be highly critical for the proposed quantum spin liquid case as the sole Cu ion is believed to cause a weak ferromagnetic interaction between the kagomé layers. This defect is presumably saturated easily by small applied fields [3, 13, 14].

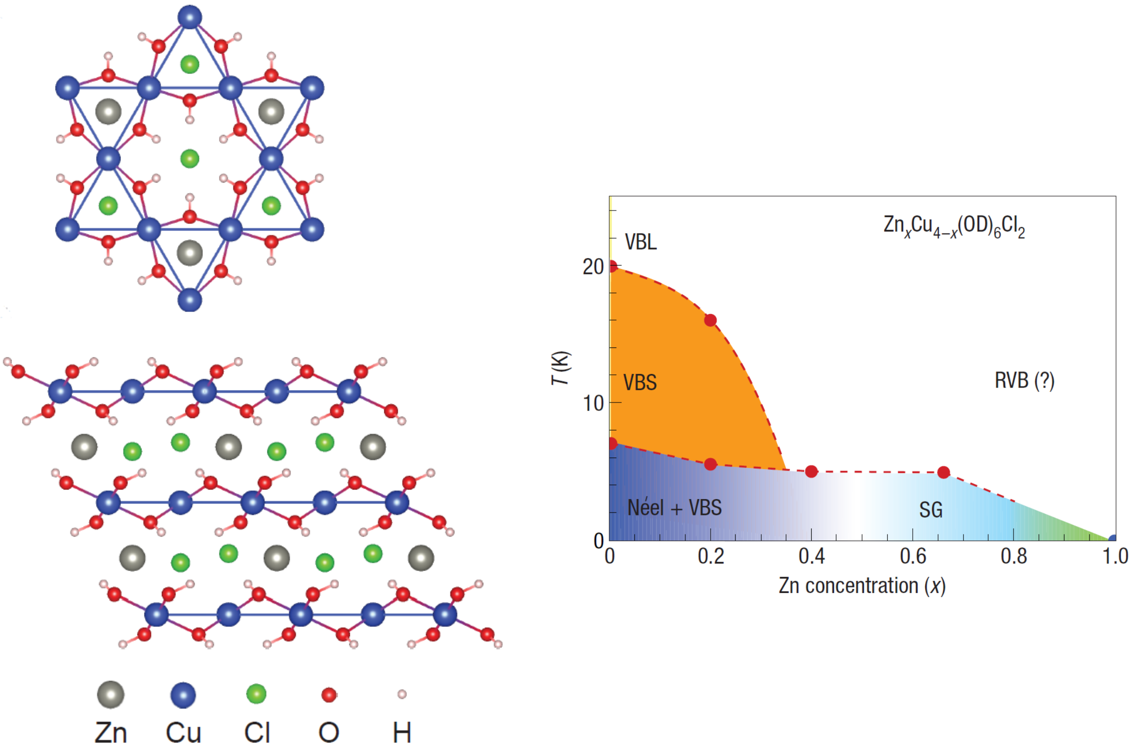

Figure 47: **Left**: Crystal structure of herbertsmithite **Top**: Structure viewed along the c-axis showing the kagomé arrangement. **Bottom**: Structure viewed along the [110] direction, showing the ABC stacking of the kagomé layers. From [14]. **Right**: Proposed phase diagram by the Ref. [69] for the Zn-paratacamite, where 'Neel' represents the antiferromagnetic long range order, 'VBS' denotes a valence bond solid phase, 'VBL' is a valence bond liquid phase, 'SG' indicates a spin glass phase and 'RVB' is the quantum spin liquid phase. From [15, 69].

6.2 High Temperature DC Molar Susceptibility Measurements

The powder sample was synthesized using deuterium (^{2}H) making it suited for neutron scattering. Based on Nuclear Magnetic Resonance (NMR) measurements conducted by M. S. Pedersen, the sample appears to be of minimal defects and the doping level of Zn ions is determined to be $x = 0.98$ - 1. However, some uncertainty remains regarding the precise doping level and the specific type of defect. The magnetic molar susceptibility as a function of temperature is shown in Fig. 48 (left), which reveals a Curie Weiss-like behaviour by increasing as temperature decreases. The inverse magnetic molar susceptibility as a function of temperature is shown in Fig. 48 (right), which additionally reveals a linear behaviour in the high temperature regime ($\geq$ 200 K). It begins to slowly deviate around $\sim$ 200 K at the point in temperature where the nearest-neighbour interaction begins to be of significance compared to the thermal fluctuations, meaning that the frustration begins take an appearance. The measured data reveal no magnetic ordering down to the lowest measured temperature (2 K). The uncertainties remain quite large and are not in the slightest a representation of the fluctuations of the data points. I do not know how these uncertainties are determined, but, they have been overestimated. This becomes quite noticeable in Fig. 48 (right), where the uncertainty $\sigma_{\chi^{-1}}$ relates to σ_χ by:

$$\sigma_{\chi^{-1}} = \frac{1}{\chi^2}\sigma_\chi. \tag{99}$$

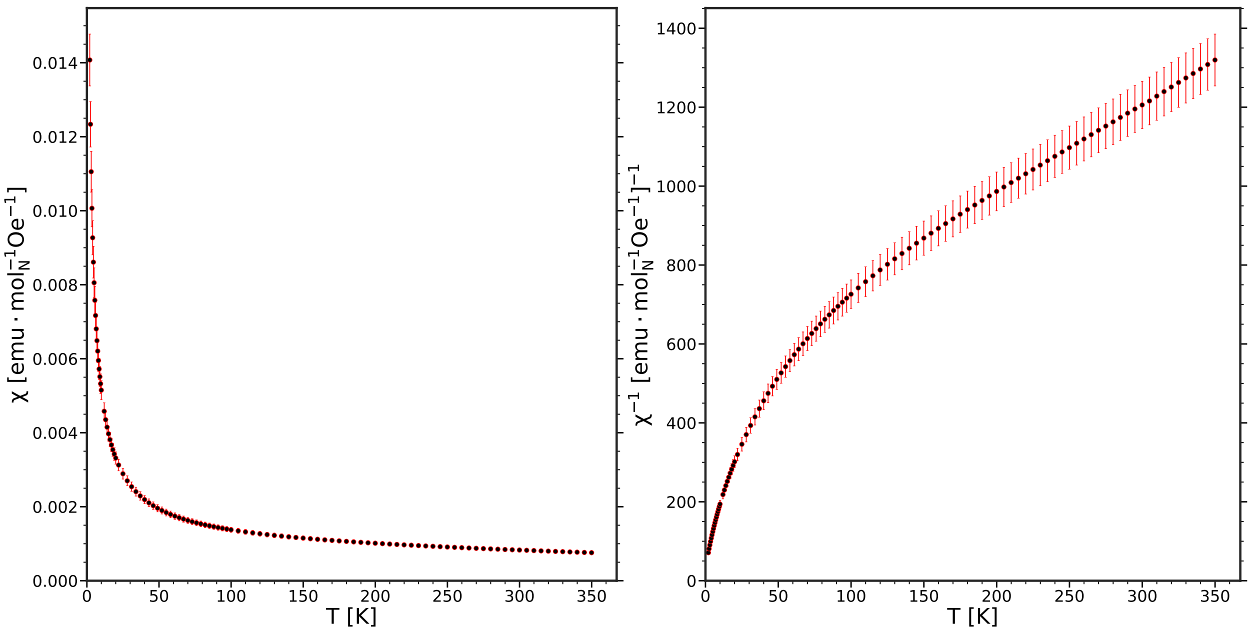

Figure 48: Left: DC molar susceptibility as a function of temperature. **Right**: Inverse DC molar susceptibility as a function of temperature. Measurements conducted by E. Y. Leander at EPFL in Lausanne.

Moving on, Fig. 49 shows the inverse susceptibility with 3 different fits applied above 200 K. Fit 1 is an inverse Curie-Weiss fit with a background term χ_0 which takes the form:

$$\chi^{-1} = \frac{T - \theta_{\mathrm{CW}}}{C + \chi_0(T - \theta_{\mathrm{CW}})}, \tag{100}$$

with the estimated fit parameters being shown in Table 6 (row 2). Fit 2 takes the same form as Eq. (100), however, where the Curie Weiss temperature fit parameter (θ_{CW}) has been fixed to $\theta_{\mathrm{CW}} = 300\,\mathrm{K}$ to match [4, 71] and show the behaviour of the background term (χ_0). Fit 3 remains a traditional inverse Curie Weiss with $\chi_0 = 0$.

Visually, all the fits appear reasonable, as seen in Fig. 49 and the good p values reported in Table 6 (column 5) would suggest a good fit quality. However, such a p-values are indicative of large uncertainties, which indeed is the case.

The overestimated uncertainties visualized in Fig. 48 (right) yield overestimated fit parameter uncertainties. The uncertainties for fit 1 are, however, significantly larger compared to fit 2 and fit 3 (see Table 6). By applying fit 2, one may notice that the uncertainty on the background term goes down by a factor of 6 and, further, by applying fit 3, it is shown that the uncertainty on θ_{CW} decreases by approximately the same factor. This would suggest that the fit parameters are correlated in fit 1, which the off-diagonal terms in the covariance matrix do show. This might be an indication that the trend is indeed linear with only a tiny background term (χ_0), if any, since fitting a linear behavior with 3 fit parameters never goes well.

If one considers the distribution of residuals across the fitting interval shown in Fig. 50, one may notice that fit 3 remains centered around zero, whereas the two remaining fits (fit 1 & fit 2) show a poor centering – they seem biased. Thus, eliminating the background term (χ_0) in case of fit 3 yields the most promising fit for the given temperature interval. The estimated Curie Weiss temperature ($\theta_{\mathrm{CW}} = -248(56)\,\mathrm{K}$) from fit 3, lies close to Ref. [70] and the tabular value from Ref. [5] who report $\theta = -241\,\mathrm{K}$.

In accordance with Ref. [25], one obtains an effective moment of $\mu_{\mathrm{eff}} = \sqrt{8C}\mu_{\mathrm{B}} = 1.91(10)\mu_{\mathrm{B}}$ in the case of cgs units, which using $\mu_{\mathrm{cal}} = g_J\sqrt{J(J+1)}\mu_{\mathrm{B}}$ yields $g = 2.20(12)$. This value, in addition, lies close to Ref. [70]. However, at the end of the day, the uncertainties are quite large and the estimation of the Curie Weiss temperature appears to be sensitive to the method of fitting. References [4, 70, 71] do not report whether they utilized a background term (χ_0) in their fitting. Based on these estimated quantities, it remains difficult to conclude rather our sample differs from the sample of Refs. [4, 70, 71]. A common feature, which can be concluded with certainty is the absence of long-range magnetic order down to 2 K.

Fit #	C [emu $\cdot$ K $\cdot$ $\mathrm{mol}_\mathrm{N}^{-1}\mathrm{Oe}^{-1}$]	χ_0 [emu $\cdot$ $\mathrm{mol}_\mathrm{N}^{-1}\mathrm{Oe}^{-1}$]	θ_CW [K]	p-value
Fit 1	0.5(7)	$-0.05(60) \times 10^{-3}$	−275(387)	1
Fit 2	0.55(6)	$-0.09(10) \times 10^{-3}$	−300	1
Fit 3	0.45(5)	0	−248(57)	1

Table 6: Table of estimated and fixed parameters for the fits shown in Fig. 49.

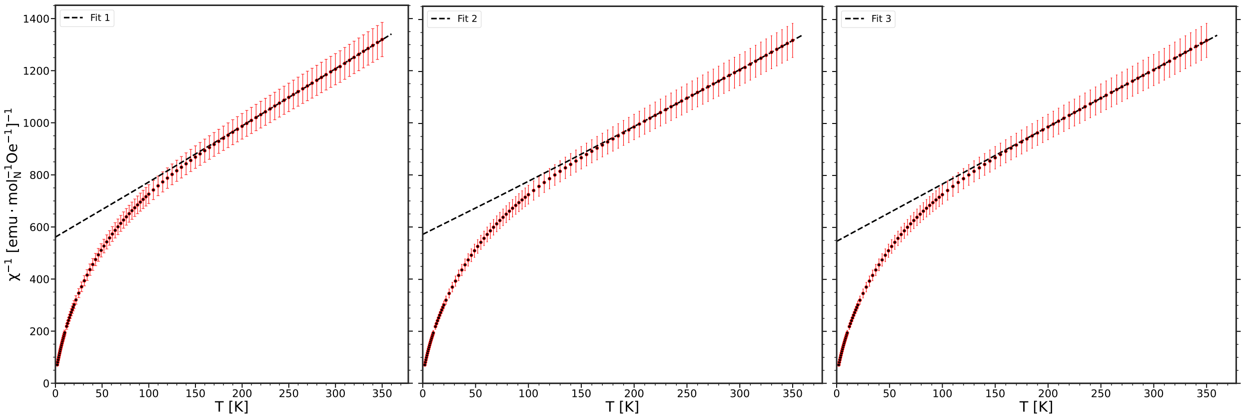

Figure 49: Inverse DC molar susceptibility as a function of temperature along with inverse Curie Weiss fits applied above 200 K. **Left**: Fit 1 ($\chi^{-1} = \frac{T-\theta}{C+\chi_0(T-\theta_{CW})}$) yielding $C = 0.5(7)\,\mathrm{emu} \cdot \mathrm{K} \cdot \mathrm{mol}_\mathrm{N}^{-1}\mathrm{Oe}^{-1}$, $\theta = -280(387)\,\mathrm{K}$ and $\chi_0 = 0.05(60) \times 10^{-3}\,\mathrm{emu} \cdot \mathrm{mol}_\mathrm{N}^{-1}\mathrm{Oe}^{-1}$. **Middle**: Fit 2 ($\chi^{-1} = \frac{T+300\,\mathrm{K}}{C+\chi_0(T+300\,\mathrm{K})}$) yielding $C = 0.55(60)\,\mathrm{emu} \cdot \mathrm{K} \cdot \mathrm{mol}_\mathrm{N}^{-1}\mathrm{Oe}^{-1}$ and $\chi_0 = -0.09(10) \times 10^{-3}\,\mathrm{emu} \cdot \mathrm{mol}_\mathrm{N}^{-1}\mathrm{Oe}^{-1}$. **Right**: Fit 3 ($\chi^{-1} = \frac{T-\theta}{C}$) yielding $C = 0.45(5)\,\mathrm{emu} \cdot \mathrm{K} \cdot \mathrm{mol}_\mathrm{N}^{-1}\mathrm{Oe}^{-1}$ and $\theta = -248(57)\,\mathrm{K}$.

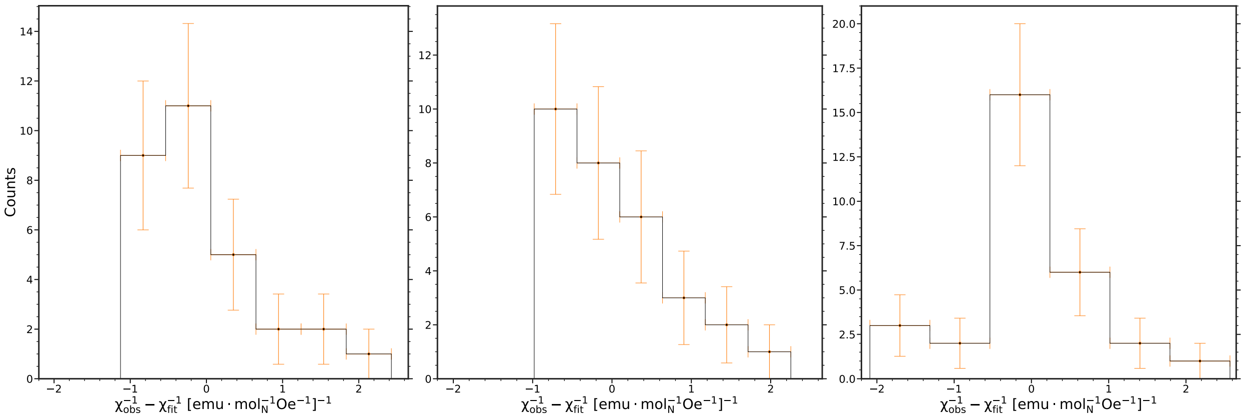

Figure 50: Distribution of residuals for temperatures above 200 K (30 data points) between the data and the fits from Fig. 49. **Left**: Fit 1. **Middle**: Fit 2. **Right**: Fit 3.

6.3 The Preparation and The Positioning for AC Susceptibility Measurements

A portion of the herbertsmithite powder (108.6 mg) was cast in an epoxy (Stycast 1266 Epoxy) with the help of E. Y. Leander. Stycast is commonly used to encapsulate powder samples for cryogenic experiments and further recommended by Ivica Zivkovic [55, 72]. In order to form the mixture of stycast such that it would be suitable for our equipment, a plate of the material teflon was cut, and holes matching the dimensions of the sample space were drilled by the NBI Mechanical and Electronic Workshop. The mixture was poured into one of the matching holes and 4 insulating copper wires of 200 micron diameter were fastened along the sides of the hole. The mixture would cure over a span of 24 hours. Unfortunately, a copper wire broke after the mixture was cured, leaving 3 copper wires serving as thermalization. The final result of the procedure is shown in Fig. 66 (right) in Appendix B. It should be noted that one cannot be certain of the mass of the herbertsmithite powder encapsulated in the stycast, due to the fact that some remains of the mixture were left. Therefore, it is without doubt less than the initial mass of 108.6 mg.

The encapsulated sample was positioned in one of the detection coils. Further, the insulating copper wires were fastened to the cold finger ensuring a thermal link, similar to the procedure of titanium and CMN mentioned in Section 4 and 5.

6.4 Sampling of Data

The AC susceptibility measurements were performed using configuration 1 and 2 (see Fig. 19). The measurements with configuration 1 utilized the same data sampling script which was previously used for the CMN sample (Section 5).

The measurements conducted with configuration 2 utilized a similar script, however, it was slightly modified, such that for each temperature measurement it would report the average of 20 measurements of the voltage – each separated by 0.6 seconds. The purpose of this was to obtain more statistics and for the outcome to be less noisy as herbertsmithite does produce a small signal compared to titanium and CMN, causing noise to play a larger role.

6.5 Overview

Section 6.7 contains a temperature-dependent AC susceptibility measurement while heating up from base temperature. During this measurement it was necessary to retrieve most of the helium in the process in order to reach the temperature of $\sim 0.6\,\mathrm{K}$.

Section 6.9 contains temperature-dependent AC susceptibility measurements for a single frequency while cooling from a temperature of $\sim 4\,\mathrm{K}$ to base temperature and heating from base temperature to $\sim 0.230\,\mathrm{K}$ for reproducible purposes. Further, Section 6.9 contains AC susceptibility measurements as a function of temperature for various excitation frequencies taken while heating. Finally, it contains AC susceptibility measurements as a function of temperature for various strengths of DC field.

The temperature control was managed in a similar way as the CMN sample, however, it was at a slightly faster pace, due to the CMN measurement being time consuming.

The electrical circuit shown in Fig. 20 (right) was utilized for all the AC susceptibility measurements regarding herbertsmithite. The change of signal generator – going from the circuit shown in Fig. 20 (left) to the circuit shown in Fig. 20 (right) – potentially modifies the phase in the circuit slightly, which will be discussed in the upcoming sections.

The measurement in Section 6.7 utilized configuration 1 shown in Fig. 19 (left), however, the metal screws were replaced with nylon screws for the purpose of reducing the heat. The measurements in Section 6.9 utilized configuration 2 shown in Fig. 19 (right), such that the applied DC field would be parallel to the AC field.

6.6 Conversion from Raw Data to Susceptibility

For both configurations (1 & 2), the raw data was measured without any phase adjustment. These are shown in Appendix K. The measured voltage drop was initially rotated with the phase reported in Table 2 (heating) for the utilized excitation frequency in order to separate the components. Subsequently, the voltage was converted to susceptibility using Eq. (85) with the calibration constant (C_S) from Table 3 (heating). However, as further discussed in Section 6.7, the out-of-phase component (χ'') gives an indication that the voltage has not been separated properly using the previous phase. Therefore, the phase Θ_{res} obtained by measuring the excitation field using a lock-in amplifier was utilized to separate the voltage components in order to compare. This was previously done in Section 5.6.1 for CMN. The effect of demagnetization has been neglected for simplification purposes, which is justified by the fact that herbertsmithite has a significantly smaller susceptibility than CMN from Section 5 at for which it was also ignored.

6.7 AC Susceptibility Measurement (Configuration 1)

The AC susceptibility for herbertsmithite as a function of the corrected cold finger temperature ($T_{\text{mc2,corrected}}$) is shown in Fig. 51 for an excitation frequency of $\nu = 982\,\text{Hz}$ and a field of $H_{\text{AC}} \approx 17\,\text{Am}^{-1}$. The cold finger temperature for $T_{\text{mc2}} > 0.285\,\text{K}$ has been corrected using the fit model from Eq. (98) from Section 5.7. The raw data of the measurement and χ' vs T_{mc2} are shown in Fig 95 and 96, respectively in Appendix K. The in-phase component (χ') in Fig. 51 (left) shows a Curie Weiss-like behaviour in the high end of the temperature range, such that the susceptibility increases with decreasing temperature. At $T_{\text{mc2,corrected}} \approx 0.116\,\text{K}$ it begins to deviate from the Curie Weiss-like behaviour and become more linear. At approximately $T_{\text{mc2,corrected}} \approx 0.05\,\text{K}$ it appears to show a peak and decrease slightly as temperature decreases. Furthermore, the insert shows a linear trend in the high end of the temperature range, and it begins to bend at $T_{\text{mc2,corrected}} \approx 0.116\,\text{K}$. The out-of-phase component (χ'') shows a negative background which, previously, has been seen in Fig. 39 (Section 5.6.1) for CMN. In addition, it appears significantly more noisy. Therefore, the data shown in Fig. 51 has been binned in terms of temperature, with a binwidth of 2 mK. The temperature has been converted to sample temperature using Eq. (92) and the parameter Δ from Table 4 (row 4 column 4). The final result is shown in Fig. 52 as a function of the binned sample temperature (T_{sample}).

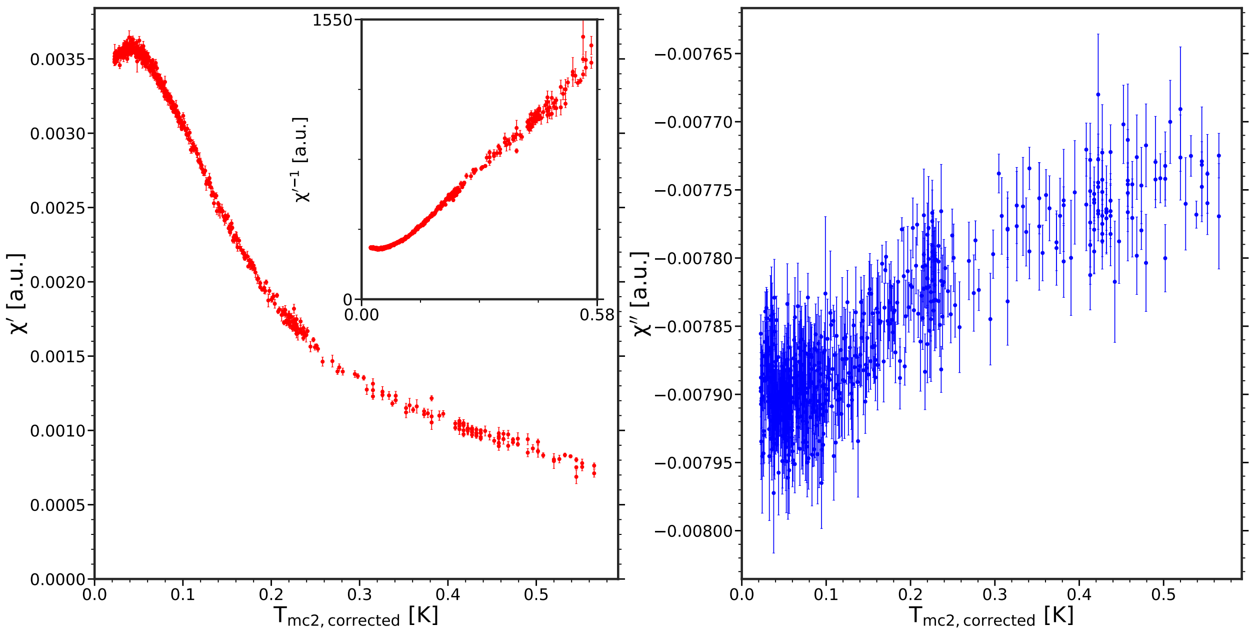

Figure 51: The AC susceptibility of herbertsmithite as a function of $T_{\mathrm{mc2,corrected}}$ where the components have been separated using Θ from Table 2 (heating). The measurement is taken at a frequency of $\nu = 982\,\mathrm{Hz}$ and a field of $H_{\mathrm{AC}} \approx 17\,\mathrm{Am}^{-1}$. **Left**: The in-phase component (χ'). The insert shows ${\chi'}^{-1}$. **Right**: The out-of-phase component (χ'').

The behaviour of the in-phase component (χ') in Fig. 52 (left) remains the same, however, it has become more smooth around the peak if one compares to the data presented in Fig. 51 (left). The temperature of the peak is estimated to $T_{\mathrm{peak}} = 48.8(3)\,\mathrm{mK}$ using a Gaussian fit in an appropriate temperature interval around the peak where T_{peak} corresponds to the centering of the fit. The out-of-phase component (χ'') has become less noisy and, visually, the decreasing behaviour for decreasing temperature is more clear and at low temperatures it seems to form a negative broad peak. The decreasing behaviour across almost the entire temperature regime would indicate that the components have not been separated properly using the phase determined from titanium (see Table 2). Given the in-phase component (χ') behaves somewhat Curie Weiss-like in the high temperature regime one would expect the out-of-phase component (χ'') to remain temperature-independent, as seen in case of CMN (see Section 5.6.1). Therefore, the phase could potentially have been modified, presumably due to the change of the signal generator – going from the circuit in Fig. 20 (left) to the circuit in Fig. 20 (right). Thus, a recalibration of the phase utilizing a new titanium sample is needed in order to obtain the correct phase. This was attempted, however, during the cooldown a leak in the cone-seal of the mixing chamber occurred, meaning helium would enter the IVC and prevent the helium to condense. The leak in the cone-seal is easily repaired by opening the seal and applying vacuum grease, although the entire process is time consuming. However, it is known that the proper phase lies close to $\Theta_{\mathrm{res,HS}}$ determined by measuring the voltage drop across the resistor as seen in Table 5, meaning we are not left completely clueless regarding the phase. A solution for this will be discussed in the upcoming section and will be utilized for the remaining measurements.

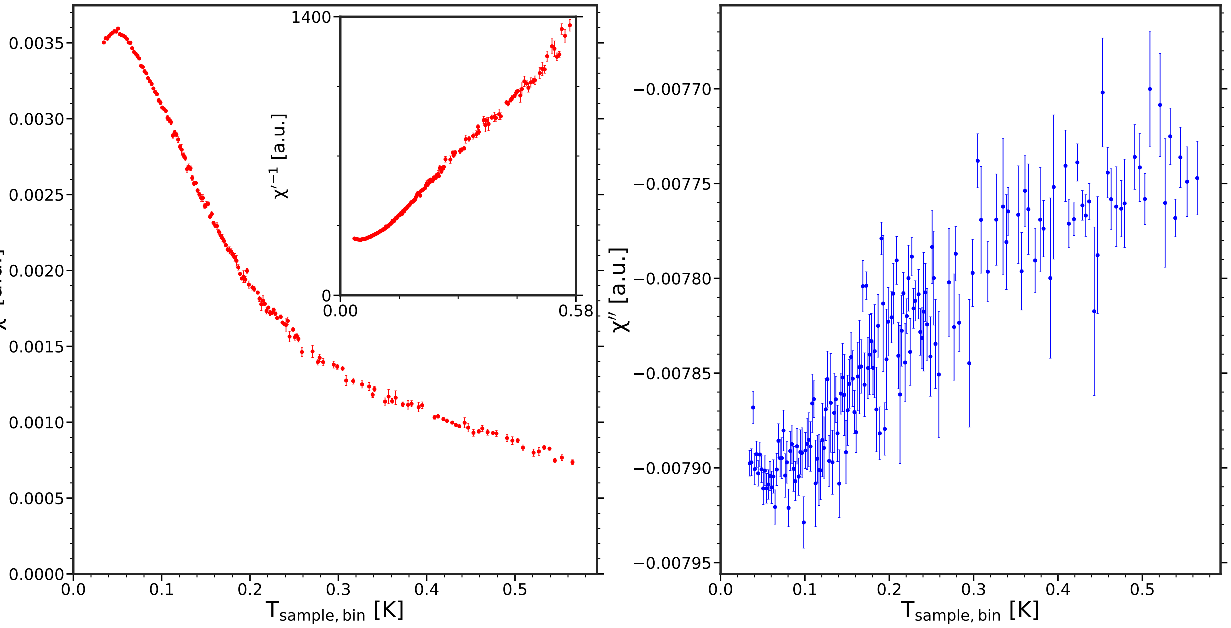

Figure 52: The AC susceptibility of herbertsmithite as a function of $T_{\text{sample,bin}}$ where the components have been separated using Θ from Table 2 (heating). The measurement is taken at a frequency of $\nu = 982\,\text{Hz}$ and a field of $H_{\text{AC}} \approx 17\,\text{Am}^{-1}$. **Left**: The in-phase component (χ'). The insert shows the reciprocal of the in-phase component (χ'^{-1}). **Right**: The out-of-phase component (χ'').

6.8 Readjustment of the Phase

The phase determined by measuring the voltage drop across the resistor for herbertsmithite ($\Theta_{\text{res,HS}}$) is reported in Table 7 (row 1). By comparing this phase ($\Theta_{\text{res,HS}}$) with the phase $\Theta_{\text{res,CMN}}$ reported in Table 4 (row 1), one may notice a difference which would suggest that the phase required to separate the components has changed upon switching the signal generator. However, assuming the difference $\Delta\Theta$ in Table 4 has not changed, it is possible to estimate the new proper phase $\Theta_{\text{new}} = \Theta_{\text{res,HS}} + \Delta\Theta$. The new estimated phase (Θ_{new}) along with $\Theta_{\text{res,HS}}$ and $\Delta\Theta$ are shown in Table 7.

ν [Hz]	333	663	982	1433
$\Theta_{\text{res,HS}}$ [radians]	1.6447815(9)	1.71667044(9)	1.7834691(8)	1.865933(2)
$\Delta\Theta$ [radians]	0.01600(10)	0.02878(9)	0.04026(5)	0.05433(4)
Θ_{new} [radians]	1.66078(10)	1.74545(9)	1.82373(5)	1.92026(4)

Table 7: Table containing the phase obtained by measuring the voltage across the resistor ($\Theta_{\text{res,HS}} = \frac{\pi}{2} + \theta_{\text{res,HS}}$), the phase difference $\Delta\Theta = \Theta - \Theta_{\text{res,CMN}}$ from Table 5 and the new proper phase $\Theta_{\text{new}} = \Theta_{\text{res,HS}} + \Delta\Theta$, assuming the difference has not changed upon replacing the signal generator.

6.8.1 AC Susceptibility Measurement With Readjusted Phase Θ_{new} (Configuration 1)

The AC susceptibility for herbertsmithite as a function of binned sample temperature ($T_{\text{sample,bin}}$) is shown in Fig. 53 where the phase (Θ_{new}) has been utilized to separate the in-phase component (χ') and the out-of-phase component (χ''). The in-phase component (χ') shows the same temperature-dependence by increasing in magnitude as temperature decreases. Further, it shows a peak at the temperature $T_{\text{peak}} = 48.8(3)\,\text{mK}$ estimated using a Gaussian fit around the peak. However, it appears that a temperature-independent background for the in-phase component (χ') might have increased as a consequence of using Θ_{new} instead of Θ if one compares Fig. 53 (left) with Fig. 52 (left).

Further, the increase of a background term is reflected in the increased negative curvature of the reciprocal susceptibility (χ'^{-1}) in the insert of Fig. 53 (left) compared to the insert of Fig. 52 (left). The out-of-phase component (χ'') in Fig. 53 (right) shows a temperature-independent behaviour at the high end of the temperature regime. At $T \approx 0.2\,\mathrm{K}$ the out-of-phase component (χ'') begins to increase as temperature decreases and appears to continue as the temperature approaches the base temperature.

The peak in the in-phase component (χ') resembles a peak one would often associate with a spin freezing (spin glass) or some sort of magnetic ordering. Such phenomena are typically complimented by dissipation processes, reflected by a non-zero out-of-phase component ($\chi'' \neq 0$) at temperatures near and during the transition. The out-of-phase component (χ'') in Fig. 53 does show a sudden change near $T \approx 0.2\,\mathrm{K}$ which could indicate an onset of dissipation processes, which presumably would be related to the peak at $T_{\mathrm{peak}} = 48.8(3)\,\mathrm{mK}$ in the in-phase component (χ').

In case of a spin glass, the mentioned features would posses a frequency-dependence such that the peak and the onset in χ' and χ'', respectively would be shifted towards higher temperatures for increasing frequency (see Fig. 109 (bottom) Appendix L). In addition, there would be a non-zero third harmonic susceptibility (χ_3) associated with the spin freezing as discussed in Section 2.10. Such frequency-dependence is investigated in Section 6.9.2.

However, the peak in the in-phase component (χ') could, in addition, promote the intriguing possibility of the herbertsmithite sample hosting a ground state of a true quantum spin liquid. In such a case, the AFM Heisenberg dimer model or the uniform AFM spin-$\frac{1}{2}$ chain presented in Section 2.6.2 could potentially serve as a simplified picture, meaning that the susceptibility would either go exponentially to zero or approach a finite value as $T \to 0\,\mathrm{K}$ in the gapped or the gapless case, respectively.

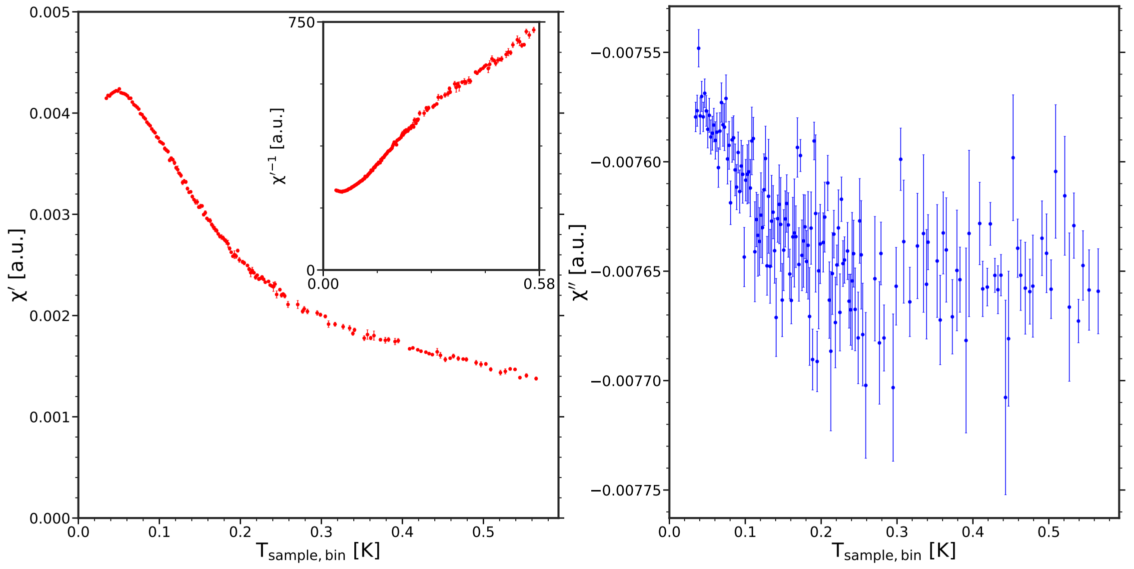

Figure 53: The AC susceptibility for herbertsmithite as a function of $T_{\mathrm{sample,bin}}$ obtained using the phase Θ_{new} from Table 7 (row 3). The measurement is taken at a frequency of $\nu = 982\,\mathrm{Hz}$ and a field of $H_{\mathrm{AC}} \approx 17\,\mathrm{Am}^{-1}$. **Left**: The in-phase component (χ') which shows a peak at the estimated temperature $T_{\mathrm{peak}} = 48.8(3)\,\mathrm{mK}$ estimated using a Gaussian fit. **Insert**: The reciprocal susceptibility (χ'^{-1}). **Right**: The out-of-phase component (χ'') which remains temperature-independent in the high end of the recorded temperature regime, whereas at $T \approx 0.2\,\mathrm{K}$ it begins to increase as temperature decreases.

It is possible to fit a Curie Weiss relation with a background term (χ_0) in a smaller temperature interval and obtain a fit which does appear reasonable. This has been done in Fig. 54 both for the in-phase component (χ') and the reciprocal in-phase component (χ'^{-1}). The insert in both the left and right plot of Fig. 54 highlights the low-temperature regime with the blue dashed line ($T_{\text{sample,bin}} \approx 0.116\,\text{K}$) delimiting the fitting interval. It is clear, visually, that the data begins to deviate from the fit in both cases.

The fit for χ' vs $T_{\text{sample,bin}}$ shown in Fig. 54 (left) yields the following fit parameters: $C = 442(6) \times 10^{-6}\,\text{a.u.}$, $\chi_0 = 0.683(11) \times 10^{-3}\,\text{a.u.}$ and $\theta_{\text{CW}} = -0.0369(18)\,\text{K}$. Whereas the fit for χ'^{-1} vs $T_{\text{sample,bin}}$ shown in Fig. 54 (right) yields the parameters: $C = 442(6) \times 10^{-6}\,\text{a.u.}$, $\chi_0 = 0.685(11) \times 10^{-3}\,\text{a.u.}$ and $\theta_{\text{CW}} = -0.0367(18)\,\text{K}$, which show no statistical difference in the two cases. The two fits show a Curie Weiss temperature (θ_{CW}) which is significantly lower compared to the high temperature regime ($> 200\,\text{K}$) that yields $\theta_{\text{CW}} = -248(57)\,\text{K}$ as seen in Section 6.2. This would indicate that a much weaker antiferromagnetic interaction gives rise to the observed peak.

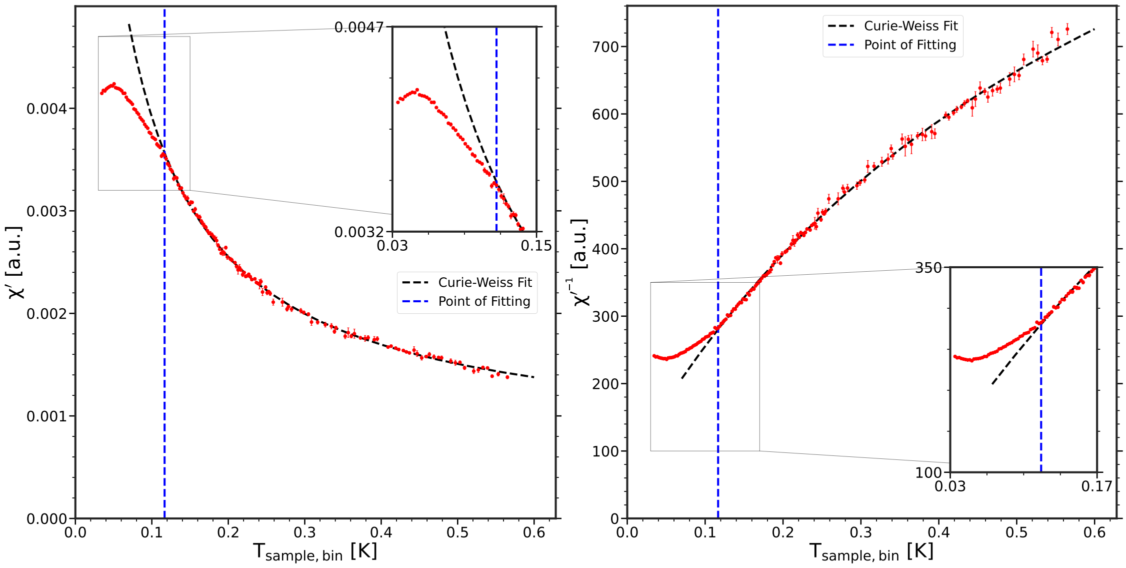

Figure 54: Fitting of (χ') and (χ'^{-1}). The measurement is taken at a frequency of $\nu = 982\,\text{Hz}$ and a field of $H_{\text{AC}} \approx 17\,\text{Am}^{-1}$. **Left**: The in-phase component (χ') vs $T_{\text{sample,bin}}$ with a fit on the form $\chi = \frac{C}{T-\theta_{\text{CW}}} + \chi_0$ applied. **Right**: The reciprocal of the in-phase component (χ'^{-1}) vs $T_{\text{sample,bin}}$ with a fit on the form $\chi^{-1} = \frac{T-\theta_{\text{CW}}}{C+\chi_0(T-\theta_{\text{CW}})}$ applied.

For illustrative purposes, a high-temperature expansion of the the 1-dimensional AFM spin-$\frac{1}{2}$ chain (Bonner-Fisher model [73]) has been applied to the in-phase component (χ') vs $T_{\text{sample,bin}}$. The fit function takes the following form:

$$\chi(T) = \frac{C}{k_{\text{B}}T} \frac{(0.25 + c_1 x + c_2 x^2)}{(1 + c_3 x + c_4 x^2 + c_5 x^3)} + \chi_0 \tag{101}$$

where $x = \frac{|\mathcal{J}|}{k_{\text{B}}T}$ [74–76]. The fit is shown in Fig. 55 and yields the following fit parameters: $C = 187.09340759(9) \times 10^{-30}\,\text{a.u.}$, $\mathcal{J} = 183(3) \times 10^{-24}\,\text{J}$, $c_1 = 7.653354083(4) \times 10^{6}$, $c_2 = 79.17739993(3) \times 10^{3}$, $c_3 = 486.6203854(2) \times 10^{3}$, $c_4 = -1.1409076129(18) \times 10^{3}$, $c_5 = 31.581821676(9)$, and $\chi_0 = 972.58534734(5) \times 10^{-6}\,\text{a.u.}$. The fit does appear promising, and it yields an exchange – in temperature units – of $\frac{\mathcal{J}}{k_B} \approx 13\,\text{K}$. However, due to the fact that this model hardly describes the system of herbertsmithite and it remains a high-temperature expansion, it should be noted that the fit and the estimated parameters do not necessarily yield any information about the physics in herbertsmithite. Further, the fit parameters are quite sensitive towards the initial guesses. However, it serves as an illustrative visualization of how the temperature-dependent susceptibility potentially could behave in case of a gapless QSL.

6.9 AC Susceptibility Measurements (Configuration 2)

The remaining measurements have been conducted using configuration 2 shown in Fig. 19 (right). Figure 56 shows the AC susceptibility as a function of $T_{\text{sample,bin}}$ for two samples: the stycast encapsulating herbertsmithite and pure stycast, where the latter serves as a realization of the background. It should, however, be noted that it is not the "true" background but rather a temperature-dependence of the background. Recall, upon changing the sample, the coil system has to be reattached, causing the coil wires not to be in an identical position for every measurement. This is reflected by a small shift in the measured voltage on the order of ($\sim 1 \times 10^{-7}\,\text{V}$) compared to a previous measuring session.

Anyhow, the measurements in Fig. 56 contain a cooling series conducted while filling the system with helium and a heating series for both samples. In Fig. 56, the measurements for the pure stycast have been shifted by adding a constant term for an easier temperature-dependent comparison with the herbertsmithite measurmeents. The exact value of the χ'_{stycast} is shown in Fig. 57.

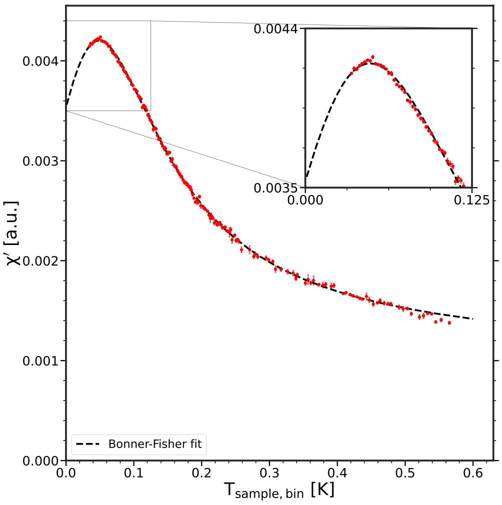

Figure 55: The in-phase component (χ') of herbertsmithite as a function of $T_{\text{sample,bin}}$ at a frequency of $\nu = 982\,\text{Hz}$ and a field of $H_{\text{AC}} \approx 17\,\text{Am}^{-1}$. A Bonner-Fisher high-temperature expansion fit (see Eq. (101)) has been applied. The insert highlights the peak. Measurement taken using configuration 1.

The in-phase component (χ') of herbertsmithite behaves as we have previously seen, by increasing for decreasing temperatures in a Curie Weiss-like manner. It peaks at $T_{\text{peak}} \approx 49\,\text{mK}$ highlighted by the insert. The out-of-phase component (χ'') of herbertsmithite has been plotted in a more narrow temperature interval for visual purposes, however, the full temperature regime is shown in Fig. 99 in Appendix K. Anyhow, χ'' shows a temperature-independent behaviour at high temperatures down to $T \approx 200\,\text{mK}$ at which point it shows an onset and proceed to increase as temperature decreases.

For this configuration, the sign for both the in-phase (χ') and out-of phase (χ'') has changed compared to the measurement of hebertsmithite using configuration 1 (see Fig. 53). This change in sign is believed to be caused by the bottom of the IVC can, which in configuration 2 remains close to one of the detection coils, therefore, causing a voltage imbalance. Given the circumstances, both the in-phase component (χ') and the out-of-phase component (χ'') for the pure stycast show only a tiny temperature-dependence compared to the in-phase component (χ') and the out-of-phase component (χ'') of herbertsmithite, meaning the IVC yields only a minor temperature-dependent contribution, if any. Although, this temperature-dependence, from the measurements of pure stycast, has to be subtracted from the measurements of herbertsmithite. This is done in the upcoming section.

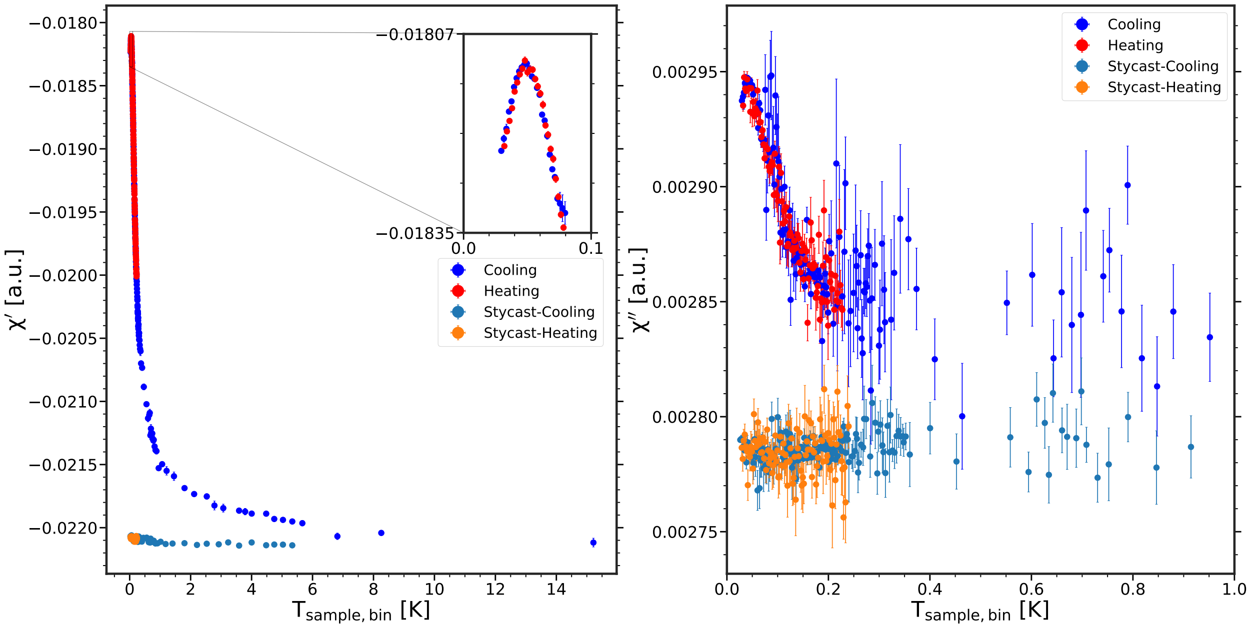

Figure 56: The AC susceptibility for herbertsmithite (blue & red) and pure stycast (cyan & orange) as a function of $T_{\mathrm{sample,bin}}$. The pure stycast measurements have been shifted with a constant term for easier comparison with the herbertsmithite measurements. The measurements are taken at a frequency of $\nu = 982\,\mathrm{Hz}$ and a field of $H_{\mathrm{AC}} \approx 17\,\mathrm{Am}^{-1}$. **Left**: The in-phase component (χ'). The data points at $T > 6\,\mathrm{K}$ is due to the fact that the cooling measurement was initiated at the same time helium was added to the system causing the temperature to rise quite a lot in the beginning. In terms of T_{mc2}, these lie at $T_{\mathrm{mc2}} > 1\,\mathrm{K}$ (see Fig. 98 Appendix K), and small deviations in this range result in a large change in the corrected temperature ($T_{\mathrm{mc2,corrected}}$) (see Fig. 44). **Right**: The out-of-phase component (χ''). The temperature range has been limited to a maximum of $T_{\mathrm{sample,bin}} = 1\,\mathrm{K}$ for visual purposes. The measurement across the entire temperature range may be seen in Fig. 99 in Appendix K.

6.9.1 Subtraction of background

The AC susceptibility for the pure stycast is shown in Fig. 57 as a function of T_{mc2}. The in-phase component (χ'_{stycast}) appears to behave linearly as a function of T_{mc2}, whereas the out-of-phase component ($\chi''_{\mathrm{stycast}}$) shows less of a temperature-dependence. The behaviour of both components have been estimated utilizing a linear fit as shown in Fig. 57 and the fit parameters are shown in Table 8. The estimated fit parameters are statistically the same, for instance the slope (a) between χ'_{stycast} (cooling) and χ'_{stycast} (heating) yield a Z value of $\sim 1.6\sigma$ using Eq. (89) which is not statistically significant [67]. Although, the uncertainties σ_a for χ'_{stycast} (heating) and $\chi''_{\mathrm{stycast}}$ (heating) are quite large, which is presumably due to the fact that there are fewer points. In the case of $\chi''_{\mathrm{stycast}}$ (heating) one could argue that a constant fit function would be a well estimation for describing the trend.

Type	χ'_{stycast} (cooling)	χ'_{stycast} (heating)	$\chi''_{\mathrm{stycast}}$ (cooling)	$\chi''_{\mathrm{stycast}}$ (heating)
a [a.u.]	$-0.075(2) \times 10^{-3}$	$-0.056(12) \times 10^{-3}$	$-0.008(2) \times 10^{-3}$	$0.003(12) \times 10^{-3}$
b [a.u.]	$-25.57011(27) \times 10^{-3}$	$-25.5764(13) \times 10^{-3}$	$2.38838(27) \times 10^{-3}$	$2.3851(13) \times 10^{-3}$

Table 8: Fit parameters obtained from the linear fits ($aT_{\mathrm{mc2}} + b$) shown in Fig. 57.

Thus, the herbertsmithite susceptibility data has been adjusted by subtracting the fit value for the corresponding series from each data point at the same temperature for consistency. Subsequently, the temperature has been converted to $T_{\text{sample,bin}}$ and the final result is shown in Fig. 58, where the temperature has been plotted on a log-scale to emphasize the low-temperature region. The in-phase component (χ') takes positive values after the subtraction and the out-of-phase component (χ'') remains positive, which in both cases is promising. The in-phase component ($\chi' - \chi'_{\text{stycast}}$) has been fitted using a Curie Weiss fit with a background term (χ_0), yielding the following fit parameters: $C = 549(3) \times 10^{-6}\,\text{a.u.}$, $\chi_0 = 3.619(5) \times 10^{-3}\,\text{a.u.}$, and $\theta_{\text{CW}} = -0.0561(9)\,\text{K}$. Fitting $(\chi' - \chi'_{\text{stycast}})^{-1}$ vs $T_{\text{sample,bin}}$ with an inverse Curie Weiss fit yields: $C = 550(3) \times 10^{-6}\,\text{a.u.}$, $\chi_0 = 3.620(5) \times 10^{-3}\,\text{a.u.}$ and $\theta_{\text{CW}} = -0.0561(10)\,\text{K}$, which show no statistical difference given the uncertainties. This deviates from the earlier estimated $\theta_{\text{CW}} = -0.0369(18)\,\text{K}$ (see Section 6.8.1), because of the difference in fitting range. Regardless, it relates a much weaker antiferromagnetic interaction, presumably, associated with the peak in χ'.

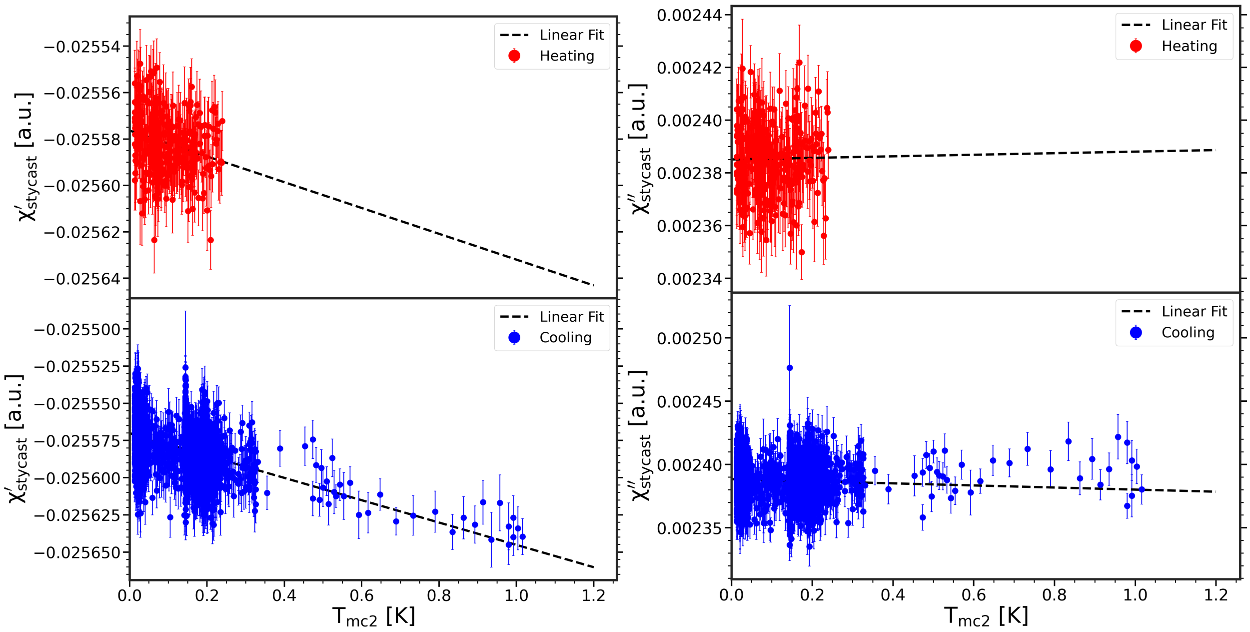

Figure 57: The AC susceptibility of the the pure stycast as a function of T_{mc2} at a frequency of $\nu = 982\,\text{Hz}$ and a field of $H_{\text{AC}} \approx 17\,\text{Am}^{-1}$ while cooling and heating. Linear fits have been applied for all the measurements to estimate the trend. The fit parameters are shown in Table 8. **Left**: The in-phase component (χ'_{stycast}). **Right**: The out-of-phase component (χ''_{stycast}).

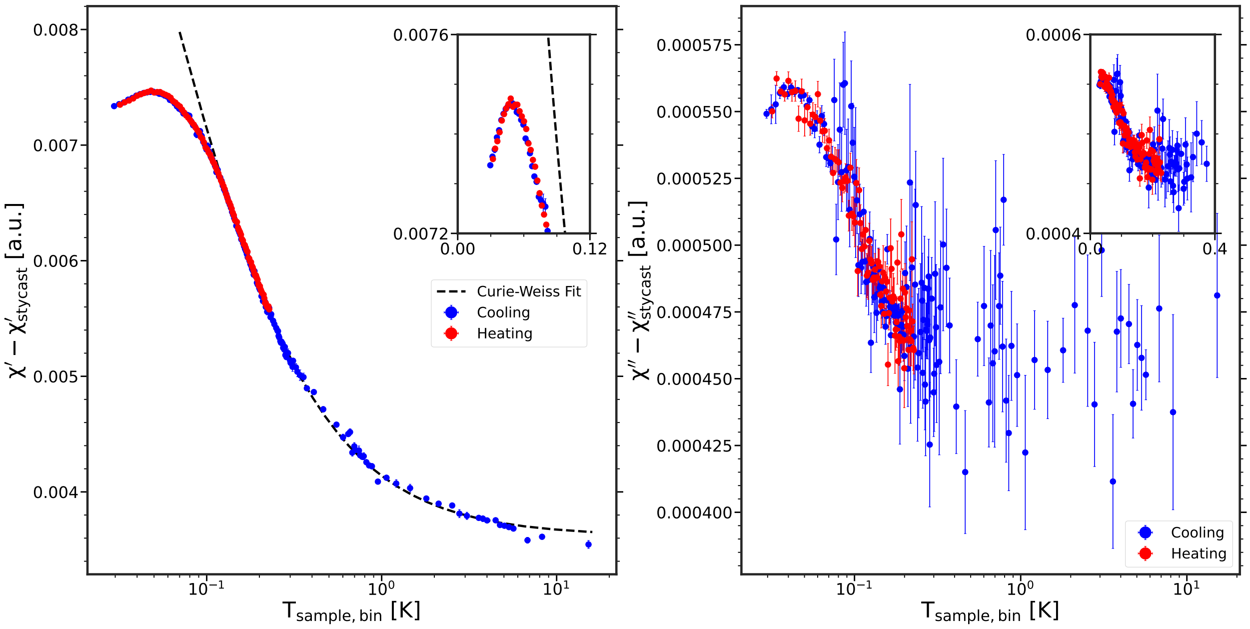

Figure 58: The AC susceptibility of herbertsmithite as a function of $T_{\rm sample,bin}$ after the subtraction the AC susceptibility from pure stycast. The temperature axis is on a log-scale visual purposes. **Left**: The in-phase component ($\chi' - \chi'_{\rm stycast}$) with a Curie Weiss fit ($\chi' = \frac{C}{T-\theta_{\rm CW}} + \chi_0$) applied. The insert highlights the peak on a normal temperature scale. **Right**: The out-of-phase component ($\chi'' - \chi''_{\rm stycast}$). The insert highlights the beginning of an onset on a normal temperature scale.

6.9.2 AC Susceptibility Measurements for Various Frequencies

In this section, it is investigated whether the peak ($T_{\rm peak} \sim 0.05\,$K) in the in-phase component (χ') as well as the onset ($T \sim 0.2\,$K) in the out-of-phase component (χ'') possess a frequency-dependence, which is a common signature for a spin glass state. Figure 59 shows $\chi' - \chi'_{\rm stycast}$ as a function of $T_{\rm mc2,bin}$ and $T_{\rm sample,bin}$ where the $T_{\rm mc2}$-dependence of pure stycast has been subtracted. The temperature-dependent behavior for pure stycast has been estimated using a linear fit for each frequency (similar to Section 6.9.1) and the measurements along with the fits are shown in Fig. 102 and 103 for $\chi'_{\rm stycast}$ and $\chi''_{\rm stycast}$, respectively. Figure 59 shows that the subtraction of the stycast is unable to position the curves on top of one another. This presumably relates to the fact that the stycast is not the "true background" but more a temperature-dependence of the background. Further, one could imagine that the scaling factor (C_S) could be affected by reattaching the coil system as discussed in Section 4 and 5. Focusing on the temperature-dependence, visually it is not clear if the peak in $\chi' - \chi'_{\rm stycast}$ shows any frequency-dependence in terms of $T_{\rm mc2,bin}$ and $T_{\rm sample,bin}$. Therefore, the peak temperatures ($T_{\rm mc2,bin,peak}$ & $T_{\rm sample,bin,peak}$) have been estimated using a Gaussian fit function in an appropriate temperature interval around the peak (see Fig. 104 along with fit parameters in Table 14 and 15). The estimated peak temperatures ($T_{\rm mc2,bin,peak}$ & $T_{\rm sample,bin,peak}$) are reported in Table 9 (row 6 and 7) and further shown in Fig. 60 as a function of frequency (ν).

The estimated $T_{\rm mc2,peak}$ does not show any frequency-dependence given the uncertainties as seen in Fig. 60 (left). Although, one could imagine that this would be the case in terms of $T_{\rm mc2,bin}$ if the sample of interest was indeed a spin glass. If increasing heat due to increasing frequency pushes the spin glass transition towards lower temperatures in terms of $T_{\rm mc2,bin}$, but at the same time, the spin glass transition occurs at higher sample temperatures for increasing frequency (see Fig. 109 (bottom) Appendix L), one could imagine that these two effects would cancel out, and

hence, reveal close to no frequency-dependence as a function of $T_{\mathrm{mc2,bin}}$. Therefore, if this was the case the frequency-dependence would show in terms of $T_{\mathrm{sample,bin}}$. Figure. 60 (right) does show an increasing trend in terms of the data points, and, given the small uncertainties, the increasing trend is statistically significant to argue for a tiny frequency-dependence. However, the model converting from $T_{\mathrm{mc2,bin}}$ to $T_{\mathrm{sample,bin}}$ remains an approximation and is based off the thermalization for the CMN sample specifically as well as the probe environment. Recall that the metal screws shown in Fig. 19 (left) were replaced with nylon screws shown in Fig. 19 (right) which would presumably reduce the effect of the heat due to induced eddy currents. With this in mind, the model might overestimate $T_{\mathrm{sample,bin}}$ which would show even less of an increasing trend for the data in Fig. 60 (right) if corrected for. This could lead to the outcome of no observed frequency-dependence in the in-phase component (χ').
The uncertainties for both the cases ($T_{\mathrm{mc2,bin,peak}}$ & $T_{\mathrm{sample,bin,peak}}$) decrease as the frequency increases, which presumably is due to the measurements tend to become more noisy for low frequencies causing the uncertainty of each data point to be larger.

Figure 61 shows the out-of-phase components ($\chi'' - \chi''_{\mathrm{stycast}}$ & $\chi'' - \chi''_{\mathrm{a.u.}}$) as a function of $T_{\mathrm{mc2,bin}}$ and $T_{\mathrm{sample,bin}}$. From the measurements of $\chi'' - \chi''_{\mathrm{stycast}}$ vs $T_{\mathrm{mc2,bin}}$ and $T_{\mathrm{sample,bin}}$ it is clear that the subtraction of the pure stycast is, yet again, unable to position the curves on top of one another. This makes a comparison difficult. Therefore, an arbitrary constant term ($\chi''_{\mathrm{a.u.}}$) has been subtracted such that the curves are stacked (see Fig. 61 (bottom)). Visually, there is not a clear frequency-dependence in $\chi'' - \chi''_{\mathrm{a.u.}}$ vs $T_{\mathrm{mc2,bin}}$ and $T_{\mathrm{sample,bin}}$. For a spin glass we would expect the onset to shift towards higher temperatures along with an increase in the magnitude for increasing frequency, which we do not observe.
Based on the measurements in Fig. 61 it remains difficult to discard a potential minor frequency-dependence as this could easily be hidden due to the already small and noisy signal of the out-of-phase component. Further, it is difficult to reject a potential minor frequency-dependence in the in-phase component (χ'). Although, the 3rd harmonic susceptibility ($\chi_{n=3}$) has been measured as a function of temperature, and, this reveals no appearance of any peak or onset. Hence, there is no sign of spin freezing.

ν [Hz]	333	663	982	1433
H_{AC} [Am^{-1}]	17.16964(3)	17.243310(42)	17.29307(12)	17.24694(6)
$H_{\mathrm{AC,stycast}}$ [Am^{-1}]	17.120185(12)	17.246443 $\pm 4 \times 10^{-16}$	17.246443 $\pm 2 \times 10^{-16}$	17.280865(7)
Θ_{new} [radians]	1.66078(10)	1.74545(9)	1.82373(5)	1.92026(4)
$\Theta_{\mathrm{new,stycast}}$ [radians]	1.66073(10)	1.74534(9)	1.82396(5)	1.92380(4)
$T_{\mathrm{mc2,bin,peak}}$ [K]	0.0425(10)	0.0426(3)	0.0433(3)	0.0431(2)
$T_{\mathrm{sample,bin,peak}}$ [K]	0.0493(4)	0.04927(15)	0.05024(10)	0.05127(7)

Table 9: Table containing the estimated AC fields (H_{AC}) and ($H_{\mathrm{AC,stycast}}$) for each measurement of herbertsmithite and stycast, respectively. The statistical uncertainties for some values of $H_{\mathrm{AC,stycast}}$ are unusually small due to very small fluctuations. This cannot be correct, however, due to lack of time I have chosen not to look into it. The estimated quantity $\Theta_{\mathrm{new,stycast}}$ represents the phase while measuring on stycast, and is reported in order to check whether the phase had changed compared to Θ_{new} from Table 7 (row 3) also shown in this Table (row 4). The estimated quantities $T_{\mathrm{mc2,bin,peak}}$ and $T_{\mathrm{sample,bin,peak}}$ from the data presented in Fig. 59 (left) and (right), respectively.

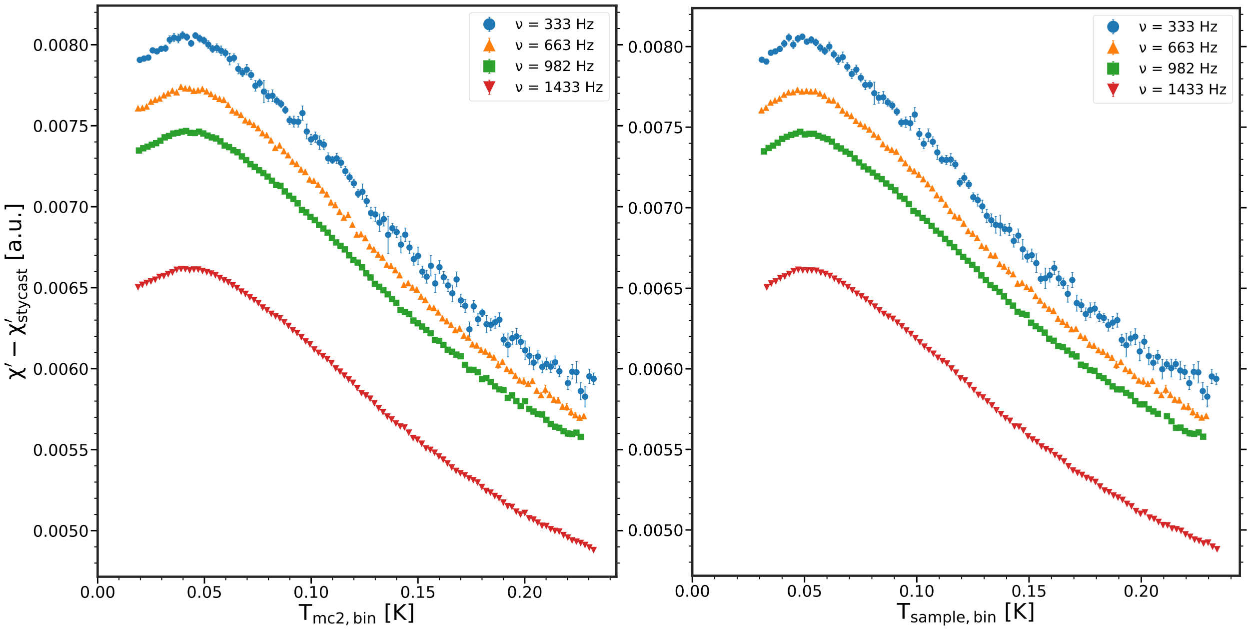

Figure 59: The in-phase component $(\chi' - \chi'_{\mathrm{stycast}})$ for the excitation frequencies of $\nu = 333\,\mathrm{Hz}$ (●), 663 Hz (▲), 982 Hz (■), and 1433 Hz (▼). χ'_{stycast} is shown in Fig. 102 for the various excitation frequencies. **Left**: $(\chi' - \chi'_{\mathrm{stycast}})$ vs $T_{\mathrm{mc2,bin}}$. **Right**: $(\chi' - \chi'_{\mathrm{stycast}})$ vs $T_{\mathrm{sample,bin}}$.

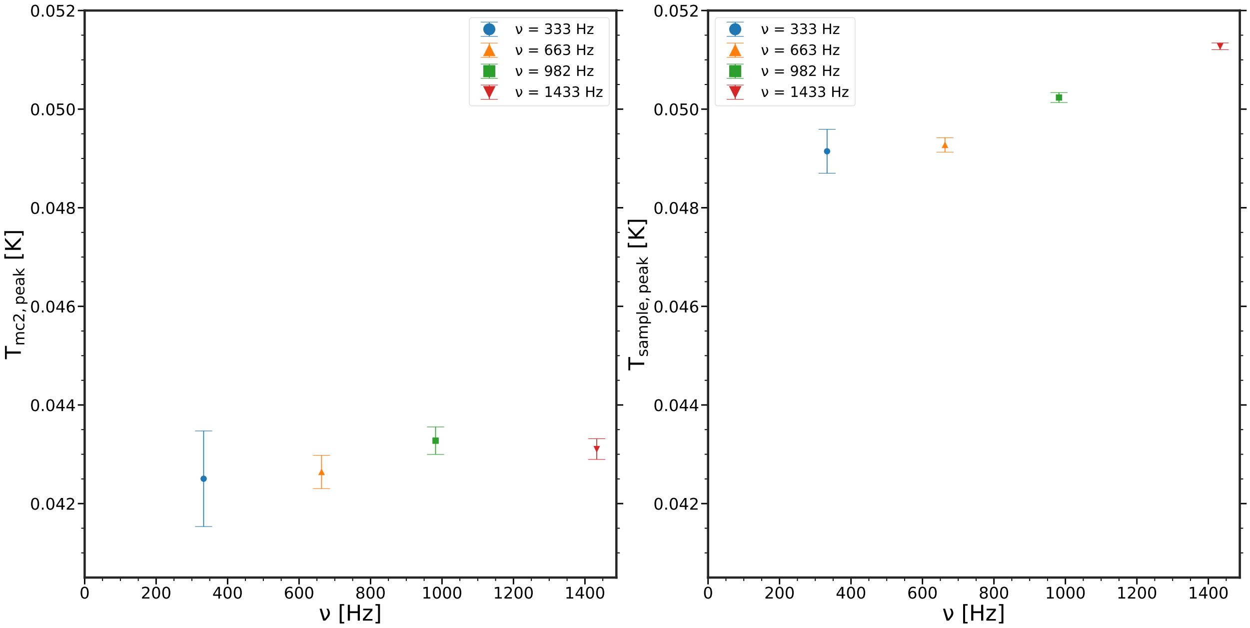

Figure 60: The peak temperatures from Table 9 (row 6 & 7) as a function of frequency. Data points at excitation frequencies of $\nu = 333\,\mathrm{Hz}$ (●), 663 Hz (▲), 982 Hz (■), and 1433 Hz (▼). **Left**: $T_{\mathrm{mc2,bin}}$. **Right**: $T_{\mathrm{sample,bin}}$.

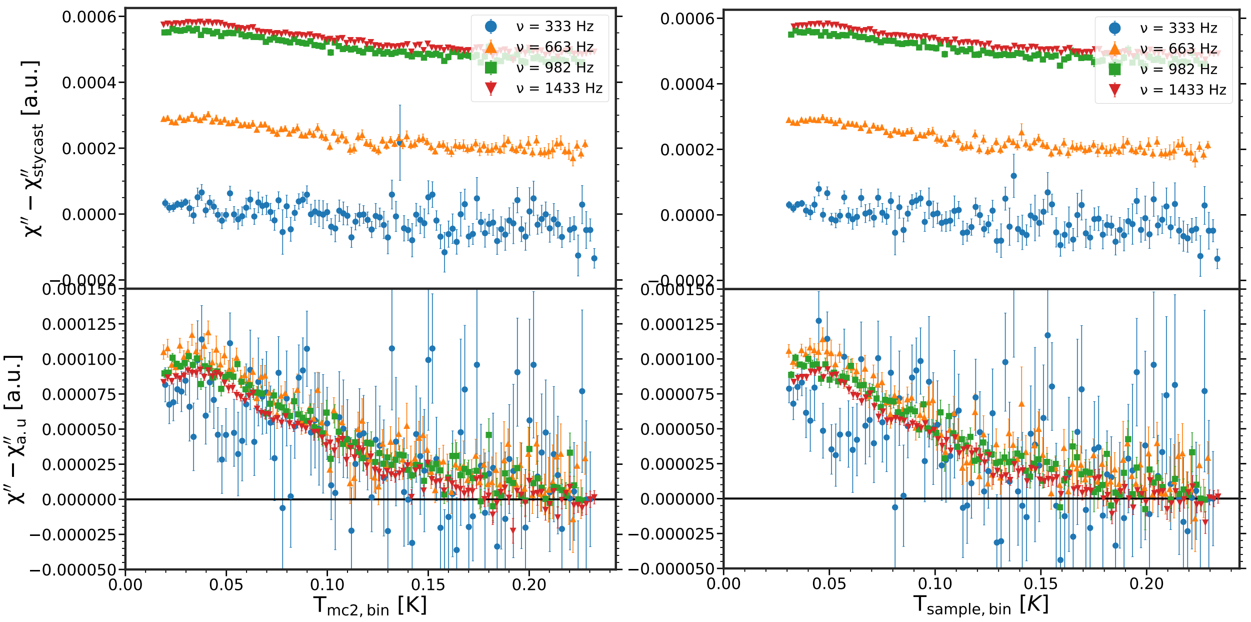

Figure 61: The out-of-phase components $(\chi'' - \chi''_{\text{stycast}})$ and $(\chi'' - \chi''_{\text{a.u.}})$ for the excitation frequencies of $\nu =$ 333 Hz (●), 663 Hz (▲), 982 Hz (🟩), and 1433 Hz (▼). χ''_{stycast} is shown in Fig. 103 for the various excitation frequencies. $\chi''_{\text{a.u.}}$ corresponds to an arbitrary offset added for an easy comparison. **Left**: $(\chi'' - \chi''_{\text{stycast}})$ and $(\chi'' - \chi''_{\text{a.u.}})$ vs $T_{\text{mc2,bin}}$. **Right**: $(\chi'' - \chi''_{\text{stycast}})$ and $(\chi'' - \chi''_{\text{a.u.}})$ vs $T_{\text{sample,bin}}$

6.9.3 AC Susceptibility Measurements in DC field

In this section it is investigated how the the temperature-dependent AC susceptibility responds to various applied DC fields. Similar to the previous sections, measurements for pure stycast have been conducted as a function of temperature for various DC fields. These measurements are shown in Fig. 107 and 108 where the trends for both the in-phase component (χ'_{stycast}) and the out-of-phase component $(\chi''_{\text{stycast}})$ have been estimated using linear fits. The fit parameters are shown in Table 16 and 17 for $\chi_{\text{stycast}'}$ and $\chi_{\text{stycast}''}$, respectively.
The in-phase component (χ') of the temperature-dependent AC susceptibility for herbertsmithite in the presence of various DC fields is shown in Fig. 62. Upon subtracting χ'_{stycast}, the curves differ a lot from one another, and the curves for $B = 0.5\,\text{T}$ and $1\,\text{T}$ remain at negative values. Thus, an arbitrary value $\chi'_{\text{a.u.}}$ have been subtracted in order to position the curves within in a more narrow susceptibility scale for easier comparison. In addition, the cooling measurement from Fig. 58 has been included. The outcome shows sign of saturation effects caused by increasing the DC field. This agrees with the behaviour Refs. [3, 4] observe. Reference [4] measures the temperature-dependent in-phase component (χ') down to $T \approx 2\,\text{K}$ in the DC field range from 0-14 T. They do observe the saturation effects, but it requires greater DC field at such temperature. Reference [3] measures the temperature-dependent DC susceptibility down to $T \approx 100\,\text{mK}$ in the DC range of 0.05-0.7 T, observing saturation effects at similar DC fields comparing to Fig. 62.

The out-of-phase component (χ'') of the temperature-dependent AC susceptibility for herbertsmithite is shown in Fig. 63. Similarly, the subtraction of χ'_{stycast} is unable to position the curves to one another (Fig. 63 (left)). Thus, an arbitrary $\chi''_{\text{a.u.}}$ has been subtracted for an easier comparison (see Fig. 63 (right)). The curve for $B = 1\,\text{T}$ has been positioned above the remaining curves for visualization purposes, as this seems more noisy. The onset observed at $T_{\text{sample,bin}} \approx 200\,\text{mK}$ for $B_{\text{DC}} = 0\,\text{T}$ appears to slowly vanish as the DC field is increased. Perhaps, this would be indicative of the DC field breaking a state related to the peak in the in-phase component (χ'). The curve for $B_{\mathrm{DC}} = 1\,\mathrm{T}$ shows an interesting, but odd, anomaly at $T_{\mathrm{sample,bin}} \approx 200\,\mathrm{mK}$ which might resemble a peak. It remains unknown if this resemblance of a peak is caused by instrumentation effects or a physical dissipation process.

Why the curves in Fig. 62 and 63 (left) are positioned this far from one another after subtraction of χ_{stycast} is still unknown. By comparing Fig. 105 and Fig. 106 in Appendix K, one can observe that there is an opposite responsive manner to increasing DC field. X and Y for herbertsmithite appear to increase for increasing DC field (see. Fig 105), whereas X_{stycast} and Y_{stycast} appear to decrease for increasing DC field. The cause of this feature remains unknown, but it might relate to some instrumentation effect or change that occurred upon switching the sample from herbertsmithite to stycast. Even the effect, that X and Y for herbertsmithite appear to increase for increasing DC fields is unexpected. This could potentially be related to ground loop effects in the circuit. In addition, it was checked whether the field and the phase had changed upon going from herbertsmithite to pure stycast. Table 10 shows that there are some statistical differences, however, these are not believed to cause the observed effect.

Nevertheless, both the susceptibility measured for stycast in terms of the in-phase component (χ'_{stycast}) and the out-of-phase component ($\chi''_{\mathrm{stycast}}$) shown in Fig. 62 and 63, respectively show almost no temperature-dependence, which is promising. This is indeed indicative that the saturation effects observed in Fig. 62 originates from the herbertsmithite sample.

B_{DC} [T]	0.1	0.2	0.5	1
H_{AC} [Am^{-1}]	17.25094(8)	17.25639(2)	17.25784(2)	17.24313(2)
$H_{\mathrm{AC,stycast}}$ [Am^{-1}]	17.234944(5)	17.246443$\pm 4 \times 10^{-16}$	17.246443$\pm 2 \times 10^{-16}$	17.2365(2)
$\Theta_{\mathrm{new,DCfield}}$ [radians]	1.824113(53)	1.82416(5)	1.82423(5)	1.82416(5)
$\Theta_{\mathrm{new,stycast,DCfield}}$ [radians]	1.82387(6)	1.82406(5)	1.82406(5)	1.82415(5)

Table 10: Table containing the estimated AC fields (H_{AC}) and ($H_{\mathrm{AC,stycast}}$) for each DC field measurement of herbertsmithite and stycast, respectively. The statistical uncertainties for some values of $H_{\mathrm{AC,stycast}}$ are unusually small, due to very small fluctuations. This cannot be correct, however, due to lack of time I have chosen not to look into it. The estimated quantity $\Theta_{\mathrm{new,stycast,DCfield}}$ represents the phase while measuring on stycast, and is reported in order to check whether the phase had changed compared to $\Theta_{\mathrm{new,DCfield}}$.

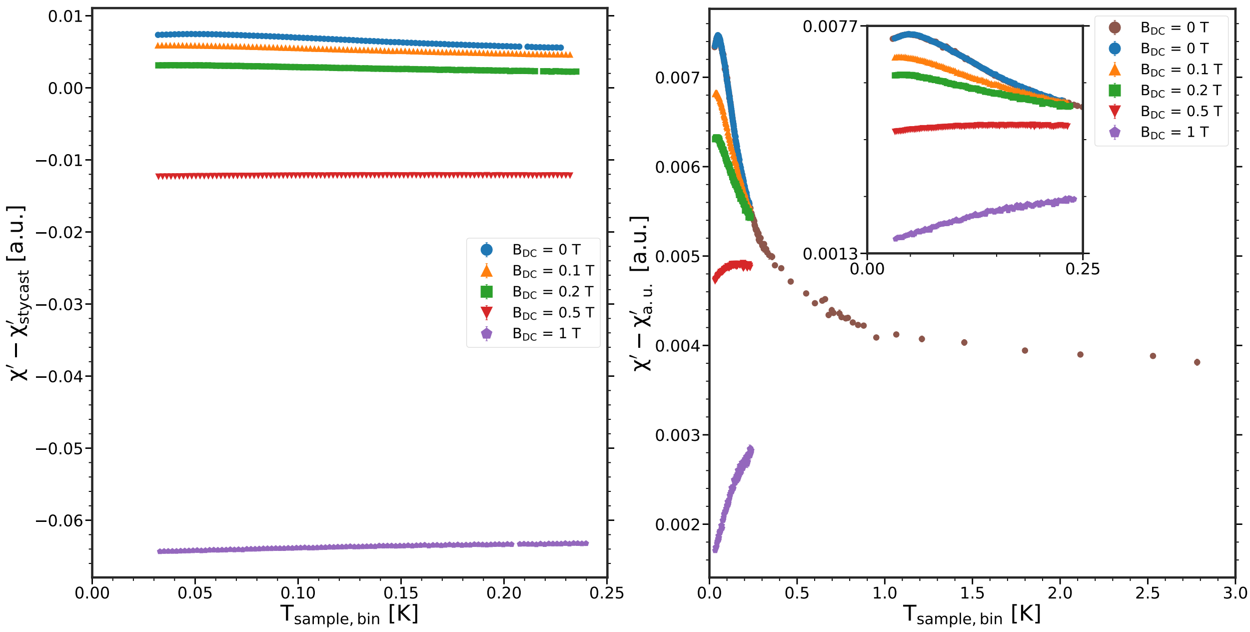

Figure 62: The in-phase component $(\chi' - \chi'_{\mathrm{stycast}})$ and $(\chi' - \chi'_{\mathrm{a.u.}})$ as a function of $T_{\mathrm{sample,bin}}$ for $H_{\mathrm{AC}} \approx 17\,\mathrm{Am}^{-1}$ at an excitation frequency of $\nu = 982\,\mathrm{Hz}$, and using a DC field of $B_{\mathrm{DC}} = 0\,\mathrm{T}$ (●), $0.1\,\mathrm{T}$ (▲), $0.2\,\mathrm{T}$ (■), $0.5\,\mathrm{T}$ (▼), and $1\,\mathrm{T}$ (⬟). χ'_{stycast} shown in Fig. 107. **Left**: $\chi' - \chi'_{\mathrm{stycast}}$. **Right**: $\chi' - \chi'_{\mathrm{a.u.}}$. The cooling measurement from Fig. 58 is included (●).

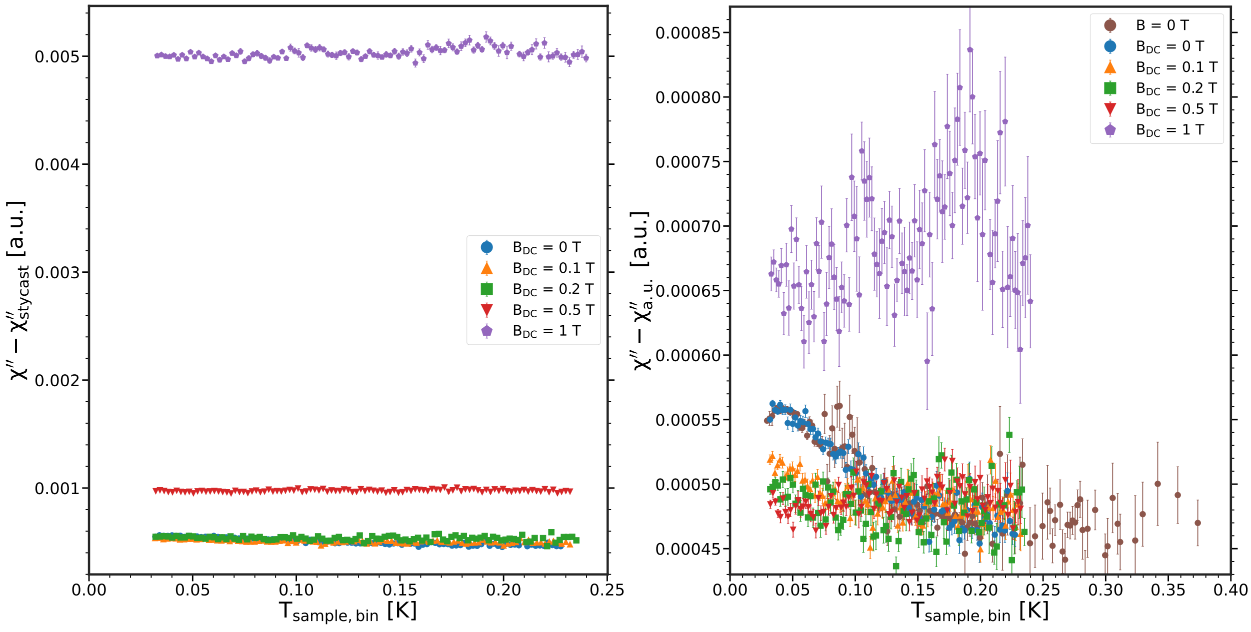

Figure 63: The out-of-phase component $(\chi'' - \chi''_{\mathrm{stycast}})$ and $(\chi'' - \chi''_{\mathrm{a.u.}})$ as a function of $T_{\mathrm{sample,bin}}$ for $H_{\mathrm{AC}} \approx 17\,\mathrm{Am}^{-1}$ at an excitation frequency of $\nu = 982\,\mathrm{Hz}$, and using a DC field of $B_{\mathrm{DC}} = 0\,\mathrm{T}$ (●), $0.1\,\mathrm{T}$ (▲), $0.2\,\mathrm{T}$ (■), $0.5\,\mathrm{T}$ (▼), and $1\,\mathrm{T}$ (⬟). χ'_{stycast} is shown in Fig. 108. **Left**: $\chi'' - \chi''_{\mathrm{stycast}}$. **Right**: $\chi'' - \chi''_{\mathrm{a.u.}}$. The cooling measurement from Fig. 58 is included (●).

7 Conclusion

In this thesis, we have managed to resolve a leak in the cone-seal of the mixing chamber causing the dilution refrigerator to be able to operate within its capabilities yet again, since the Master's thesis of Mathias Mikkelsen [57] back in the year 2019. The dilution refrigerator has been brought to temperatures of $\leq 25\,\mathrm{mK}$ consistently, according to the ruthenium oxide (RuO_2) thermometers located in the mixing chamber and on the cold finger. In addition, a new set of detection coils have been produced, consisting of 460 turns each. These accomplishments have allowed us to conduct experiments measuring the AC susceptibility close to absolute zero.

The temperature-dependent fundamental ($n = 1$) AC susceptibility was measured at various excitation frequencies and magnetic DC fields for a titanium sample provided by the NBI Mechanical and Electronic Workshop. These measurements served as a purpose of determining the phase Θ required to separate the in-phase (χ') and the out-of-phase (χ'') component of the AC susceptibility.

The measurements of titanium for various frequencies showed a large separation of the susceptibility curves in terms of temperature using an excitation field of $H_{\mathrm{AC}} \approx 36\,\mathrm{Am}^{-1} \approx 0.45\,\mathrm{Oe}$. This separation was substantially decreased as a result of lowering the field to $H_{\mathrm{AC}} \approx 21\,\mathrm{Am}^{-1} \approx 0.27\,\mathrm{Oe}$, which lead to the explanation that the separation originates from heating the sample presumably due to induced eddy currents in metallic parts of the equipment. The critical temperature was estimated to be $T_{\mathrm{c,onset}} \approx 74.3\,\mathrm{mK}$ and $T_{\mathrm{c,onset}} \approx 77\,\mathrm{mK}$ for $\nu = 333\,\mathrm{Hz}$ while heating and cooling, respectively. The difference in the former and the latter suggested an imperfect thermal link to the sample. The estimation of such critical temperature deviates by a significant amount from Ref. [2] and the literature value of $T_{\mathrm{c}} \approx 450\,\mathrm{mK}$ [1], which is presumed to originate from the sample being greatly impure.

The measurements for various DC fields showed a suppression of the estimated critical temperature and lead to an estimated critical field of $B_{\mathrm{c}}(T = 0) = 0.013454(2)\,\mathrm{T}$. This value is noticeably greater than the literature value ($B_{\mathrm{c}} \approx 0.01\,\mathrm{T}$) [1], which is unexpected, considering the strongly reduced critical onset temperature. The cause for this remains unknown.

Further, taking a detour from the goal of the thesis, the temperature-dependence of the non-linear 3rd harmonic contribution to the AC susceptibility was measured for various excitation frequencies. These were presented as 3 different representations, with the in-phase (χ_3') and the out-of-phase (χ_3'') component being separated by $\Theta_3 = 0$, Θ, and 3Θ. The representations were compared with Refs. [38, 41, 42] who have published studies of 3rd harmonic AC susceptibilities for various type-II superconducting compounds. These studies are found to show some similar features, compared to our measurements of titanium, in terms of the temperature-dependent behaviour and its response to a change in excitation frequency.

In the subsequent part of the thesis, the temperature-dependent AC susceptibility of cerium magnesium nitrate was measured for various frequencies with the purpose of converting the cold finger temperature to sample temperature. From a model which assumes the sample remains in a steady state in terms of temperature upon measuring, the cold finger temperature (T_{mc2}) was related to the sample temperature (T_{sample}) via. $T_{\mathrm{sample}} = \sqrt{T_{\mathrm{mc2}}^2 + 2\Delta}$ such that $T_{\mathrm{sample}} \approx T_{\mathrm{mc2}}$ for $T_{\mathrm{mc2}}^2 \gg 2\Delta$ with Δ being a fit parameter, relating to the type of thermalization. The sample temperature was, at $T_{\mathrm{mc2}} \approx 13\,\mathrm{mK}$, estimated to be $T_{\mathrm{sample}} = 26.95(2)\,\mathrm{mK}$ and $T_{\mathrm{sample}} = 29.883(6)\,\mathrm{mK}$ for $\nu = 333\,\mathrm{Hz}$ and $1433\,\mathrm{Hz}$, respectively.

In addition, the thermometer T_{mc2} was found to deviate at temperatures above $\sim 285\,\mathrm{mK}$. This was corrected for using the same model. The relation between $T_{\mathrm{mc2,corrected}}$ and T_{mc2} was estimated using a 5th. order polynomial fit function outside of the thermometer's (T_{mc2}) reliable range ($\geq 285\,\mathrm{mK}$).

In the final part of this thesis, herbertsmithite (a well-known quantum spin liquid candidate) was investigated through high-temperature-dependent (2-350 K) DC susceptibility measurements and low-temperature-dependent ($\sim$ 0.03-6 K) AC susceptibility measurements for various frequencies and DC fields.
The DC susceptibility measurements showed a deviation from a true Curie Weiss relation at $T \approx 200\,\mathrm{K}$, but no magnetic ordering down to $T = 2\,\mathrm{K}$. A Curie Weiss fit applied above 200 K yielded a Curie constant of $0.45(5)\,\mathrm{emu} \cdot \mathrm{K} \cdot \mathrm{mol}_{\mathrm{N}}^{-1}\mathrm{Oe}^{-1}$ resulting in an effective moment of $\mu_{\mathrm{eff}} = 1.91(10)\mu_{\mathrm{B}}$ and a g-factor of $g = 2.20(12)$. Further, it yielded a Curie Weiss temperature of $\theta_{\mathrm{CW}} = -248(57)\,\mathrm{K}$.
The AC susceptibility measurements, in the absence of a DC field, showed a clear peak in the in-phase component (χ') at $\sim 50\,\mathrm{mK}$ and an onset in the out-of-phase component in (χ''). Further, a Curie Weiss fit with a background term (χ_0) applied in the approximate range ($\sim$ 0.12-6 K) yielded a Curie Weiss temperature of $\theta_{\mathrm{CW}} = -0.0561(10)\,\mathrm{K}$, a factor of ~ 5000 lower in value than $\theta_{\mathrm{CW}} = -248(57)\,\mathrm{K}$.
We could not statistically reject a tiny frequency-dependence in the peak or onset in the in-phase (χ') and out-of-phase component (χ''), respectively. However, it is possible that the frequency-dependence of the conversion from $T_{\mathrm{mc2,bin}}$ to $T_{\mathrm{sample,bin}}$ for herbertsmithite was overestimated due to the fact that metallic screws were replaced with nylon screws upon switching from CMN to herbertsmithite. With that being said, a measurement of the 3rd harmonic susceptibility yielded no sign of any non-linear response. Hence, no sign of spin glass freezing was observed.
The signal was, however, altered by the application of a DC field which was believed to be caused by instrumentation effects. Therefore, arbitrary values $\chi'_{a.u.}$ and $\chi''_{a.u.}$ were required to be subtracted from the in-phase (χ') and the out-of-phase component (χ''), respectively, in order to position the curves on a comparative scale. Nevertheless, the in-phase component (χ') was found to show signs of saturation effects for increasing DC field which agrees with observations by Refs. [3, 4]. The onset at $\sim 200\,\mathrm{mK}$ in the out-of-phase component (χ'') was found to be suppressed for increasing fields. This could potentially correspond to the DC field breaking a state of matter, associated with the peak in χ' at $\sim 50\,\mathrm{mK}$. The measurement with $B_{\mathrm{DC}} = 1\,\mathrm{T}$ showed an anomaly in resembling a peak in χ'' at $\sim 200\,\mathrm{mK}$. Whether this phenomenon corresponds to the occurrence of some dissipation process or instrumentation effects remains unknown.

8 Outlook

Considering the initial state of the project, and the accomplishments during the past year, we have indeed gone far in understanding the workings of AC susceptometry as well as operating the dilution refrigerator consistently. Further, we have obtained various intriguing measurements for herbertsmithite, which promotes the excitement of studying the system with neutron scattering in the future.
With that being said, there are multiple ways to improve the equipment used. During the last few months, a ruthenium oxide ($\mathrm{RuO_2}$) thermometer calibrated in the range $\sim$ 0.015-4 K, as well as a high purity titanium piece were purchased. Installing the thermometer would yield the availability to conduct measurements in this temperature regime without the use of a cold finger temperature correction. Performing DC field measurements on the titanium piece of high purity could potentially yield some insight as to why the titanium piece in this thesis yielded the reported value of H_{c}.
As for the aspect of AC susceptometry, a more stable coil setup, with the coil wires being soldered

to a fixed point, hence, avoiding a reattachment of the coil system upon the change of sample, would be ideal. An investigation of the electrical circuit, eliminating possible unwanted effects such as a potential ground loop, could reduce noise, which plays a major factor pursuing weak susceptibility signals such as frustrated magnetism. The construction of a primary coil using superconducting wire would eliminate heating effects originating from resistive parts. And last, but not least, a new set of detection coils – each with the number of turns (800-1200) as recommended by Ivica Zivkovic [55] – would enhance the measured signal without causing disturbance. The implementation of the above mentioned improvements could be the first step towards extracting relaxation times of materials, well matched with the accessible frequency domain (0.1-10^4 Hz), thus, utilizing the full spectrum of available features within AC susceptometry.

References

[1] W. Buckel and R. Kleiner, *Superconductivity: an introductiton* (John Wiley & Sons, Ltd, 2015).

[2] A. Amann et al., "Fully automated ac susceptometer for milli-kelvin temperatures in a dynacool ppms", IEEE Transactions on Applied Superconductivity **27**, 1–4 (2017).

[3] F. Bert et al., "Low temperature magnetization of the $S = \frac{1}{2}$ kagome antiferromagnet $ZnCu_3(OH)_6Cl_2$", Phys. Rev. B **76**, 132411 (2007).

[4] J. S. Helton et al., "Dynamic scaling in the susceptibility of the spin-1/2 kagome lattice antiferromagnet herbertsmithite", Physical Review Letters **104** (2010).

[5] L. Balents, "Spin liquids in frustrated magnets", Nature **464**, 199–208 (2010).

[6] J. Wen et al., "Experimental identification of quantum spin liquids", npj Quantum Materials **4**, 12 (2019).

[7] S. Blundell, *Magnetism in Condensed Matter* (Oxford University Press, 2001).

[8] R. Moessner and A. Ramirez, "Geometrical frustration", Physics Today **59**, 24– (2006).

[9] G. H. Wannier, "Antiferromagnetism. The Triangular Ising Net", Phys. Rev. **79**, 357–364 (1950).

[10] P. Fazekas and P. W. Anderson, "On the ground state properties of the anisotropic triangular antiferromagnet", The Philosophical Magazine: A Journal of Theoretical Experimental and Applied Physics **30**, 423–440 (1974).

[11] P. Anderson, "Resonating valence bonds: a new kind of insulator?", Materials Research Bulletin **8**, 153–160 (1973).

[12] P. W. Anderson, "The Resonating Valence Bond State in La_2CuO_4 and Superconductivity", Science **235**, 1196–1198 (1987).

[13] C. Lacroix, P. Mendels, and F. Mila, *Introduction to Frustrated Magnetism: Materials, Experiments, Theory* (Springer Berlin, Heidelberg, 2011).

[14] A. Hallett, C. Avarvarei, and J. W. Harter, "Combinatorial exploration of quantum spin liquid candidates in the herbertsmithite material family", Physical Review Materials **7** (2023).

[15] M.R.Norman, "Herbertsmithite and the search for the quantum spin liquid", Reviews of Modern Physics **88** (2016).

[16] F. Pobell, *Matter and methods at low temperatures* (Springer Berlin, Heidelberg, 2007).

[17] C. V. Topping and S. J. Blundell, "A.C. susceptibility as a probe of low-frequency magnetic dynamics", Journal of Physics: Condensed Matter **31**, 013001 (2018).

[18] B. D. Victorino Franco, *Magnetic measurement techniques for materials characterization* (Springer Cham, 2021).

[19] A. B. David A. Cardwell David C. Larbalestier, *Handbook of superconductivity: characterization and applications* (CRC Press, 2021).

[20] D. Martien, "Introduction to ac susceptibility", Quantum Design, URL: https://qdusa.com/siteDocs/appNot 201.pdf, (Accessed: 2023-08-04).

[21] S. H. Simon, *The Oxford Solid State Basics* (Oxford University Press, 2013).

[22] P. Coleman, *Introduction to many-body physics* (Cambridge University Press, 2015).

[23] N. W. Ashcroft and N. D. Mermin, *Solid state physics*, 1st Edition (Cengage Learning, 1976).

[24] J. Sólyom, *Fundamentals of the physics of solids - volume 1: structure and dynamics* (Springer Berlin, Heidelberg, 2007).

[25] S. Mugiraneza and A. M. Hallas, "Tutorial: a beginner's guide to interpreting magnetic susceptibility data with the Curie-Weiss law", Communications Physics **5** (2022).

[26] J. Piatek, "Ultra low temperature susceptometer and magnetometer study of the spin glass series $LiHo_xEr_{1-x}F_4$", (2012).

[27] H. Kageyama et al., "Exact Dimer Ground State and Quantized Magnetization Plateaus in the Two-Dimensional Spin System $SrCu_2(BO_3)_2$", Phys. Rev. Lett. **82**, 3168–3171 (1999).

[28] M. Azuma et al., "Observation of a spin gap in $SrCu_2O_3$ comprising spin-1/2 quasi-1d two-leg ladders", Phys. Rev. Lett. **73**, 3463–3466 (1994).

[29] D. C. Johnston et al., "Thermodynamics of spin $\frac{1}{2}$ antiferromagnetic uniform and alternating-exchange Heisenberg chains", Physical Review B **61**, 9558–9606 (2000).

[30] A. Klümper and D. C. Johnston, "Thermodynamics of the spin-$\frac{1}{2}$ Antiferromagnetic Uniform Heisenberg Chain", Physical Review Letters **84**, 4701–4704 (2000).

[31] K. Fossheim and A. Sudbø, *Superconductivity: physics and applications* (John Wiley & Sons, Ltd, 2004).

[32] J. F. Annett, *Superconductivity, superfluids and condensates* (Oxford University Press, 2004).

[33] M. Youssif and A. Bahgat, "Ac magnetic susceptibility technique for the characterization of high temperature superconductors", **23**, 231 (2000).

[34] D. Drobac et al., "The role of lock-in phase setting in ac susceptibility measurement", The Review of scientific instruments **84**, 054708 (2013).

[35] M. Bałanda, "Ac susceptibility studies of phase transitions and magnetic relaxation: conventional, molecular and low-dimensional magnets", Acta Physica Polonica A **124**, 964–976 (2013).

[36] K.H.Fischer and J.A.Hertz, *Spin glasses* (Cambridge University Press, 1991).

[37] T. Lookman and X. Ren, *Frustrated materials and ferroic glasses* (Springer Cham, 2018).

[38] A. Pal et al., "Investigation of fundamental and higher harmonic AC magnetic susceptibility of $FeSe_{0.5}Te_{0.5}$ superconductor", Materials Research Express **6**, 096004 (2019).

[39] M. Nikolo, "Superconductivity: a guide to alternating current susceptibility measurements and alternating current susceptometer design", American Journal of Physics - AMER J PHYS **63**, 57–65 (1995).

[40] K. Buchkov et al., "Fundamental and 3rd harmonic magnetic susceptibility of over-doped polycrystalline $Y_{1x}Ca_xBa_2Cu_3O_7$ (x=0.025 and x=0.20) samples", Physica C: Superconductivity **473**, 48–56 (2012).

[41] D. D. Gioacchino et al., "The a.c. susceptibility third harmonic component of $NdO_{1-0.14}F_{0.14}FeAs$: A flux dynamic magnetic analysis", Journal of Physics and Chemistry of Solids **71**, SMEC 2009, 1046–1052 (2010).

[42] M. Polichetti, M. G. Adesso, and S. Pace, "Third harmonics of the AC magnetic susceptibility: a method for the study of flux dynamics in high temperature superconductors", The European Physical Journal B - Condensed Matter **36**, 27–36 (2003).

[43] T. Bitoh et al., "Linear and Nonlinear Susceptibilities in $Cu_{97}Co_3$ Alloy for Ferromagnetic Fine Particles in Metallic Matrix: Comparison with Spin Glass $Au_{96}Fe_4$ Alloy", Journal of the Physical Society of Japan **62**, 2583–2586 (1993).

[44] J. Hyatt, "Experimental AC Susceptometry - Developing a control system for AC susceptometry measurements", Master's thesis (University of Copenhagen, 2019).

[45] O. P. Hansen, M. Olsen, and F. B. Rasmussen, "Køling ved blanding af heliumisotoper", Fysisk Tidsskrift 73, 1975, nr. 4.

[46] D. D. Osheroff et al., "New Magnetic Phenomena in Liquid He^3 below 3 mK", Phys. Rev. Lett. **29**, 920–923 (1972).

[47] D. D. Osheroff, R. C. Richardson, and D. M. Lee, "Evidence for a New Phase of Solid He^3", Phys. Rev. Lett. **28**, 885–888 (1972).

[48] D. S. Greywall, "Specific heat of normal liquid ^{3}He", Phys. Rev. B **27**, 2747–2766 (1983).

[49] M. W. Zheng et al., "Thermodynamic process and analysis of dilution refrigerator", IOP Conference Series: Materials Science and Engineering **1240**, 012128 (2022).

[50] L. Cryogenics, "Microkelvin 50-100/400 tof dilution refrigerator", Instruction Manual.

[51] C. Limited, "Sms series superconducting magnet controllers", User's Manual.

[52] C. Limited, "16 tesla cryogen free superconducting magnet system with mck50-dr ccompatibility".

[53] D. J. Griffiths, *Introduction to electrodynamics*, Fourth Edidtion (Cambridge University Press, 2013).

[54] P. Laurent et al., "An ac susceptometer for the characterization of large, bulk superconducting samples", Measurement Science and Technology **19**, 085705 (2008).

[55] I. Zivkovic, Personal Communication (2022).

[56] Manual - MODEL SR830 DSP Lock-In Amplifier, Standford Research System.

[57] M. Mikkelsen, "Measuring Magnetism - Designing and calibrating an AC susceptometer", Master's thesis (University of Copenhagen, 2019).

[58] M. Sato and Y. Ishii, "Simple and approximate expressions of demagnetizing factors of uniformly magnetized rectangular rod and cylinder", Journal of Applied Physics **66**, 983–985 (1989).

[59] M. C. Steele and R. A. Hein, "Superconductivity of titanium", Phys. Rev. **92**, 243–247 (1953).

[60] G. J. Butterworth, C. B. P. Finn, and K. Kiymac, "The paramagnetic susceptibility of partially dehydrated cerium magnesium nitrate.", Journal of Low Temperature Physics **15** (1974).

[61] W. R. Abel and J. C. Wheatley, "Magnetic thermometry with cerium magnesium nitrate and its relation to the properties of ^{3}He", Phys. Rev. Lett. **21**, 597–601 (1968).

[62] R. P. Hudson and W. R. Hosler, "Magnetic susceptibility of cerous magnesium nitrate", Phys. Rev. **122**, 1417–1420 (1961).

[63] D. J. Abeshouse, D. R. Kelland, and E. Maxwell, "Low-temperature phase transition in cerium magnesium nitrate", Phys. Rev. Lett. **23**, 308–310 (1969).

[64] G. Zimmerman et al., "A note on the phase transition in cerium magnesium nitrate", Physica **51**, 623–626 (1971).

[65] A. Zalkin, J. D. Forrester, and D. H. Templeton, "Crystal Structure of Cerium Magnesium Nitrate Hydrate", The Journal of Chemical Physics **39**, 2881–2891 (2004).

[66] *CMR-Direct*, `http://www.cmr-direct.com/en/ge-varnish/cmr-gevar-25ml`, Accessed: 2023-07-19.

[67] R. J. Barlow, *Statistics: a guide to the use of statistical methods in the physical sciences* (John Wiley & Sons, Ltd, 1989).

[68] O. Ofer et al., "Ground state and excitation properties of the quantum kagomé system $ZnCu_3(OH)_6Cl_2$ investigated by local probes", (2006).

[69] S. H. Lee et al., "Quantum-spin-liquid states in the two-dimensional kagome antiferromagnets $Zn_xCu_{4-x}(OD)_6Cl_2$", Nature Materials **6**, 853–857 (2007).

[70] Z. Hiroi et al., "Spin-1/2 kagome compounds: Volborthite vs Herbertsmithite", Journal of Physics: Conference Series **145**, 012002 (2009).

[71] J. S. Helton et al., "Spin Dynamics of the Spin-1/2 Kagome Lattice Antiferromagnet $ZnCu_3(OH)_6Cl_2$", Phys. Rev. Lett. **98**, 107204 (2007).

[72] *CMR-Direct*, `https://www.cmr-direct.com/en/cmr-epoxy-1266-1kg?filter_name=Stycast&filter_description=true`, Accessed: 2023-07-19.

[73] J. C. Bonner and M. E. Fisher, "Linear magnetic chains with anisotropic coupling", Phys. Rev. **135**, A640–A658 (1964).

[74] S. J. Sebastian et al., "Quasi-one-dimensional magnetism in the spin-$\frac{1}{2}$ antiferromagnet $BaNa_2Cu(VO_4)_2$", Phys. Rev. B **103**, 064413 (2021).

[75] M. Dumm et al., "Magnetic susceptibility, heat capacity, and optical conductivity of LiPc and LiPcI", Physics of Condensed Matter **6**, 317–322 (1998).

[76] J. Sannigrahi et al., "Two dimensional magnetic correlation in the unconventional corrugated layered oxides $(Ba,Sr)_4Mn_3O_{10}$", Journal of Physics: Condensed Matter **27**, 056001 (2015).

[77] S. Nagata, P. Keesom, and H. Harrison, "Low-dc-field susceptibility of CuMn spin glass", Physical Review B **19**, 1633–1638 (1979).

[78] M. Szlawska, "Spin-glass freezing in single-crystalline Pr_2NiSi_3", Intermetallics **115**, 106616 (2019).

A Coil Forms

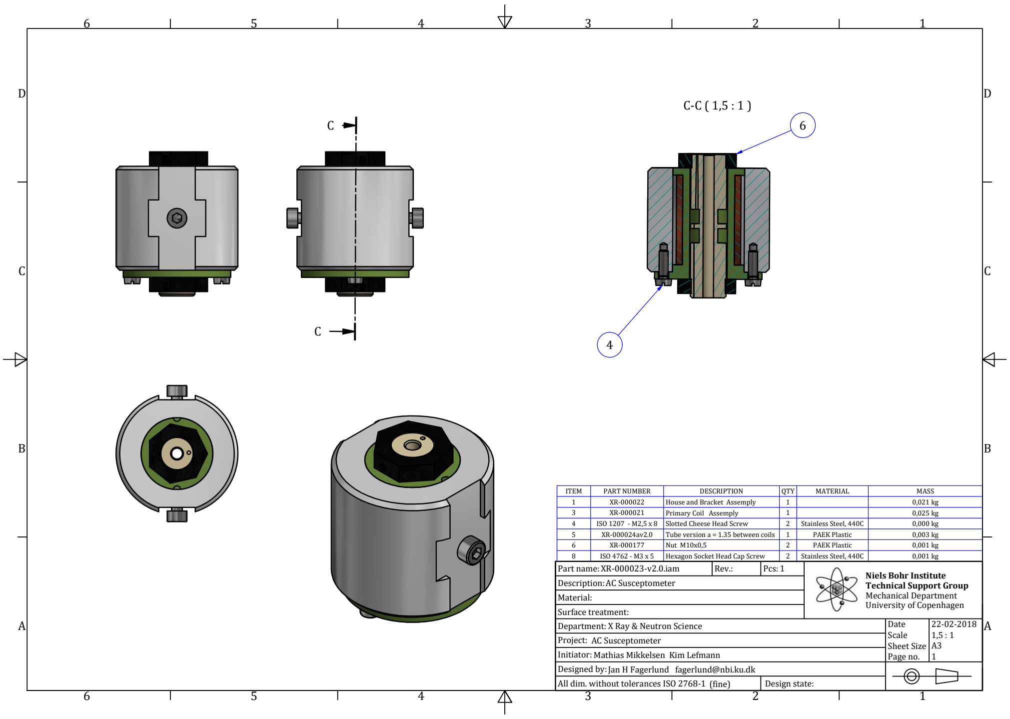

ITEM	PART NUMBER	DESCRIPTION	QTY	MATERIAL	MASS
1	XR-000022	House and Bracket Assemply	1		0,021 kg
3	XR-000021	Primary Coil Assemply	1		0,025 kg
4	ISO 1207 - M2,5 x 8	Slotted Cheese Head Screw	2	Stainless Steel, 440C	0,000 kg
5	XR-000024av2.0	Tube version a = 1.35 between coils	1	PAEK Plastic	0,003 kg
6	XR-000177	Nut M10x0,5	2	PAEK Plastic	0,001 kg
8	ISO 4762 - M3 x 5	Hexagon Socket Head Cap Screw	2	Stainless Steel, 440C	0,001 kg

Part name: XR-000023-v2.0.iam
Rev.:
Pcs: 1
Description: AC Susceptometer
Material:
Surface treatment:
Niels Bohr Institute
Technical Support Group
Mechanical Department
University of Copenhagen
Department: X Ray & Neutron Science
Project: AC Susceptometer
Initiator: Mathias Mikkelsen Kim Lefmann
Designed by: Jan H Fagerlund fagerlund@nbi.ku.dk
All dim. without tolerances ISO 2768-1 (fine)
Design state:
Date 22-02-2018
Scale 1,5 : 1
Sheet Size A3
Page no. 1

Figure 64: The drawing of the housing for the coils. Made by NBI Mechanical and Electronic Workshop. This is also shown in Master's thesis by Mathias Mikkelsen [57].

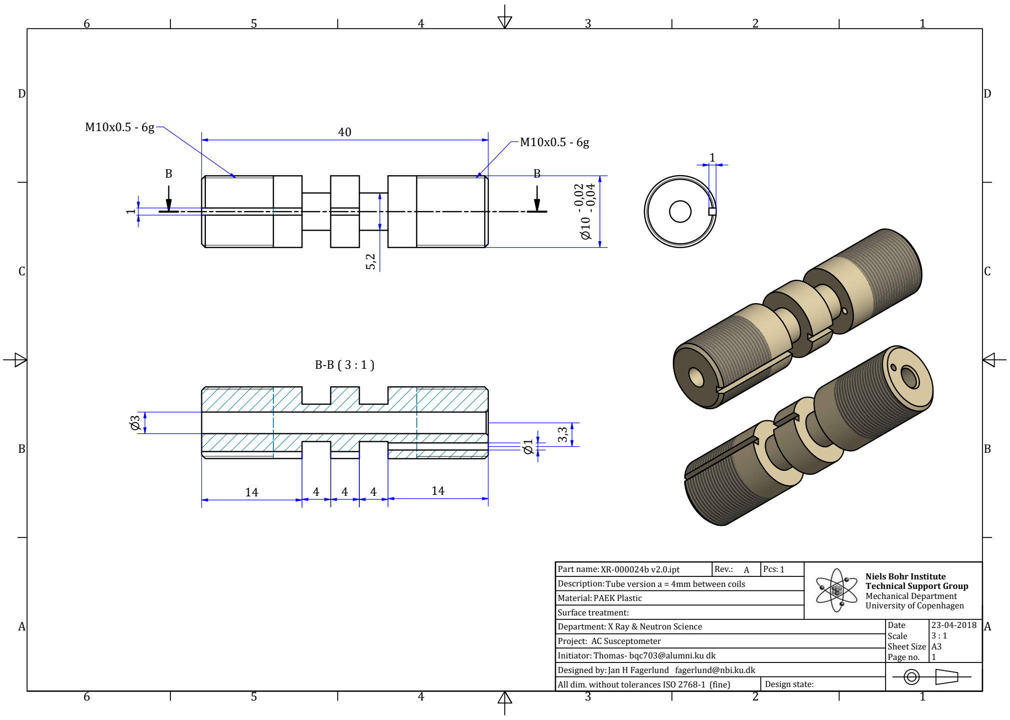

Part name: XR-000024b v2.0.ipt
Rev.: A
Pcs: 1
Description: Tube version a = 4mm between coils
Material: PAEK Plastic
Surface treatment:
Niels Bohr Institute
Technical Support Group
Mechanical Department
University of Copenhagen
Department: X Ray & Neutron Science
Project: AC Susceptometer
Initiator: Thomas- bqc703@alumni.ku dk
Designed by: Jan H Fagerlund fagerlund@nbi.ku.dk
All dim. without tolerances ISO 2768-1 (fine)
Design state:
Date 23-04-2018
Scale 3 : 1
Sheet Size A3
Page no. 1

Figure 65: The drawing of the coilform for the detector coils. Drawn by NBI Mechanical and Electronic Workshop.

B Images of the Samples

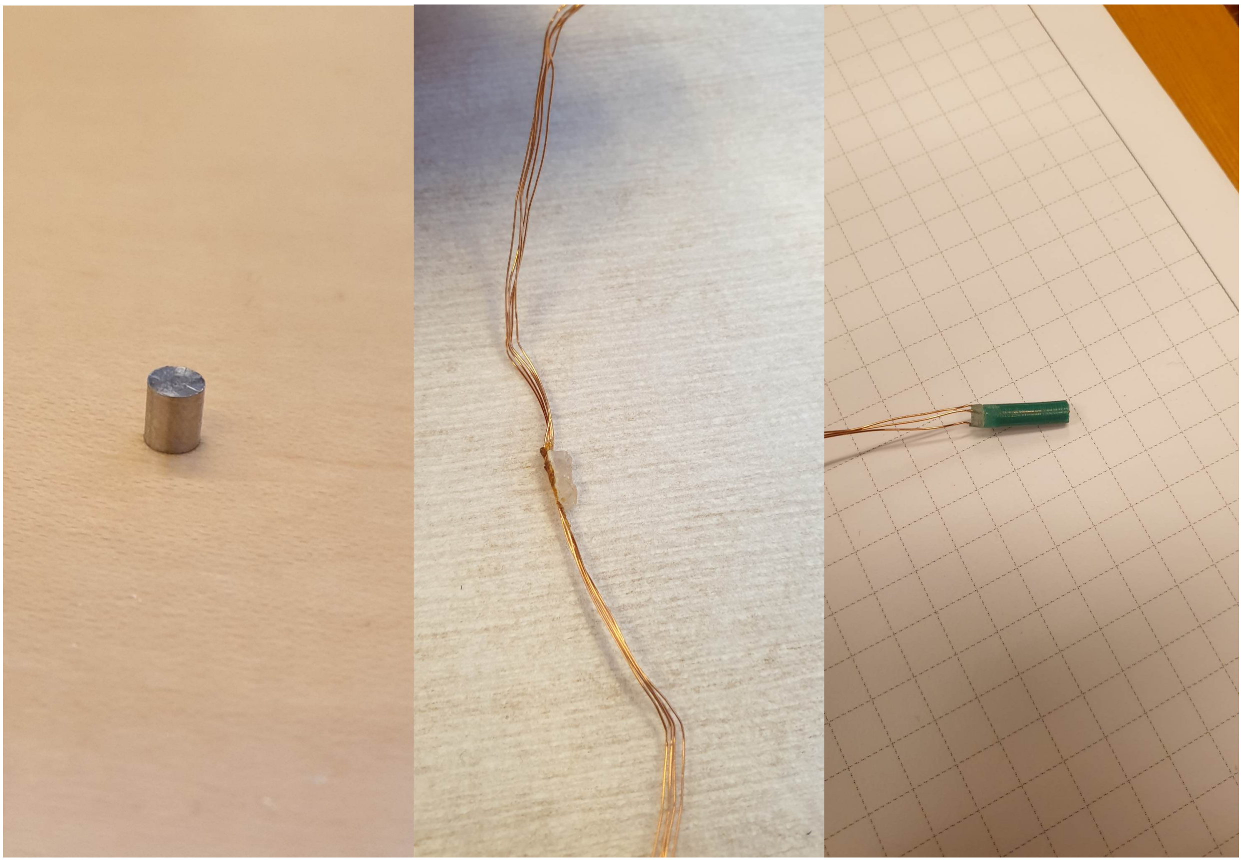

Figure 66: Left: Titanium. **Middle**: Cerium magnesium nitrate **Right** Herbertsmithite.

C Titanium Raw Data ($H_{AC} \approx 36\,\mathrm{Am}^{-1}$)

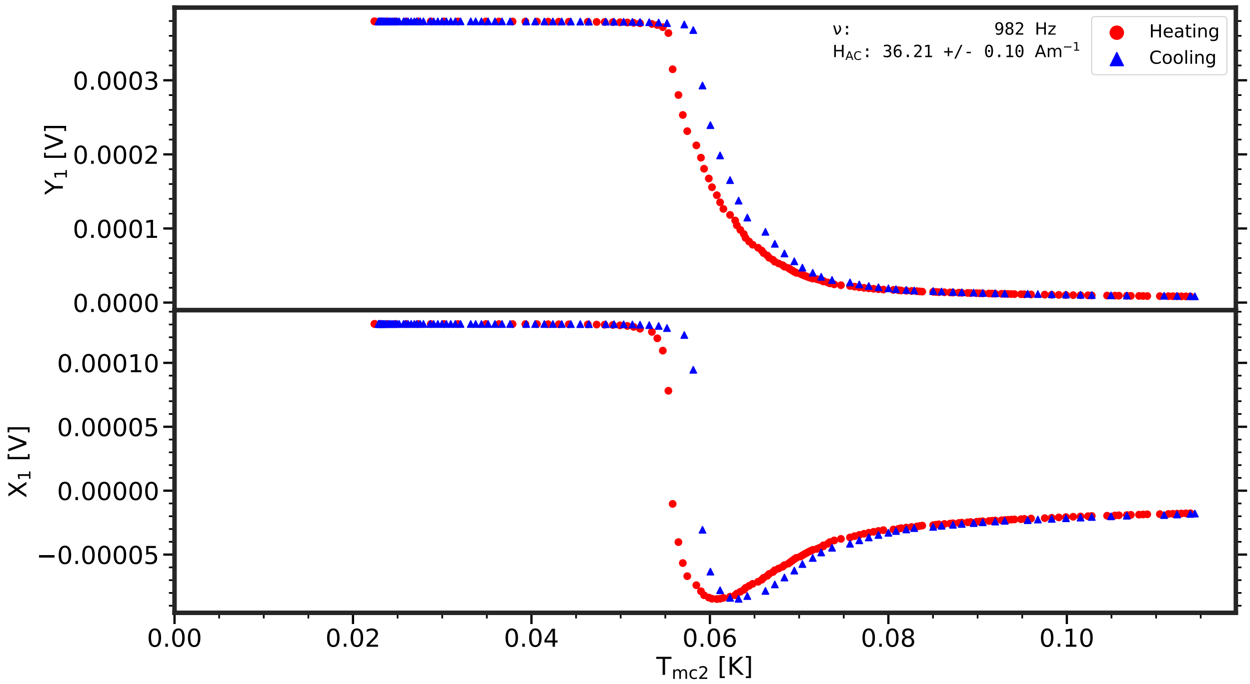

Figure 67: Raw data of the measured voltage across the detection coils as a function of T_{mc2} for $H_{\mathrm{AC}} = 36.2(1)\,\mathrm{Am}^{-1}$ and $\nu = 982\,\mathrm{Hz}$ while heating (●) and cooling (▲). **Top**: The Y_1 component of the voltage. **Bottom**: The X_1 component of the voltage.

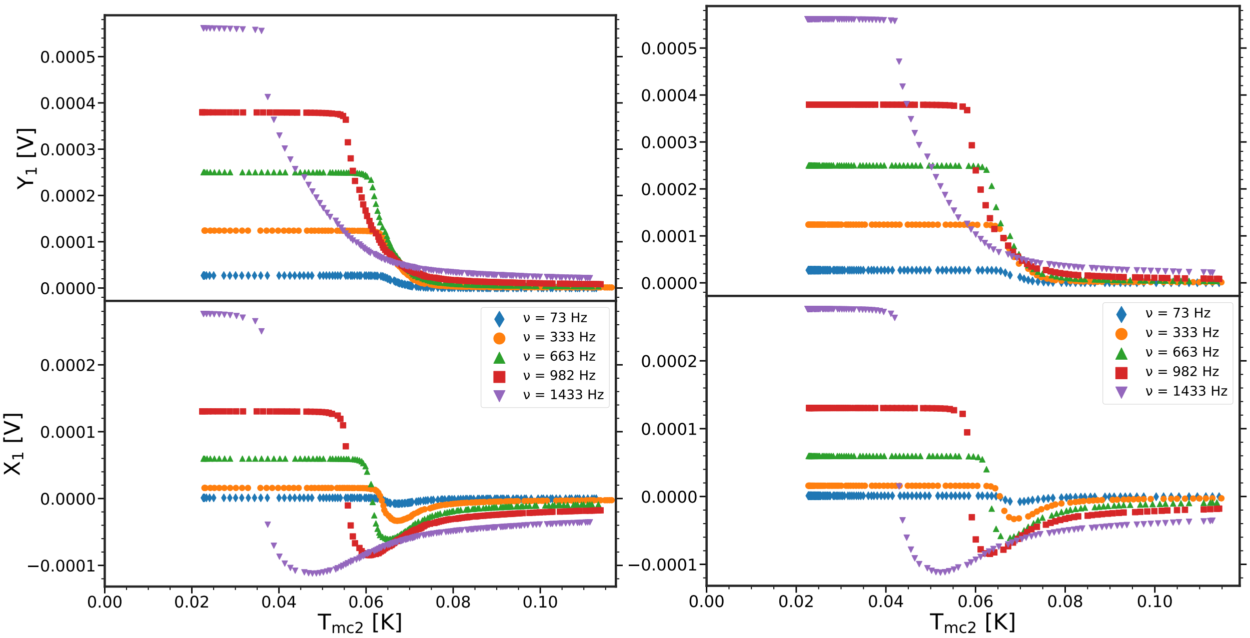

Figure 68: Raw data of the measured voltage across the detection coils as a function of T_{mc2} for $H_{\mathrm{AC}} \approx 36\,\mathrm{Am}^{-1}$ and for excitation frequencies of $\nu = 73\,\mathrm{Hz}$ (◆), $333\,\mathrm{Hz}$ (●), $663\,\mathrm{Hz}$ (▲), $982\,\mathrm{Hz}$ (■) and $1433\,\mathrm{Hz}$ (▼). **Top**: The out-of-phase component (χ_1''). **Bottom**: The in-phase component (χ_1'). **Left**: Measurement taken while heating. **Right**: Measurement taken while cooling.

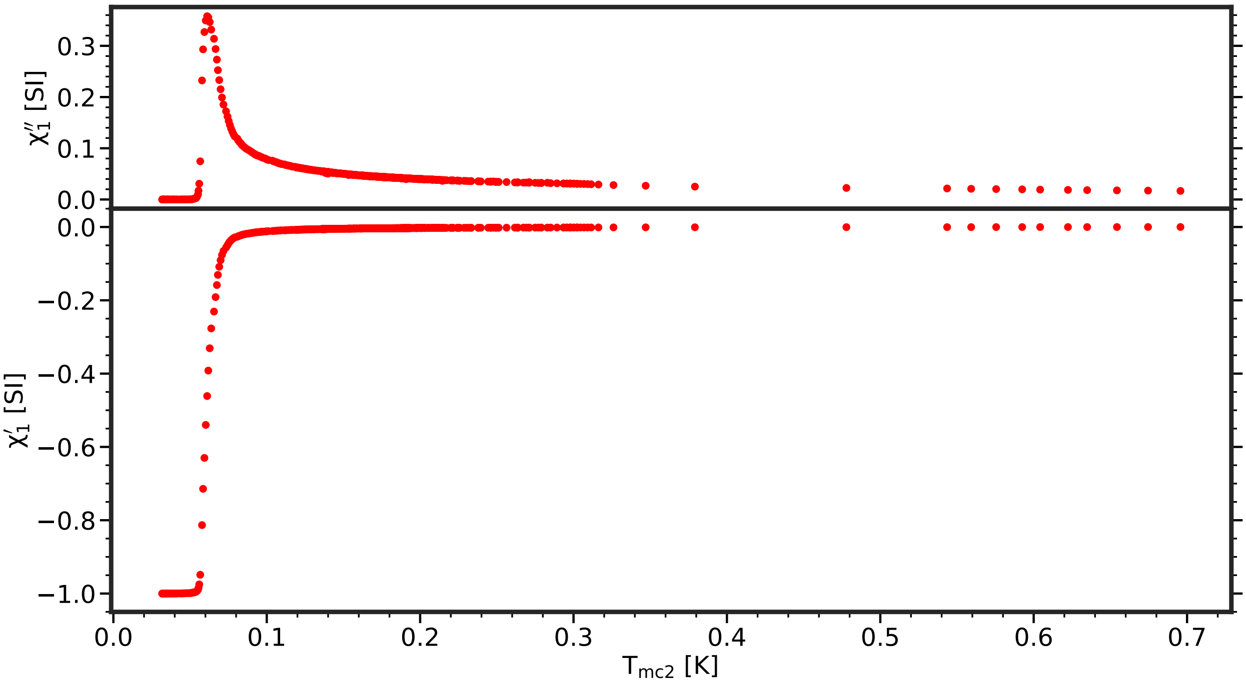

Figure 69: AC susceptibility as a function of T_{mc2} for $H_{\mathrm{AC}} \approx 36\,\mathrm{Am}^{-1}$ and $\nu = 982\,\mathrm{Hz}$ while adding helium to the system such that the sample is cooling down. For high temperatures the thermometer on the cold finger T_{mc2} records a lower temperature than what we would expect the system to be at. This is further dealt with in section 5. **Top**: The out-of-phase component (χ_1''). **Bottom**: The in-phase component (χ_1').

D Titanium Raw Data & Additional Plots ($\mathrm{H_{AC}} \approx 21\,\mathrm{Am^{-1}}$)

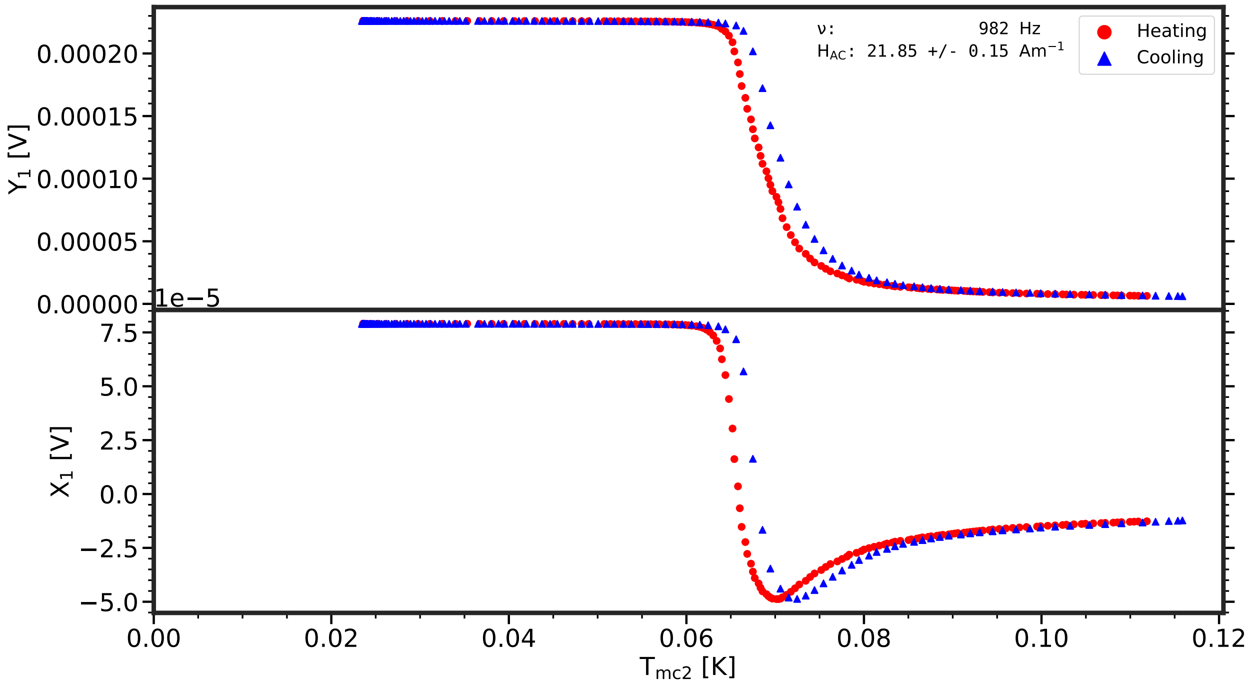

Figure 70: Raw data of the measured voltage across the detection coils as a function of T_{mc2} for $H_{\mathrm{AC}} = 21.9(2)\,\mathrm{Am^{-1}}$ and $\nu = 982\,\mathrm{Hz}$ while heating (●) and cooling (▲). **Top**: The Y_1 component of the voltage. **Bottom**: The X_1 component of the voltage.

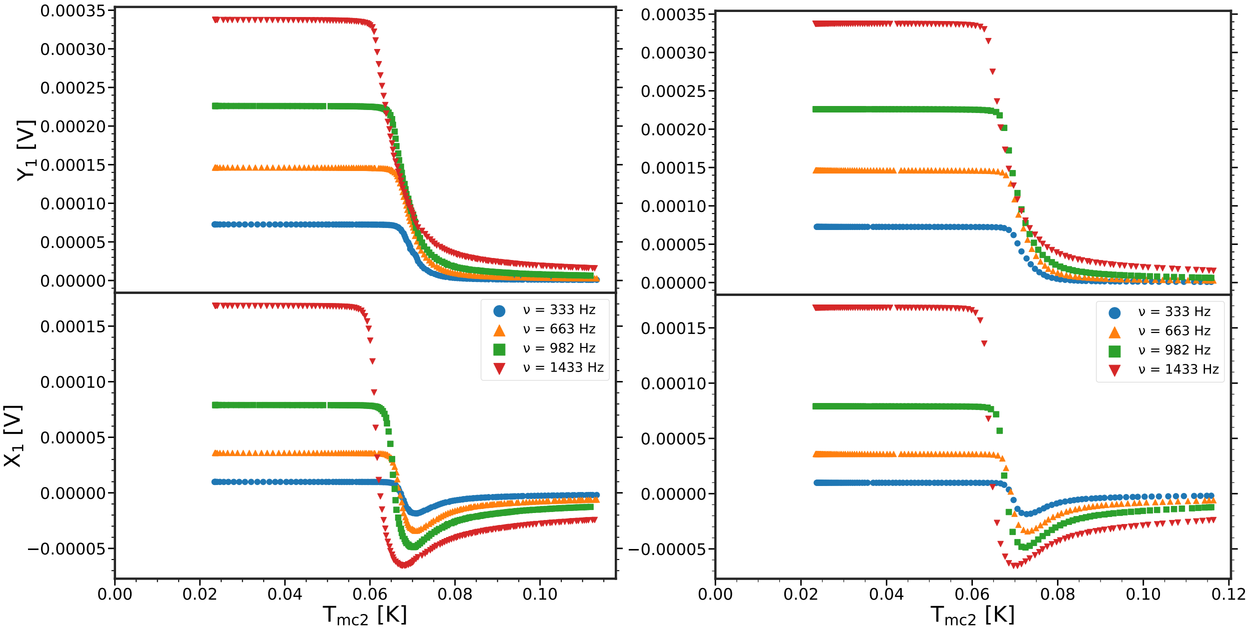

Figure 71: Raw data of the measured voltage across the detection coils as a function of T_{mc2} for $H_{\mathrm{AC}} \approx 21\,\mathrm{Am^{-1}}$ and for excitation frequencies of ν =333 Hz (●), 663 Hz (▲), 982 Hz (■) and 1433 Hz (▼). **Top**: The out-of-phase component χ_1''. **Bottom**: The in-phase component χ_1'. **Left**: Measurement taken while heating. **Right**: Measurement taken while cooling.

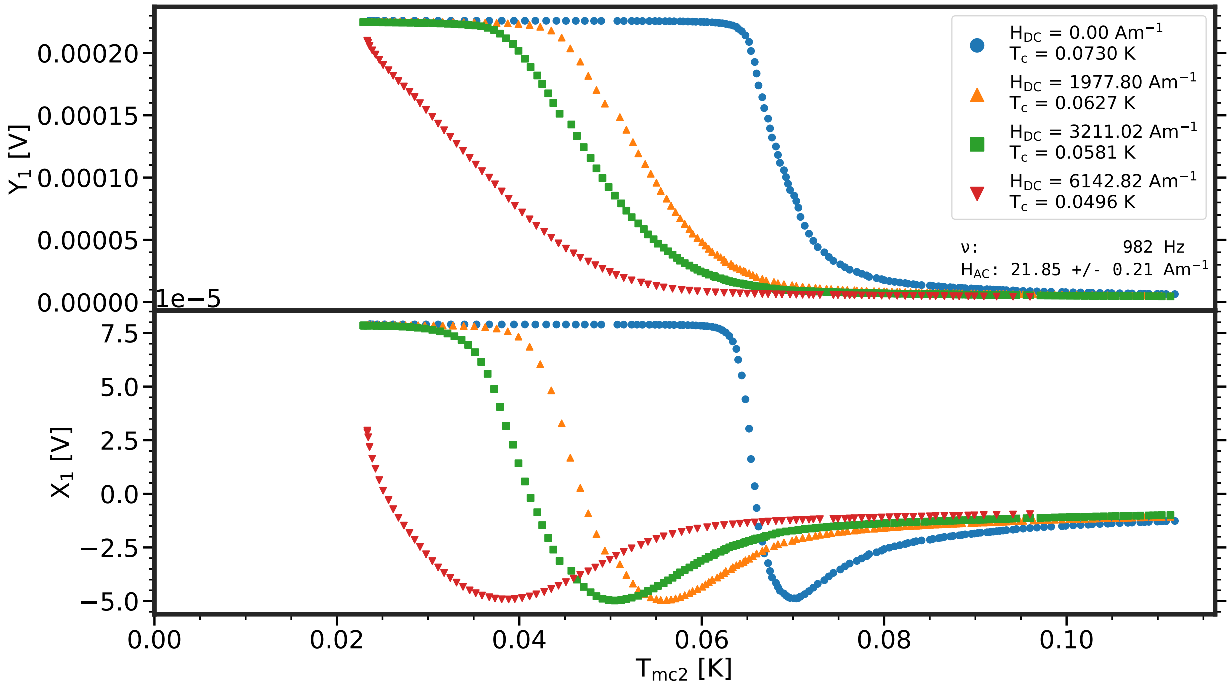

Figure 72: Raw data of the measured voltage across the detection coils as a function of T_{mc2} for $H_{\mathrm{AC}} = 21.9(2)\,\mathrm{Am}^{-1}$ and for DC background fields of $\mathrm{H}_{\mathrm{DC}} = 0\,\mathrm{Am}^{-1}$ (●), $1977.80\,\mathrm{Am}^{-1}$ (▲), $3211.02\,\mathrm{Am}^{-1}$ (■) and $6142.82\,\mathrm{Am}^{-1}$ (▼). **Top**: The Y_1 component of the voltage. **Bottom**: The X_1 component of the voltage.

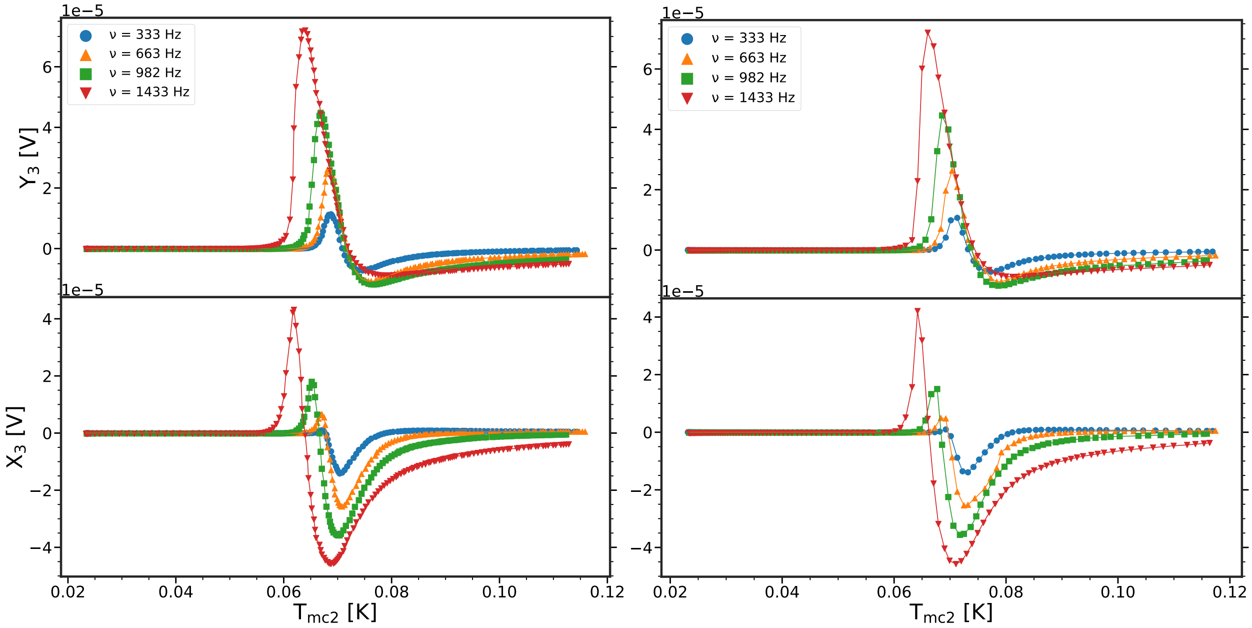

Figure 73: 3rd harmonic raw data of the measured voltage across the detection coils as a function of T_{mc2} for $H_{\mathrm{AC}} \approx 21\,\mathrm{Am}^{-1}$ and for excitation frequencies of $\nu = 333\,\mathrm{Hz}$ (●), $663\,\mathrm{Hz}$ (▲), $982\,\mathrm{Hz}$ (■) and $1433\,\mathrm{Hz}$ (▼). **Top**: The Y_3 component of the voltage. **Bottom**: The X_3 component of the voltage. **Left**: Measurement taken while heating. **Right**: Measurement taken while cooling.

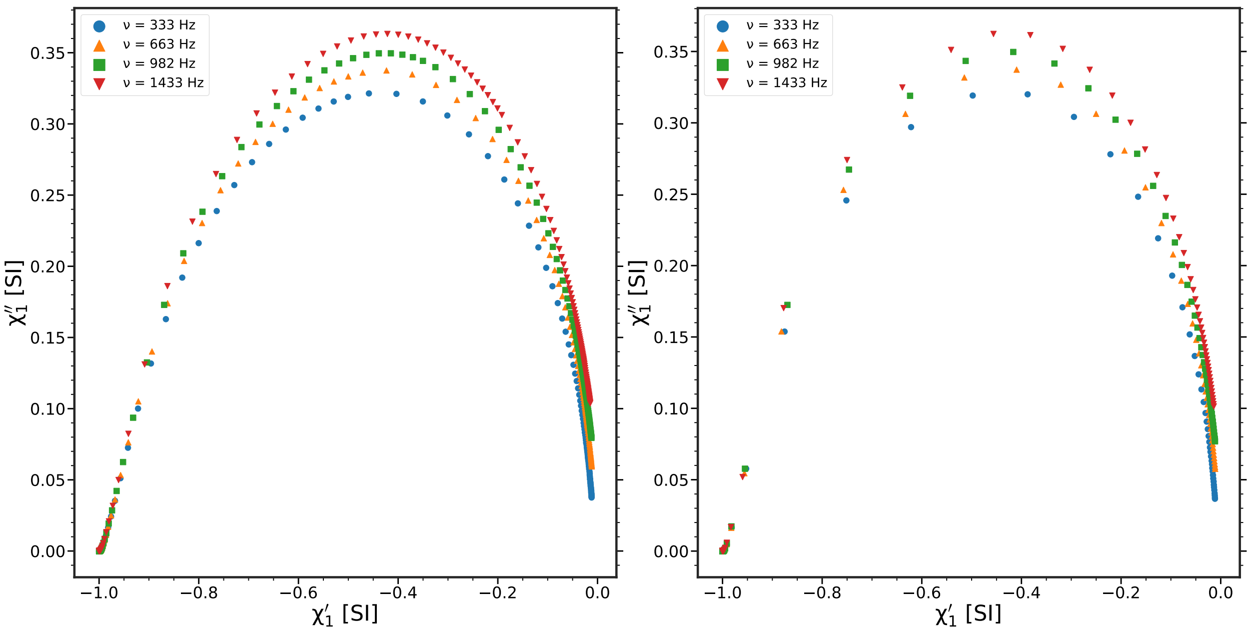

Figure 74: Cole-Cole plots as a function of T_{mc2} for $H_{\mathrm{AC}} \approx 21\,\mathrm{Am}^{-1}$ and for excitation frequencies of ν =333 Hz (●), 663 Hz (▲), 982 Hz (■) and 1433 Hz (▼). This figure corresponds to the susceptibilities plotted in Fig. 26. **Left**: Measurement taken while heating. **Right**: Measurement taken while cooling.

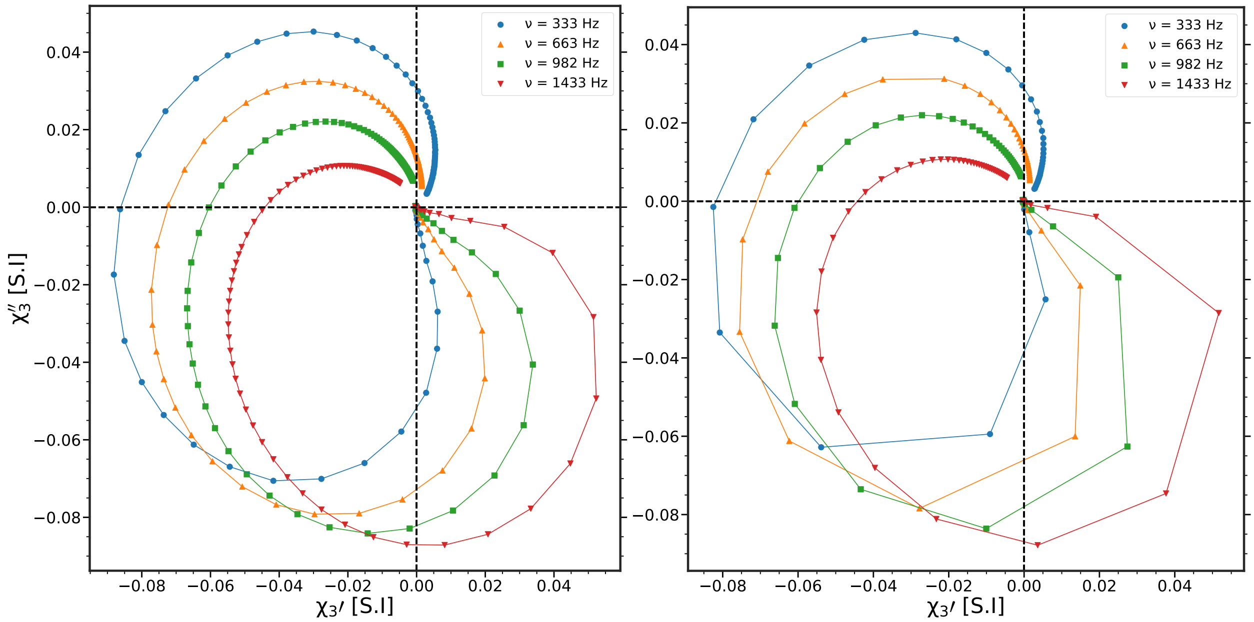

Figure 75: 3rd harmonic ($\Theta_3 = 0$) Cole-Cole plots as a function of T_{mc2} for $H_{\mathrm{AC}} \approx 21\,\mathrm{Am}^{-1}$ and for excitation frequencies of ν =333 Hz (●), 663 Hz (▲), 982 Hz (■) and 1433 Hz (▼). This figure corresponds to the susceptibilities plotted in Fig. 30. **Left**: Measurement taken while heating. **Right**: Measurement taken while cooling.

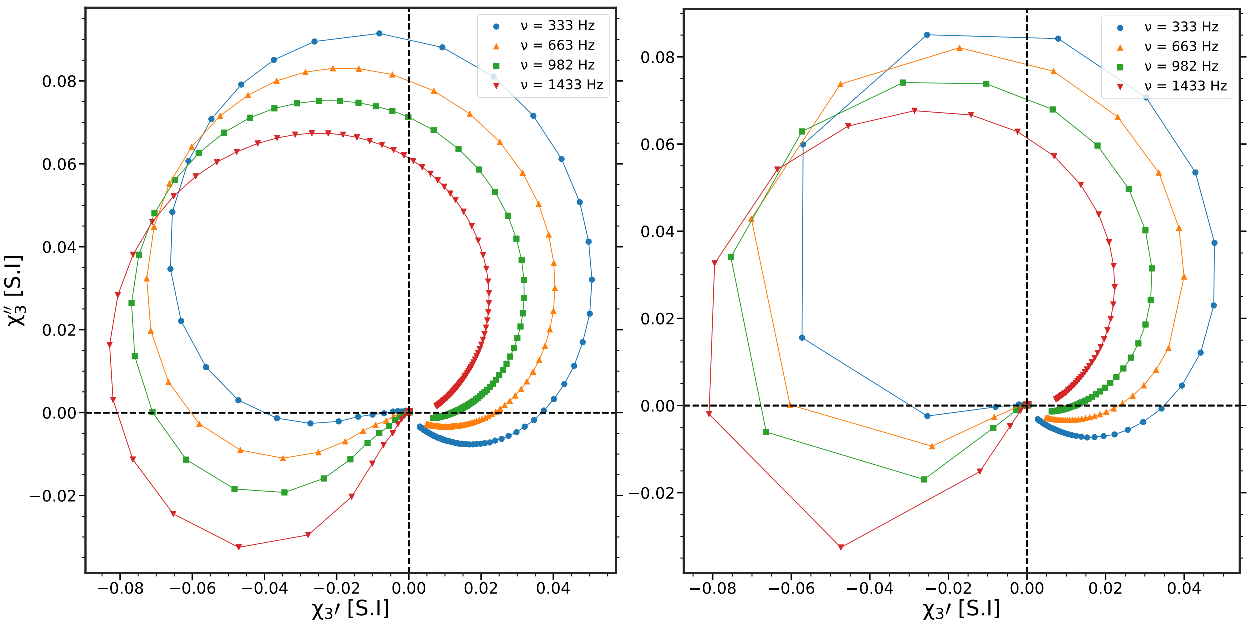

Figure 76: 3rd harmonic ($\Theta_3 = \Theta_{n=1}$) Cole-Cole plots as a function of T_{mc2} for $H_{AC} \approx 21\,Am^{-1}$ and for excitation frequencies of ν =333 Hz (●), 663 Hz (▲), 982 Hz (■) and 1433 Hz (▼). This figure corresponds to the susceptibilities plotted in Fig. 31. **Left**: Measurement taken while heating. **Right**: Measurement taken while cooling.

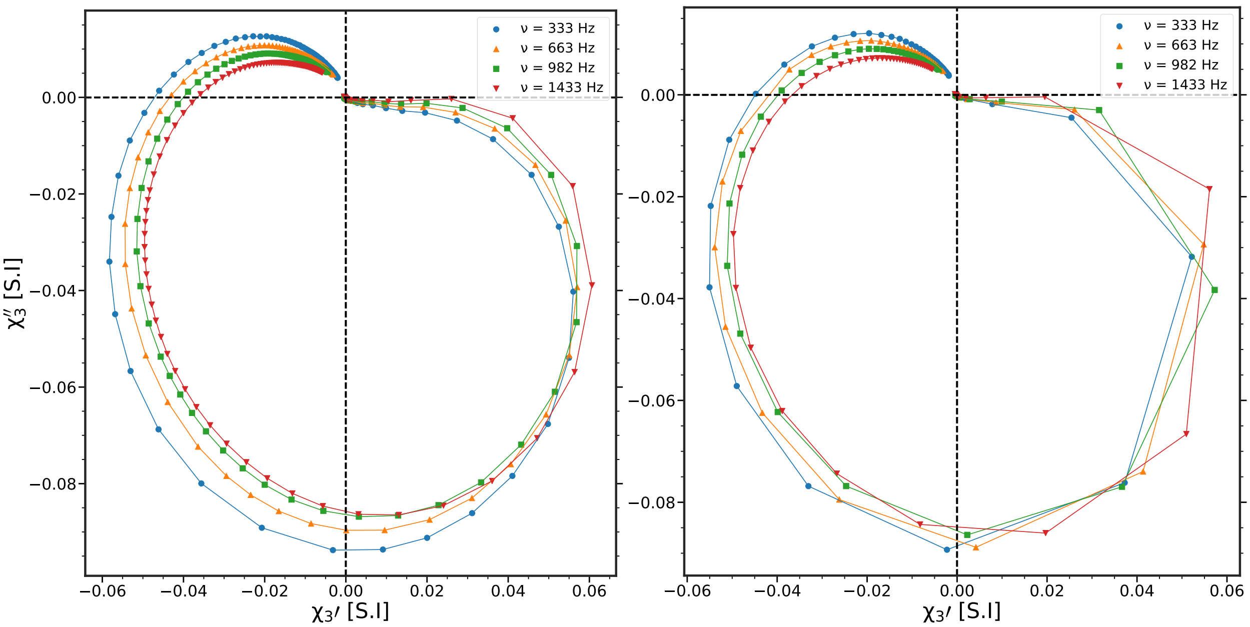

Figure 77: 3rd harmonic ($\Theta_3 = 3 \cdot \Theta_{n=1}$) Cole-Cole plots as a function of T_{mc2} for $H_{AC} \approx 21\,Am^{-1}$ and for excitation frequencies of ν =333 Hz (●), 663 Hz (▲), 982 Hz (■) and 1433 Hz (▼). This figure corresponds to the susceptibilities plotted in Fig. 32. **Left**: Measurement taken while heating. **Right**: Measurement taken while cooling.

E Amen Et Al Measurements for Comparison

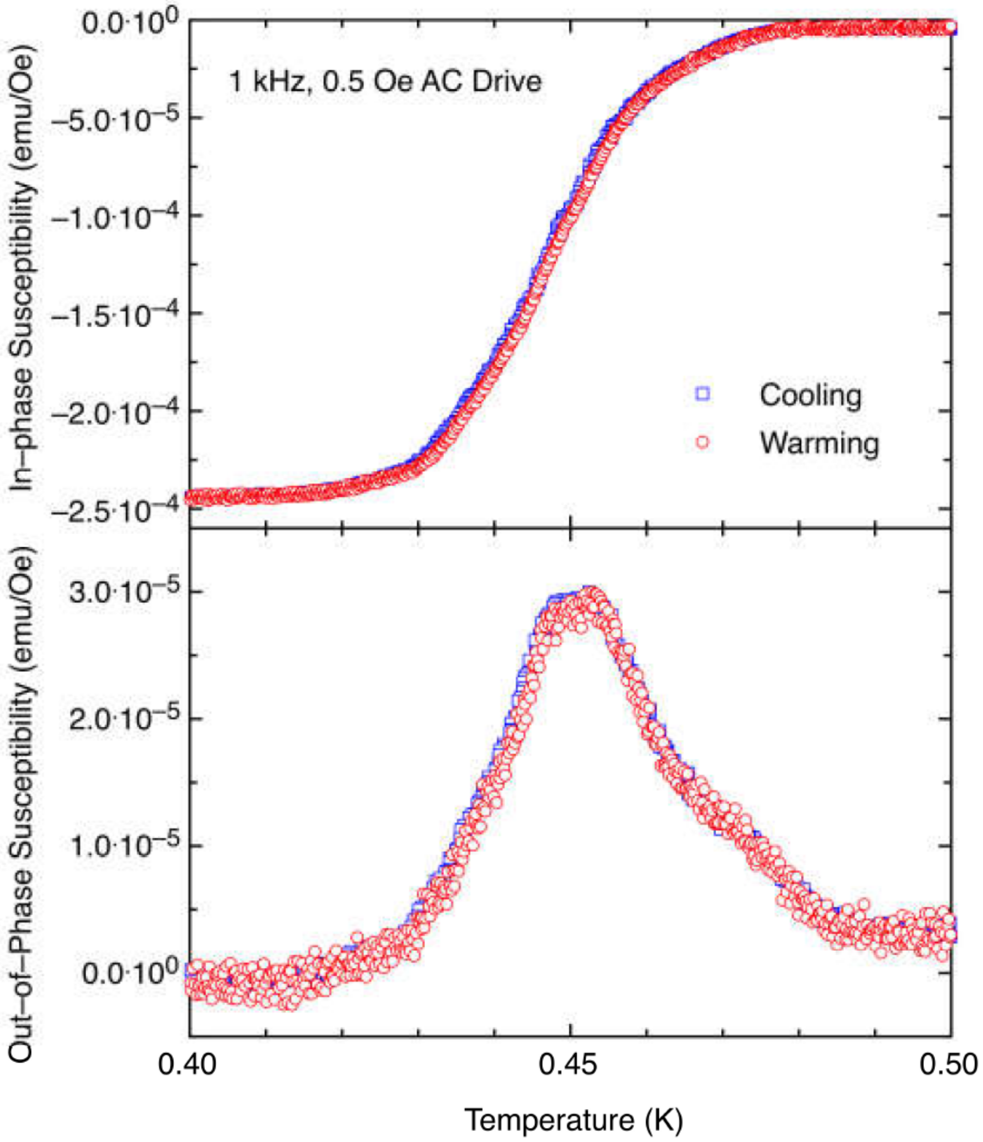

Figure 78: AC susceptibility of titanium at 1 kHz while cooling and warming from [2]. **Top**: In-phase susceptibility. **Bottom**: Out-of-phase susceptibility.

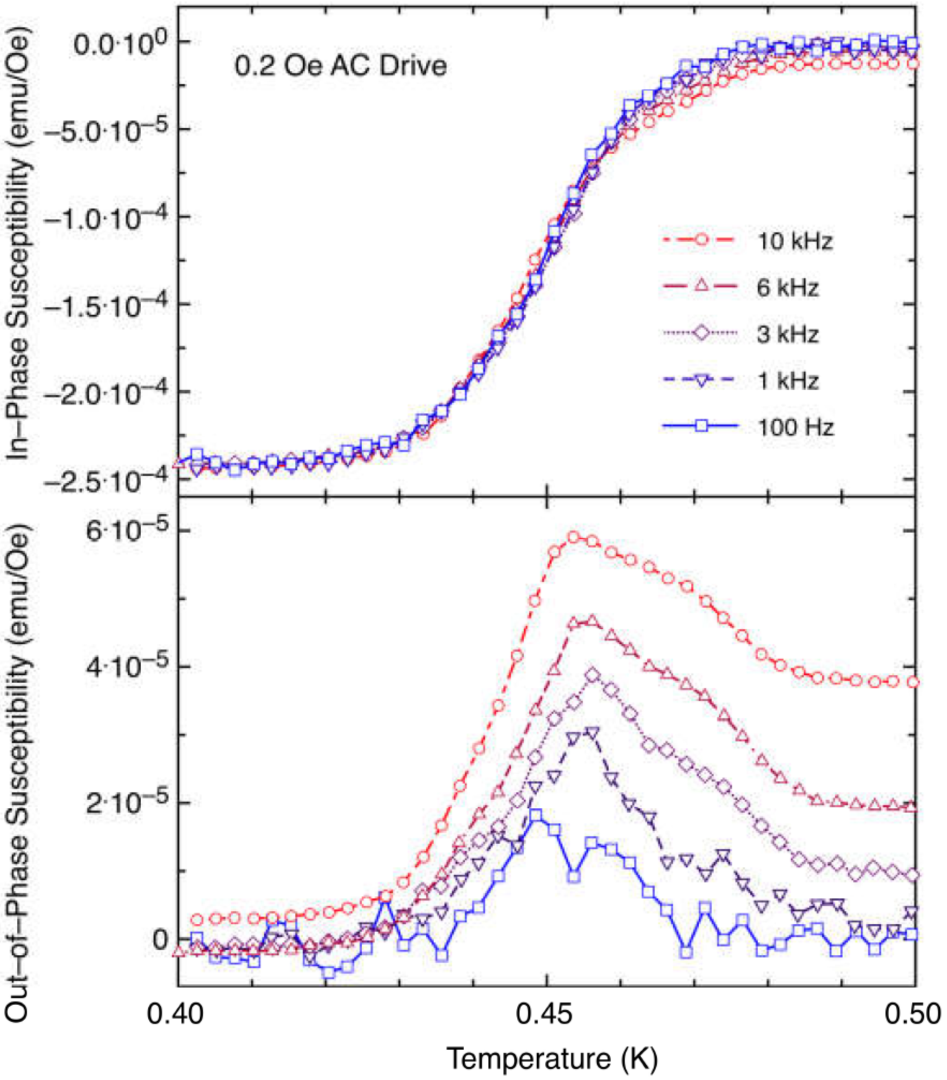

Figure 79: AC susceptibility of titanium for various excitation frequencies from [2]. **Top**: In-phase susceptibility. **Bottom**: Out-of-phase susceptibility.

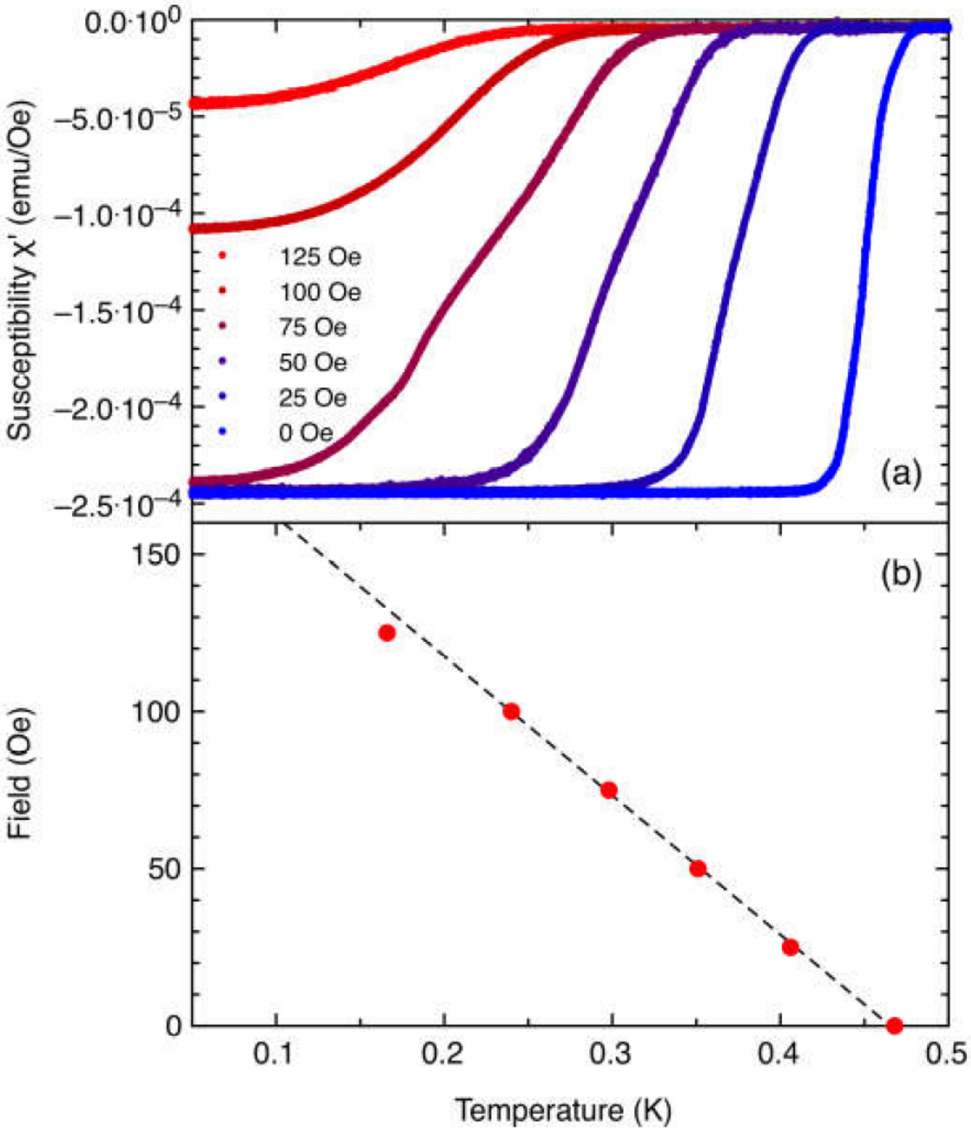

Figure 80: AC susceptibility of titanium for various DC fields from [2]. **Top**: In-phase susceptibility. **Bottom**: DC field vs the estimated onset critical temperatures. The slope of the dashed line is reported to be - 443 $\frac{\mathrm{Oe}}{\mathrm{K}}$.

F Pal Et Al Measurements for Comparison

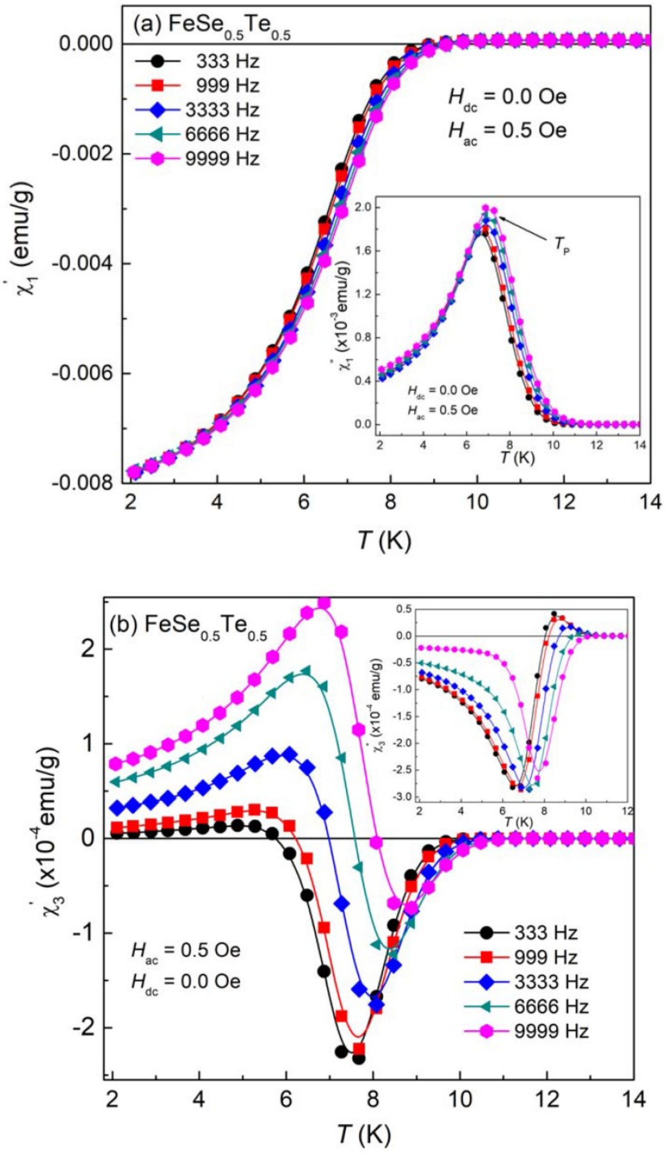

Figure 81: 1st and 3rd harmonic AC susceptibility of the superconductor FeSe$_{0.5}$Te$_{0.5}$ as a function of temperature for various excitation frequencies from [38]. This is used for comparison in section 4.7.1. **Top**: 1st harmonic susceptibility, where the main plot is the in-phase component vs temperature and the insert is the out-of-phase component vs temperature. **Bottom**: 3rd harmonic susceptibility for different frequencies, where the main plot is the in-phase component vs temperature and the insert shows the out-of-phase component vs temperature.

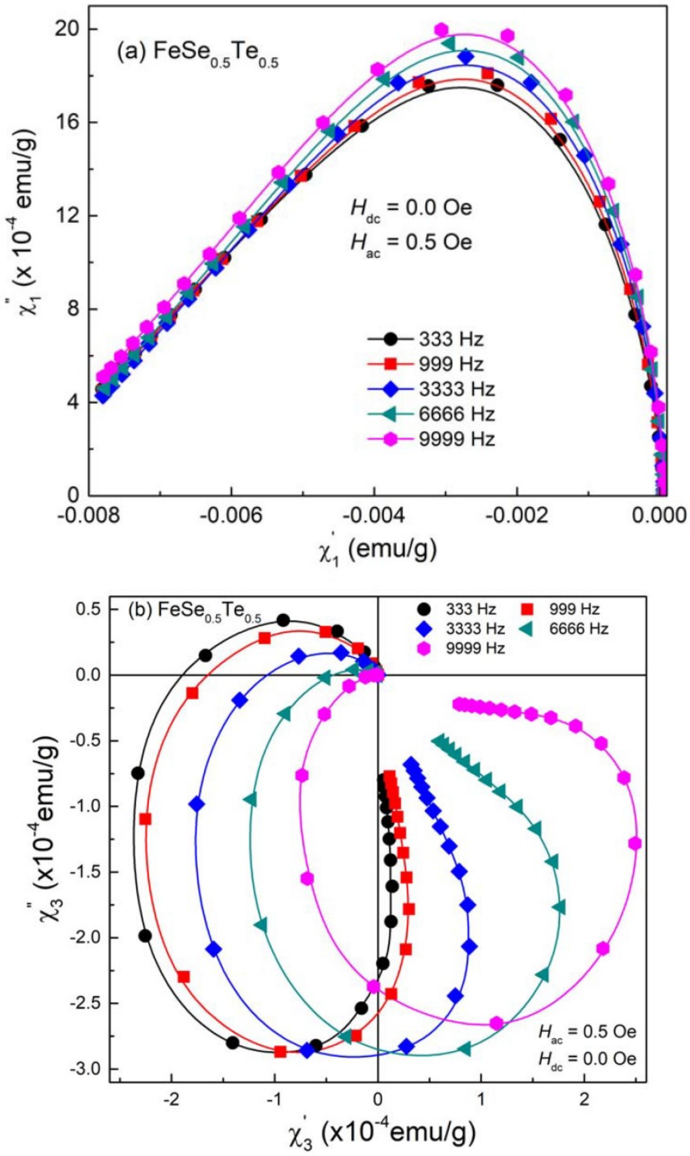

Figure 82: Cole-Cole plots for 1st and 3rd harmonic AC susceptibility of $FeSe_{0.5}Te_{0.5}$ as a function of temperature for various excitation frequencies from [38]. **Top**: 1st harmonic susceptibility. **Bottom**: 3rd harmonic susceptibility.

G Polichetti et al Measurements for Comparison

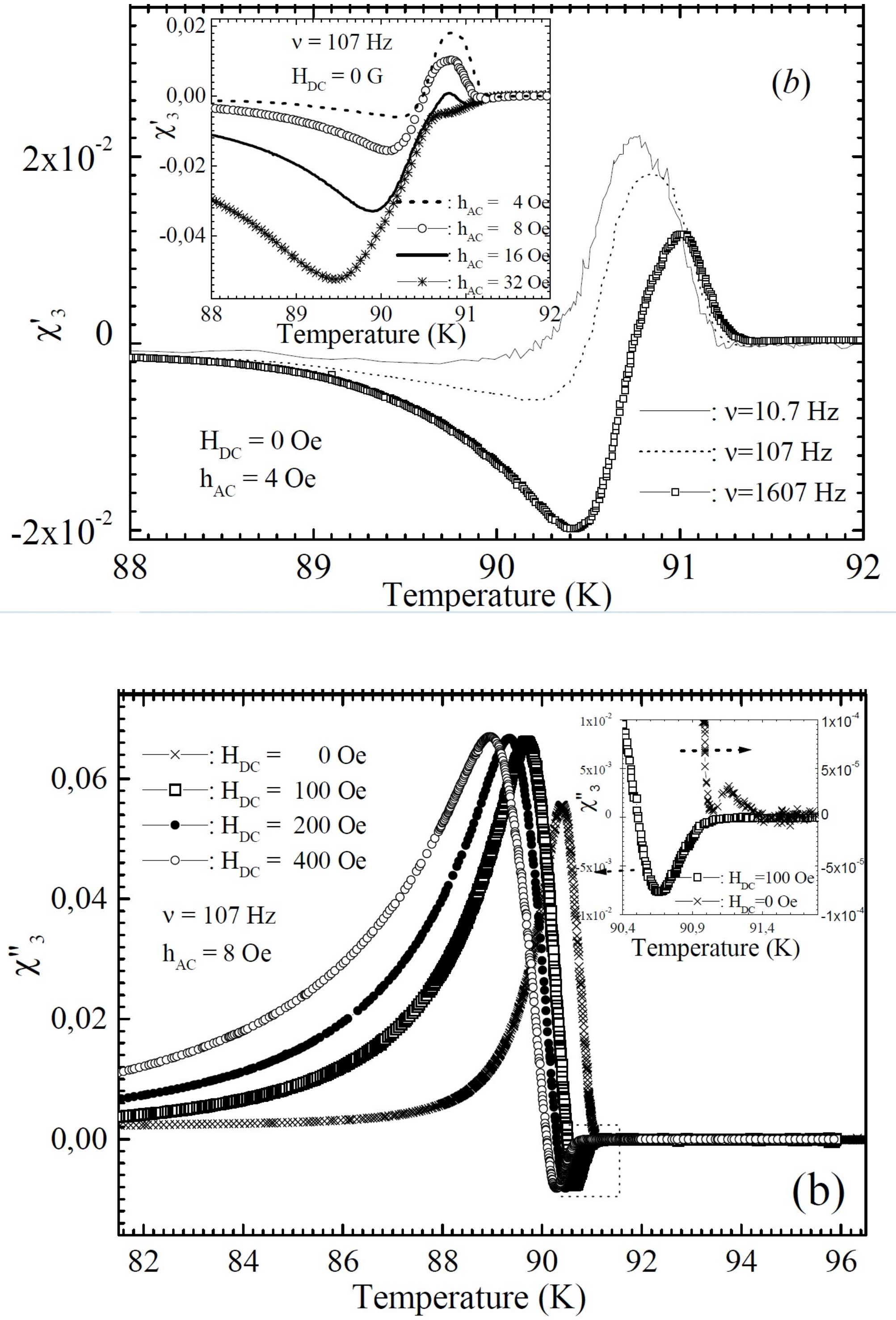

Figure 83: 3rd harmonic (for the phase adjustment of $\Theta' = \Theta_{n=1}$) AC susceptibility of $Y_1Ba_2Cu_3O_{7-x}$ as a function of temperature for various excitation frequencies from [42]. This is used for comparison in section 4.7.2. **Top**: The in-phase component (χ_3') **Bottom**: The out-of-phase component (χ_3'')

H Gioacchino Et Al Measurements for Comparison

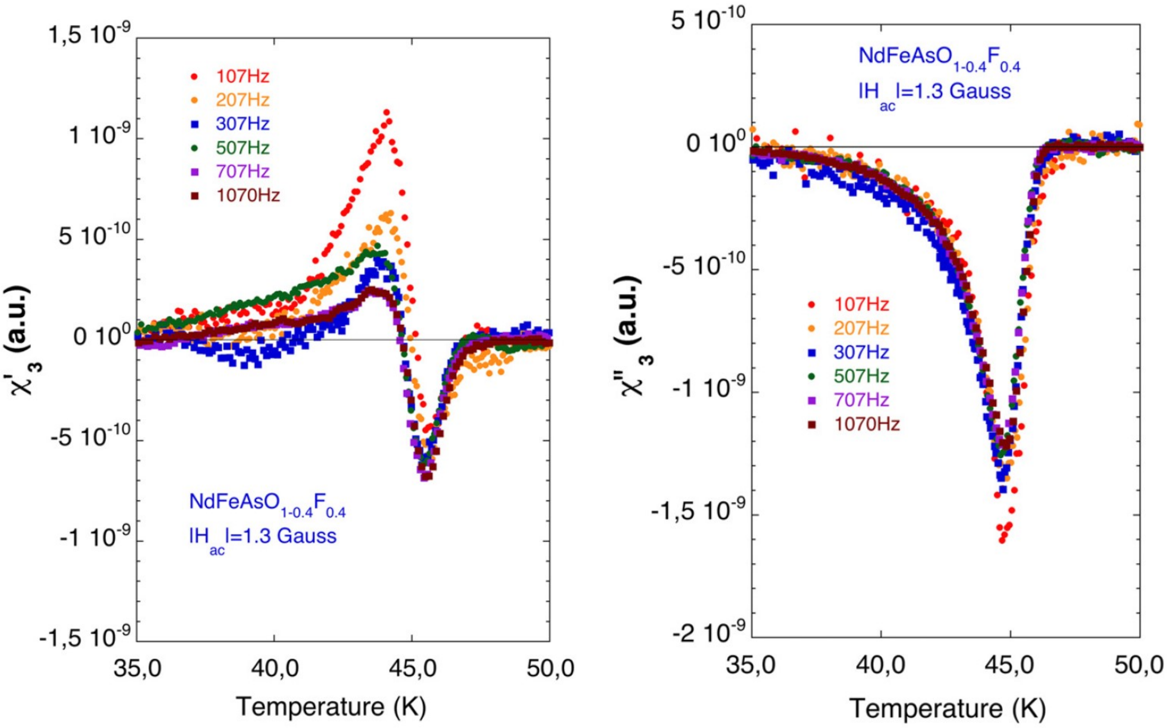

Figure 84: 3rd harmonic AC susceptibility of NdO$_{1-0.14}$F$_{0.14}$FeAs as a function of temperature for various excitation frequencies from [41]. It is used for comparison in section 4.7.3. **Left**: The in-phase component (χ_3'). **Right**: The out-of-phase component (χ_3'').

I 3rd Harmonic Susceptibilities Phase adjustment of $\Theta_3 = \frac{\pi}{2} + 3 \cdot \left(\Theta_{n=1} - \frac{\pi}{2}\right)$

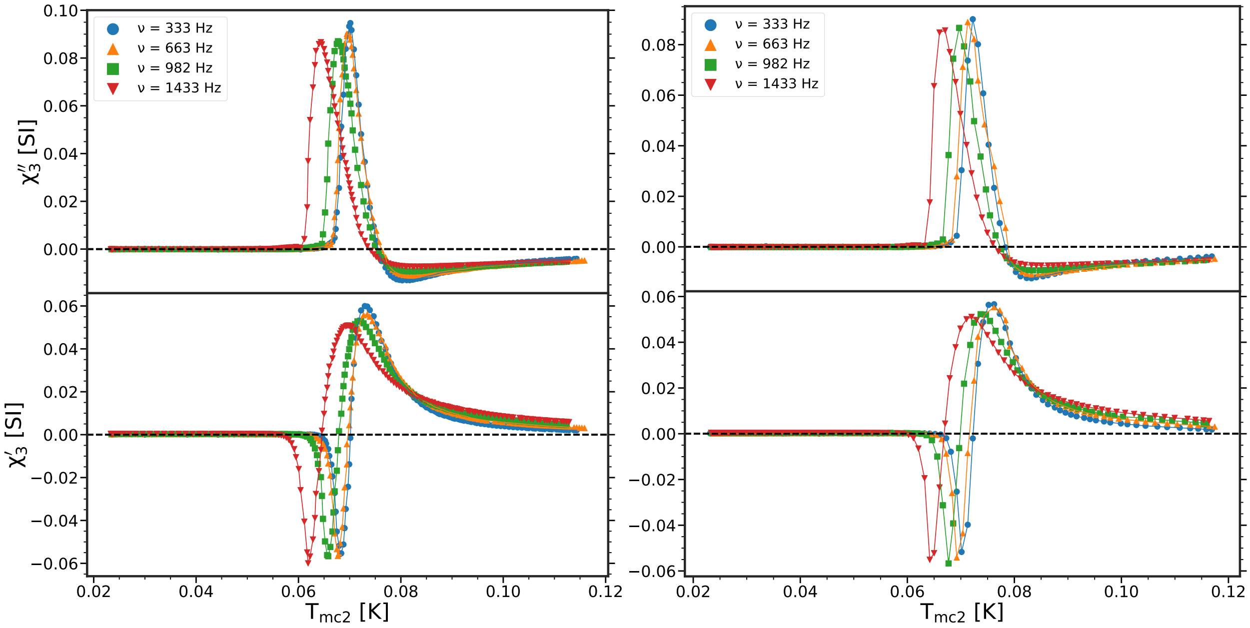

Figure 85: 3rd harmonic ($\Theta_3 = \frac{\pi}{2} + 3 \cdot \left(\Theta_{n=1} - \frac{\pi}{2}\right)$) AC susceptibility as a function of T_{mc2} for $H_{\mathrm{AC}} \approx 21\,\mathrm{Am}^{-1}$ and for excitation frequencies of $\nu = 333\,\mathrm{Hz}$ (●), 663 Hz (▲), 982 Hz (■) and 1433 Hz (▼). The linear spline connecting the data points is simply to guide the eye. **Top**: Shows the out-of-phase component (χ_3''). **Bottom**: Shows the in-phase component (χ_3'). **Left**: Measurements taken while heating. **Right**: Measurements taken while cooling.

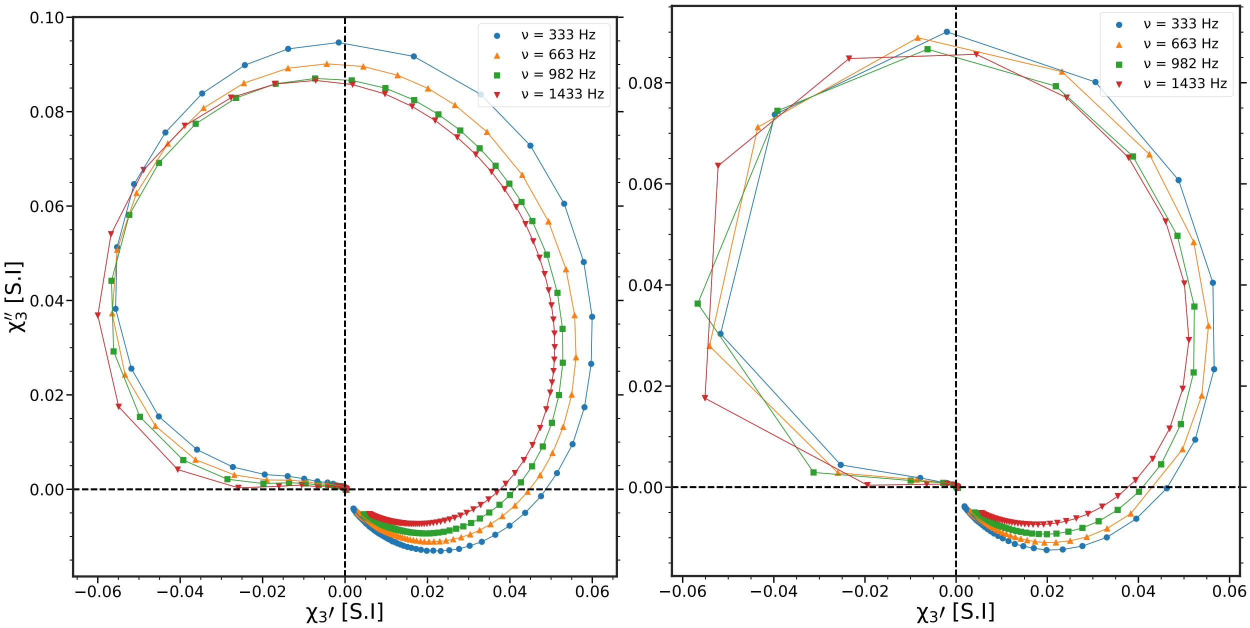

Figure 86: 3rd harmonic ($\Theta_3 = \frac{\pi}{2} + 3 \cdot \left(\Theta_{n=1} - \frac{\pi}{2}\right)$) Cole-Cole plots as a function of T_{mc2} for $H_{\mathrm{AC}} \approx 21\,\mathrm{Am}^{-1}$ and for excitation frequencies of ν =333 Hz (●), 663 Hz (▲), 982 Hz (■) and 1433 Hz (▼). This figure corresponds to the susceptibilities plotted in figure 32. **Left**: Measurement taken while heating. **Right**: Measurement taken while cooling.

J Appendix of CMN

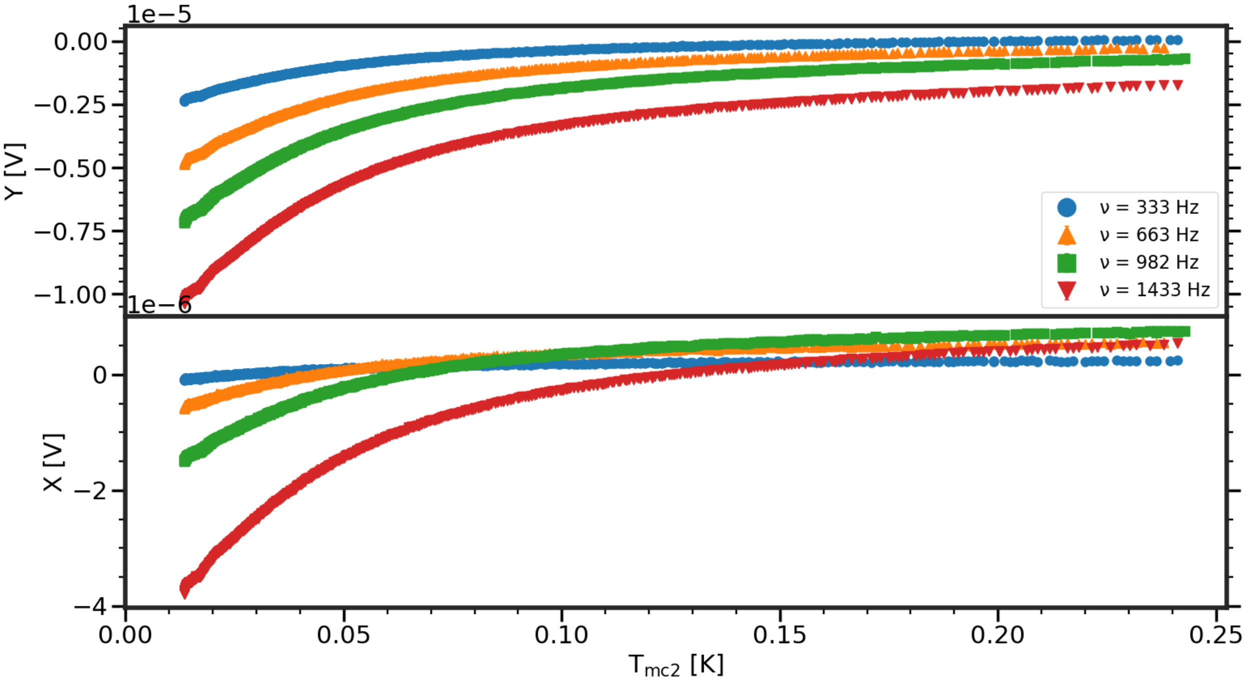

Figure 87: Raw data of the measured voltage across the detection coils as a function of T_{mc2} for $H_{\mathrm{AC}} = 17\,\mathrm{Am}^{-1}$ and for excitation frequencies of ν =333 Hz (●), 663 Hz (▲), 982 Hz (■) and 1433 Hz (▼). **Top**: The Y_1 component of the voltage. **Bottom**: The X_1 component of the voltage.

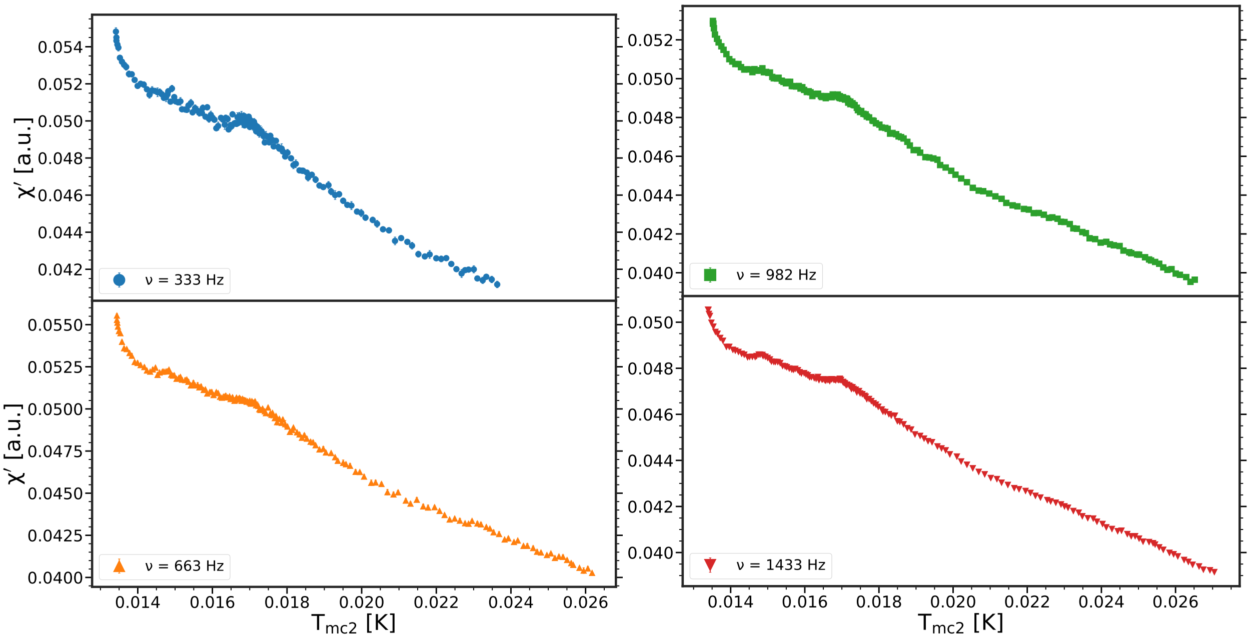

Figure 88: AC susceptibility as a function of T_{mc2} for $H_{\mathrm{AC}} = 17\,\mathrm{Am}^{-1}$ and for excitation frequencies of ν =333 Hz (●), 663 Hz (▲), 982 Hz (■) and 1433 Hz (▼). A zoom in of Fig. 34 at low temperatures to show the slight unstable signal, presumably caused the poor thermal conductivity of the CMN sample.

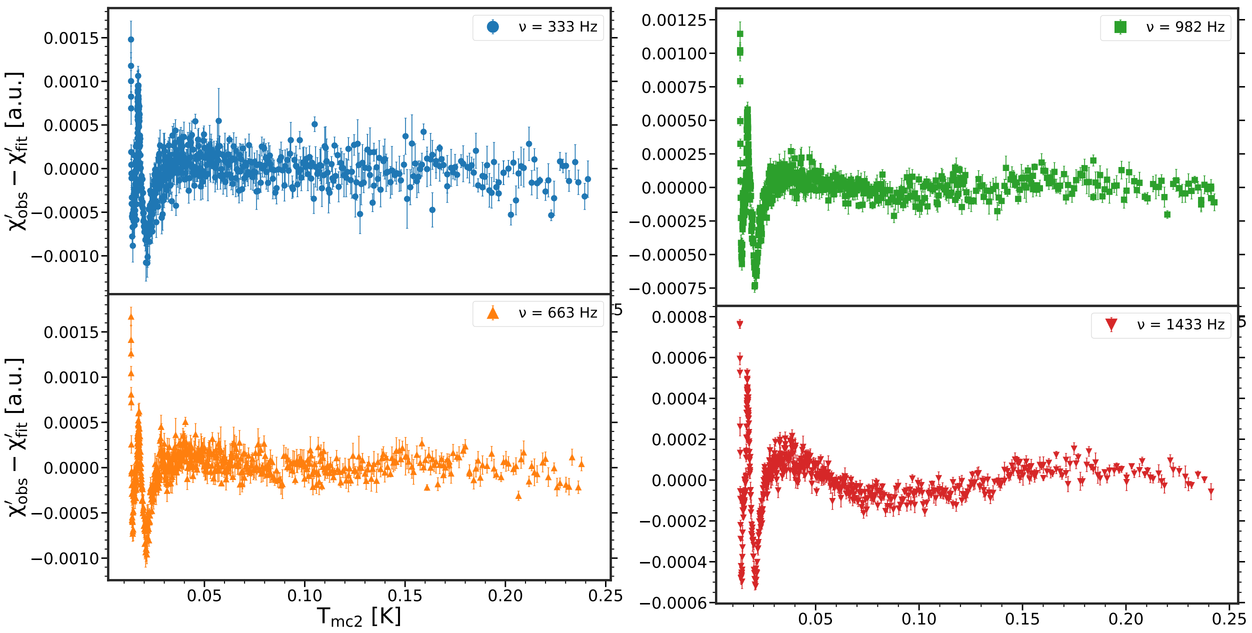

Figure 89: Residuals between the data and the fit from Fig. 35 as a function of T_{mc2} for $H_{\mathrm{AC}} \approx 17\,\mathrm{Am}^{-1}$ and for excitation frequencies of ν =333 Hz (●), 663 Hz (▲), 982 Hz (■), and 1433 Hz (▼). Shows that the data deviates slightly at lower temperatures. Further, there is a small deviation at $\sim$ 100 mK in the case of 1433 Hz (▼).

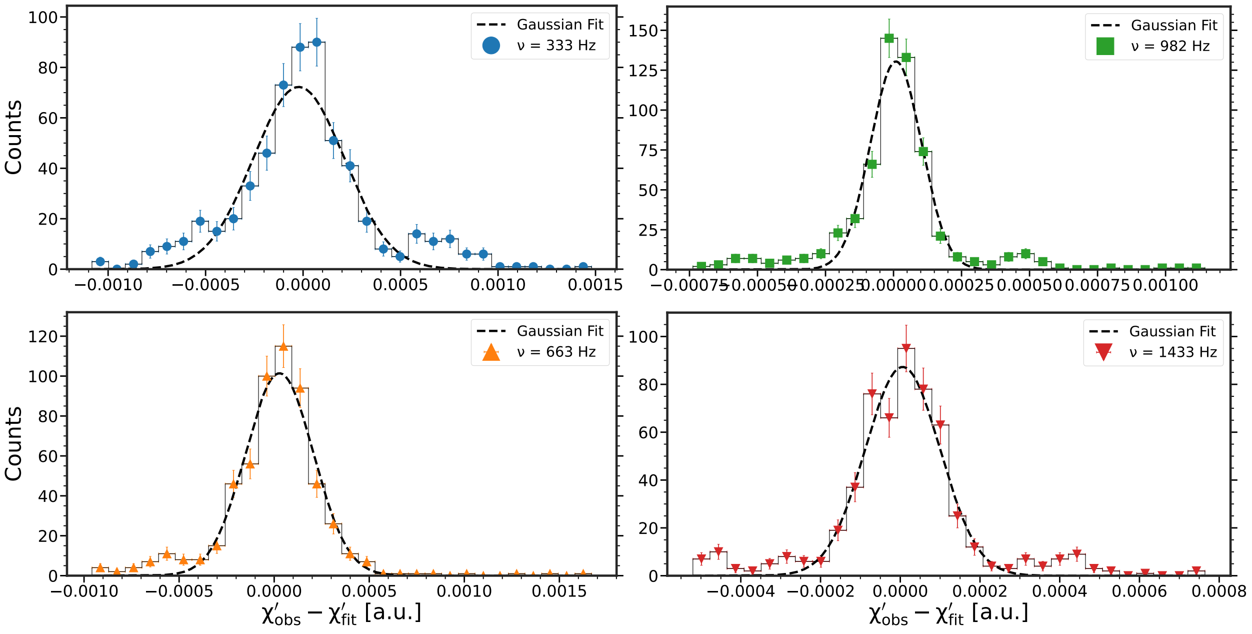

Figure 90: Distribution of residuals between the data and the fit from Fig. 35 for $H_{\mathrm{AC}} \approx 17\,\mathrm{Am}^{-1}$ and for excitation frequencies of ν =333 Hz (●), 663 Hz (▲), 982 Hz (■), and 1433 Hz (▼). A Gaussian fit has been applied to each frequency to illustrate the Gaussian-like behaviour.

ν [Hz]	333	663	982	1433
N	496(23)	518(23)	488(22)	479(22)
μ	$-0.022(12) \times 10^{-3}$	$28(8) \times 10^{-6}$	$9(5) \times 10^{-6}$	$6(4) \times 10^{-6}$
σ	$0.234(15) \times 10^{-3}$	$178(7) \times 10^{-6}$	$94(5) \times 10^{-6}$	$94(4) \times 10^{-6}$

Table 11: Fit parameters on the Gaussian fits in Fig. 90

J.1 Procedure From Section 5 For Cooling Measurements

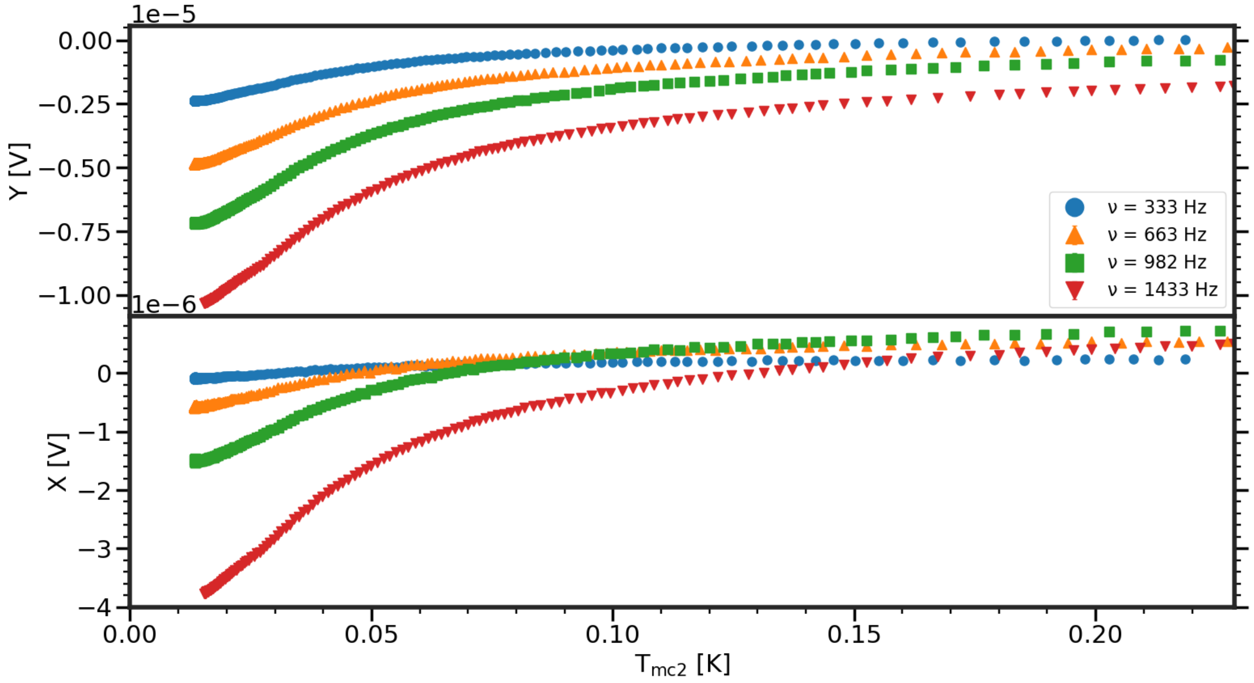

Figure 91: Raw data of the measured voltage across the detection coils as a function of T_{mc2} for $H_{\mathrm{AC}} = 17\,\mathrm{Am}^{-1}$ and for excitation frequencies of ν =333 Hz (●), 663 Hz (▲), 982 Hz (■), and 1433 Hz (▼). **Top**: The Y_1 component of the voltage. **Bottom**: The X_1 component of the voltage.

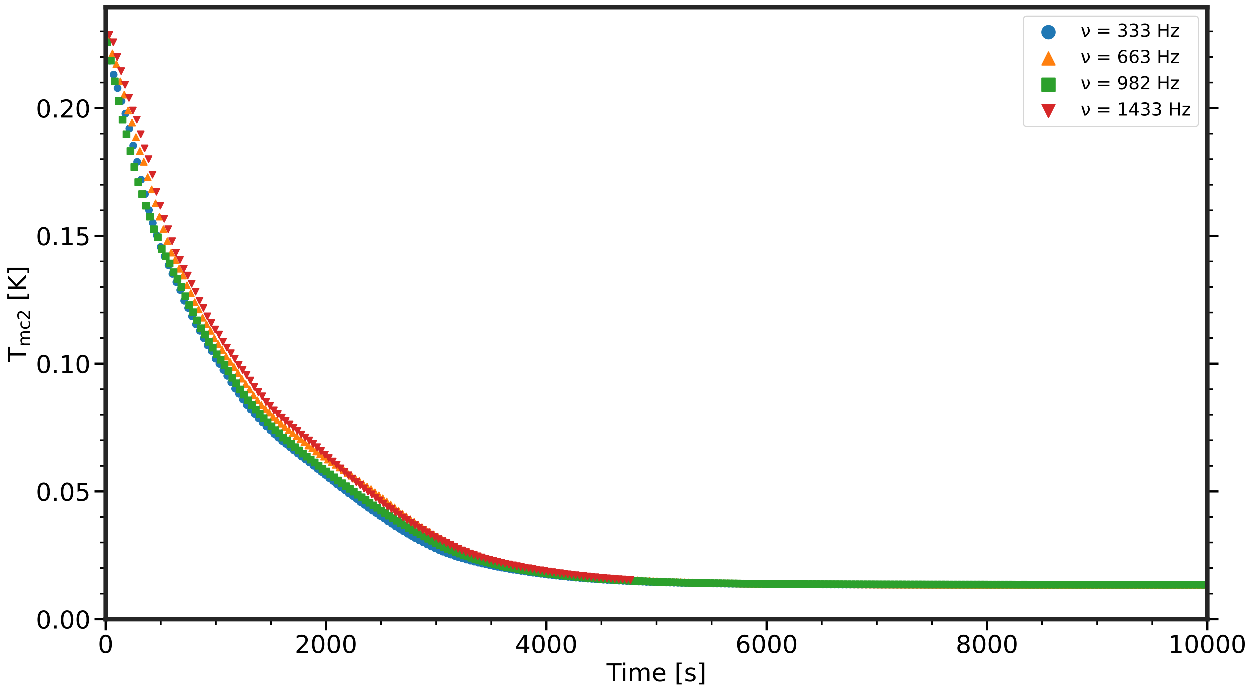

Figure 92: Cold finger temperature T_{mc2} as a function of time during the AC susceptibility measurements for a field strength of $H_{\mathrm{AC}} \approx 17\,\mathrm{Am}^{-1}$ and excitation frequencies of $\nu = 333\,\mathrm{Hz}$ (●), 663 Hz (▲), 982 Hz (■), and 1433 Hz (▼).

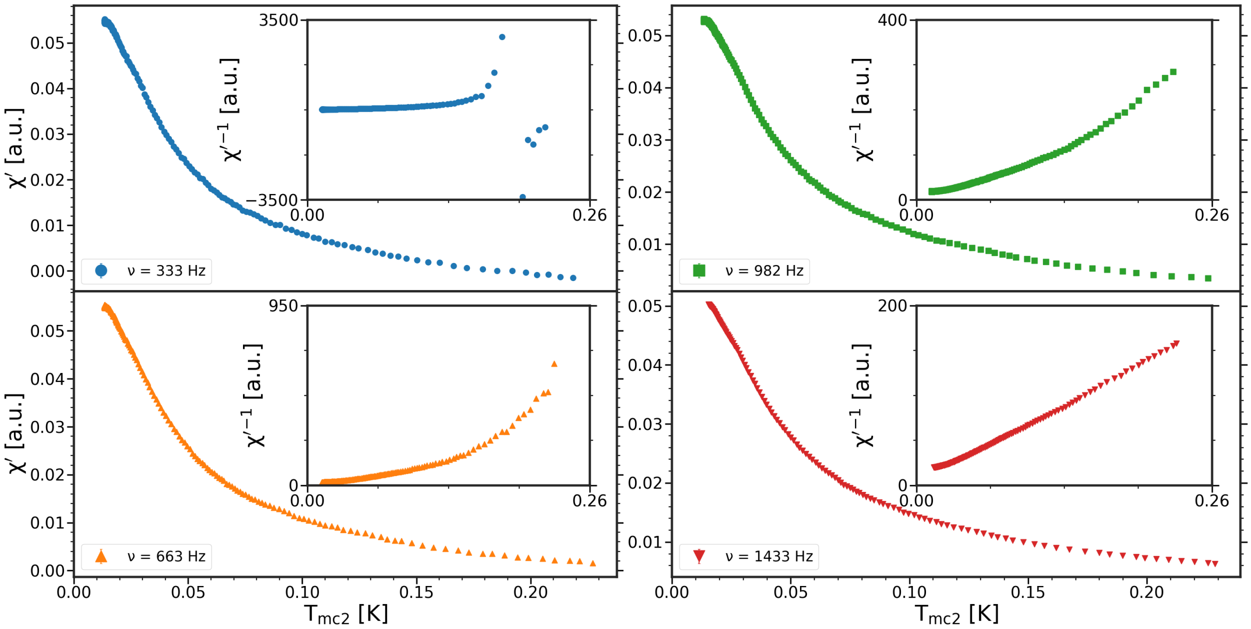

Figure 93: This figure is the analogue to Fig. 34 but where they have been conducted while cooling.

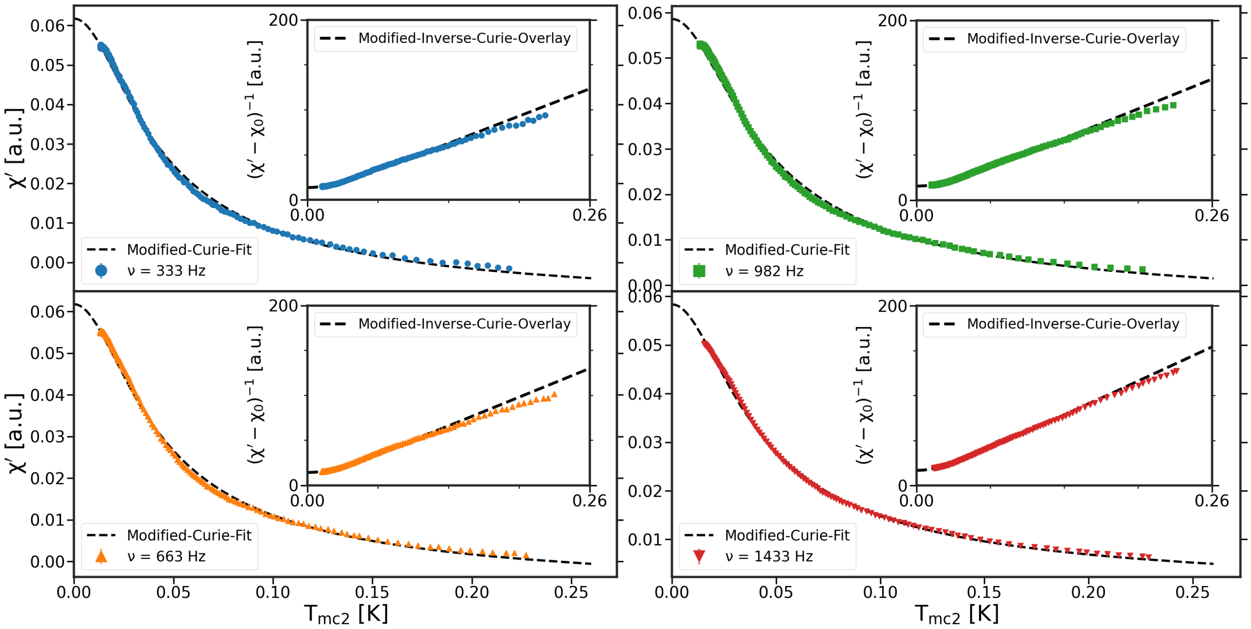

Figure 94: This Figure is the analogue to Fig. 35. It is meant to show that the fit from Eq. 93 is poor for cooling measurements of the pace shown in Fig. 92.

K Appendix of Herbertsmithite

K.1 Setup Configuration 1

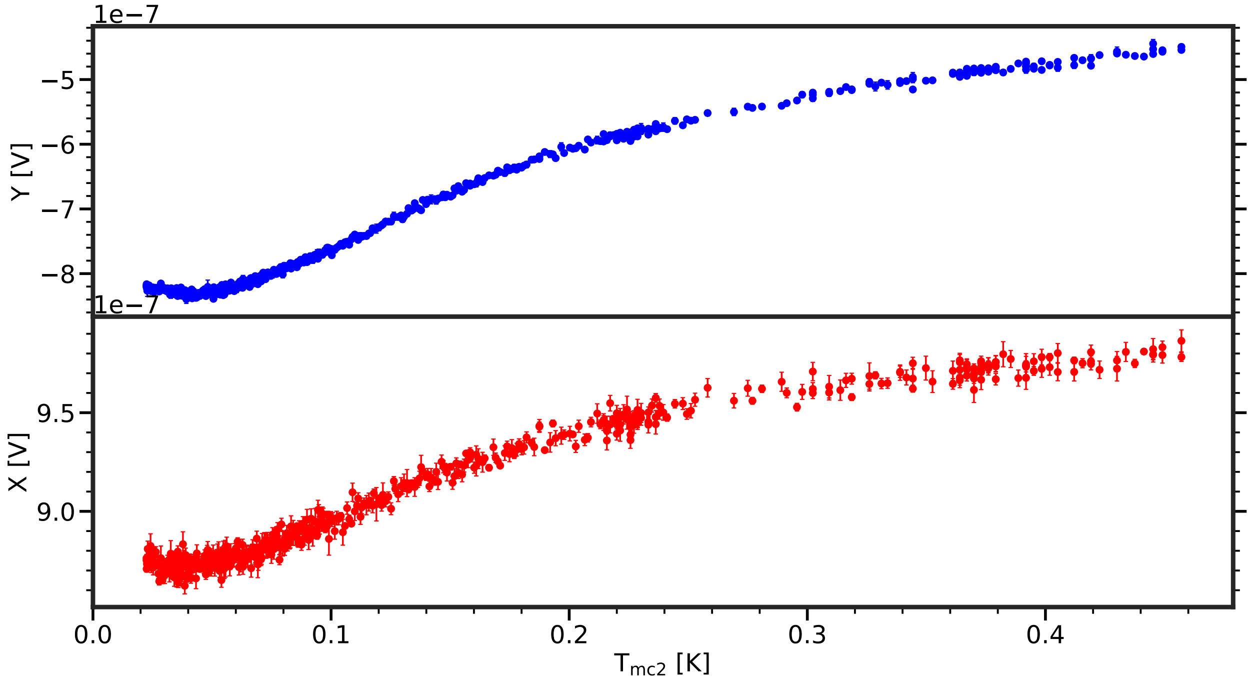

Figure 95: Raw data of herbertsmithite as a function of T_{mc2} for $H_{\mathrm{AC}} \approx 17\,\mathrm{Am}^{-1}$ and at an excitation frequency of $\nu = 982\,\mathrm{Hz}$ using configuration 1. This measurement relates to the measurement discussed in Section 6.7. **Top**: The Y component of the voltage. **Bottom**: The X component of the voltage.

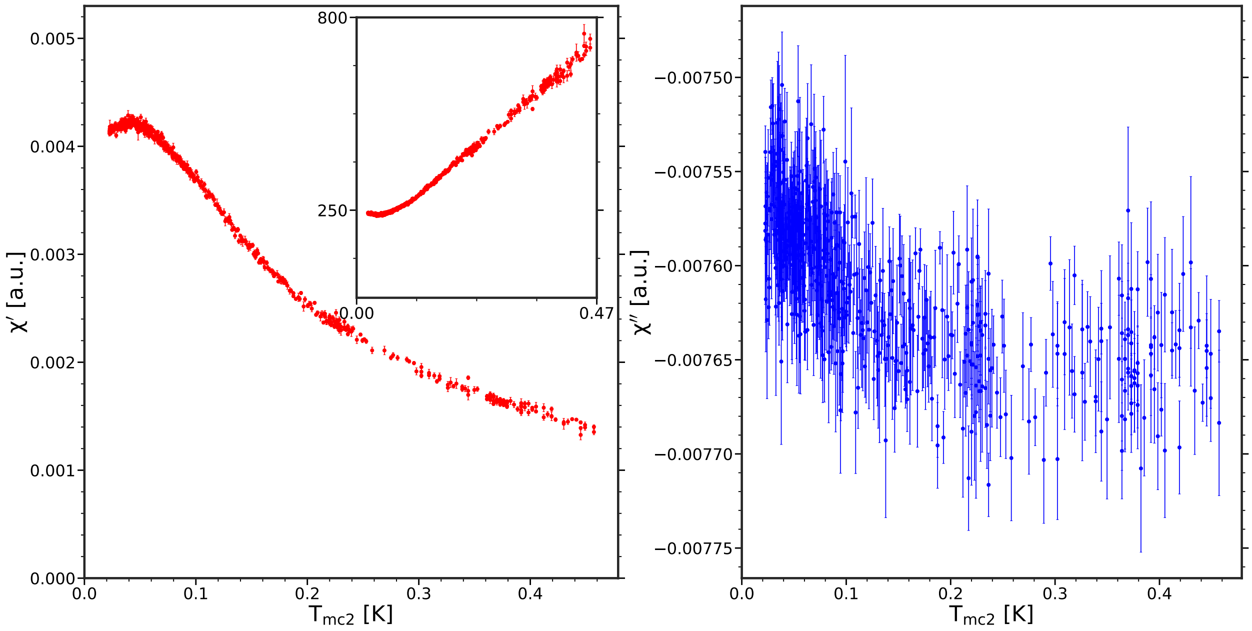

Figure 96: The AC susceptibility of herbertsmithite as a function of T_{mc2} for $H_{\mathrm{AC}} \approx 17\,\mathrm{Am}^{-1}$ and at an excitation frequency of $\nu = 982\,\mathrm{Hz}$ using configuration 1. The components have been separated using Θ from Table 2. This measurement relates to the measurement shown in Fig. 51 and 52. **Top**: The out-of-phase component (χ'') **Bottom**: The in-phase component.

K.2 Setup Configuration 2

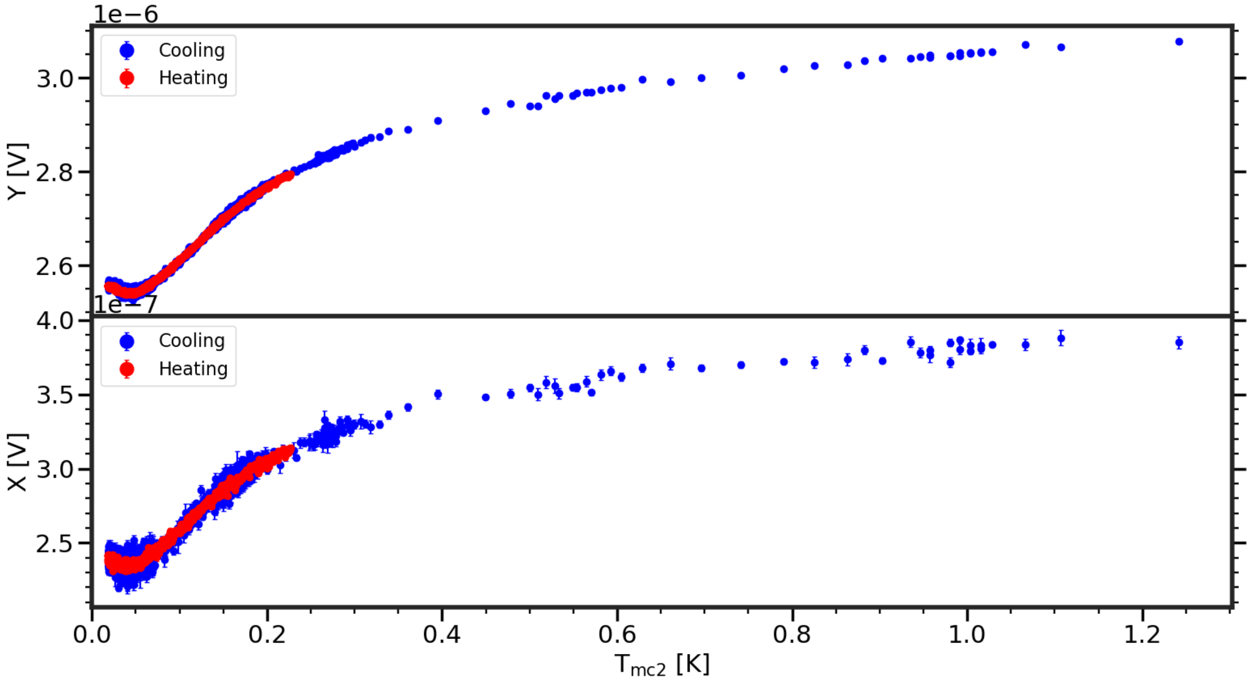

Figure 97: Raw data of herbertsmithite as a function of T_{mc2} for $H_{\mathrm{AC}} \approx 17\,\mathrm{Am}^{-1}$ and at an excitation frequency of $\nu = 982\,\mathrm{Hz}$ using configuration 2. This measurement relates to Fig. 56 and 58. **Top**: The Y component of the voltage. **Bottom**: The X component of the voltage.

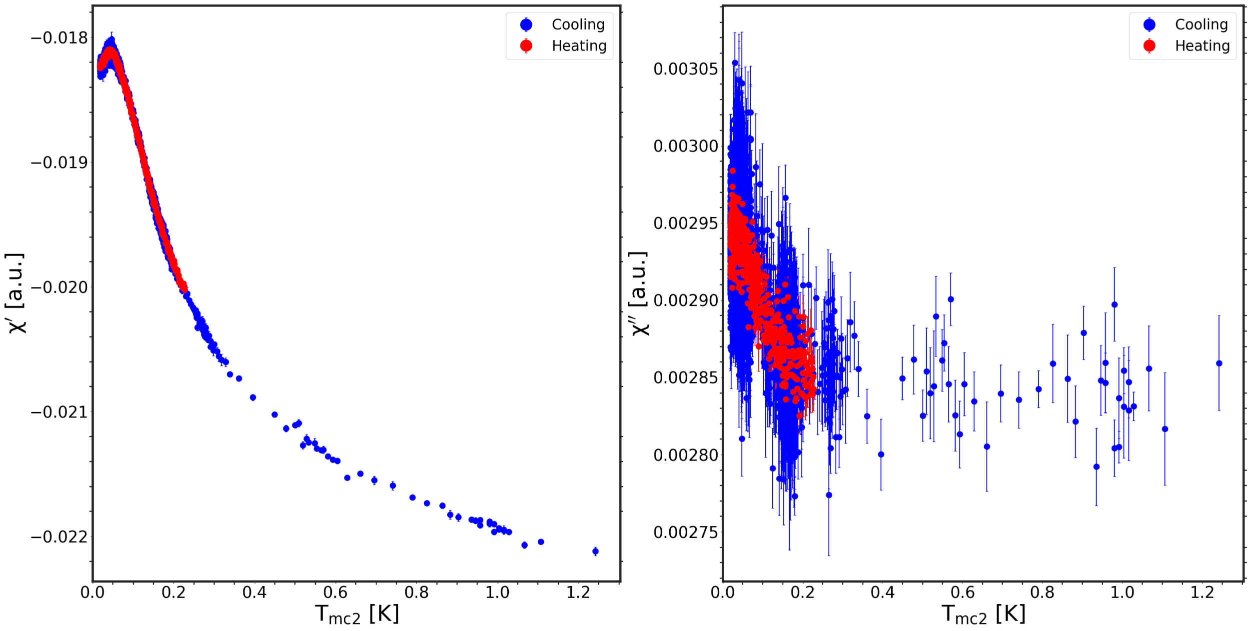

Figure 98: The AC susceptibility of herbertsmithite as a function of T_{mc2} for $H_{\mathrm{AC}} \approx 17\,\mathrm{Am}^{-1}$ and at an excitation frequency of $\nu = 982\,\mathrm{Hz}$ using configuration 2. The components have been separated using Θ_{new} from Table 7 and 9. This measurement relates to the measurement shown in Fig. 51 and 52. **Top**: The out-of-phase component (χ'') **Bottom**: The in-phase component.

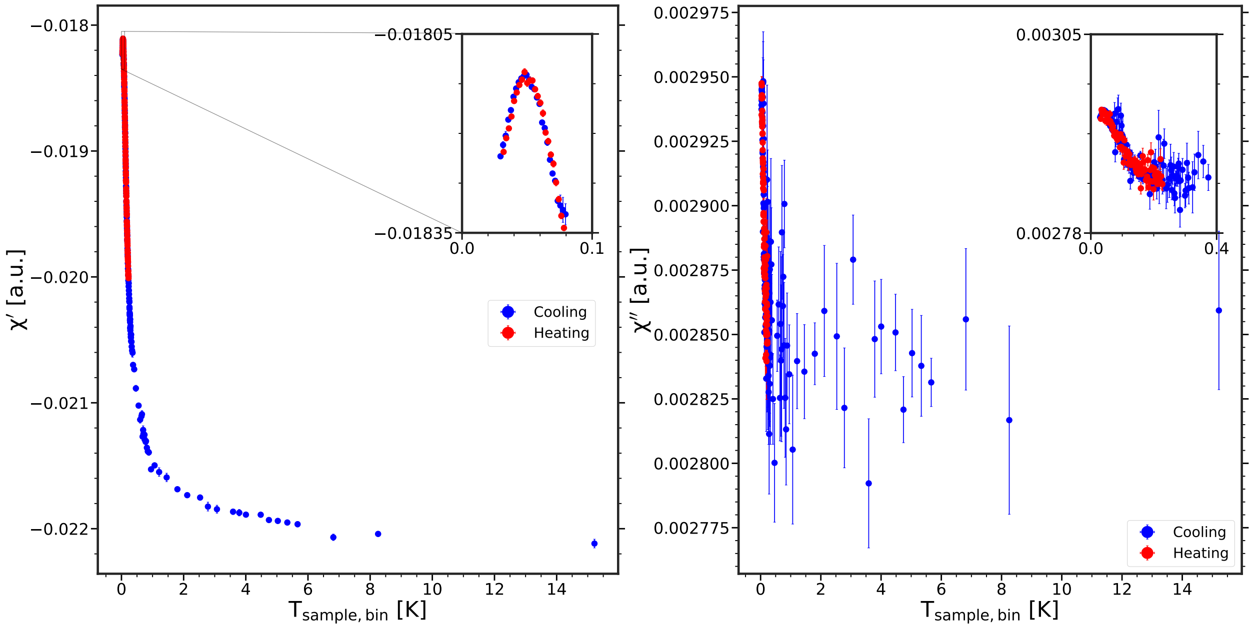

Figure 99: The AC susceptibility of herbertsmithite as a function of $T_{\mathrm{sample,bin}}$ for $H_{\mathrm{AC}} \approx 17\,\mathrm{A\,m^{-1}}$ and at an excitation frequency of $\nu = 982\,\mathrm{Hz}$ using configuration 2. The components have been separated using Θ_{new} from Table 7 and 9. This measurement relates to the measurement shown in Fig. 51 and 52 but shows the full temperature range with no log-scale. The large temperature uncertainties are propagated through Eq. (92). **Top**: The out-of-phase component (χ''). **Bottom**: The in-phase component.

K.3 Various Frequencies Configuration 2

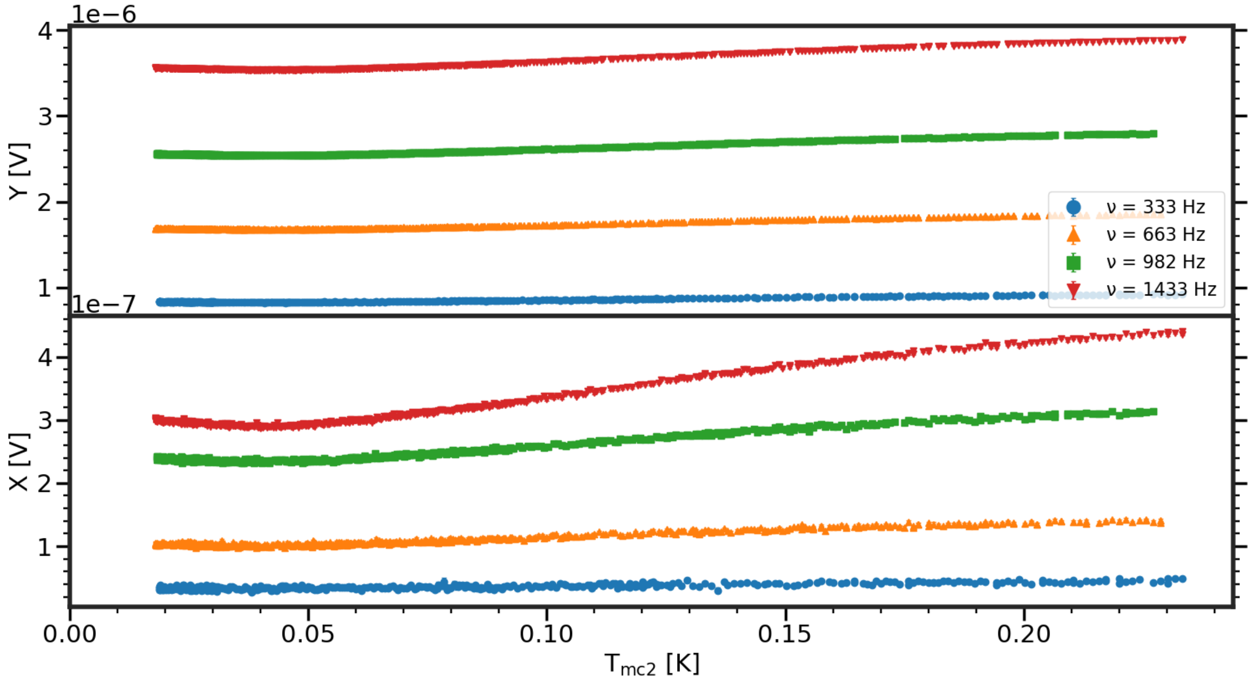

Figure 100: Raw data of herbertsmithite as a function of T_{mc2} for $H_{\mathrm{AC}} \approx 17\,\mathrm{A\,m^{-1}}$ and at an excitation frequency of $\nu = 333\,\mathrm{Hz}$ (●), $663\,\mathrm{Hz}$ (▲), $982\,\mathrm{Hz}$ (■) and $1433\,\mathrm{Hz}$ (▼) using configuration 2. These measurements relates to Fig. 59 and 61. **Top**: The Y component of the voltage. **Bottom**: The X component of the voltage.

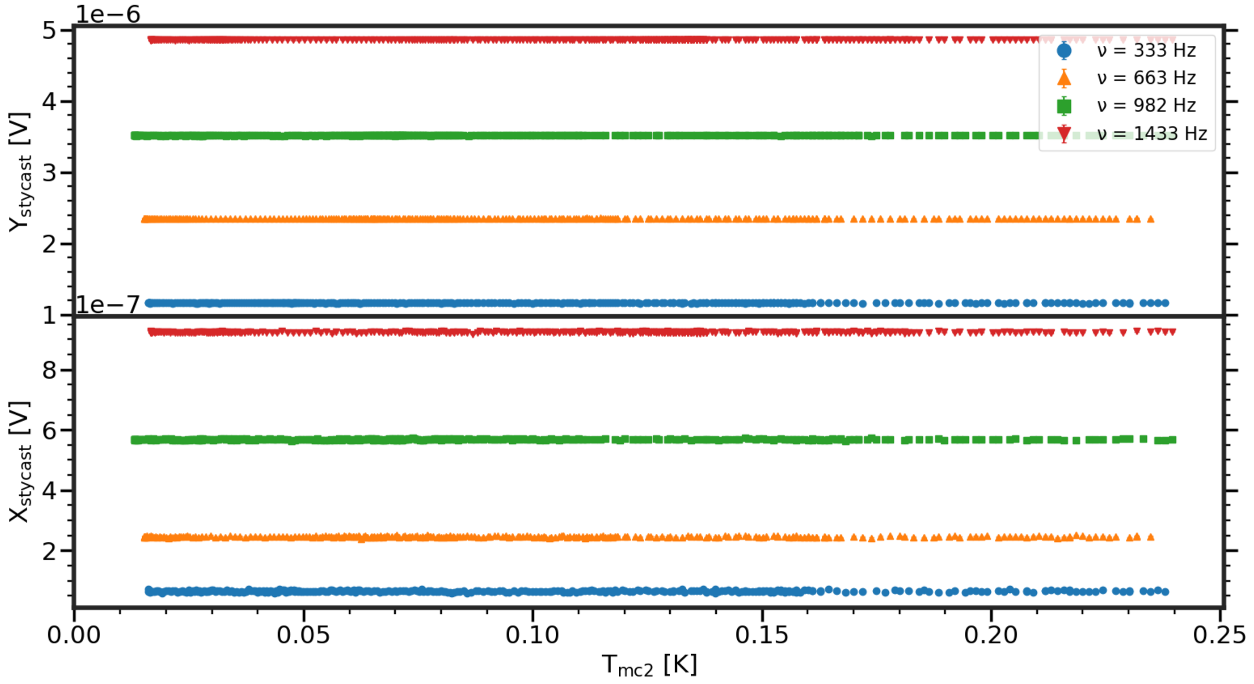

Figure 101: Raw data of pure stycast as a function of T_{mc2} for $H_{\mathrm{AC}} \approx 17\,\mathrm{Am}^{-1}$ and at an excitation frequency of $\nu = 333\,\mathrm{Hz}$ (●), 663 Hz (▲), 982 Hz (■) and 1433 Hz (▼) using configuration 2. These measurement relates to Fig. 102 and 103. **Top**: The Y component of the voltage. **Bottom**: The X component of the voltage.

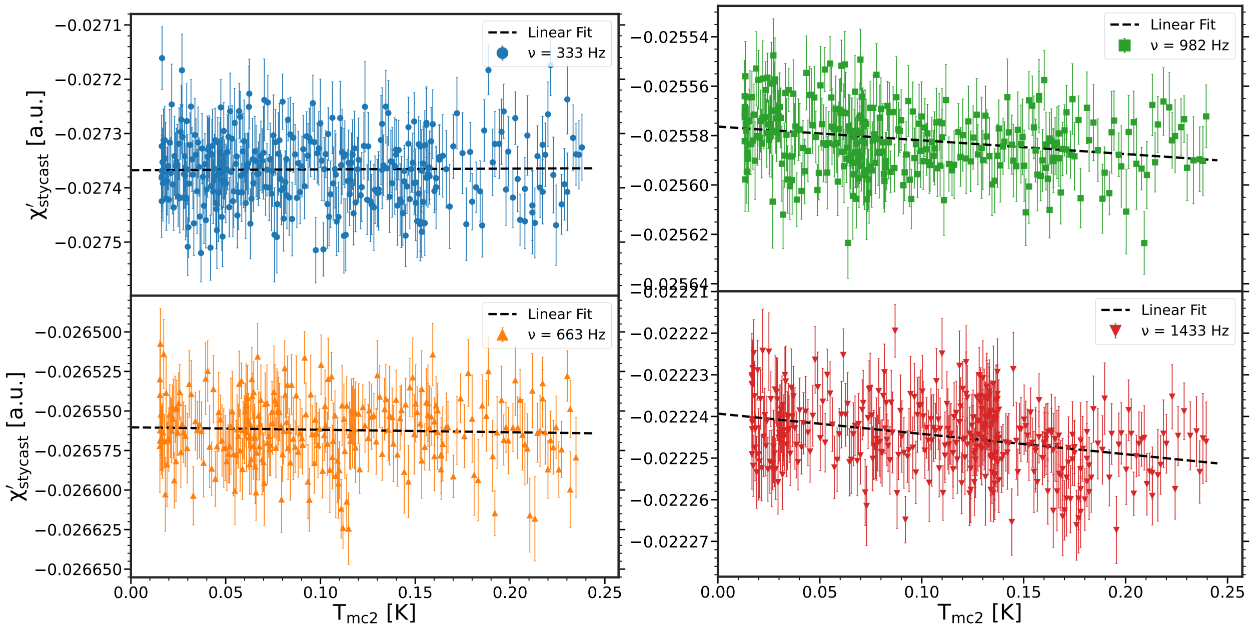

Figure 102: The in-phase component for pure stycast (χ'_{stycast}) as a function of T_{mc2} for $H_{\mathrm{AC}} \approx 17\,\mathrm{Am}^{-1}$ and at an excitation frequencies of $\nu = 333\,\mathrm{Hz}$ (●), 663 Hz (▲), 982 Hz (■) and 1433 Hz (▼) along with linear fits applied. The fit parameters are shown in Table 12. These measurements relate to Fig. 59.

ν [Hz]	333	663	982	1433
a [a.u.]	$0.02(5) \times 10^{-3}$	$-0.02(2) \times 10^{-3}$	$-0.056(12) \times 10^{-3}$	$-49(7) \times 10^{-6}$
b [a.u.]	$-27.368(6) \times 10^{-3}$	$-26.5603(24) \times 10^{-3}$	$-25.5764(13) \times 10^{-3}$	$-22.2393(9) \times 10^{-3}$

Table 12: Fit parameters obtained from the linear fits ($aT_{\mathrm{mc2}} + b$) shown in Fig. 102. The uncertainty on the slope (a) for $\nu = 333\,\mathrm{Hz}$ and $\nu = 663\,\mathrm{Hz}$ remains quite large considering the fit value which is an indication of the data trend being flat. Thus, one could argue that a weighted mean here would be sufficient. However, for $\nu = 982\,\mathrm{Hz}$ and $\nu = 1433\,\mathrm{Hz}$ the uncertainty is larger due to the fact that the temperature dependent behavior of χ'_{stycast} behaves in a linear manner.

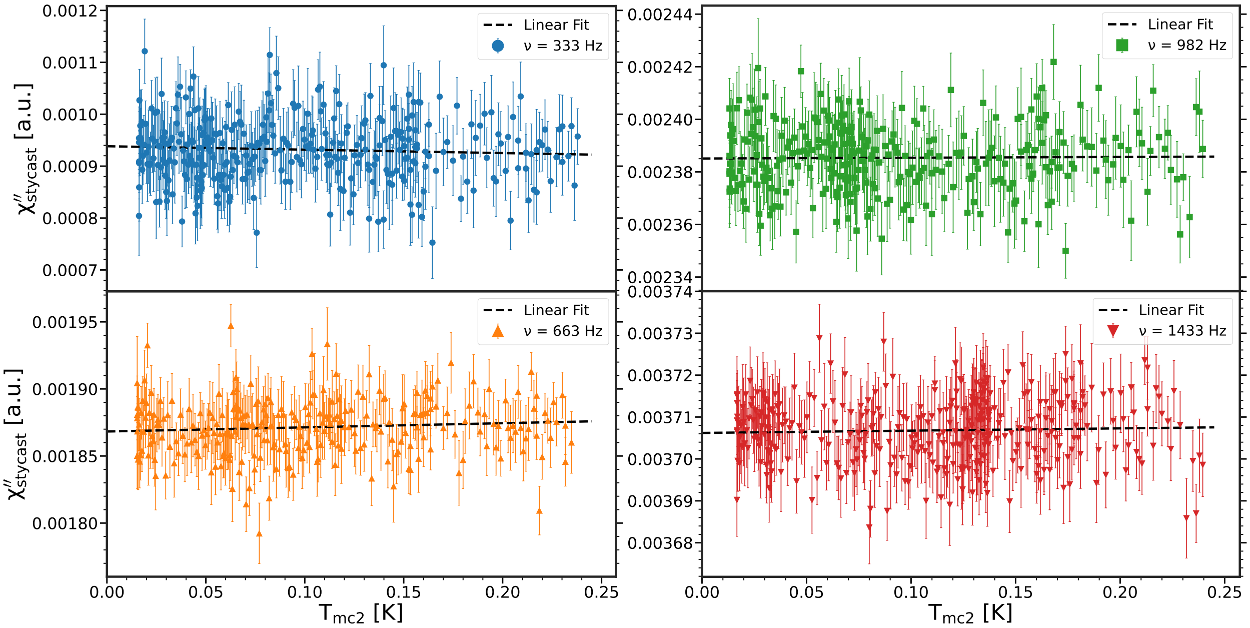

Figure 103: The out-of-phase component for pure stycast ($\chi''_{\mathrm{stycast}}$) as a function of T_{mc2} for $H_{\mathrm{AC}} \approx 17\,\mathrm{Am}^{-1}$ and at an excitation frequencies of $\nu = 333\,\mathrm{Hz}$ (●), 663 Hz (▲), 982 Hz (■) and 1433 Hz (▼) along with linear fits applied. The fit parameters are shown in Table 13. These measurements relate to Fig. 61.

ν [Hz]	333	663	982	1433
a [a.u.]	$-0.07(5) \times 10^{-3}$	$0.031(19) \times 10^{-3}$	$0.003(12) \times 10^{-3}$	$5(7) \times 10^{-6}$
b [a.u.]	$938(6) \times 10^{-6}$	$1.868(2) \times 10^{-3}$	$2.3851(13) \times 10^{-3}$	$3.7062(9) \times 10^{-3}$

Table 13: Fit parameters obtained from the linear fits ($aT_{\mathrm{mc2}} + b$) shown in Fig. 103. The uncertainty on the slope (a) for all excitation frequencies remains quite large considering the fit value which is an indication of the data trend being flat. Thus, one could argue that a weighted mean here would be sufficient.

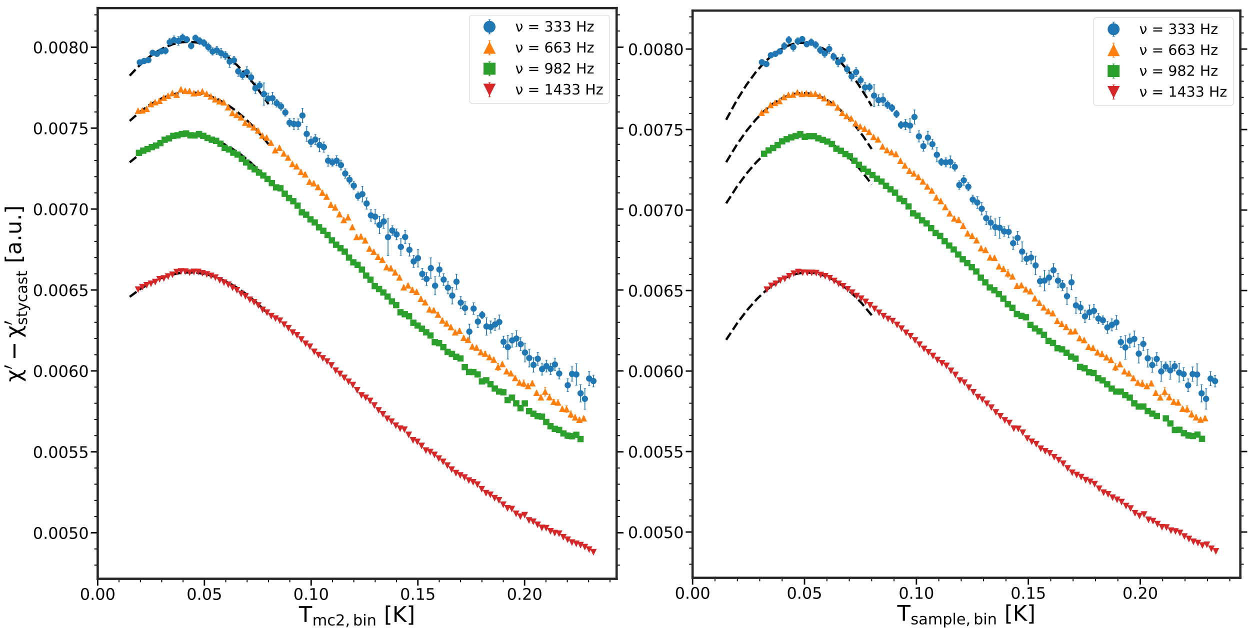

Figure 104: The in-phase component $(\chi' - \chi'_{\mathrm{stycast}})$ for the excitation frequencies of $\nu = 333\,\mathrm{Hz}$ (●), 663 Hz (▲), 982 Hz (■) and 1433 Hz (▼) along with applied Gaussian fits estimating the peak temperature. Fit parameters are shown in Table 14 and 15. These measurements relate to Fig. 59. **Left**: $(\chi' - \chi'_{\mathrm{stycast}})$ vs $T_{\mathrm{mc2,bin}}$. **Right**: $(\chi' - \chi'_{\mathrm{stycast}})$ vs $T_{\mathrm{sample,bin}}$.

ν [Hz]	333	663	982	1433
N	$2.41(16) \times 10^{-3}$	$2.48(6) \times 10^{-3}$	$2.49(5) \times 10^{-3}$	$2.166(27) \times 10^{-3}$
μ	$42.5(10) \times 10^{-3}$	$42.6(3) \times 10^{-3}$	$43.3(3) \times 10^{-3}$	$43.1(2) \times 10^{-3}$
σ	0.120(8)	0.128(3)	0.133(2)	0.1308(17)

Table 14: Table containing the fit parameters from the Gaussian fits applied on to $(\chi' - \chi'_{\mathrm{stycast}})$ vs $T_{\mathrm{mc2,bin}}$ in Fig. 104 (left).

ν [Hz]	333	663	982	1433
N	$1.96(8) \times 10^{-3}$	$1.962(90) \times 10^{-3}$	$1.94(2) \times 10^{-3}$	$1.664(11) \times 10^{-3}$
μ	$49.1(4) \times 10^{-3}$	$49.27(14) \times 10^{-3}$	$50.24(10) \times 10^{-3}$	$51.27(7) \times 10^{-3}$
σ	0.097(4)	0.1013(16)	0.1037(11)	0.1004(7)

Table 15: Table containing the fit parameters from the Gaussian fits applied on to $(\chi' - \chi'_{\mathrm{stycast}})$ vs $T_{\mathrm{sample,bin}}$ in Fig. 104 (right).

K.4 Various Fields Configuration 2

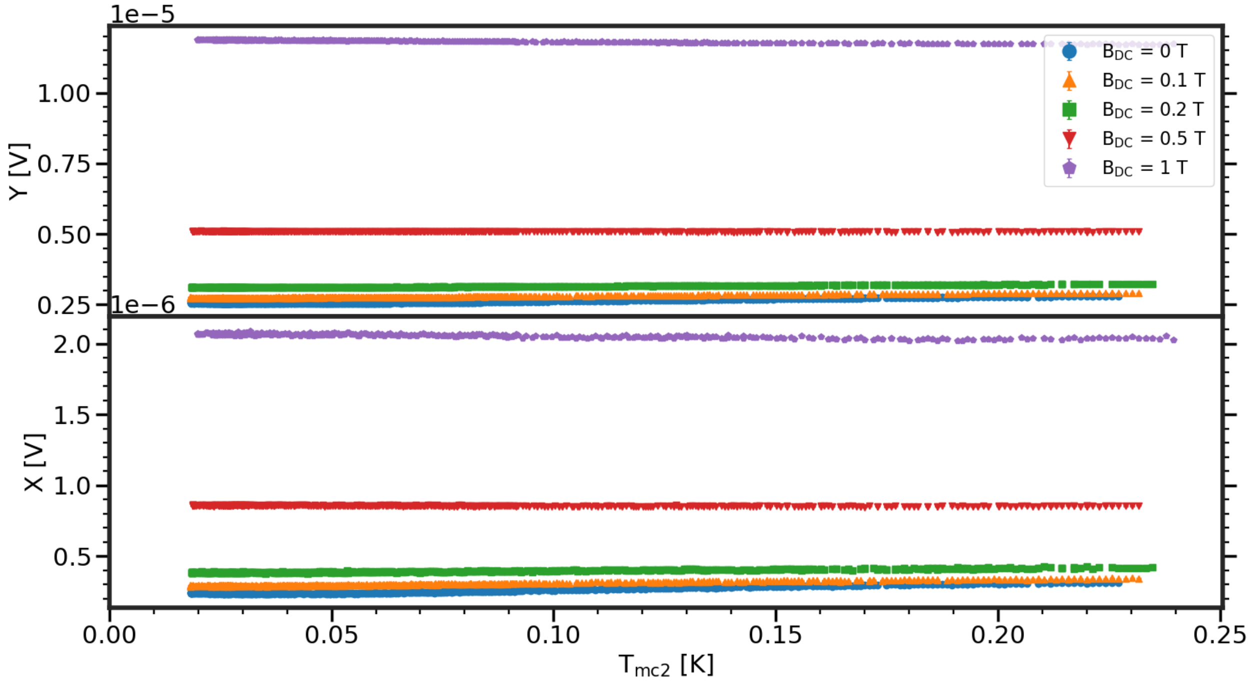

Figure 105: Raw data of HS as a function of T_{mc2} for $H_{\mathrm{AC}} \approx 17\,\mathrm{Am}^{-1}$ at an excitation frequency of $\nu = 982\,\mathrm{Hz}$ and using a DC field of $B_{\mathrm{DC}} = 0\,\mathrm{T}$ (●), $0.1\,\mathrm{T}$ (▲), $0.2\,\mathrm{T}$ (■), $0.5\,\mathrm{T}$ (▼) and $1\,\mathrm{T}$ (⬟) using configuration 2.

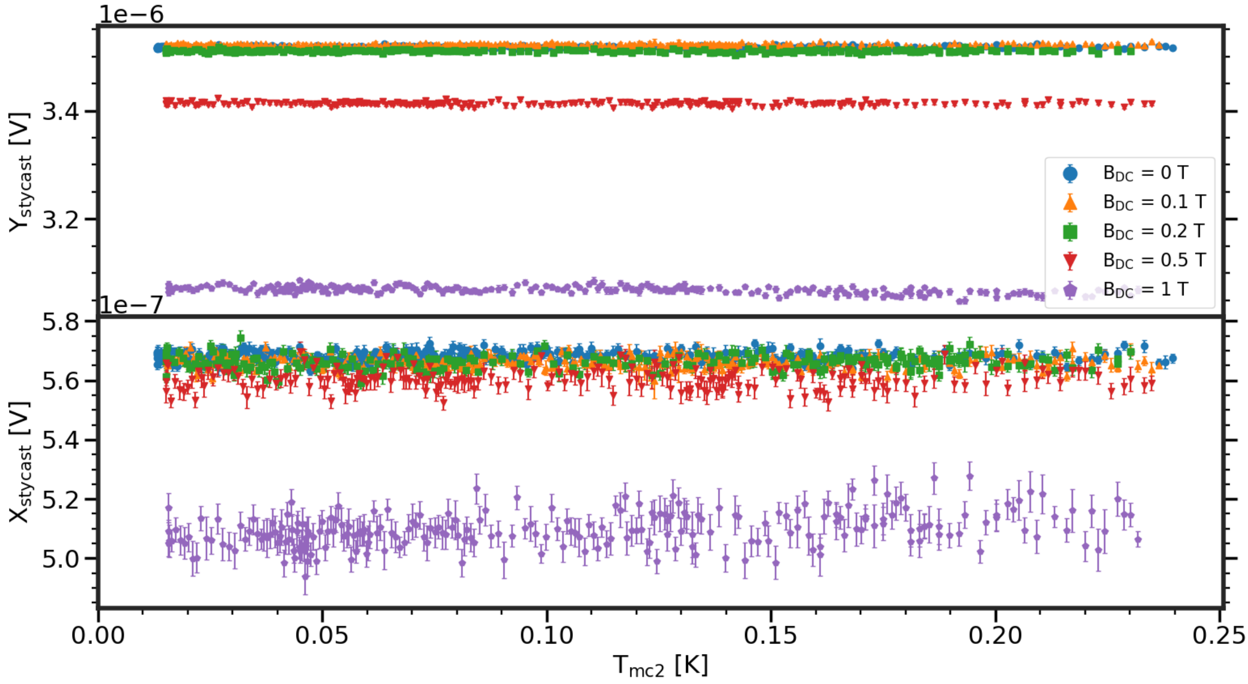

Figure 106: Raw data of HS as a function of T_{mc2} for $H_{\mathrm{AC}} \approx 17\,\mathrm{Am}^{-1}$ at an excitation frequency of $\nu = 982\,\mathrm{Hz}$ and using a DC field of $B_{\mathrm{DC}} = 0\,\mathrm{T}$ (●), $0.1\,\mathrm{T}$ (▲), $0.2\,\mathrm{T}$ (■), $0.5\,\mathrm{T}$ (▼) and $1\,\mathrm{T}$ (⬟) using configuration 2. These measurements relate to Fig. 107 and 108. **Top**: The Y component of the voltage. **Bottom**: The X component of the voltage.

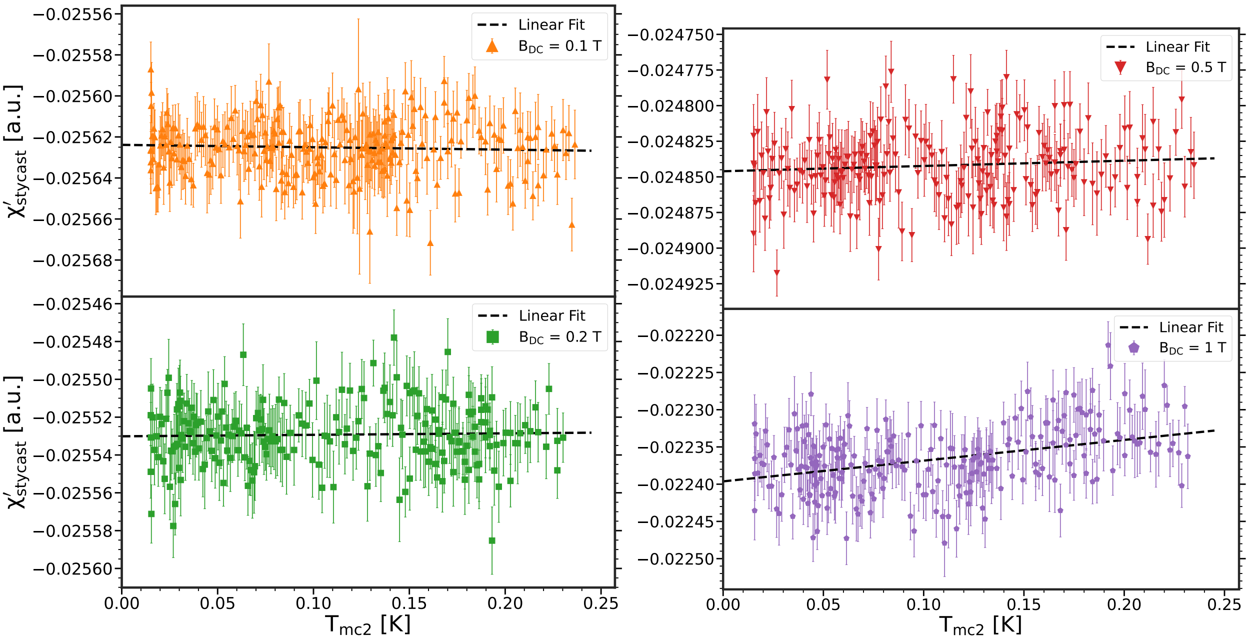

Figure 107: The in-phase component for pure stycast (χ'_{stycast}) as a function of T_{mc2} for $H_{\text{AC}} \approx 17\,\text{Am}^{-1}$ at an excitation frequency of $\nu = 982\,\text{Hz}$ and using a DC field of $B_{\text{DC}} = 0\,\text{T}$ (●), 0.1 T (▲), 0.2 T (■), 0.5 T (▼) and 1 T (⬟) along with linear fits applied. The fit parameters are shown in table 16. These measurements relate to Fig. 62.

B_{DC} [T]	0.1	0.2	0.5	1
a [a.u.]	$-0.012(14) \times 10^{-3}$	$0.008(16) \times 10^{-3}$	$0.04(3) \times 10^{-3}$	$0.28(4) \times 10^{-3}$
b [a.u.]	$-25.6239(17) \times 10^{-3}$	$-25.5301(21) \times 10^{-3}$	$-24.8460(31) \times 10^{-3}$	$-22.396(4) \times 10^{-3}$

Table 16: Fit parameters obtained from the linear fits ($aT_{\text{mc2}} + b$) shown in Fig. 107. The uncertainty on the slope (a) of the majority of fits remain large compared to the value, which is an indication of the data trend being flat. Thus, one could argue that a weighted mean here would be sufficient. However, for $B_{\text{DC}} = 1\,\text{T}$ the uncertainty is large due to the fact that the temperature dependent behavior of χ'_{stycast} is not flat.

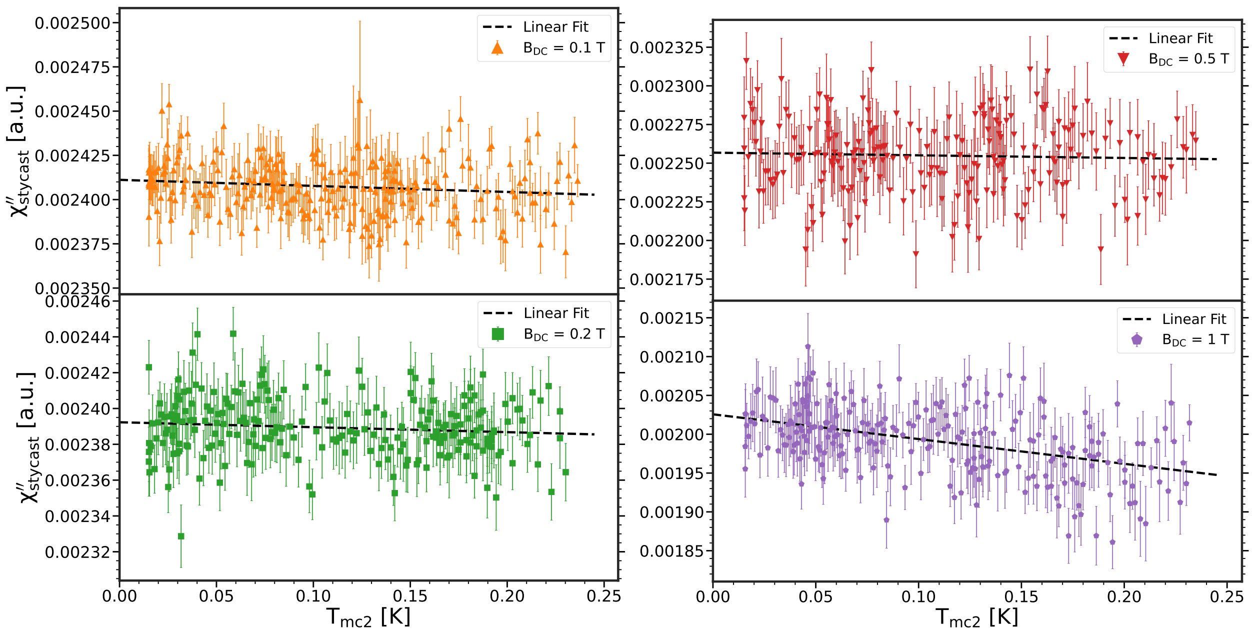

Figure 108: The out-of-phase component for pure stycast ($\chi''_{\mathrm{stycast}}$) as a function of T_{mc2} for $H_{\mathrm{AC}} \approx 17\,\mathrm{Am}^{-1}$ at an excitation frequency of $\nu = 982\,\mathrm{Hz}$ and using a DC field of $B_{\mathrm{DC}} = 0\,\mathrm{T}$ (●), $0.1\,\mathrm{T}$ (▲), $0.2\,\mathrm{T}$ (■), $0.5\,\mathrm{T}$ (▼) and $1\,\mathrm{T}$ (⬟) along with linear fits applied. The fit parameters are shown in Table 17. These measurements relate to Fig. 63.

B_{DC} [T]	0.1	0.2	0.5	1
a [a.u.]	$-0.034(13) \times 10^{-3}$	$-0.028(16) \times 10^{-3}$	$-0.017(24) \times 10^{-3}$	$-0.32(4) \times 10^{-3}$
b [a.u.]	$2.4112(17) \times 10^{-3}$	$2.3923(20) \times 10^{-3}$	$2.2568(29) \times 10^{-3}$	$2.026(4) \times 10^{-3}$

Table 17: Fit parameters obtained from the linear fits ($aT_{\mathrm{mc2}} + b$) shown in Fig. 108. The uncertainty on the slope (a) of the majority of fits remain large compared to the value, which is an indication of the data trend being flat. Thus, one could argue that a weighted mean here would be sufficient. However, for $B_{\mathrm{DC}} = 1\,\mathrm{T}$ the uncertainty is large due to the fact that the temperature dependent behavior of $\chi''_{\mathrm{stycast}}$ is not flat.

L Spin Glass Signatures

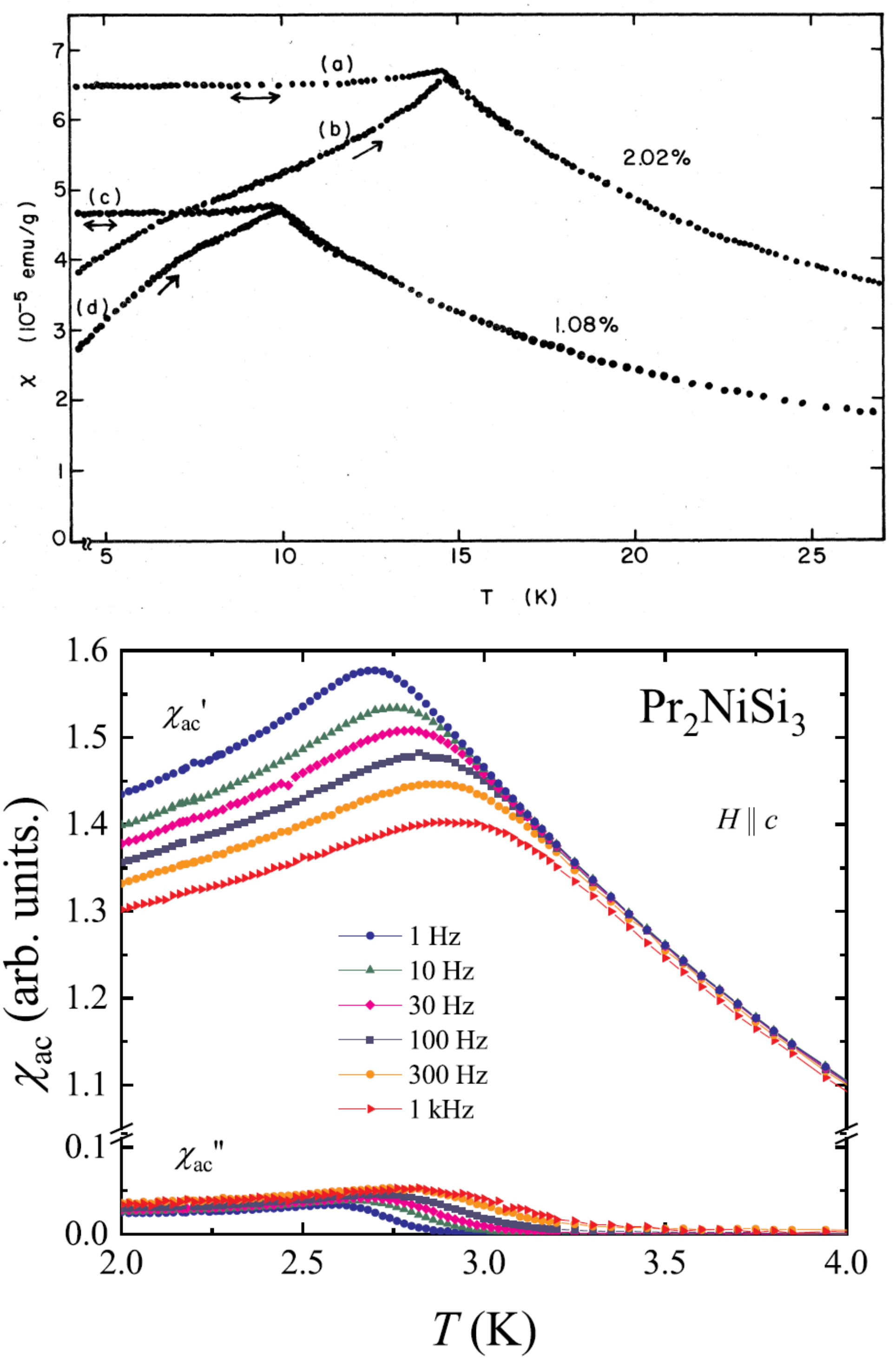

Figure 109: The magnetic Susceptibility of a spin glass. **Top**: The temperature-dependent magnetic DC susceptibility for CuMn spin glass at two different doping percentages of Mn. (a) and (c) show the Field-Cooling susceptibility, whereas (b) and (d) show the Zero-Field-Cooling. A ZFC-FC splitting refers to the splitting in the magnetization between the two scenarios. From [77] **Bottom**: The temperature-dependent AC susceptibility for various excitation frequencies of Pr_2NiSi_3 spin glass. From [78].

M Derivation - Curie Law

The Hamiltonian of the paramagnetic term is given by:

$$\hat{\mathcal{H}} = \mu_{\mathrm{B}}\mathbf{B}\cdot(\mathbf{L}+g\mathbf{S}) = g_J\mu_{\mathrm{B}}\mathbf{B}\cdot\mathbf{J} \tag{102}$$

where g_J represents the *Landé g-factor* and is given by:

$$g_J = \frac{1}{2}(g+1) + \frac{1}{2}(g-1)\left[\frac{S(S+1)-L(L+1)}{J(J+1)}\right] \tag{103}$$

Assuming a applied magnetic field along the z axis, the energy becomes:

$$E = \mu_{\mathrm{B}} g_J B m_J \tag{104}$$

where the quantum number m_J can take the following values $m_J = -J, -J+1, -J+2 ... J-1, J$ resulting in the partition function. The partition function is defined as:

$$Z = \sum_i e^{-\frac{E_i}{k_{\mathrm{B}}T}} \tag{105}$$

where the sum is over each energy level in the system. In this case the amount of energy levels are given by the number of values m_J can take. Thus, the partition function becomes:

$$Z = \sum_{m_J=-J}^{m_J=J} e^{-\mu_{\mathrm{B}} g_J \frac{Bm_J}{k_{\mathrm{B}}T}} \tag{106}$$

By performing the following substitution $m_J \to p - J$, the partition function becomes:

$$= e^{\mu_{\mathrm{B}} g_J \frac{BJ}{k_{\mathrm{B}}T}} \sum_{p=0}^{p=2J} e^{-\mu_{\mathrm{B}} g_J \frac{Bp}{k_{\mathrm{B}}T}} = e^{\mu_{\mathrm{B}} g_J \frac{BJ}{k_{\mathrm{B}}T}} \sum_{p=0}^{p=2J} \left(e^{-\mu_{\mathrm{B}} g_J \frac{B}{k_{\mathrm{B}}T}}\right)^p \tag{107}$$

Using the series $1 + x + x^2 ... x^n = \frac{1-x^{n+1}}{1-x}$ the partition function can be reduced to the following expression:

$$= e^{\mu_{\mathrm{B}} g_J \frac{BJ}{k_{\mathrm{B}}T}} \left[\frac{1-\left(e^{-\mu_{\mathrm{B}} g_J \frac{B}{k_{\mathrm{B}}T}}\right)^{2J+1}}{1-e^{-\mu_{\mathrm{B}} g_J \frac{B}{k_{\mathrm{B}}T}}}\right] = \frac{e^{\mu_{\mathrm{B}} g_J \frac{B(2J+1)}{2k_{\mathrm{B}}T}} - e^{-\mu_{\mathrm{B}} g_J \frac{B(2J+1)}{2k_{\mathrm{B}}T}}}{e^{\mu_{\mathrm{B}} g_J \frac{B}{2k_{\mathrm{B}}T}} - e^{-\mu_{\mathrm{B}} g_J \frac{B}{2k_{\mathrm{B}}T}}} = \frac{\sinh\left(\frac{1}{2}\mu_{\mathrm{B}} g_J \frac{B(2J+1)}{k_{\mathrm{B}}T}\right)}{\sinh\left(\frac{1}{2}\mu_{\mathrm{B}} g_J \frac{B}{k_{\mathrm{B}}T}\right)} \tag{108}$$

The Helmtholtz free energy per n spins per unit volume is given by $F = -nk_{\mathrm{B}}T\ln(Z)$. Thus, the free energy for the given partition function is:

$$F = -nk_{\mathrm{B}}T\left[\ln\left(\sinh\left(\frac{1}{2}\mu_{\mathrm{B}} g_J \frac{B(2J+1)}{k_{\mathrm{B}}T}\right)\right) - \ln\left(\sinh\left(\frac{1}{2}\mu_{\mathrm{B}} g_J \frac{B}{k_{\mathrm{B}}T}\right)\right)\right] \tag{109}$$

which results in the following expression for the magnetization:

$$M = -\left(\frac{\partial F}{\partial B}\right)_T = \frac{1}{2}n\mu_{\mathrm{B}} g_J\left[(2J+1)\coth\left(\frac{1}{2}\mu_{\mathrm{B}} g_J \frac{B(2J+1)}{k_{\mathrm{B}}T}\right) - \coth\left(\frac{1}{2}\mu_{\mathrm{B}} g_J \frac{B}{k_{\mathrm{B}}T}\right)\right] \tag{110}$$

for small magnetic fields we can make the approximation $\coth(x) \approx \frac{1}{x} + \frac{x}{3}$ for $x \ll 1$, meaning the magnetization becomes:

$\coth(x) \approx \frac{1}{x} + \frac{x}{3}$ for $x \ll 1$ the susceptibility becomes:

$$\approx \frac{1}{2} n\mu_{\mathrm{B}} g_J \left[\frac{\mu_{\mathrm{B}} g_J B (2J+1)^2}{6k_{\mathrm{B}}T} - \frac{\mu_{\mathrm{B}} g_J B}{6k_{\mathrm{B}}T} \right] = \frac{n\mu_{\mathrm{B}}^2 g_J^2 B J(J+1)}{3k_{\mathrm{B}}T} \tag{111}$$

at which point the susceptibility becomes:

$$\chi = \mu_0 \frac{\partial M}{\partial B} = \frac{n\mu_0 \mu_{\mathrm{B}}^2 g_J^2 J(J+1)}{3k_{\mathrm{B}}T} \tag{112}$$

which is known as the *Curie Law* for any value of $\mathbf{J}$ provided $\mathbf{J} \neq 0$